Superconducting Generators for Large Direct-Drive Wind Turbines

---

Kevin Kails

Doctor of Philosophy

The University of Edinburgh

2020

Abstract

This thesis further improves upon the original 10 MW design of the double claw pole generator, by systematically addressing its shortcomings. The original design is a fully iron-cored machine with a stationary superconducting field winding. Its structure allows it to be highly modular, reliable and cost-effective. Its main disadvantages are, when compared to other superconducting generator designs, its weight and efficiency.

The double claw pole generator is a large diameter iron-cored axial-flux machine, due to these features a very stiff mechanical structure is required to main the air gap clearances, which leads to a very heavy structural mass. A novel stator design is introduced, which partially deviates the air gap closing forces into the radial direction, reducing the axial component of forces. This enabled the structural mass to be reduced from 126 tonnes to 115 tonnes.

Secondly, the field core of the double claw pole machine was replaced by an inner stator. The additional stator increases the electric loading of the machine while also further increasing its modularity and improving the generator efficiency. With a target efficiency of 95 %, the power output of the generator was increased from 10 MW to 11.5 MW, while maintaining the same machine diameter and axial length.

To further increase the power density and modularity, the possibility of stacking machine modules was explored. Stacking two standardised modules concentrically was found to result in a smaller and lighter machine than the original design. Additionally, the standardised modules, due to their smaller size, greatly simplify the transportation of the generator.

The addition of the inner stator was found to be a very promising design. It improves the original concept of the machine in terms of power density, efficiency and modularity. It is believed that this makes the design even more competitive in the high-temperature superconducting generator market.

Finally, detailed electromagnetic modelling of superconductors was performed in the electromagnetic environment relevant to electrical machines. Particular focus was put on the dynamic loss mechanisms in superconducting field windings. Through the new knowledge gained on the loss characteristics, the cooling requirements can be better understood, potentially increasing the reliability of superconducting windings and their associated cooling systems.

Declaration

I declare that this thesis was composed by myself, that the work contained herein is my own except where explicitly stated otherwise in the text, and that this work has not been submitted for any other degree or professional qualification except as specified.

Significant parts of the work outlined in this thesis have been published:

Chapter 5 is based on: Kails K. *et al., "*Novel model of stator design to reduce the mass of superconducting generators", *Superconductor Science and Technology,* vol. 31 no. 5, p. 1-8, 2018.

Chapter 6 in based on

- Kails K. *et al.*, "Mass reduction of superconducting generators for large wind turbines", *Journal of Engineering,* vol. 2019, no. 17, p. 3972 – 3975, 2019.
- Kails K. *et al.*, "A modular and cost-effective HTS generator for large direct-drive wind turbines", *IET Renewable Power Generation (* under review).

Chapter 7 is based on: Kails K. *et al.*, "Modular and Stackable Power Generators for Efficient Renewable Power Generation", *IET Renewable Power Generation*, vol. 13, no. 15, 2019.

Chapter 8 is based on:

- Kails K. *et al.,* "Dynamic loss of HTS field windings in rotating electric machines", *Superconductor Science and Technology,* vol. 33, no. 4, 2020
- Kails K. *et al.,* "Loss characteristics of HTS coated conductors in field windings of electric aircraft propulsion motors", *Superconductor Science and Technology,* vol. 33, no. 6, 2020.
- Kails K. *et al.,* "T - formulation based numerical modelling of dynamic loss with a DC background field", *Journal of Physics: Conference Series,* vol. 1559, EUCAS 2019, 2020.

The full list of publications is presented on the next page.

List of Publications

Kails K., Li Q. and Mueller M., "Novel model of stator design to reduce the mass of superconducting generators", *Superconductor Science and Technology*, vol. 31 no. 5, p. 1-8, 2018.

Kails K., Li Q. and Mueller M., "Mass reduction of superconducting generators for large wind turbines", *Journal of Engineering*, vol. 2019, no. 17, p. 3972 – 3975, 2019.

Kails K., Li Q. and Mueller M., "Modular and Stackable Power Generators for Efficient Renewable Power Generation", IET Renewable Power Generation, vol. 13, no. 15, 2019.

Kails K., Zhang H., Machura P., Mueller M. and Li Q., "Dynamic loss of HTS field windings in rotating electric machines", *Superconductor Science and Technology*, vol. 33, no. 4, 2020

Kails K., Zhang H., Mueller M. and Li Q., "Loss characteristics of HTS coated conductors in field windings of electric aircraft propulsion motors", *Superconductor Science and Technology*, vol. 33, no. 6, 2020.

Kails K., Yao M., Zhang H., Machura P., Mueller M. and Li Q., "T - formulation based numerical modelling of dynamic loss with a DC background field", *Journal of Physics: Conference Series*, vol. 1559, EUCAS 2019, 2020.

Zhang H., Yao M., **Kails K.**, Machura P., Mueller M., Jiang Z., Xin Y. and Li Q., "Modelling of electromagnetic loss in HTS coated conductors over a wide frequency band", *Superconductor Science and Technology*, vol. 33, no. 2, 2020.

Machura P., Zhang H., **Kails K.** and Li Q., "Loss characteristics of superconducting pancake, solenoid and spiral coils for wireless power transfer", *Superconductor Science and Technology*, vol. 33, no. 7, 2020.

Machura P., **Kails K.** and Li Q., "Loss analysis of superconducting wireless charging for electric vehicles", *Journal of* Physics: Conference Series, vol. 1559, EUCAS 2019, 2020.

Kails K., Li Q. and Mueller M., "A modular and cost-effective HTS generator for large direct-drive wind turbines", *IET Renewable Power Generation* (under review).

Acknowledgements

I would like to thank my supervisors Dr Quan Li and Prof Markus Mueller for their support during my PhD and for giving me the freedom to conduct my research. I would also like to thank Douglas Carmichael and Jamie Graham for their excellent technical support. Additionally, I would like to thank Matt Tasker for the guidance in establishing the applied superconductivity laboratory. Furthermore, I would like to thank all the friends that I have made throughout my PhD for their support and all the good times.

Finally, I would like to thank my family for always being there for me and enabling me to pursue my university studies.

Contents

List of Figures

Chapter 1 Introduction and Motivation

1.1 Wind Energy

In 2017, the World Economic Forum surveyed 750 experts on what the most likely and impactful risks facing humanity are. Climate change was ranked among the world's biggest threats, ranking extreme weather as the most likely risk and among the most impactful [1]. Renewable energy is one of the answers in the fight against climate change. Wind energy in particular has seen a tremendous increase in installed capacity over the past decades. In fact, wind energy is considered to be the world's fastest-growing energy [2]. Figure 1.1 shows the global total installed capacity for onshore and offshore wind turbines over the past two decades. As can be seen there has been a steady increase in the installed capacity.

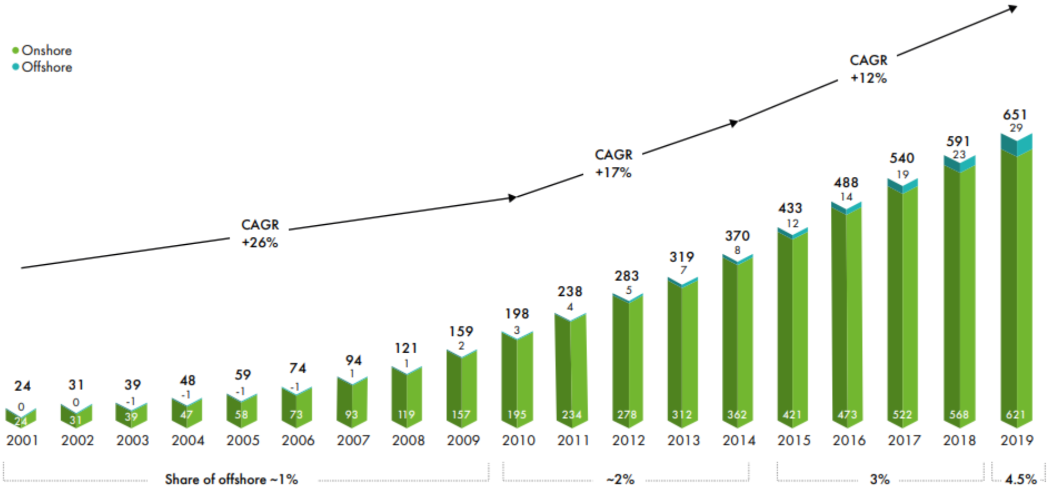

Figure 1.1. Historic development of total installations (in GW) for onshore and offshore wind turbines [3].

Especially the offshore wind energy capacity has seen a remarkable increase in recent years. Figure 1.2 shows the global new installed offshore wind turbines from 2015 to 2019. In 2019 almost twice the capacity of offshore wind turbines was installed when compared to 2015. China in particular has increased the number of installed wind turbines per year significantly. Offshore wind turbines benefit from increased wind speeds, which result in a higher power production. Additionally, wind turbines cover large areas of land, a 3.6 MW wind turbine for example approximately needs 0.37 km^2 of space. A wind farm of 54 turbines would require 20 km^2. Deploying offshore wind turbines can save land rental expenses equivalent to 10 – 18 % of the total operating and maintenance costs of a wind farm [4]. One major factor for the growth of wind energy is the cost of energy.

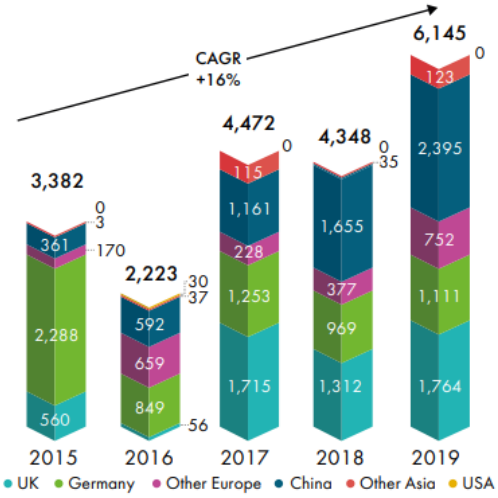

Figure 1.2. New installations (in GW) of offshore wind turbines [3].

In the wind energy industry, there is an ever present strive towards further reducing the cost of energy. To reduce the cost of energy, one method in particular stands out, which is to increase the size of the turbine. In simple terms, it is cheaper and easier to construct and maintain a few very large wind turbines, rather than many smaller ones. The power available from the wind, P_w, is proportional to the cube of its velocity, v, the density of air, ρ_air, and the turbines swept area, A as shown in equation 1.1.

$$P_w = \frac{1}{2}\rho_{\mathrm{air}} A v^3 \tag{1.1}$$

For large wind turbines, the rotational speed of the rotor blades is limited by the rotor blade's maximum tip speed, to minimise noise and excessive centrifugal forces acting on the wind turbine blades. For large wind turbines the tip speed is limited to approximately 75 ms^{-1} [5]. Hence, to increase the harvested power, increasing the swept area is the most efficient method. Figure 1.3 shows the average turbine MW rating for Germany, China and the UK. It can be seen that the average MW rating is predicted to increase significantly in the near future.

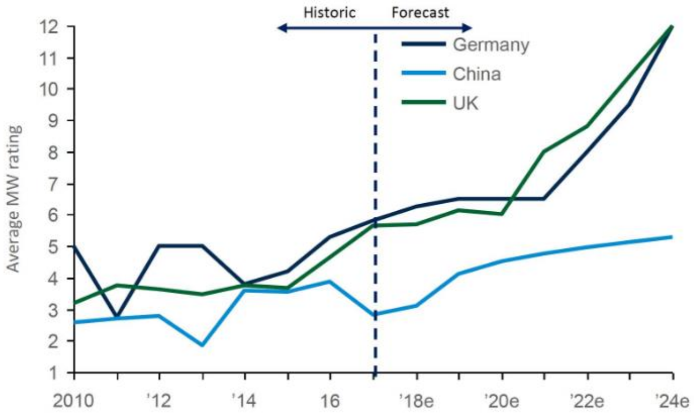

Figure 1.3. MW rating trend for offshore wind turbines [6].

In fact, one big announcement that was made in 2019, confirms some of the MW rating predictions. General Electric commissioned the world's biggest offshore wind turbine and it produced its first kWh in November of the same year. It is rated at 12 MW and is 260 m high with 107-meter long. It generates almost 45 % more energy than the next most powerful wind turbine on the market [7].

In addition, a new generation of offshore wind turbines is expected to emerge in the near future, floating offshore wind turbines. Figure 1.4. shows different floating wind turbine concepts. Having a floating wind turbine promises to further reduce the cost of energy [8].

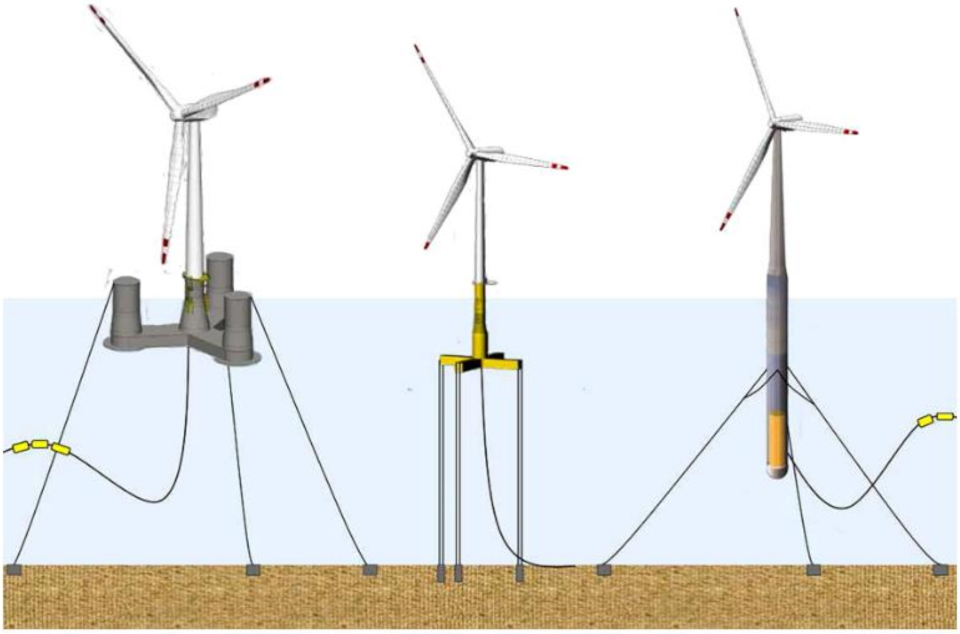

Figure 1.4. Illustration of floating offshore wind turbine concepts [8].

As wind turbines become bigger, the related components become heavier as well. In [2] it is stated that for conventional direct-drive (DD) machines rated higher than 8 MW, the geometric dimensions and total weight increase exponentially resulting in a tower head mass problem. For wind turbines using floating foundations, the tower head mass becomes even more important. A small tower head mass allows to have lighter floaters and less demanding buoyancy requirements for floaters [9]. The tower head mass problem is discussed in further detail in the next section.

1.2 Tower Head Mass Problem

As the rotor blade diameter increases, the rotational speed needs to decrease to maintain the optimal tip speed, to ensure a reasonable energy harvesting efficiency. For instance, the ideal rotational speed for a 10 MW wind turbine is 10 rpm and for 12 MW it is 8 rpm. Two methods exist to connect the wind turbine rotor shaft to an electrical generator. It can either be connected directly or over a gear box. However, the output power of electrical machines is proportional to their rotational speed. Hence, if a direct-drive method is chosen, the generator is expected to be very large and heavy due to the large torque requirements, which also makes it more expensive. With a gearbox the rotational speed of the generator can be increased, hence the generator can be smaller and lighter making it also cheaper. In [10], a 6 MW permanent magnet (PM) generator for wind turbines is investigated for different drivetrain configurations. For the study, the wind turbine, gearbox, converter and generator were modelled to calculate the resultant cost of energy for the different scenarios. The findings of the paper are summarised in table 1.1. The detailed generator design specifications can be found in [10].

Table 1.1. 6 MW permanent magnet generator (PMG) cost comparison

	DD PMG	**PMG 1G**	**PMG 2G**	**PMG 3G**
Generator specifications				
Generator speed (rpm)	12	96	480	1200
Gearbox ratio	-	1:8	1:40	1:100
Stator radius (m)	3.5	2.5	0.7	0.5
Stack length (m)	1.5	0. 4	0.8	0.9
Cost (k€)				
Generator active material	330	77	39	38
Generator construction	436	115	24	10
Gearbox	-	672	1170	1330
Generator system cost	**766**	**864**	**1233**	**1378**

It can be seen that the direct-drive generator is bigger in size than the generators which are connected over a gearbox. The increased size also leads to an increased capital cost. However, when taking the cost of the gearbox into account as well, the direct-drive configuration offers the cheapest generator system cost.

Furthermore, gearboxes are an additional source of failure [11], a major generator failure in offshore wind turbines can lead to several weeks of downtime [12], which in turn has a significant impact on the cost of energy. In [2], generator reliability is stated as one of the major concerns for offshore wind turbine generators. Introducing modularity into the generator designs to allow the generator to continue operating under partial load for certain fault conditions can also offer a significant advantage. Hence, a direct-drive generator is preferred, but with the increasing power rating trend of the offshore wind turbine industry, conventional direct-drive generators simply become too heavy, due to the limited properties of copper and permanent magnets. The generator weight makes up the majority of the nacelle weight, for a 5 MW wind turbine for instance, the nacelle weight is approximately 300 tonnes, of which the rotor blades only represent 120 tonnes. In [4] for example, the weight of a 10 MW PM generator is given as 300 tonnes and in [13] as 325 tonnes, making them as heavy as the complete nacelle of a 5 MW wind turbine. The tower strength and diameter depend mostly on the nacelle weight and expected wind loads. For a 2.3 MW wind turbine, the foundation size is 314 m^2 with an approximate weight of 2000 tonnes, as the nacelle weight increases the associated costs increase exponentially [4]. Furthermore, in an offshore area, the cost of installation is extremely high. On average, approximately 20% of the capital costs are associated with installation. A reduction in mechanical loading is expected to lead to enormous savings in terms of tower construction and turbine installation costs [4].

Hence, the wind energy industry requirements can be summarised as:

a) Power ratings beyond 10 MW at a low generator weight
b) Maintain DD drivetrain to maintain reliability
c) Achieve a) and b) at reasonable costs

For these main reasons, it is necessary to search for alternative technologies to enable direct-drive offshore wind turbines with power ratings beyond 10 MW at a lower generator volume and weight while maintaining reasonable costs.

1.3 Superconducting Generators

Superconducting machines are expected to break the barrier that conventional machines are facing. With the use of superconductors, the magnetic and electric loading of a machine can be increased, which enables them to be much more power dense than conventional machines. Superconducting generators however face two challenges in particular.

Firstly, the cost of superconductors is extremely high. In [14], the cost of YBCO-coated conductors, which are the most promising of the superconductors due to the high current carrying ability, was stated as 69 $/m. With many of the 10 MW superconducting generator designs using several hundreds of kilometres of superconducting material [15, 16], these designs become economically unviable due to the high cost. The cost of YBCO tape is predicted to decrease in the future as the production of the tape is ramped up. However, while costs remain high, the use of superconducting material should be limited. In [17], the cost of the 10 MW direct-drive AMSC design [18], which uses 36 km of superconducting tape, is compared to a 10 MW direct-drive PM generator design. It was concluded that the generator cost is equivalent to the PMG while being significantly lighter. The superconducting generator design proposed by Keysan and Mueller [15], uses even less superconducting material than the AMSC design, hence showing potential to be even more cost-effective. This design served as the basis for the conducted research work presented in this thesis, the generator concept will be discussed in more detail in chapter 4.

The second major issue superconducting machines are facing is their unproven reliability. While cryocoolers have been in commission for several decades now [19], their reliability in combination with a rotational machine requiring cryocouplers and the harsh sea environment is unclear. In addition, superconducting coils can only maintain their superconducting state within strict boundaries determined by the temperature, magnetic field environment and transport current. If any of these parameters is exceeded, the superconductor can abruptly lose its superconducting state and a quench occurs, potentially destroying the superconducting coil. A big step into the direction of proving the reliability of superconducting generators was made in 2019. The world's first high-temperature superconducting (HTS) generator, rated at 3.6 MW, was commissioned and tested in a direct-drive wind turbine [9]. The commissioned generator was the result of an EU-funded project named EcoSwing. A permanent magnet generator in an existing wind turbine was replaced with the EcoSwing HTS generator. Figure 1.5. shows the two generators side by side. It can be seen that the HTS generator is significantly smaller than the PM generator. The EcoSwing HTS generator was under more or less continuous operation for 7 month feeding more than 650 MWh into the grid. A sophisticated quench protection system was developed to protect the superconducting coils, however, the project actually had little to no problems with the superconducting coils during the operation of the generator [9]. The EcoSwing project concluded that the technology readiness level of superconducting generators was increased to 6-7 for the first time [9]. Additionally, the project gave actual data for the first time on the reliability of the superconductors and their associated systems in an offshore wind turbine environment.

Figure 1.5. PM generator (left) and EcoSwing generator (right) [20].

In the future, further developments such as the EcoSwing project are expected to emerge and each new project will further increase the confidence in superconductor technology and its reliability. However, cost-effective designs are still required to enable 10 MW and higher rated direct-drive wind turbine generators. The design of superconducting machines and their cooling systems is discussed in further detail in chapter 3.

1.4 Summary and Aim of Thesis

Wind energy is the world's fastest growing energy. The average power rating of offshore wind turbines is expected to further increase in the near future. Additionally, floating wind turbines are expected to emerge to further lower the cost of energy. One major issue with the increasing wind turbine power ratings is that conventional direct-drive generators become too heavy, increasing foundations costs or requiring the need to use less reliable geared systems. Superconductors can enable more power dense electrical machines, enabling DD drivetrains for 10 MW and higher rated wind turbines. However, the major issues of superconducting machines are their cost and reliability.

The aim of this thesis is to further improve upon the double claw pole generator design proposed by Keysan [15], by investigating new design concepts to further increase the power density, efficiency and modularity of the design. Additionally, detailed superconductor modelling is performed to gain a better understanding of the electromagnetic behaviour of superconductors in the machine environment.

1.5 Thesis Layout

The next chapter covers the fundamentals of superconductivity. The different superconductor properties, theories and models, which when combined produce the classic superconductivity theory, are introduced and explained. Additionally, the chapter discusses the different loss mechanisms of superconductors and how to quantify the loss using analytical and numerical methods.

Chapter 3 introduces applied superconductivity projects in the area of electric power engineering, with focus on rotating machines. The different superconducting machine topologies are introduced, and their shortcomings are addressed. Furthermore, the different cryocooling systems that are available for cooling in superconducting devices are discussed.

Chapter 4 discusses and summarizes the original design of the double claw pole machine. The analytical and numerical modelling methods used during the research work are introduced and verified. Additionally, a more detailed investigation of the double claw pole machine performance is conducted.

Chapter 5 addresses one of the major shortcomings of the double claw pole generator, its structural mass. The chapter introduces a new stator design, which partially deviates the air gap closing forces from the axial direction into the radial direction. The reduction in axial forces simplifies the structural design of the generator.

In Chapter 6, the electric loading of the double claw pole generator is increased by replacing the stationary field core with an inner stator. A homopolar field transverses the inner stator, hence producing additional power. Moreover, the inner stator further increases the modularity of the machine.

Chapter 7 investigates the different stacking methods that are available for the double claw pole generator design, to increase the power density. A 5 MW generator module was designed and stacked axially and concentrically. The concentrically stacked design was found to offer a higher power density than the original design of the double claw pole machine.

Chapter 8 introduces the numerical modelling results for superconducting tapes and coils. For the first time, the dynamic loss in the superconducting field winding of the double claw pole generator was calculated. Furthermore, the chapter addresses the loss in superconductors for a much wider range of magnetic field environments, giving valuable insight into the loss mechanisms in superconducting rotating machines. Additionally, the chapter introduces the applied superconductivity laboratory at the University of Edinburgh and its experimental capabilities.

In Chapter 9, the proposed machine concepts are reviewed with the aim to identify the most promising designs. Furthermore, suggestions are given for future research work.

Chapter 2 Superconductivity Fundamentals

Superconductivity was first discovered in 1911 in Mercury by the scientist H. Kamerlingh Onnes. An abrupt decrease in resistivity ρ was observed when a Mercury sample was cooled down to a temperature of 4 K. While the resistivity of conventional conductors is expected to decrease with temperature, it always remains non-zero. The resistivity of a superconductor on the other hand reduces abruptly to zero when the so-called critical temperature T_c is reached. The resistivity behaviour of conventional conductors and superconductors is illustrated in figure 2.1.

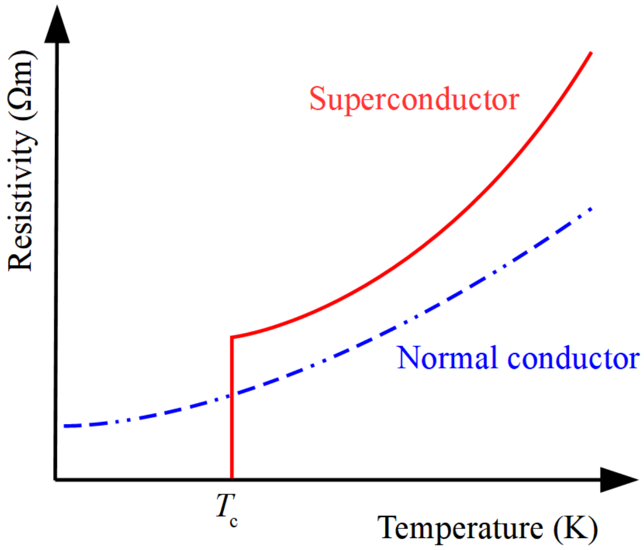

Figure 2.1. Resistivity with temperature for conventional conductors and superconductors.

When the resistivity of the superconductor reduces to zero, the superconductor enters its superconducting state. In this state, a superconducting wire loop can carry a DC current indefinitely without an external power source. In addition to the critical temperature, the superconducting state is also highly dependent on the magnetic field environment and the current density the superconductor is carrying. The critical magnetic field strength is defined as H_c and the critical current density as J_c. When either of the critical parameters is exceeded, the superconductor leaves its superconducting state, this phenomenon is also called quenching. Already at this stage, the importance of either critical parameter can be seen. This concept is highlighted in figure 2.2.

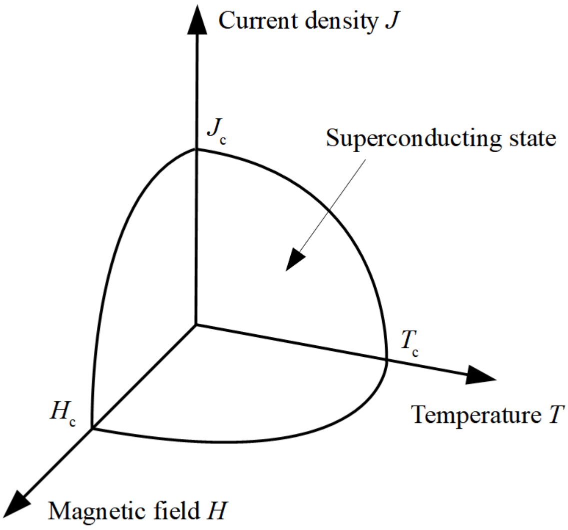

Figure 2.2. Superconducting state boundaries.

The following sections of this chapter will go into further detail regarding the properties and characteristics of superconductors.

2.1 Superconductivity Theory

In 1933, the discovery was made that, when a magnetic field is applied to a superconductor when it is in its superconducting state (Zero field cooling), non-decaying screening currents are induced on the surface of the superconductor, which repel the external magnetic field. One key difference from a superconductor when compared to a perfect conductor ($\rho = 0$) is that, even if the magnetic field is applied before the superconductor is in its superconducting state (Field cooling), a superconductor still repels the magnetic field from its inner geometry when cooled down to its critical temperature. Whereas for a perfect conductor, the magnetic field remains within the conductor geometry. This phenomenon is called the Meissner-Ochsenfeld effect, it is illustrated in figure 2.3.

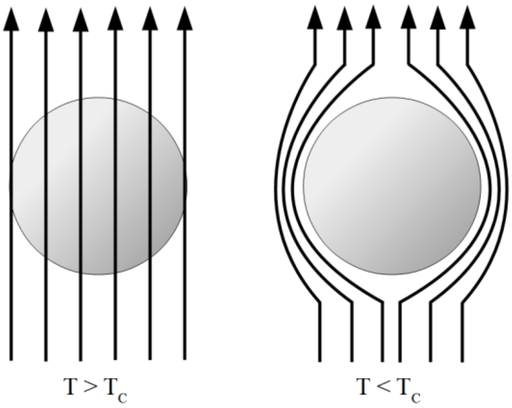

Figure 2.3. Perfect diamagnetism in a superconductor.

The Meissner effect can be explained through the following equations. Equation 2.1 describes the relation between the flux density $\boldsymbol{B}$ and the magnetic field $\boldsymbol{H}$.

$$\boldsymbol{B} = \mu_0(\boldsymbol{H} + \boldsymbol{M}) \tag{2.1}$$

where $\boldsymbol{B}$ is the magnetic flux density, μ is the permeability of free space, $\boldsymbol{H}$ is the magnetic field and $\boldsymbol{M}$ is the magnetisation.

Since the magnetic field inside of a superconductor is 0, this implies that:

$$\boldsymbol{B} = \mu_0(\boldsymbol{H} + \boldsymbol{M}) = 0 \rightarrow \boldsymbol{H} = -\boldsymbol{M} \tag{2.2}$$

Giving the magnetic susceptibility, which is the ratio of the magnetisation $\boldsymbol{M}$ to the applied magnetic field $\boldsymbol{H}$**,** as:

$$\chi = \frac{\boldsymbol{M}}{\boldsymbol{H}} = -1 \tag{2.3}$$

This in combination with the superconductor having zero resistivity in its superconducting state explains the perfect diamagnetism of a superconductor. The induced shielding currents induce a magnetic field equal in magnitude to the external field but into the opposite direction, hence leading to the sum of magnetic fields inside of the superconductor geometry being equal to 0 [21].

The Meissner effect theory can be further expanded through applying the London theory. Since the induced surface currents are not infinitely large, the magnetic field, whether it is an external or a self-generated field from a transport current, can penetrate a finite depth into the superconductor. This penetration depth λ was defined in the London Model in 1935 and is hence known as the London penetration depth [22]. The London penetration depth gives rise to the critical state boundaries highlighted in figure 2.2. A magnetic field higher in magnitude than the critical magnetic field H_c, penetrates the conductor beyond the London penetration depth and hence the superconductor loses its superconducting state. Similarly, for a transport current density beyond the critical current density, the current cannot be contained within the penetration depth λ, hence again resulting in the superconductor leaving its superconducting state [23].

In 1950, a new theory was proposed by Ginzburg and Landau, The Ginzburg-Landau Theory was the first mathematical model giving an explanation of superconductivity with the use of thermodynamics [24]. The Ginzburg-Landau equations introduce two new characteristic lengths to characterise superconductors. The first characteristic length is the coherence length ξ, which limits the variation rate of the superconducting electron density. If this change in electron density happens too quickly it will collapse the superconductivity of the material. The second length is the penetration depth λ, which was previously introduced in the London Model. The equations for both lengths are shown below.

$$\xi = \sqrt{\frac{\hbar^2}{2m|\alpha|}} \text{ for } \mathrm{T} > \mathrm{T_c} \tag{2.4}$$

$$\xi = \sqrt{\frac{\hbar^2}{4m|\alpha|}} \text{ for } \mathrm{T} < \mathrm{T_c} \tag{2.5}$$

where ħ is the reduced Plank's constant, m is the mass of a cooper pair as introduced by the BCS theory in the next paragraph, α is a temperature dependent constant defined by the Ginzburg-Landau equation.

$$\lambda = \sqrt{\frac{m}{4\mu_0 e^2 \psi_0^2}} \tag{2.6}$$

where ψ_0 is the equilibrium value of the order parameter in the absence of an electromagnetic field. Producing the ratio of the two lengths, results in the Ginzburg-Landau parameter:

$$\kappa = \frac{\lambda}{\xi} \tag{2.7}$$

The Ginzburg-Landau parameter can be used to differentiate between Type-I and Type-II superconductors. These two different types of superconductors will be addressed in further detail in the next sub-section.

The first microscopic theory of superconductivity was introduced in 1957 by Bardeen, Cooper and Schrieffer, for which they received the Nobel Prize in Physics in 1972. Their theory became known as the BCS theory [25]. The BCS theory proposed that the forming of the superconducting current is due to two electrons being pressed together, resulting in a pair of electrons called a cooper pair. Cooper pairs are inherently more stable and resistant to vibrations, hence as cooper pairs travel through the lattice of superconducting materials, they experience much less resistance. The BCS theory matches perfectly for low temperature superconductors LTS), however the physical phenomenon behind high temperature superconductors (HTS) is still unknown to this date. The combination of the BCS theory with the Meissner effect, the London Model and the Ginzburg-Landau Theory form the classic theoretical model of superconductivity.

2.2 Type-I & Type-II Superconductors

As was mentioned in the previous section, with the Ginzburg-Landau parameter, a differentiation can be made between Type-I and Type-II superconductors. For Type-I superconductors $\kappa < \frac{1}{\sqrt{2}}$ whereas for type-II superconductors $\kappa > \frac{1}{\sqrt{2}}$. The low Ginzburg-Landau parameter of Type-I superconductors is due to the long coherence length. One further classification that can be made between superconductors in addition to what type, is through their critical temperature. The first superconductors that were discovered were all low temperature superconductors with a critical temperature below 30 K [26]. Most low temperature superconductors are classified as Type-I superconductors and mostly metal and metalloid based superconductors are classified as Type-I superconductors [27]. In recent years, high temperature superconductors have been discovered as well. BSCCO was the first high temperature superconductor (HTS) to be used for making superconducting wires. It has a critical temperature of 108 K. BSCCO is also called the first generation (1G) HTS wire. YBCO was discovered in 1986 and has a critical temperature of 93 K. YBCO is also known as the second generation (2G) HTS wire. YBCO in particular is considered one of the most promising superconductors for manufacturing commercial grade HTS wire. Both BSCCO and YBCO are metal alloys and are considered Type-II superconductors. In general, it can be said that LTS are Type-I and HTS are Type-II. The key difference in the two superconductor types is in the Meissner effect. The Meissner effect in a Type-I superconductor behaves like the superconductors described in the previous section. If an applied magnetic field increases beyond the critical field, the superconductor returns to its normal state. Type-II superconductors on the other hand have a mixed-state in-between the superconducting state and their normal state, into which they enter if the applied field is between H_{c1} and H_{c2} [28]. In the mixed state, some magnetic flux can penetrate into the superconductor in the form of vortexes while allowing the material to maintain its superconducting state [23]. When the magnetic field increases beyond H_{c2}, the superconductor leaves its critical state just as Type-I superconductors. This is illustrated in figure 2.4.

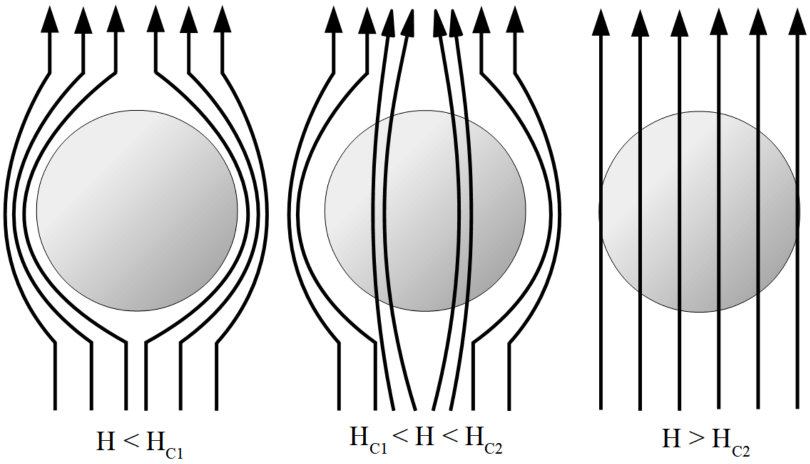

Figure 2.4. Meissner effect, mixed state and normal state in Type-II superconductors.

The mixed-state is essentially the reason why a Type-II superconductor can float in mid-air above a magnet, the pinned magnetic flux keeps the superconductor in place.

One major advantage of Type-II superconductors is that H_{c2} is usually several magnitudes bigger than H_c of Type-I superconductors. While Type-I superconductors possess extremely good conductivity, in practice they perform relatively badly when conducting current, since even the self-generated magnetic field can exceed the critical field H_c, causing the superconductor to leave its superconducting state. Type-II superconductors have much better current carrying abilities due to the significantly higher critical field H_{c2}, they rely on their mixed state to transport large current in high magnetic fields [29]. However, operating in the mixed state means that some flux has penetrated the superconductor. When the superconductor is carrying a current in this state, a Lorentz force exists between the current and magnetic flux vortexes. If these vortexes move, an electric field is induced according to Faraday's law and hence heat is dissipated [30]. For Type-II superconductor to have a large current carrying ability and be of practical use [31], the movement of these vortexes needs to be prevented. In practice this is done by adding impurities and crystalline defects into the superconducting material, which increases the flux pinning force, these superconductors are then called hard superconductors [32]. When a hard superconductor carries a DC current, which is below its critical current, the superconductor exhibits no loss due to the pinned vortexes. However, once the superconductor carries an alternating current, the magnetic field must change, and hence the superconductor exhibits AC losses. These losses will be discussed in further detail in the next section.

2.3 Superconductor AC Losses

One of the critical challenges for high temperature superconducting applications are the AC losses. AC losses lead to heat, which needs to be removed at a very low temperature. Cryogenic coolers operate at an inherently low efficiency, hence any heat that is dissipated can be detrimental to the overall efficiency of superconducting devices. One of these loss mechanisms was already addressed in the end of the previous section. The movement of flux vortexes leads to an induced electric field and hence heat dissipation. This loss is called hysteresis loss. High temperature superconductors consist of several different materials, which can include ferromagnetic substrates and copper stabilizers. Hence in addition to hysteresis losses, superconductors can also exhibit ferromagnetic and eddy current losses. Lastly, if the superconductor consists of superconducting filaments, coupling losses can additionally occur [33]. Each of these loss mechanisms will be addressed in detail in the following subsections.

2.3.1 Hysteresis Loss

In Type-II superconductors, hysteresis loss is the most important loss contributor when considering high temperature superconductors. As was discussed briefly, hysteresis loss occurs due to the movement of the magnetic flux vortexes when subject to alternating current conditions, whether it is an AC transport current or an external AC magnetic field. The movement induces an electric field $\boldsymbol{E}$ according to Faraday's law, which drives screening currents in the material, hence resulting in local heat loss. The induced screening currents additionally produce their own magnetic field according to Ampere's law and hence determine the magnetic field distribution in the superconductor. Faraday's law (equation 2.8), Ampere's law (equation 2.9) and the equation for the local instantaneous power dissipation (equation 2.10) are highlighted below.

$$\nabla \times \boldsymbol{E} = -\frac{d\boldsymbol{B}}{dt} \tag{2.8}$$

$$\nabla \times \boldsymbol{B} = \mu \boldsymbol{J} \tag{2.9}$$

$$p = \boldsymbol{J} \cdot \boldsymbol{E} \tag{2.10}$$

As was discussed in the previous section, the induced screening currents shield the interior of the material from the magnetic field. This is due to the screening currents causing the magnetisation $\boldsymbol{M}$, which is equal in magnitude to the external field $\boldsymbol{B}$ but acts in the opposite direction, hence cancelling out. The screening currents and the shielding effect are highlighted in figure 2.5, the greyed-out area in the middle of the superconductor is the shielded region, which does not exhibit any loss. This is assuming that ***B*** is relatively low, as the magnetic field increases, the shielded region shrinks due to the field penetrating further into the sample, and hence the exhibited loss increases [34].

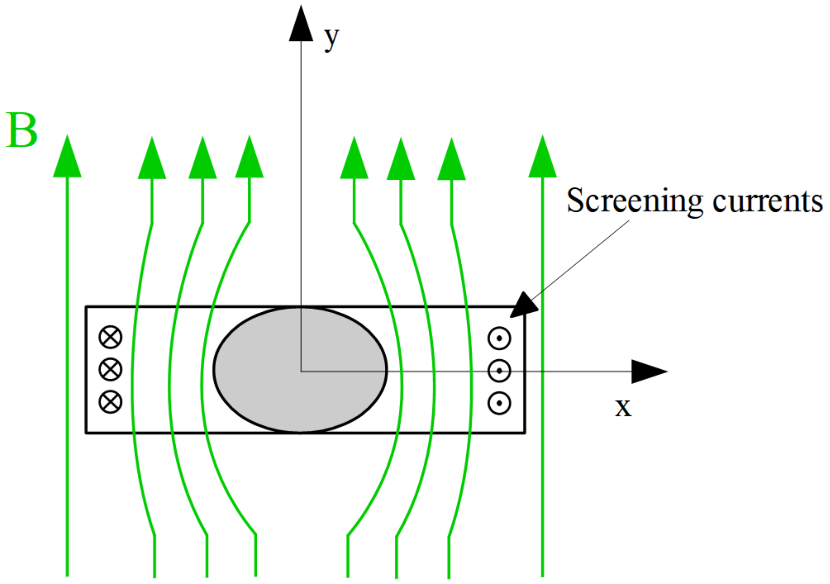

Figure 2.5. Superconductor in an alternating magnetic field.

While the above example was in regard to applying an external magnetic field, the same mechanisms can be applied to a superconductor carrying an alternating current. The alternating current produces a self-field, which also partially penetrates the superconductor itself and hence the changing magnetic field results in loss being exhibited.

2.3.2 Eddy Current Loss

Eddy current losses are present in all electric devices operating with an alternating current. If a conductor is subject to an alternating magnetic field, eddy currents are induced and due to the ohmic resistance of the conductor, these induced currents generate additional heat. Eddy currents can usually be neglected in the power frequency range. However, as the operating frequency increases, the total resistance of a conductor can be represented by the summation of the DC resistance and an AC resistance. The AC resistance can be several times bigger than the DC resistance. For a single wire, the AC resistance of the conductor essentially consists of the resistance due to the skin effect, which pushes the transport current towards the outer edges of the conductor geometry, decreasing the transport current area and hence increasing the ohmic resistance. When considering the resistance of a coil, such as in a high-frequency transformer, the AC resistance consists of the skin effect and the proximity effect of the surrounding windings. The surrounding windings generate magnetic fields, which affect the conductors and hence eddy currents are induced. The losses increase even further when considering a gapped inductor, since the magnetic fringing field from the air gap further contributes towards the proximity loss in copper windings [35]. The management and mitigation of eddy current induced losses is one key research area in the domain of high frequency magnetic components. When considering the structure of YBCO wire, it can be seen that the superconducting layer is sandwiched between two copper stabilizers, which depending on the frequency can contribute to the overall loss in a non-negligible manner.

2.3.3 Ferromagnetic Loss

When considering the structure of high temperature superconductors, some superconducting wires use magnetic components as stabilizers or reinforcing layers. Some YBCO-coated conductors for instance are manufactured with a ferromagnetic substrate, similarly the first generation BSCCO wires were manufactured with magnetic layers. The ferromagnetic material in superconducting wires further contributes to the hysteretic losses in superconductors. Additionally, surrounding iron can negatively impact the losses in superconductors by changing the magnetic field distribution in the superconducting wire, this is especially important in iron-cored superconducting machines [33]. However, since iron can change the magnetic field distribution on superconducting tapes, it can also be used to reduce the overall AC losses. A superconducting coil can be sandwiched between two iron rings, which are called flux diverters, the aim is essentially to move hysteresis losses from the superconductor to ‘less bad’ iron losses in the flux diverters [36]. The potential of flux diverters to reduce AC losses will be further discussed in the superconductor modelling chapter.

2.3.4 Coupling Loss

Coupling loss occurs in superconducting wires, which consist of several filaments. Coupling loss is defined as the loss that arises as a current loop transverses from a superconducting filament through normal material to another superconducting filament due to an alternating applied magnetic field. Superconducting wires which consist of filaments are for example BSCCO wires. Additionally, filaments are explored for YBCO-based wire to reduce the hysteresis loss. However, the method of manufacturing these filaments is of utmost importance and the benefits gained from reduced hysteresis losses can be completely negated or even worsened by introducing high coupling losses [37].

2.4 Analytical Methods for AC Loss Calculation

To calculate AC loss results with high accuracy, 2D or even 3D numerical models are required. Especially when considering wire or coil configurations, which can involve several hundreds of turns or more. However, for initial rough estimations of AC loss, analytical equations exist, which can offer results very quickly. Norris' analytical equation gives the AC transport current loss of superconducting tapes. Brandt's equation can give the magnetization loss due to an external magnetic field. Each equation will be introduced and discussed in this section.

2.4.1 Norris Equation for Transport Current Loss

The analytical Norris equation for the calculation of transport current loss was introduced by W. Norris in 1970. It has shown to estimate the hysteresis losses due to the generated self-field of an alternating transport current relatively accurately. It does not account for external magnetic fields, nevertheless it can provide a good reference for the magnitude of the generated loss. The Norris equation for rectangular superconductors such as YBCO tapes is shown below [38]:

$$Q_t = \frac{\mu_0 I_{\mathrm{c}}^2}{\pi}\left[\left(1-\frac{I_{\mathrm{t}}}{I_{\mathrm{c}}}\right)\ln\left(1-\frac{I_{\mathrm{t}}}{I_{\mathrm{c}}}\right)+\left(1+\frac{I_{\mathrm{t}}}{I_{\mathrm{c}}}\right)\ln\left(1+\frac{I_{\mathrm{t}}}{I_{\mathrm{c}}}\right)-\left(\frac{I_{\mathrm{t}}}{I_{\mathrm{c}}}\right)^2\right] \tag{2.11}$$

where Q_{t} is the unit loss in J/cycle/meter, I_{c} is the critical current and I_{t} is the transport current. The calculated loss can be multiplied by the frequency to obtain the unit loss in watts per meter.

2.4.2 Brandt Equation for Magnetisation Loss

In 1993, E. H. Brandt proposed his analytical equations for the calculation of magnetisation losses in rectangular superconducting strips with the assumption that the width $2a$ of the tape is much bigger than the thickness of the superconducting layer d. The equation is shown below [39].

$$Q_m = \frac{4\pi a^2 B_{\mathrm{a}} B_{\mathrm{c}}}{\mu_0}\left[\frac{2B_{\mathrm{c}}}{B_{\mathrm{a}}}\ln\left(\cosh\frac{B_{\mathrm{a}}}{B_{\mathrm{c}}}\right)-\tanh\left(\frac{B_{\mathrm{a}}}{B_{\mathrm{c}}}\right)\right] \tag{2.12}$$

where Q_{m} is the unit loss in J/cycle/meter, a is half the width of the tape, B_{a} is the applied magnetic field and B_{c} is the critical magnetic field.

The critical magnetic field can be calculated for thin strips through the critical current I_{c} with the use of equation 2.13 [40].

$$B_c = \frac{\mu_0 I_{\mathrm{c}}}{2a\pi} \tag{2.13}$$

2.5 Numerical AC Loss Modelling

While the analytical equations introduced in the previous section offer very good results when only considering a single tape, the loss results deviate from the actual loss when stacks of tapes or coil configurations need to be considered, in combination with complex magnetic fields. For more complicated scenarios, numerical modelling of superconductors is necessary. However, the modelling of the superconducting properties is not as straight forward as for normal conductors. High temperature superconducting tapes, such as YBCO-coated conductors, possess highly anisotropic and nonlinear electromagnetic properties. Several models have been developed to calculate the magnetic field and current density distributions within superconductors, to enable the calculation of AC losses. These models will be introduced in further detail in this section. Additionally, several different numerical modelling formulations exist, which need to be coupled with the established superconductor models. In this thesis mainly the ***H***-formulation and ***T***-formulation based numerical models were used, these will be introduced in further detail towards the end of this section.

2.5.1 Critical State Models

As was discussed in section 2.2.4, Type-II superconductors, such as YBCO, operate in the "mixed-state", where some of the magnetic flux is able to penetrate the outer edges of the superconductor geometry, while leaving the centre of the superconductor completely shielded. Superconducting screening currents are induced in the outer edges of the tape, leaving the centre free from any current. This behaviour is described by the critical state model (CSM), which assumes that the outer edges of the superconducting material enter the critical state, where superconducting currents exist, while the internal region of the superconductor remains in the normal state. The first CSM, which is also known as the Bean model, was introduced by Bean [41]. The two main assumptions that are made in the Bean model are that 1) The magnetic field magnitude does not influence the critical current density J_c and 2) the current density in the superconductor can only assume three values, $\pm J_c$ in the critical state and zero in the normal state. A superconducting slab of infinite length placed in an external magnetic field is one of the most prominent examples to illustrate the concept. Due to the infinite length, the assumption is made that current only flows in the z-direction and that the x-direction current is negligible. The current only flows in the outer edges of the slab and the centre remains in the normal state and free of any current. Figure 2.6 shows a front view and top view of the superconducting slab. Figure 2.7 shows the current and magnetic field distributions for different magnitudes of magnetic field. $2a$ is the width of the superconducting slab. From the figure it can be seen that shielding current only exists where the magnetic field has penetrated the slab and the current can only take on the values of $\pm J_c$, independent of the magnetic field magnitude.

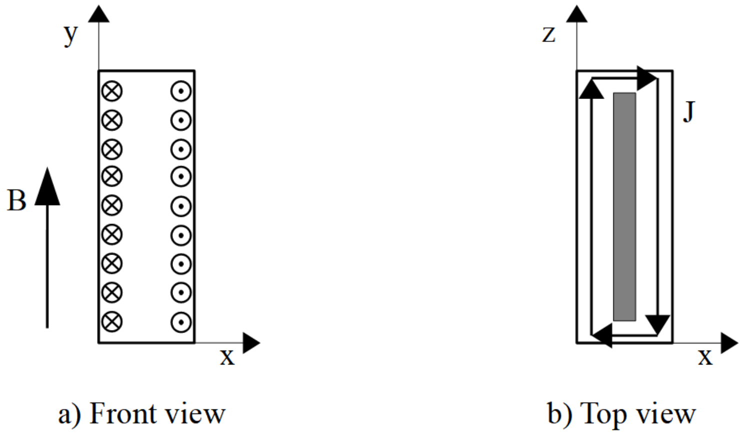

Figure 2.6. Infinitely long (into z-direction) superconducting slab in an external magnetic field for a) the front view and b) the top view

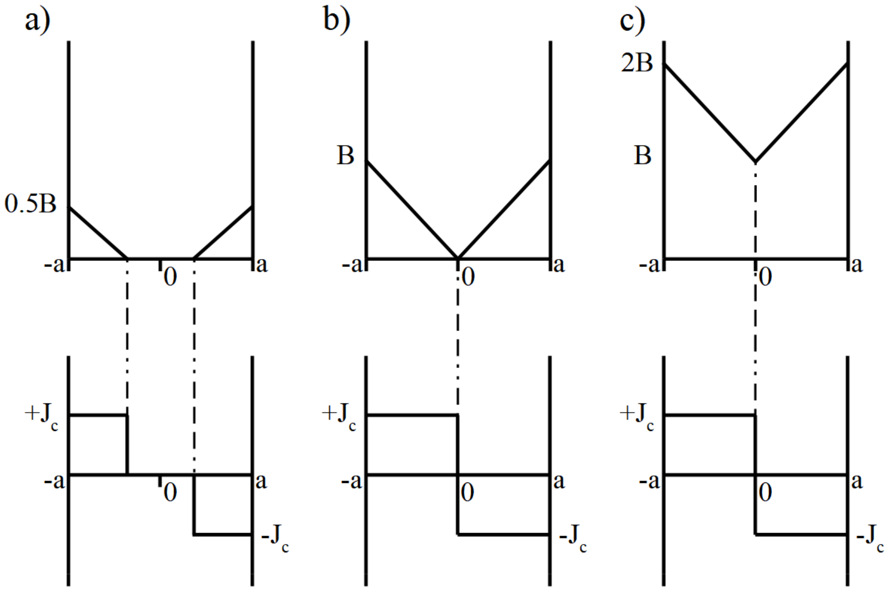

Figure 2.7. Magnetic field and current density relationship according to Bean's model (adapted from [42])

The Bean model represents the simplest of the critical state models. In 1962, the Bean model was extended by Kim to include the temperature and magnetic field dependences of the critical current J_c. The relationship is shown in equation 2.14 [43].

$$J_c(B) = \frac{\alpha(T)}{B_0 + B} = J_{c0}(T)\frac{1}{1 + \frac{B}{B_0}} \tag{2.14}$$

where J_{c0}(T) is the critical current density due to the self-field alone at a given temperature T, B_0 is the magnetic field constant, which is dependent on the superconducting tape and B is the applied magnetic field.

This equation can be further expanded to include the anisotropic behaviour of HTS, *i.e.* the dependence of J_{c0} to the angle at which the magnetic field penetrates the superconducting material, by introducing perpendicular and parallel field components [44].

$$J_c(B) = \frac{J_{c0}(T)}{\left(1 + \frac{\sqrt{k^2 B_{\mathrm{para}}^2 + B_{\mathrm{perp}}^2}}{B_0}\right)^{\alpha}} \tag{2.15}$$

where k is the anisotropy factor, B_{para} and B_{perp} are the respective parallel and perpendicular field components and α is the exponent of field dependence. It should be noted that $k < 1$, hence the perpendicular field component is the major contributor to the decrease in critical current.

2.5.2 E-J Power Law

The Bean model fit the electromagnetic behaviour of low temperature superconductors very well, however for high temperature superconductors this was not the case anymore. This was mainly due to the assumed step change of the current density from the region in a critical state to the current free regions, causing a discontinuity of the electric field at the boundaries. In [45], Anderson proposed that the origin of the electric field in HTS material is due to the slow propagation of the magnetic flux, which he called flux creep, leading to a continuous distribution of the electric field in the HTS material. Based on Anderson’s work, Rhyner proposed the *E-J* power law, which better reflects the non-linear relationship between the electric field and the current density [46]. This model has become the most dominant way of describing the electromagnetic properties of high temperature superconductors. Equation 2.16 shows the *E-J* power law.

$$E = E_0 \left(\frac{J}{J_c}\right)^n \tag{2.16}$$

Where E_0 is set to be equal to 10^{-4} Vm^{-1} by convention, J_c is the critical current when E is equal to E_0 and n is a parameter, which is determine through measurements to fit the E-J power law.

The n-value essentially determines how steep the change in electric field is. A n-value of 1 leads to a linear relationship between E and J as defined by Ohm's law. As n trends towards infinity, the E-J power law reflects the behaviour of Bean's critical state model. This behaviour is shown in figure 2.8, which plots the E-J power law for different n-values. In practice n ranges between 20 and 50 for HTS [23].

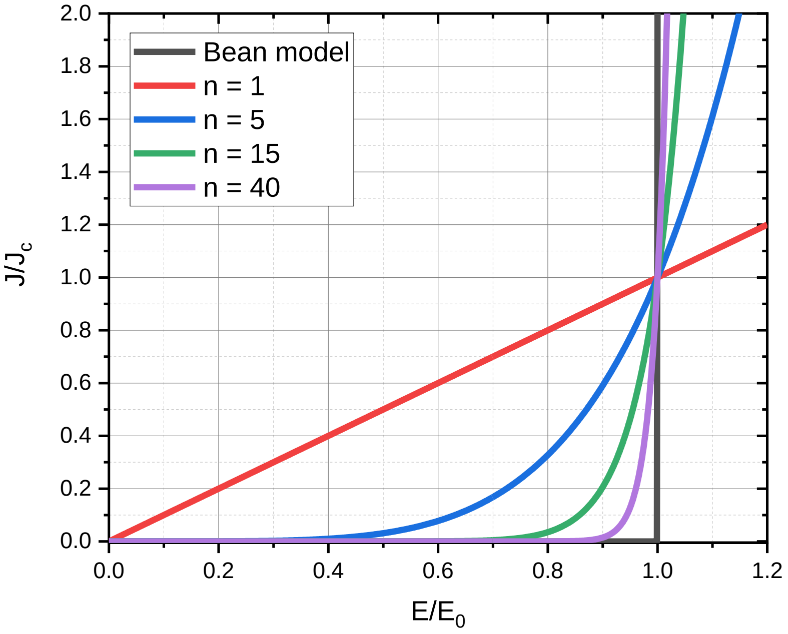

Figure 2.8. *E*-*J* power law with for different *n*-values.

2.5.3 *H*-Formulation

While numerous formulations for numerical HTS models exist, the ***H***-formulation based numerical model is the most popular in the HTS community. The ***H***-formulation solves the Maxwell equations directly and by incorporating the electromagnetic behaviour of HTS materials, it becomes possible to enable superconductor modelling. The ***H***-formulation essentially consists of the following equations: Ampere's law (2.17), Faraday's law with constitutive law (2.18) and the E-J power law with Ohm's law (2.19).

$$\nabla \times \boldsymbol{H} = \boldsymbol{J} \tag{2.17}$$

$$\nabla \times \boldsymbol{E} = -\mu_0 \mu_\mathrm{r} \frac{\partial \boldsymbol{H}}{\partial t} \tag{2.18}$$

where μ_0 is the permeability of air and μ_r the relative permeability of the material.

$$\boldsymbol{E} = \rho \boldsymbol{J} \tag{2.19}$$

where Ohm's law is applied in conjunction with the *E-J* power law, which was shown in equation 2.16, for the HTS material and the resistivity ρ is used for other materials in the HTS wire such as for the copper stabilizers.

Equations 2.17 to 2.19 can be combined into equation 2.20 in a general form, which is known as the ***H***-formulation.

$$\frac{\partial(\mu_0 \mu_\mathrm{r} \boldsymbol{H})}{\partial t} + \nabla \times (\rho \nabla \times \boldsymbol{H}) = 0 \tag{2.20}$$

For the HTS modelling, the commercial software COMSOL was used. Chapter 8 will go into further details on how the equations are setup within the software and present detailed simulation results.

2.5.4 T-Formulation

The ***T***-formulation based numerical model was the first model capable of simulating the current and magnetic field distributions across HTS materials. It was first introduced by Amemiya in 1998 [47]. In this formulation, the current vector potential *T* is introduced to connect the Maxwell equations with the superconductor specific electromagnetic properties. Most ***T***-formulation based numerical models were established in open-source codes, giving this formulation a much higher degree of flexibility. Furthermore, it is considered that this formulation offers the highest calculation efficiency. Equations 2.20 to 2.22 show the governing equations for the ***T***-formulation.

$$\boldsymbol{J} = \nabla \times \boldsymbol{T} \tag{2.21}$$

$$\nabla \times (\rho \nabla \times \boldsymbol{T}) = -\frac{\partial \boldsymbol{B}}{\partial t} \tag{2.22}$$

$$\rho = \rho(\boldsymbol{J}) \tag{2.23}$$

Further details on ***T***-formulation based numerical modelling can be found in [23].

2.6 Chapter Summary

This chapter introduced the fundamentals of superconductivity. It was shown that superconductors in addition to having zero resistivity, exhibit perfect diamagnetism. The perfect diamagnetism exists due to superconducting screening currents shielding the interior of superconducting materials. Several models, which describe the electromagnetic behaviour of superconducting materials, were introduced, such as the London model, which defined the London penetration depth. It gives the distance a magnetic field can travel into a superconducting material, due to the superconducting screening currents not being infinitely large. The Ginzburg-Landau model was then introduced, which defined the Ginzburg-Landau parameter, which can be used to differentiate between Type-I and Type-II superconductors. The difference between the two types of superconductors was discussed, stating that Type-II superconductors operate in a ‘mixed state’, where some magnetic flux can penetrate the superconducting material. All HTS are Type-II superconductors and it is the mixed state, which allows HTS to carry a very large current density. The chapter then moved on to describe the different loss mechanisms in HTS. Hysteresis loss occurs, due to flux vortexes being in motion when operating under alternating current conditions. Additionally, HTS can exhibit eddy current loss, ferromagnetic loss and coupling loss. The chapter finishes with discussing how the loss can be quantified. Analytical equations are introduced, which work very well for simple configurations. Numerical modelling is required for more complex scenarios. Different formulations exist to perform calculations such as the $\boldsymbol{H}$-formulation and $\boldsymbol{T}$-formulation. Each formulation requires equations to describe the electromagnetic behaviour of the HTS material, which is done by combining the formulations with a CSM.

The next chapter will discuss the applications of superconductors in electric power, with focus on superconducting rotating machines and their advantages and challenges.

Chapter 3 Superconductivity in Electric Power Applications

This chapter will discuss the different areas in which HTS materials are applied. Particular focus will be put on superconducting rotating machines. The different superconducting machine design choices will be introduced and discussed, and various existing prototypes will be highlighted in further detail. Furthermore, the different cryogenic cooling systems that are available will be introduced.

3.1 Applied Superconductivity Areas

High temperature superconductors are applied in a wide range of applications, some of which will be introduced in this section. Superconducting rotating machines will be highlighted in further detail in the next section.

3.1.1 Power Cables

Superconducting power cables have attracted a lot of attention in recent years. The main advantages of superconducting power cables can be summarized as [23]:

- Significantly increased current carrying capability
- Minimal power loss
- Lower transmission voltage level
- Compact structures

The typical structure of a superconducting power cable is shown in figure 3.1. As can be seen, a superconducting power cable consists of several layers of superconducting tapes, essentially twisted together, the superconductors are cooled with liquid nitrogen and enclosed by a cryostat.

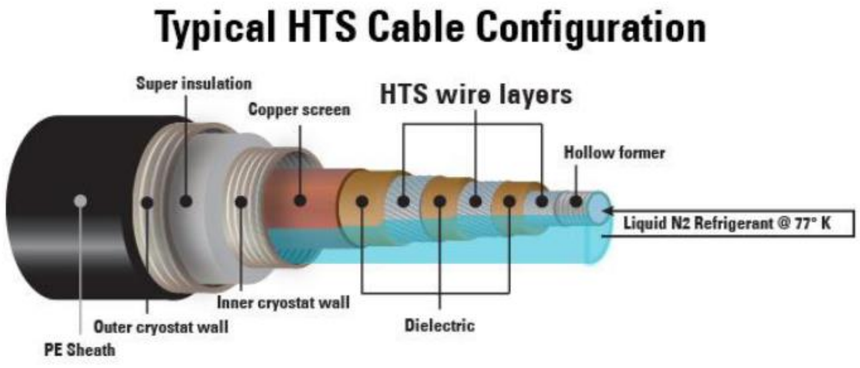

Figure 3.1. HTS cable configuration (Courtesy of Shanghai Superconductor [48])

Some of the more recent superconducting power cable projects are summarised in table 3.1.

Table 3.1. YBCO cable projects (adapted from [23])

Developer	Length	Power Rating	Time
Superpower/Sumitomo	30 m	34.5 kV, 800 A	2008
Furukawa	10 m	66 / 77 kV	2009
LS Cable	500 m	22.9 kV	2010
AMSC	600 m	138 kV	2011
KEPCO/LS Cable	500 m	80 kV, 500 MW	2014

One major disadvantage of superconducting power cables is their very high capital cost, leading to the need to further optimize the design of the cables to reduce the HTS material requirements [23].

3.1.2 Fault Current Limiters

Fault current limiters are another major research area when considering applied superconductivity. Fault current limiters, as the name indicates, are required to limit potential fault current in the electric grid caused by short circuits or lightning strikes for example. The idea behind superconducting fault current limiters is to take advantage of the quench properties of the superconductor. Conventional fault current limiters require zero crossing to clear a fault, however this can often take up to several milliseconds plus additionally several cycles to finally clear the fault. The quenching of superconductor on the other hand happens within microseconds, when a superconductor quenches, the superconductor enters its normal state, which means its resistivity is not equal to zero anymore [49]. Hence, in simple terms, when a fault current occurs, the superconductor quenches and its resistivity increases, hence the fault current is limited.

This method of clearing a fault is particularly interesting when considering DC grids, since zero crossing fault clearing in not possible in a DC environment, which makes the clearing of faults here much more challenging and expensive [50].

3.1.3 Superconducting Accelerator Magnets

In the medical field, high temperature superconductors have become an interesting avenue for the treatment of cancer. Carbon ion radiotherapy (CIRT) in particular is very promising, unlike with proton radiotherapy, the carbon beams operate with a kinetic energy of 430 MeV/u, which is almost three times larger than that required for proton beams. The higher kinetic energy makes CIRT a much more effective cancer treatment and lowers risk of inducing secondary malignancies. Rotating gantries are ideal for the treatment since they allow to precisely target the cancer. Numerous proton therapy rotating gantries exit however, only two CIRT facilities exist in the world. This is due to the high kinetic energy leading to a very large and heavy structure [51]. The previous carbon-ion rotating gantries employed low temperature superconductors. Very long straight sections are required to accelerate the particles to the necessary kinetic energy level. High temperature superconductors could reduce the size of these devices by shortening accelerator path considerably, due to their much increased current density when compared to LTS [52]. Figure 3.2. highlights the design of a superconducting rotating gantry for heavy-ion therapy.

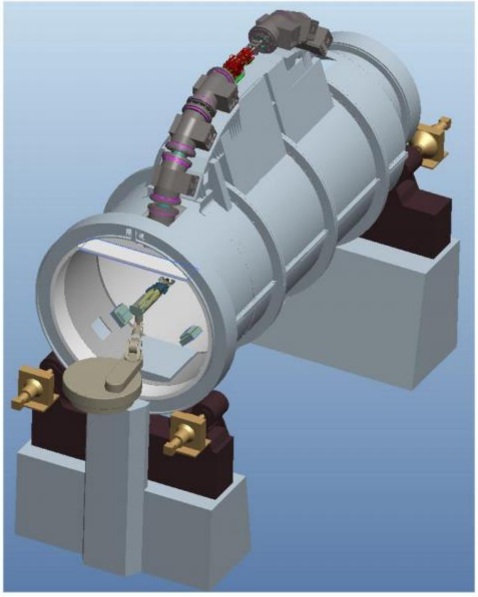

Figure 3.2. Superconducting rotating gantry for heavy-ion therapy [53].

Reducing the size of these devices could enable the technology to become more widely spread.

3.1.4 Superconducting Flux Pumps

Superconducting flux pumps have become a major research area. HTS magnets operating in persistent current mode can be free from the heat loss caused by current leads. However, due to flux creep in high-T_c superconductors and additionally introduced joint resistance to close the loop, current in the closed superconducting circuit suffers an inevitable decay. With a flux pump, current can be indirectly injected into a closed superconducting loop [54]. This mechanism is particularly interesting for injecting current into the field windings in rotating electric machines. These field windings operate with a DC current, however due to the magnetic field environment in the machine, losses are present, and a persistent current would eventually decay. Applying flux pumps to superconducting rotating electric machines is an active area of research. The flux pump can be used to indirectly inject current into the HTS coils on the rotor. This method eliminates the brushes, which are otherwise required to enable electrical connections between a stationary and rotating component. An example of an HTS flux pump setup is shown in figure 3.3.

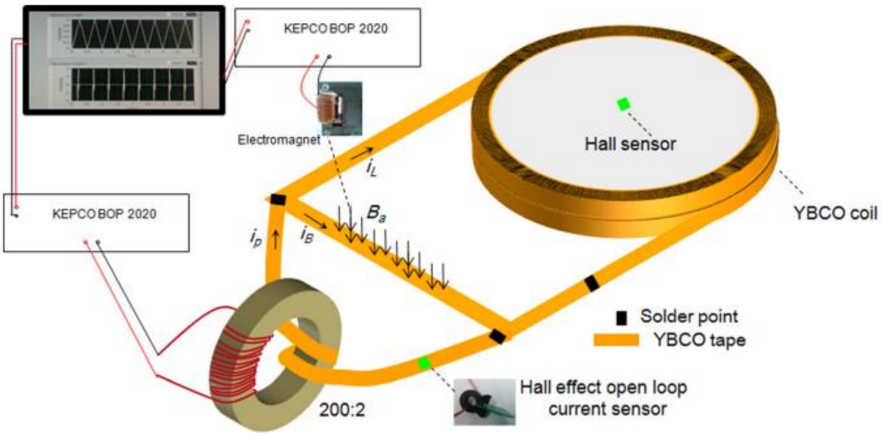

Figure 3.3. HTS flux pump setup [54]

3.1.5 Wireless Power Transfer

Another emerging market for high-temperature superconductors is in the area of wireless power transfer, in particular for applications where a large amount of power needs to be transferred. Additionally, superconducting coils can achieve a much lower quality factor and hence improved system efficiencies. Wireless charging for electric vehicles (EVs) is one of the major research areas. The expected power rating is expected to be in the range of several tens of kW [55].

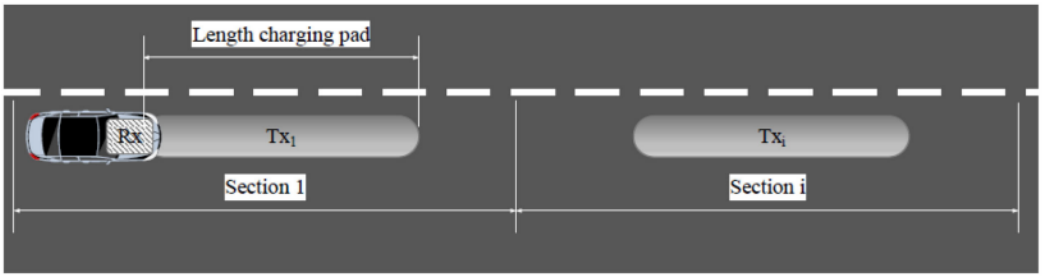

Figure 3.4. Dynamic wireless charging for electric vehicles [56].

Wireless charging of electric vehicles is expected to alleviate the driving range anxiety. With a combination of stationary and dynamic charging, the driving range of EVs can be increased significantly [56]. Figure 3.4 shows a conceptual design for dynamic wireless charging. Superconducting transmitting coils are buried in the street and as EVs drive along, the EV is charged. A power rating of 30 kW with 30 % road coverage was found to essentially offer an unlimited driving [56].

3.2 Superconducting Rotating Machines – Advantages and Challenges

Superconducting rotating machines are one of the major applications when considering high temperature superconductors. Due to the high current density carrying ability of HTS, superconducting machines can be much lighter, more power dense and more efficient. This makes HTS machines a very attractive candidate where an extremely high power density is required or where machine mass and size are to be limited. Especially, direct-drive low-speed machines have become a major point of interest. These machines tend to be very large and heavy due to the low rotational speeds. As was discussed in the introduction, the tower head mass of large offshore wind turbines becomes very heavy with direct-drive generators, complicating the foundation of the wind turbine. By applying HTS to the generator the size and weight of the machine can be reduced, which in turn can enable larger wind turbines, which capture more energy. The advantage of applying superconductors to rotating machines is relatively simple and can be showcased by examining the basic machine equation below:

$$P = B A_{\mathrm{E}} \frac{\pi}{2} D^2 L \omega \tag{3.1}$$

where B is the air gap flux density, A_{E} is the electric loading, D is the machine air gap diameter, L is axial length of the machine and ω is the rotational speed.

For conventional machines, the flux density B and the electrical loading A_{E} are essentially fixed by the limitations of copper and permanent magnets, hence the dimension of a machine can roughly be estimated by considering the required output power and rotational speed. If a direct-drive low-speed machine is considered, the rotational speed is very low, which leads to a low power output. Since the power output scales with the square of the machine diameter D, the best way to compensate for the low rotational speed, is to increase the machine diameter. Hence, for very high power ratings, very large diameter machines are required. By incorporating superconducting field windings, the magnetic loading B is no longer limited by the current carrying capabilities of copper or the flux density limitations of permanent magnets. Hence the size of the machine can be significantly reduced by operating with a higher magnetic loading.

Rotating electric machines with superconducting field windings but conventional copper stators would be considered to be partially superconducting. If the stator windings were to be replaced with HTS as well, the machine would also benefit from an increased electric loading A_{E}. This type of machine would be considered to be fully superconducting, these machines offer the highest power densities that can be achieved. The electrification of aircraft propulsion is one major area of research where fully superconducting machines are considered due to the very challenging requirements of the propulsion motors. The Advanced Propulsion Centre (APC) and Aerospace Technology Institute (ATI) Roadmaps seek electrical machines approaching 9-25 kW kg^{-1} by 2035. In [57], the minimum required power density is stated as 12.7 kW kg^{-1}.

Clearly superconducting machines can offer a big advantage in size and weight when compared to conventional machines, however the increased power density comes with many technical challenges, namely cost, cooling and the mechanical structure. These issues will be further discussed throughout this chapter.

3.3 Superconducting Machine Topologies

Superconducting machine designs come in a wide range of topologies. This section will cover the main aspects of superconducting machines. The section will mainly focus on the application of high-temperature superconducting (HTS) tapes to conventional synchronous machines. HTS tapes exhibit little to no losses under DC conditions, depending on the magnetic field environment of the superconducting coils. This makes the synchronous machine, the ideal candidate for the application of superconductors since the field winding carries a DC current.

3.3.1 Air-cored and Iron-cored

One of the major differences between superconducting machine designs is whether the machine is air-cored or iron-cored. Due to the high current density of HTS tapes, conventional iron quickly saturates, limiting the true advantage of superconductors. For air-cored designs however, the HTS material requirements are significantly increased. Several combinations of using magnetic (iron) and non-magnetic composites (NMC) exist, this is highlighted in table 3.2 [58]. The table shows the different combinations of iron and non-magnetic material, where topology T1 is a fully air-cored machine with no magnetic material at all and T9 is a fully iron-cored machine where all the active mass consists of magnetic material. The topologies in between feature a combination of magnetic materials and non-magnetic composites. Each topology was optimized for minimum amount of active material cost. It was concluded that using iron as the active mass leads to lower active material cost and a shorter axial length. Hence, when active material cost is the main design focus, the machine should incorporate as much iron as possible to minimize the amount of superconducting material required. However, this study only considered the active material cost, other machine parameters such as size, weight and efficiency are of importance as well.

Table 3.2. Iron-cored and air-cored topology combinations

Topology	**Field yoke**	**Field pole core**	**Armature tooth**	**Armature yoke**
T1	NMC	NMC	NMC	NMC
T2	Iron	NMC	NMC	NMC
T3	Iron	Iron	NMC	NMC
T4	NMC	NMC	NMC	Iron
T5	Iron	NMC	NMC	Iron
T6	Iron	Iron	NMC	Iron
T7	NMC	NMC	Iron	Iron
T8	Iron	NMC	Iron	Iron
T9	Iron	Iron	Iron	Iron

When considering the weight, air-cored machines are considerably lighter than iron-cored machines [59, 60, 61], while this might come at the cost of increased active material costs, it is the machine design requirements, which dictate the specifications of the machine. As concluded in [58], active material cost and generator efficiency might be of higher importance than the mass of the machine. However, when considering electric motors for aircraft propulsion, to achieve the required power densities, an air-cored design becomes essential. In fact, many superconducting propulsion motor designs feature air-cored superconducting field windings [62]. This however leads to another major issue, when considering aircraft propulsion motors, these machines rotate at very high rotational speeds, often up to several thousand RPM. The high rotational speed leads to high centrifugal forces acting on the superconducting field windings which, due to the air-cored design, have little to no support. In this case, the support structure needed to support the field windings can be very challenging. Lastly regarding the efficiency, as was mentioned in the previous chapter, superconductors exhibit loss when penetrated by changing magnetic fields. Considering a partially superconducting machine with a superconducting field winding, as the winding rotates in the machine environment, it will experience induced losses. These losses can either be increased or reduced by having iron in the machine [33], the result is highly dependent on the machine design. If the iron changes the magnetic flux profile on the superconducting winding by causing more flux to penetrate the tape, the losses are increased. On the other hand, if the iron acts as a flux diverter, reducing the magnetic flux penetration of the superconductors, the loss is reduced. Figure 3.5 shows an excellent comparison between the different configurations that are available for a radial flux machine. While the figure shows a fully superconducting machine, it should be noted that the same options apply to partially superconducting machines where the stator consists of conventional copper.

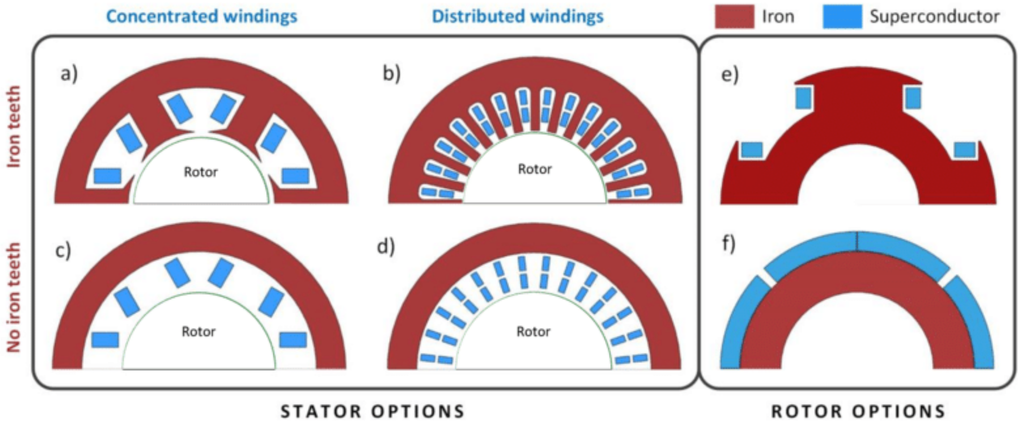

Figure 3.5. Stator and rotor configurations for a radial flux machine [62].

Clearly, each configuration has its own benefits and drawbacks, and it is highly dependent on the application requirements to determine which configuration is the most suitable for the superconducting machine design.

3.3.2 Warm Rotor and Cold Rotor

The cooling system of a superconducting generator has a large influence on the overall cost, efficiency and reliability of the machine. For synchronous generators with superconducting field windings, essentially two cryostat configurations exist, a warm core rotor and cold core rotor. For the warm core rotor, only the superconducting coils are contained within the cryostat. This option offers a small thermal budget at the cost of a more complicated support structure, since the support structure is required to make connections between ambient and cryogenic temperature while transmitting the torque from the superconducting windings to the rotor body. This option is preferred in large diameter superconducting machines to reduce the required cooling power. In a cold core rotor, the complete rotor is cooled down. The main advantage of this design is that the cryostat as well as the superconducting field coil support structures are significantly simplified [63]. A comparison between the cold rotor and warm rotor configurations is shown in figure 3.6.

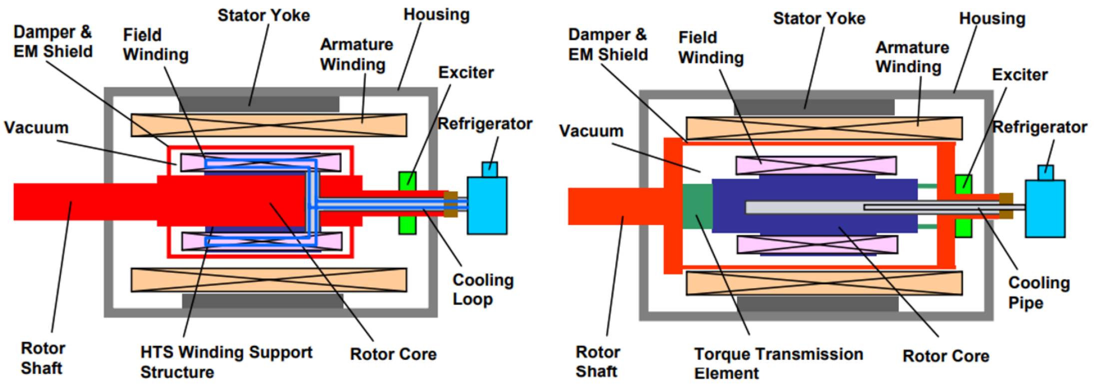

Figure 3.6. Superconducting machine with a warm rotor configuration (left) and cold rotor configuration (right) [63].

3.3.3 Partially and Fully Superconducting

Superconducting machines can be either fully superconducting or partially superconducting. A fully superconducting machine employs superconducting tape for the field winding as well as stator windings. This configuration offers the highest power density since both the magnetic loading and the electric loading are increased. The field winding carries a DC current, while the stator operates under AC conditions. Since the superconducting coils in the stator operate under AC conditions, AC losses are present [33]. The cooling budget for this setup is in general relatively high due to the large volume of superconducting material that is required to be cooled down. In addition, due to the AC losses in the stator windings an additional heat source is present. Depending on the operating frequency, the AC losses in conjunction with the required cooling system could even surpass the losses in copper [62]. Partially superconducting machines on the other hand only deploy superconducting material in the field winding. Since the field winding operates with a DC current, the losses in the field winding are less bad than in the stator windings, however due to the changing magnetic field environment in the machine, dynamic losses and magnetisation losses are still present [64]. However, the heat load for partially superconducting machines is significantly lower due to the much-reduced AC losses. In addition, the volume of superconducting material is significantly lower than for fully superconducting machines reducing the required cooling budget even further.

3.4 Major Superconducting Machine Projects

This section focuses in particular on existing 10 MW generator designs for direct drive wind turbines. A significant amount of research has been done within industry as well as academia into superconducting 10 MW generators. Table 3.3 summarizes some of the most prominent examples in the recent years. The table shows whether the machine is iron-cored or air-cored, fully superconducting or partially superconducting and radial flux or axial flux. The outer diameters are given and where possible the total mass or active mass. And finally, the type of superconductor, the conductor length and the operating temperatures are listed.

When examining the table, several aspects become apparent. Almost all designs are based on the radial flux configuration of the synchronous machine, and almost all of the radial flux designs use hundreds of kilometers of superconducting tape. One exception here is the design from AMSC, which only uses 36 km, but this design is fully-iron cored and is among the heaviest of the concepts listed.

Several reasons for the high HTS requirements exist. Firstly, since the machines are rotating very slowly, it is desirable to have a high number of poles. A high number of poles leads to a quicker variation in magnetic flux across the stator windings, and according to Faraday's law, this leads to a higher induced voltage and hence a higher power output. However, as the number of poles in radial flux machines increases, the required length of superconducting material increases significantly as well due to the axial length of the machines and the additional end windings.

Secondly, in conventional synchronous machines, the mechanical air gap clearance is equivalent to the magnetic air gap. In superconducting machines, the field winding needs to be enclosed by a cryostat and potentially an electromagnetic shield. These additional components lead to the electromagnetic air gap being bigger than the mechanical air gap [50]. To compensate for the increased electromagnetic air gap, a higher amount of superconducting material is required. There is a high variation in air gap lengths for the various design due to this reason, a good correlation between HTS length and air gap clearance can be seen in the following subsections when several designs are investigated in further detail.

When considering the mass of the generators, it can be seen that most designs do not include the structural mass required to maintain the air gap clearance. However, the structural mass can make up more than half of the total mass of the generator. For example, the double claw pole generator design proposed by Keysan requires a structural mass of approximately 120 tonnes which is 2/3 of the total mass [15]. The calculation of the structural mass and how to reduce it will be discussed in further detail in chapter 5.

One further observation that can be made is that the vast majority of designs operate on the lower end of the operating temperatures at around 20 to 30 K. The low temperatures are required to lower the HTS requirements. However, removing heat at temperatures as low as 20 K is relatively difficult and inefficient. The different cryogenic cooling systems are discussed in further detail in the next section.

Table 3.3. Comparison of superconducting 10 MW generator designs

Year	**Developer**	**Topology**	**Diameter [m]**	**Weight [tonnes]**	**SC Type**	**SC Length [km]**	**Temperature [K]**
2010	Abrahamsen *et al.* [65]	Iron-cored rad. S.M.	4.7	88	YBCO	200-300	20
2011	AMSC [18]	Iron-cored rad. S.M.	4.5 to 5	180*	YBCO	36	30
2012	Terao *et al.* [66]	Fully SC air-cored rad. S.M.	3.67	31.7	MgB_2 + HTS	270	20
2012	General Electric [67]	Air-cored rad. S.M.	4.87	143*	NbTi	720	6
2013	Sung *et al.* [68]	Iron-cored rad. S.M.	5.3	147*	YBCO	586	20
2013	Kostopoulos *et al.* [61]	Fully SC air-cored rad. S.M.	5.6	60-70	MgB_2	55	20
2013	Kim *et al.* [59]	Air-cored rad. S.M.	3	41.7	YBCO	289	22
2014	Kalsi [60]	Fully SC air-rad. cored S.M.	5	52.4	MgB_2	42.6	20
2015	Song *et al.* [20]	Fully SC air-rad. cored S.M.	4.1	N/A	YBCO + MgB_2	94	20
2015	Keysan *et al.* [15]	Iron-cored ax. S.M.	6.63	184*	YBCO	13.5	65
2016	Tecnalia [69]	Iron-cored rad. S.M.	5	161	MgB_2	153	20

*with structural mass

** 11.7 MW generator instead of 10 MW

Some of the more popular or distinctive designs are introduced in further detail in the sub-sections below. The double claw pole generator proposed by Keysan will be discussed in the next chapter.

3.4.1 DTU / INNWIND (2010)

The design of the 10 MW generator is based on the design of a previous 5 MW superconducting wind turbine generator iteration, which was also developed at the Technical University of Denmark [70]. It is a partially air-cored synchronous generator using YBCO for the field windings. The generator has 16 poles. The poles consist of racetrack wound superconducting coils, which are supported by non-magnetic support tubes. Figure 3.7 shows a schematic of a field winding, as can be seen the rotor is in warm configuration since only the coil is being cooled down.

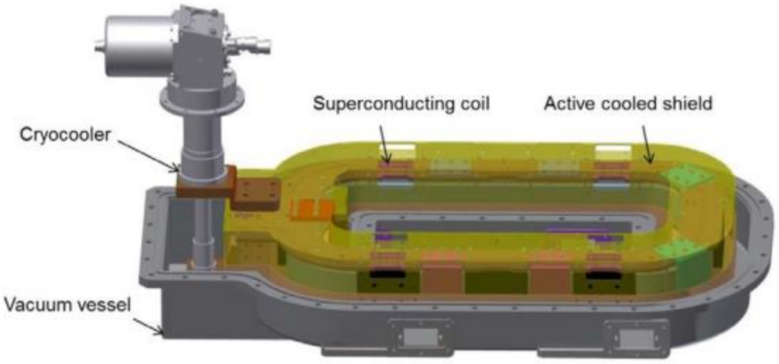

Figure 3.7. Schematic of the superconducting field coil [71].

The air gap is 110 mm. Table 3.4 summarizes the key parameters. The unoptimized “extreme” generator uses 1450 km and weighs 88 tonnes.

Table 3.4. Key parameters

Iteration	extreme generator		optimized generator	
Parameters	**Value**	**Unit**	**Value**	**Unit**
Rating	10	MW	10	MW
Power factor	N/A	/	N/A	/
Diameter	4.7	m	N/A	m
Weight	88	tonnes	N/A	tonnes
Efficiency	N/A	%	N/A	%
Superconductor type	YBCO	/	YBCO	/
Length of superconducting material	1450	km	200-300	km
Cooling system	N/A	/	N/A	/
Operating temperature	20	K	20	K

According to A. B. Abrahamsen *et al*. the optimized generator would only require 200 to 300 km of YBCO tape by increasing the amount of iron in the machine and reducing the magnetic field strength. The conclusion of the paper is to show that several hundreds of kilometres of tape are required to build lightweight machines. The design of this generator was taken forward and further improved during the INNWIND project, which is an EU funded projected with DTU as the co-ordinator [71].

3.4.2 AMSC (2011)

This 10 MW design is based a lot on a previous design of a 36.5 MW HTS propulsion motor for ships [72]. The assumption is made that the experience gained while running the HTS propulsion motor can also be applied to the HTS wind generator proving its reliability. The HTS synchronous generator was designed with cost targets determined by the AMSC Windtec business unit based on data on the emerging multi-megawatt offshore market. The cost of a 10MW wind turbine was estimated to be around $12M to $26M. The generator has 24 poles with an air gap of 20 mm. Due to the low rotational speed it was decided to mount the coldheads straight onto the rotor. The cooling system used is CTI-1020 which is based on GM technology. 6 to 10 cryocoolers with N + 1 redundancy are employed. Small superconducting coils were first fabricated and tested to collect data on the thermal as well as mechanical properties. A full-scale coil was then fabricated and tested at 77 K and 30 K. The dimensions are of the full-scale coil are 1270 mm by 525 mm using 1500 m of YBCO tape [18]. A manufacturer racetrack coil for the 10 MW design is shown in figure 3.8. The generator is designed for high reliability, maintenance is only required every 2 years or potentially longer mainly for the cryocoolers, fans and seals. Table 3.5 summarizes the key data of the proposed design.

Figure 3.8. 2G HTS pole set designed and tested for a 10 MW class generator [18].

Table 3.5. Key parameters

Parameters	**Value**	**Unit**
Rating	10	MW
Power factor	>0.95	/
Diameter	4.5 to 5	m
Weight	180	tonnes
Efficiency	96	%
Superconductor type	YBCO	/
Length of superconducting material	36	km
Cooling system	GM Cryocooler	/
Operating temperature	30-40	K

3.4.3 KIER (2013)

This superconducting synchronous generator is a partially iron-cored machine, the rotor body, vacuum shield and stator teeth consist of non-magnetic material. The rotor poles are racetrack type HTS coils. Laminated silicon steel is used for the magnetic shield. The concept of the machine is highlighted in figure 3.9.

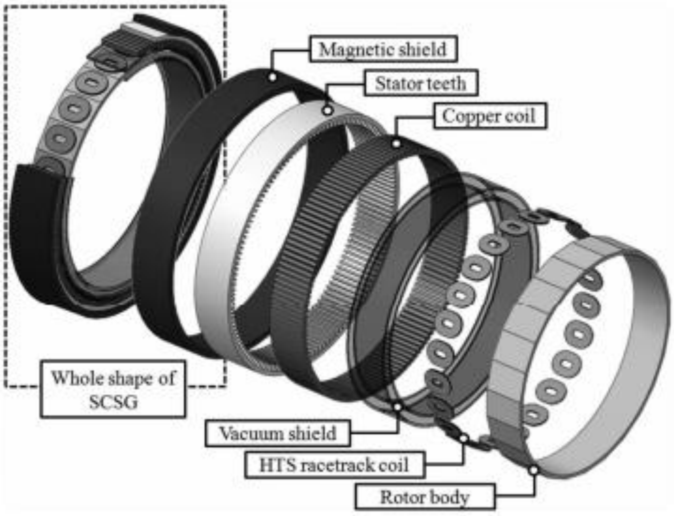

Figure 3.9. Korea Institute of Energy Research generator concept [68].

Two designs exist, one using YBCO and one using BSCCO. YBCO dimensions are 0.1 mm think and 4mm wide. BSCCO is 0.36 mm thick and 4.5 mm wide. The stator winding configuration is double-layered, distributed three-phase windings. Space factor of rotor and stator coils are 1 and 0.4 respectively. Both designs have an air gap of 50 mm. The basic design is found through the modified Taguchi method with the major design factors being, the length of HTS wire and the weight and volume of the superconducting synchronous machine. The control parameters which affect the electromotive forces are (A) the number of double pancake coil (DPC) layers, (B) the number of turns in the DPC, (C) the number of stator turns and (D) the number of poles. The optimal parameters were found to be (A) 5 layers, (B) 2000 turns, (C) 25 turns, (D) 24 poles for YBCO and (A) 4 layers, (B) 800 turns, (C) 30 turns and (D) 24 poles for BSCCO. The YBCO design is operating with 1000 A (engineering current density of 251.23 A/mm^2) and the BSCCO design is operating with 187 A (engineering current density of 115.56 A/mm^2), both operate at a temperature of 20 K. The YBCO design is the lightest with 147 tonnes but using 586 km of wire. BSCCO design weighs 196 tonnes using 222 km wire. The key parameters are summarised in table 3.6.

Table 3.6. Key parameters

Iteration	YBCO design		BSCCO design	
Parameters	**Value**	**Unit**	**Value**	**Unit**
Rating	10	MW	10	MW
Power factor	N/A	/	N/A	/
Diameter	5.3	m	6.72	m
Weight	147	tonnes	196	tonnes
Efficiency	N/A	%	N/A	%
Superconductor type	YBCO	/	BSCCO	/
Length of superconducting material	586	km	222	km
Cooling system	N/A	/	N/A	/
Operating temperature	20	K	20	K

3.4.4 Delft University of Technology (2013)

Unlike the previous designs, this is a fully superconducting synchronous generator. Both the field windings as well as the stator windings are constructed with superconductors. The machine is almost completely made from non-magnetic material except for the EM shield, which is made out of iron. The design schematic is shown in figure 3.10.

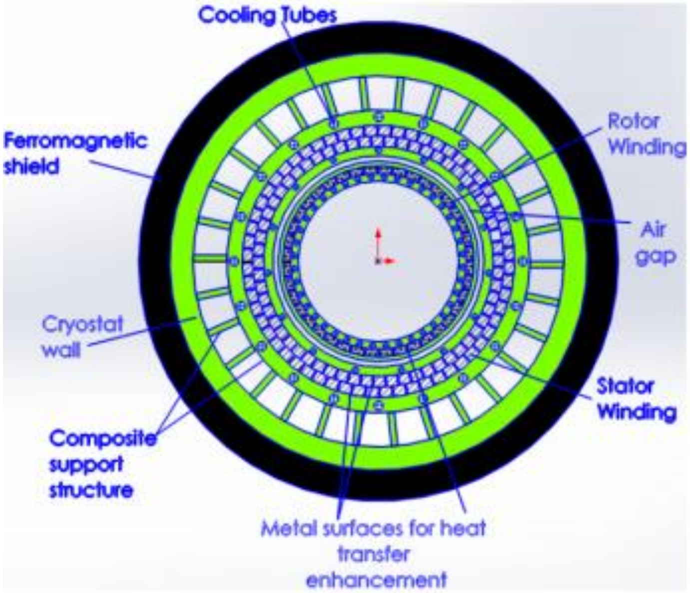

Figure 3.10. Delft 10 MW generator design [61].

Since the machine does not feature any iron to provide mechanical support for the superconducting field windings, a sophisticated support structure is required to maintain the mechanical integrity of the windings. MgB_2 is used due to its superior AC loss characteristics as compared to YBCO tapes. The complete machine is inside of a cryostat with an EM shield around the cryostat. For the cooling system the adiabatic forced flow winding concept is used. The design requires 2.2 kW of cooling power at 20 K, which is extremely difficult to achieve. The peak flux density is set at 2 T at an operating temperature of 20 K. The number of pole pairs of the machine is 10, however studies have shown that a pole pair number of 20 is more desirable for weight as well as efficiency reasons [61]. Table 3.7 summarizes the key parameters of this design.

Table 3.7. Key Parameters

Parameters	**Value**	**Unit**
Rating	10	MW
Power factor	N/A	/
Diameter	5.6	m
Weight	60-70	tonnes
Efficiency	97	%
Superconductor type	MgB_2	/
Length of superconducting material	55	km
Cooling system	N/A	/
Operating temperature	20	K

3.4.5 Kalsi Green Power Systems (2014)

This design is fully air-cored and fully superconducting. The field winding consists of race-track coils, each coil is 600 turns and the current per turn is 1000 A. A total of 38 km of MgB_2 wire is used for 24 poles on the rotor. The race-track coils are mounted onto a non-magnetic stainless-steel cylinder in a warm rotor configuration. The design concept is shown in figure 3.11. The armature consists of a single layer winding configuration. The stator features 288 slots, and a total of 4.6 km of MgB_2 wire is required. The operating current is 1360 A. The air gap is 20 mm. The stator windings are fixed with a multitude of torque tubes from within the cryostat onto the stator yoke at ambient temperature. A cost calculation for the generator was done and the author concluded that the generator is economically within the economic model of most wind farm developers. The cost of the generator was estimated to be approximately $ 2.2 million.

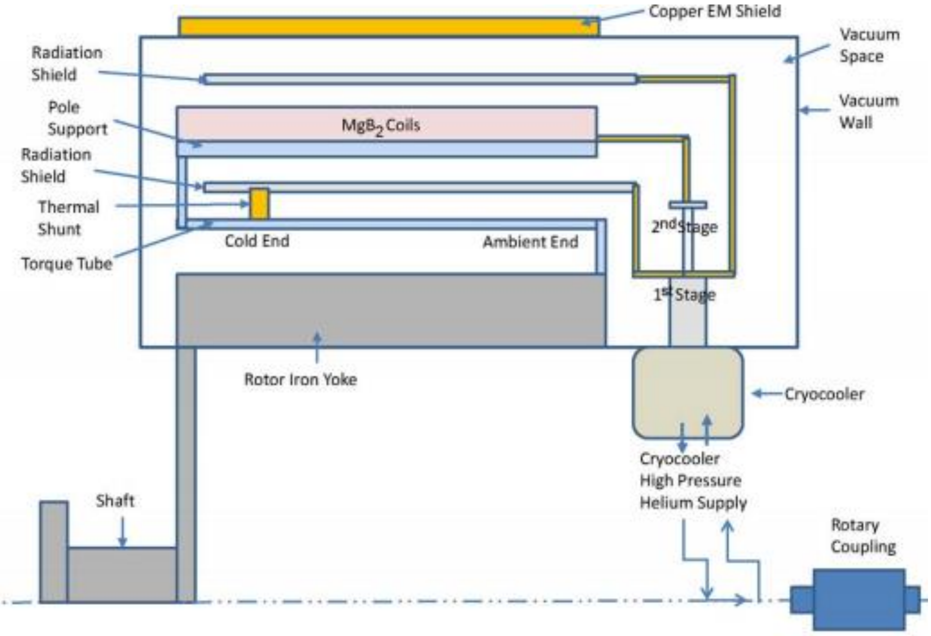

Figure 3.11. Kalsi Green Power Systems generator concept [60].

Table 3.8 summarises the main design parameters of this generator design.

Table 3.8. Key parameters

Parameters	Value	Unit
Rating	10	MW
Power factor	0.99	/
Diameter	<5	m
Weight	52	tonnes
Efficiency	>98	%
Superconductor type	MgB_2	/
Length of superconducting material	42.6	km
Cooling system	GM coolers	/

3.4.6 Tecnalia/Suprapower (2016)

After several iterations, the design was fixed at an iron salient pole synchronous generator with an air gap diameter of 10.1m and 48 poles. The polar pitch was one of the major design constraints due to the coil and cryostat dimensions. The peak flux density in the air gap along the pole pitch was found to be 1.5 T. The armature does not feature any magnetic teeth as those were expected to saturate quickly, a distributed winding configuration is used, which allowed to fit a large amount of copper in the air-cored stator. The paper covers in detail the construction and performance of the superconducting racetrack coils. The poles consist of 9 racetrack MgB_2 double pancake coils connected in series with insulation layers in between. Small scale versions of the coils were tested before any full-size coils were constructed, figure 3.12 shows one of the first racetrack type prototypes. First a circular one layer 7 turn coil was manufactured to analyse the wire behaviour and the cryogen-free refrigeration. Then a second circular 30 turn DP coil was built to validate manufacturing and testing process. The quench behaviour of the coils was investigated. Table 3.9 summarises the key parameters of this design.

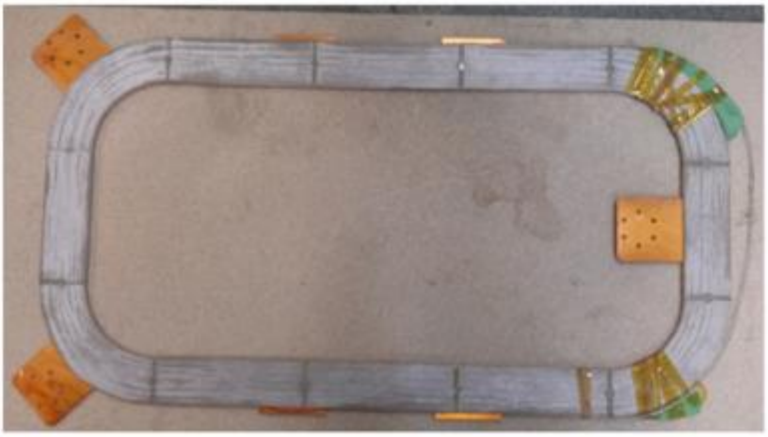

Figure 3.12. MgB_2 coil prototype [69].

Table 3.9. Key parameters

Parameters	**Value**	**Unit**
Rating	10	MW
Power factor	0.95	/
Diameter	5.05	m
Weight	60-70	tonnes
Efficiency	95.2	%
Superconductor type	MgB_2	/
Length of superconducting material	153	km
Cooling system	GM coolers	/
Operating temperature	20	K

3.5 Cryocooling Systems

Cryocoolers have been used in a wide range of applications for decades already. One of the earliest applications appeared about 50 years ago in the military sector. Over 140,000 Stirling coolers have been manufactured since then for military applications, indicating that the technology is very mature and tested. One issue with using cryocoolers for HTS power applications is that the cooling power is considerably higher when compared to the usual applications where the cooling power ranges from 0.15W to 7W. Another major application sector is in the medical industry. Cryocoolers are used widely to cool down superconducting coils in MRIs, mainly GM cryocoolers are used here [19]. Several different kinds of cryocoolers are available each, with their own advantages and disadvantages, the cooling principles and types of cryocooler will be briefly introduced and discussed in this section.

3.5.1 Carnot Efficiency

Figure 3.13 shows a schematic of a refrigerator with all important thermodynamic components associated with it.

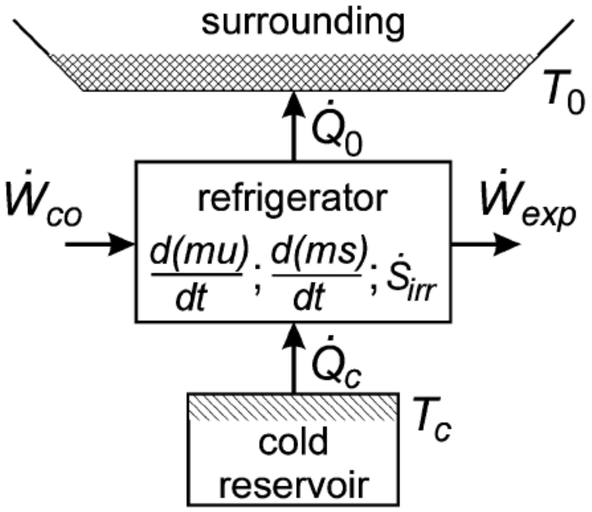

Figure 3.13. Schematic of a refrigerator [19].

The operation of the refrigerator can be described as follows [19]. The refrigerator absorbs the heat flow $\dot{Q}_C$ from a cold reservoir at a temperature T_c and rejects the heat flow $\dot{Q}_0$ to the surroundings at an ambient temperature T_0. The net input power required to operate the refrigerator is $\dot{W}_{\text{co}}$, the refrigerator may also provide some external power flow $\dot{W}_{\text{exp}}$ due to an expander for example. However, for a complete refrigeration system $\dot{W}_{\text{exp}}$ is usually equal to zero. The internal energy and entropy of the refrigerator are given by mu and ms where m

is the mass of refrigerator, u is the specific internal energy and s the specific entropy. For steady state conditions these variables are independent of time. $\dot{S}_{\mathrm{irr}}$ is the entropy production rate due to irreversible effects, for an ideal refrigerator $\dot{S}_{\mathrm{irr}}$ is equal to zero.

For a refrigerator in steady-state operation the coefficient of performance *COP* is given by:

$$\mathrm{COP} = \frac{\dot{\mathrm{Q}}_{\mathrm{C}}}{\dot{\mathrm{W}}_{\mathrm{co}}} \tag{3.2}$$

And the specific power is given by:

$$p_{\mathrm{s}} = \frac{1}{COP} \tag{3.3}$$

A relationship between all parameters mentioned in the earlier paragraph can be found by combining the first (energy balance) and second (entropy balance) laws of thermodynamics giving the *COP* for steady-state conditions as:

$$\mathrm{COP} = \frac{\dot{\mathrm{Q}}_{\mathrm{C}}}{\dot{\mathrm{W}}_{\mathrm{co}}} = \frac{\mathrm{T_C}}{\mathrm{T_0} - \mathrm{T_C}}(1 - \frac{\mathrm{T_0}\dot{\mathrm{S}}_{\mathrm{irr}} + \dot{\mathrm{W}}_{\mathrm{exp}}}{\dot{\mathrm{W}}_{\mathrm{co}}}) \tag{3.4}$$

For an ideal refrigerator $\dot{S}_{\mathrm{irr}} = 0$ and $\dot{W}_{\mathrm{exp}} = 0$ giving:

$$COP_{\mathrm{Carnot}} = \frac{T_{\mathrm{C}}}{T_0 - T_{\mathrm{C}}} \tag{3.5}$$

COP_{Carnot} is known as the maximum or ideal coefficient of performance. Assuming a room temperature of 300 K, the maximum efficiency for 77 K for example can be calculated to be 34.53 % and 7.14 % for 20 K.

The efficiency of actual refrigerators is usually given as a fraction of the Carnot efficiency as:

$$\eta = \frac{COP}{COP_{\mathrm{Carnot}}} \tag{3.6}$$

At this stage it can already be seen that cooling down to cryogenic temperatures is very challenging and requires a lot of energy. Hence minimizing the cooling power required in HTS machines is vital to maintain a high efficiency. In [73] for example, it is stated that in a small cryostat, it approximately takes 10 W of power to remove 1 W of heat at 77 K, giving an efficiency of only 10 %.

3.5.2 Types of Cryocoolers

This section will cover the most common types of cryocoolers available and attempt to identify the most suitable refrigerator for high-temperature superconducting applications such as in rotating electrical machines. Figure 3.14 shows the most commonly used cryocoolers, they are split into two groups, recuperative and regenerative.

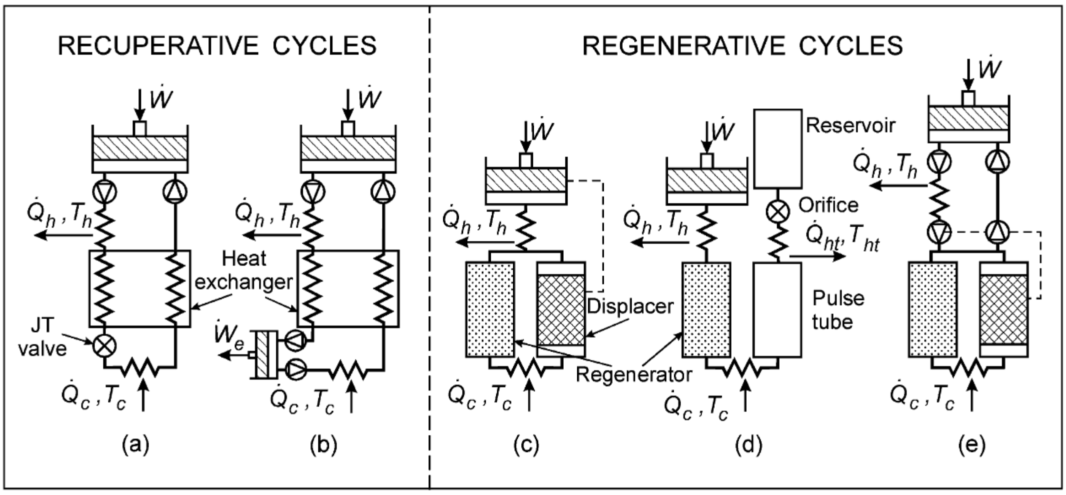

Figure 3.14. Types of cryocoolers available [19].

The Joule-Thomson (a) and Brayton (b) cryocoolers are of the recuperative type. The Stirling (c), Pulse Tube (d) and Gifford-McMahon (e) are of the regenerative type.

- **Recuperative cycles [19]**

In the recuperative type cryocoolers, the working fluid always flows steadily in one direction with steady low-and high-pressure lines analogous to dc electrical systems. The recuperative heat exchangers transfer heat from the high-pressure stream to the low-pressure stream through a pressure partition. The steady pressure allows for the use of large gas volumes to be used anywhere in the system with almost no consequences except for larger radiation heat if located at the cold end. This enables recuperative type cryocoolers to ‘transfer cold’ to any number of distant locations after the gas is expanded and cooled. This also implies that the cold end can be separated by a large distance from the compressor. Heating of the gas occurs in the compressor during compression, the gas is then transported to the desired location, which is supposed to be cooled, here the gas is expanded from high-pressure to low-pressure, cooling the location down.

a) Joule-Thompson cryocoolers [19]

JT refrigerators produce cooling when the high-pressure gas expands through a flow impedance, often referred to as a JT valve. The process occurs without an additional energy input hence the process occurs at a constant enthalpy. The most commonly used gases in conjunction with JT refrigerators are nitrogen and argon at pressures of 20 MPa (200 bar) or more to achieve reasonable cooling. Pressures of this magnitude require special compressors which tend to have a short life cycle. JT refrigerators do not have any moving parts at the cold end which allows them to be miniaturized. Hence JT cryocoolers are mostly used for smaller applications such as cooling electronics as the cooling power only lies in the range of a few Watt, making them not very applicable for superconductor applications.

b) Brayton cryocoolers [19]

Same as for JT refrigerators the cooling in Brayton cryocoolers occurs as the working gas expands. The gas is expanded by using an expansion turbine as can be seen in 3.14 (b). In general, it can be said that Brayton cryocoolers are more efficient than JT cryocoolers.

- **Regenerative cycles [19]**

These cryocoolers operate with oscillating pressures and mass flows in the cold head. Almost always helium is used as the working fluid. The oscillating pressure is either created through a valveless compressor as shown in 3.14 for Stirling (c) and Pulse Tube cryocoolers (d) or with valves that switch between the high and low pressure source for GM refrigerators (e).

c) Stirling cryocoolers [19]

The principle of operation can be explained as follows. The first moving part, the pressure oscillator, causes temperature to oscillate. The second moving part, the displacer, separates heating and cooling effects by causing motion in the gas in the right phase relationship with the pressure oscillator. When the displacer is moved downward, gas is displaced to the warm end of the system through the regenerator. The piston in the compressor then compresses the gas and the heat of compression is removed through the heat exchange with the ambient. The displacer is then moved upward, and gas is displaced to the cold end of the system. The piston expands the gas and the cooled gas absorbs heat from the system and the cycle then repeats. Motion of piston and displacer are nearly sinusoidal but with a phase difference of about 90°. Stirling coolers are more efficient than GM coolers however they have problems with reliability and EMI. The main application for Stirling coolers in HTS power applications is for cooling power cables [74].

d) Gifford-McMahon cryocoolers [19]

The cooling head of GM coolers is the same as for Stirling coolers, they both use a moving displacer with a regenerator matrix on the inside. Hence, the principle of operation for both coolers is the same. However, the operating frequency of the moving displacer is only about 1-2 Hz as opposed to 30-60 Hz for Stirling coolers. Due to the lower operating frequency GM coolers have a longer lifetime.

GM cryocoolers are considered the workhorses in the cooling industry, they are reliable and provide higher efficiency in the 20-35 K range. Their Mean Time Before Maintenance (MTBM) is about 1-2 years which makes them very suitable for offshore wind turbines. A common setup for cooling HTS machines is using a thermosiphon cooling system in conjunction with several GM cryocoolers to provide the required cooling power as well as to introduce some redundancy. Figure 3.15 shows the main components of a GM cryocooler and the main sources of concern for users. As can be seen most components have a lifetime of a couple years except for the adsorber cartridge which needs to be replaced every year.

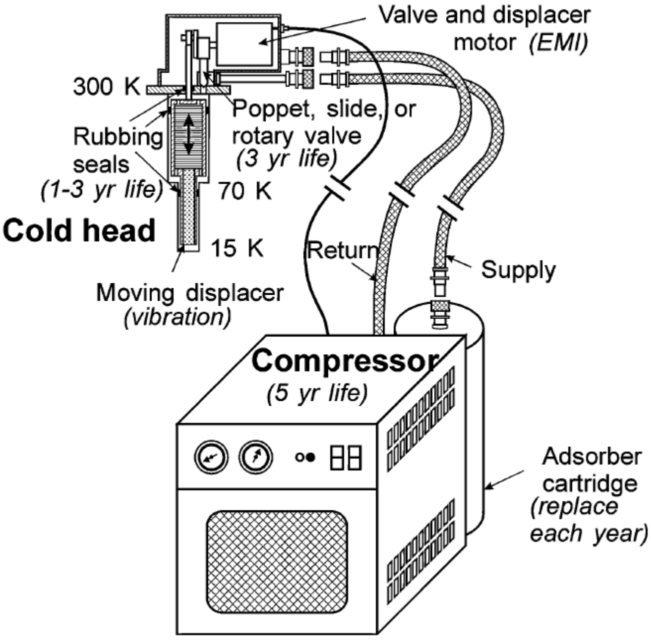

Figure 3.15. Main components of a GM cryocooler [19].

Companies such as Siemens use a thermosiphon cooling system with GM cryocoolers for their HTS synchronous machine prototypes [75, 76]. Researchers at the University of Tokyo have also developed a 100 W thermosiphon cooling system using GM coolers to use in conjunction with a 100 kW synchronous machine [77]. Also, a group of researchers in Korea designed a 1 MW HTS synchronous motor using a thermosiphon GM cooling system [78].

e) Pulse tube crycocoolers [19]

Pulse tube cryocoolers can be thought of as a further improvement on Stirling and GM coolers by removing the moving displacer which is a source of vibration and has a limited lifetime. The gas movement in phase with the pressure oscillation is achieved using an orifice with a reservoir volume to store the gas during a half cycle. The oscillating flow through the orifice separates the heating and cooling effects just like a displacer would. The four steps in the operating cycle of a pulse tube cryocooler are as follows:

1) The compressor piston moves down to compress the gas (usually Helium) in the pulse tube.
2) The heated compressed gas is now at a higher pressure than the average in the reservoir. Due to this, the gas now flows through the orifice into reservoir, on the way it exchanges heat with ambient through the heat exchanger at the warm end of the pulse tube. The flow stops when the pressure in the pulse tube reduces to the average pressure.
3) The piston now moves up and the gas in the pulse tube is expanded adiabatically.
4) The cold low-pressure gas in the pulse tube is now forced past the cold end and heat is exchanged by the gas flow from the reservoir into the pulse tube through the orifice. The flow again stops once the average pressure in the pulse tube is reached. The cycle then repeats.

The operating temperature of pulse tube coolers is around 20 K nowadays for one stage or around 2 K for two stages. Figure 3.16 shows a pulse tube cooler with an even further increased efficiency by adding two more passive components, a secondary orifice which allows some of the oscillating fluid to bypass the regenerator reducing the regenerator losses and an inertance tube which shifts the phase between flow and pressure to a more optimal value.

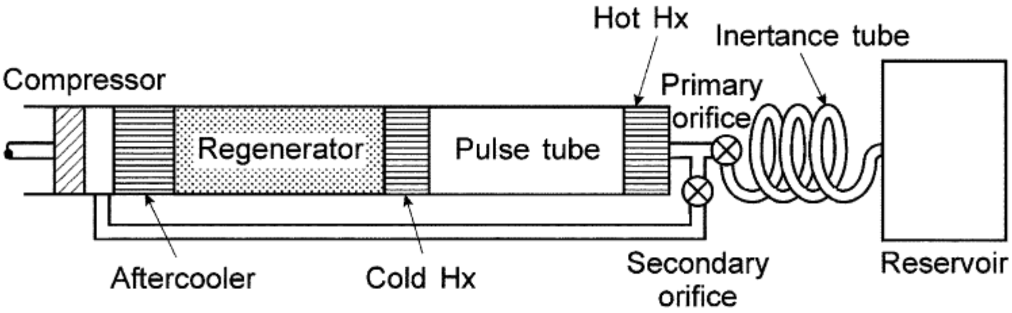

Figure 3.16. Pulse tube cooler with secondary orifice and inertance tube [19].

Siemens used a thermo-siphon cooling system in conjunction with a GM cooler for their 400 kW as well as 4 MVA HTS synchronous machines. However they stated that the aim is to move towards a pulse-tube cooler to take advantage of their prolonged service intervals [75]. It is important to note that many of these cryocoolers can be applied to superconducting technology with little to no modifications required at all. To reduce the main issue with cryocoolers, their cost, it is important to share cryocooler development with other applications. For further details on the different cryocoolers available and their operation, reference [19] provides an excellent review.

3.5.3 Cryocooler Comparison

Figure 3.17 shows the operating range in terms of temperature and cooling power of common cryocoolers. It can be seen that the temperature requirements for the various HTS applications can vary a great deal. Transmission cables, transformers and fault current limiters tend to operate in the temperature range of 70 K. However, their cooling power requirements are much higher than for other applications. For rotating machines, which tend to operate in the range of 20 K up to 40 K, the required cooling power was estimated to be several hundreds of watts. The most suitable cryocooler would be a single stage GM cryocooler or a two-stage Stirling cooler. Pulse tube versions of both coolers could be considered as well for higher efficiency and reliability.

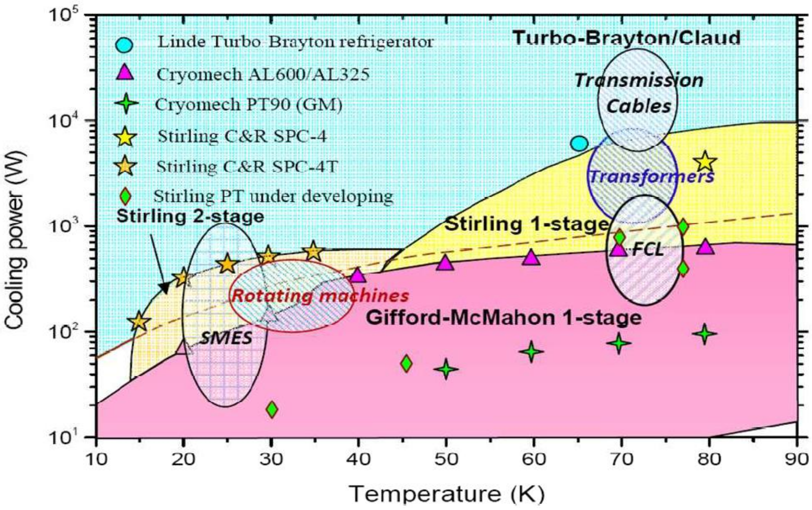

Figure 3.17. Temperature and cooling power ranges for common cryocoolers [74]

3.5.4 Cooling Power

To determine the required cooling power budget there are two commonly used methods. Firstly, an analytical analysis can be performed. This is a quick method which can give approximate results and a general idea about the cooling power that will be required. The second method is performing a finite element analysis for detailed results. This section will cover the analytical analysis of the various heat loads that exist for a superconducting machine, approximate equations for the heat loads will be stated and explained. Combining all the losses gives a good first indication about the cooling power required [79].

a) Current Lead Loss Q_C

A current lead is essential a type of metal (copper for example) making the connection from the power supply at room temperature to the superconductors at the cold-end temperature. Since it carries the current to the superconductors and has non-zero ohmic resistance it produces heat. The current lead loss at the cold end can be approximately calculated as [80]:

$$\frac{I_0 l}{A} = \sqrt{\frac{2k(T_c - T_0)}{\rho}} \tag{3.7}$$

where I_0 is the operating current, l is the current lead length, A is the cross-sectional area of the current lead, k is the thermal conductivity, ρ is the resistivity, and T_c and T_0 are the respective cold end and warm end temperatures.

Differentiating equation 3.7 with respect to l/A and setting the equation to zero yields [81]:

$$\dot{q}_{lead} = I_0\sqrt{2k\rho(T_{\mathrm{c}} - T_0)} \tag{3.8}$$

Taking k as 460 W/(mK) and the reduced resistivity of copper as 10^{-8} Ωm due to the lower temperature [81], the current heat loss can be given as approximately 45 mW/A, for brass the heat loss is 32 mW/A, indicating that brass is preferable over copper for conduction-cooled leads [81].

b) Radiation Heat Loss Q_r

The radiation heat loss can significantly be reduced by wrapping the HTS coil in superinsulation layers (MLI), the heat loss is a function of the number of layers used, equation 3.9 shows how to calculate the radiation heat loss.

$$\dot{q}_{\mathrm{r}} = \frac{\epsilon\sigma}{N_{\mathrm{i}} + 1}({T_0}^4 - {T_{\mathrm{c}}}^4) \tag{3.9}$$

where ϵ is reflectivity of the material, for YBCO-coated conductors the reflectivity of polished copper can be used, which is equivalent to approximately 0.02 between 80 K and 4 K. σ is the Stefan-Boltzmann constant and N_{i} is the number of superinsulation layers.

c) Conduction Heat Leak

The heat conduction from suspension straps in the cryostat to keep the superconducting winding in place or the rotor shaft in a cold rotor configuration can be calculated as [79]:

$$Q_t = \frac{kA}{l}\Delta T \tag{3.10}$$

where A and l are the respective cross-sectional area and length of the component in question.

d) Heat conduction in a vacuum

Since a perfect vacuum cannot be achieved, residual gas in the cryostat leads to some heat transfer, this heat leak can be approximated by assuming the heat transfer occurs between two parallel plates [81]:

$$\dot{q}_{\mathrm{g}} = \eta_{\mathrm{g}}P_{\mathrm{g}}\Delta T \tag{3.11}$$

where $\dot{q}_{\mathrm{g}}$ is heat leak in mW/m^2, η_{g} is dependent on the warm and cold temperatures as well as on accommodation coefficients, which for Helium can range from 0.3 at 300 K to 1 at 4.2 K. P_{g} is the pressure in the cryostat, which can be assumed to be around 10^{-5} mbar for practical purposes. Experimental setups can reach pressures as low as 10^{-8} mbar with the use of turbomolecular pumps [82].

These heat leaks make up the majority of the losses found in a cryostat. However, additionally to the above listed losses, the losses in the superconducting winding need to be considered as well. Chapter 8, which covers the superconductor modelling, will provide the expected heat losses for various transport currents and magnetic field environments.

3.6 Chapter Summary

In this chapter some of the HTS power applications were introduced, with particular focus on superconducting machines. It was shown that both the magnetic and electric loading of a machine can be increased by applying HTS, which lead to higher power density machines. Different configurations of superconducting machines exist. The machine can be partially superconducting where only the field winding consists of superconducting material or fully superconducting where the stator is superconducting as well. Machines can be fully iron-cored or fully air-cored or be a combination of the two. It was shown that iron helps to decrease the active material cost through lowering the HTS material requirements. However, mass and efficiency need to be considered as well, to decide on the best topology, it is necessary to consider design on a case by case basis. For superconducting direct-drive generators for wind turbines, it can be said that cost and efficiency are of highest importance while trying to maintain a relatively light and small design. Various designs are discussed in further detail, it was shown that the majority of concepts are based on the radial flux synchronous machine, which in most cases results in high HTS tape requirements due to the electromagnetic air gap being bigger than the mechanical air gap. The chapter finishes with a short review of the different cryocoolers available and defining the heat losses that exist in cryostats.

The next chapter will discuss the advantages of the double claw pole generator introduced by Keysan and Mueller. It will discuss the simulation methods developed to investigate the machine performance in further detail. The following chapters will then address the various shortcomings of the design and provide further improvements to the original design.

Chapter 4 Double Claw Pole Machine Design and Modelling

This chapter will summarise the previous work done on the superconducting double claw pole generator and highlight the main design features. The double claw pole generator was designed with two key strategies in mind, modularity and reliability, while still offering a high torque density. The design is fully iron-cored to reduce the length of superconducting tape required and hence the design benefits of a significant reduction in capital cost as compared to other superconducting generator concepts. To fully understand the evolution and the design philosophy, it is necessary to investigate previous iterations of the machine, which are highlighted in the first section of this chapter. The chapter then proceeds to discussing the different modelling methods that were used to investigate the electromagnetic performance of rotating electrical machines. Firstly, a reluctance network model is introduced, which is used to quickly assess machine performance. The model is compared to the FEA results published in previous works. Additionally, new FEA models were setup and the magnetostatic and transient performance of the double claw pole generator design were investigated in further detail.

4.1 Double Claw Pole Generator Evolution

4.1.1 Axial Flux Homopolar Superconducting Generator

This machine is the first iteration of the double claw pole design and serves as its basis. Figure 4.1 shows a rendition of the homopolar machine design.

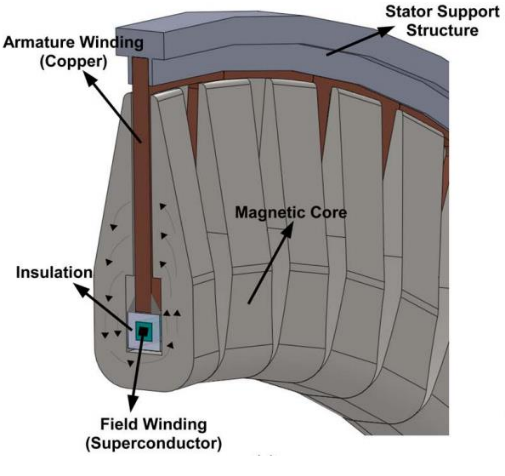

Figure 4.1. Axial flux homopolar superconducting machine [83].

The design features a stationary field winding, which produces the required magneto-motive force. The rotor consists of claw poles that are oriented around the field winding. Stator coils are located within the air gap hence, as the claw poles rotate, a homopolar field variation is produced in the stator coils. The main advantage of this design is the field winding. Since it is a large toroidal winding, it uses less superconducting tape than racetrack coils in a classic radial flux synchronous machines. In addition, since the field winding is stationary, brushes and cryocouplers are eliminated, simplifying the design of the cooling system significantly and improving the reliability of the overall machine. One major disadvantage of this machine design is however that the power density is very limited due to the homopolar field. This can be explained through Faraday's law, which is highlighted in equation 4.1.

$$E = -N\frac{d\phi}{dt} \tag{4.1}$$

The induced electromotive force (EMF) depends on the rate of change of the magnetic flux. For a homopolar machine design the magnetic flux only varies between ϕ_{min} and ϕ_{peak}. The peak flux density is highly dependent on the core-to-pole ratio, which can be defined as the ratio of the core pitch to the pole pitch. This is highlighted in figure 4.2, which shows a side view schematic of the homopolar machine.

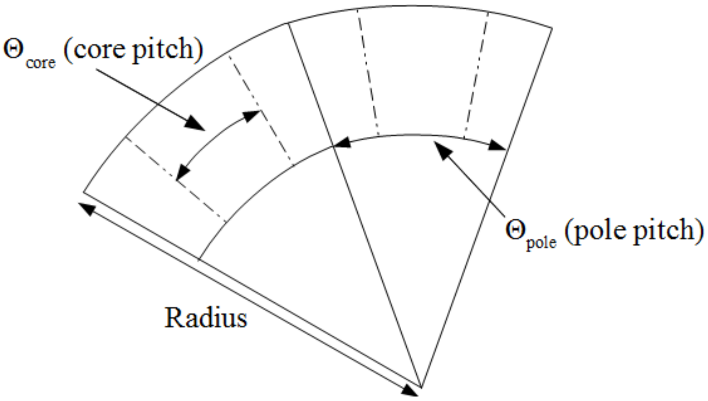

Figure 4.2. Side view schematic of the homopolar machine.

The pole pitch or pole angle is dependent on the number of poles of the machine and is given by equation 4.2.

$$\theta_{\text{pole}} = \frac{360°}{p} \tag{4.2}$$

Where θ_{pole} is the pole pitch and p *is* the number of poles.

The core pitch or core angle is then defined as

$$\theta_{\text{core}} = \theta_{\text{pole}} * core\ to\ pole\ ratio \tag{4.3}$$

where the core to pole ratio can vary between > 0 and < 1.

In general, the higher the core to pole ratio, the bigger the cross-sectional area of the core and hence the higher the saturation limit of the iron. However, a higher core to pole ratio also reduces the distance between the poles and leads to a higher fringing flux between the claw poles. In [83] it was shown that that air gap flux density increases with the core to pole ratio, reaching a maximum at 1.35 T for a ratio of 0.8. However, the difference between B_{min} and B_{peak} was found to be only 0.43 T due to the fringing flux, which leads to B_{min} being approximately 0.92 T. A core to pole ratio of around 0.4 to 0.5 was found to lead to the highest difference in flux density with approximately 0.78 T. Hence, even though a relatively high air gap flux density can be achieved, homopolar machines perform worse than a bipolar machine due to the limited rate of change of the magnetic flux, while essentially using the same amount of active mass material. Since the power density potential of this machine was found to be relatively low, a bipolar version was investigated, which will be highlighted in the next subsection.

4.1.2 Axial Flux Bipolar Superconducting Generator

The bipolar superconducting generator addresses the main issue of the homopolar machine, namely, the homopolar field. To improve the design, an additional field winding was added, the resultant design of the bipolar superconducting generator is shown in figure 4.3.

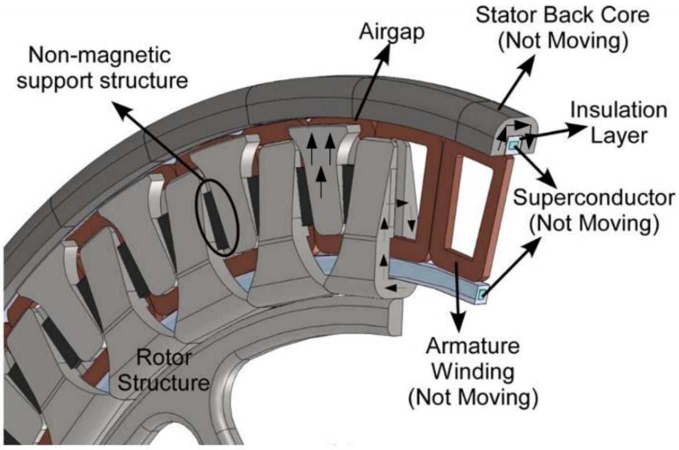

Figure 4.3. Axial-flux bipolar superconducting machine design [83].

Both field windings carry a DC current in the same direction, hence the field crossing the air gap for the upper claw poles is in the opposite direction as compared to the lower claw poles, creating a bipolar field variation. Since the flux variation is now from $-B_{\text{peak}}$ to $+B_{\text{peak}}$, the power density was significantly increased. However, this was achieved at the cost of needing an additional superconducting field winding, increasing the capital cost significantly, in addition to complicating the cooling system design. To optimize the bipolar machine, the design of the claw poles was improved by changing the core to pole ratio, substituting active mass with non-magnetic support material and varying the overlapping area of the inner and outer claw poles. The final design parameters for a 6 MW direct-drive generator are shown in table 4.1.

Table 4.1 Bipolar machine design specifications [83]

Rated power	6	MW
Rated speed	12	RPM
Rated torque	4775	kNm
Outer diameter	12	m
Number of poles	360	/
Number of coils	270	/
Electrical frequency	46	Hz
Efficiency	94.5	%
Length of SC wire	43	km
Total mass	134	tonnes
Torque density	28	kg/kNm

While the electromagnetic design of an electrical machine is of upmost importance, the structural design cannot be neglected. The mechanical support for the homopolar machine was very simple due to the self-supporting C-shaped magnetic cores. For the bipolar machine, the rotor structure is much more complicated. While the inner cores are identical to the ones in the homopolar machine, the outer cores are required to be connected to the inner cores through a non-magnetic support structure, which can cope with the air gap closing forces that exist within the machine. In addition, the superconducting field windings need to be connected to the air-cored armature coils. It is uncertain whether the armature can support such a large structure. While the electromagnetic performance of the bipolar machine was found to be very good, the mechanical issues were found to be too significant to be suitable for low-speed high-torque applications. The next section will cover a transverse flux variation of the claw pole machines introduced in this chapter.

4.1.3 Transverse Flux Claw Pole Superconducting Generator

In a transverse flux machine (TFM) the electromagnetic force vector is perpendicular to the magnetic flux lines as opposed to parallel as in standard (radial or axial) flux machines. In general, the stator of a transverse flux machine consists of a toroidal single-phase winding embraced by U-shaped cores. The rotor consists of buried PMs and a laminated or solid core. A three-phase machine can be built using three single phase machines as shown in figure 4.4.

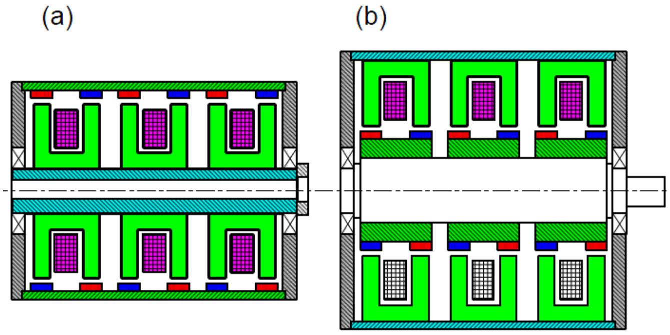

Figure 4.4. Three phase TFM consisting of three single phase units with: (a) internal stator and (b) external stator [84],

A TFM with internal stator has a smaller external diameter and it is easier to assemble the winding and inner stator cores. The heat transfer conditions for internal stators are however worse. The number of stator U-shaped cores is equal to the number of rotor pole pairs *p*. The more poles, the better utilization and smoother operation of the machine. The force density (shear stress) is proportional to the product of A_E and B (electric loading × magnetic loading). The electromagnetic torque is proportional to the number of pole pairs, the higher the number of poles the higher the torque density of a TFM. Due to these characteristics TFMs are well suited for gearless high torque applications such as for wind turbines or ship propulsion systems [85]. In figure 4.5 the flux solely due to the magnets is shown, the working principles of a TFM are explained in the next paragraph.

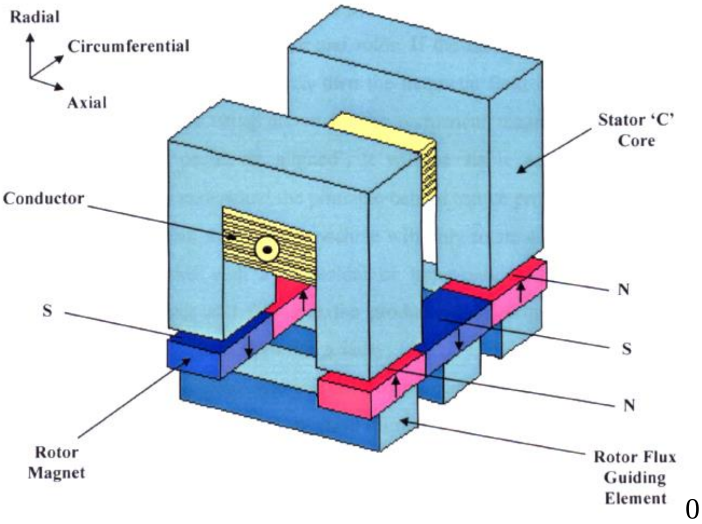

Figure 4.5. Rectilinear model of a single sided TFM [86].

The flux path throughout the machine can be described as follows:

- Radially across the right-hand airgap
- Radially up the right-hand leg of each ‘C’ core
- Axially across the top of each ‘C’ core
- Radially down the left-hand leg of each ‘C’ core
- Across the second airgap into the left-hand magnet
- Axially across the flux guiding elements completing the magnetic circuit

If the conductor is now excited, according to Lenz’s law, a magnetic field will be generated around it. With the current direction shown in figure 4.5, the generated magnetic field will be in positive correlation with the magnetic flux generated by the magnets. At this stage the machine is ‘positively aligned’, the machine is in a stable state and no torque is being generated. At this stage it becomes clear that an alternating current is required in order for the machine to produce any torque. When the current in the conductors starts reversing, the generated magnetic field starts opposing the magnetic flux which is being driven by the magnets. As the current rises in the negative sense the opposing force between the stator and rotor becomes higher as well. Immediately next to the opposing magnets is another pair of magnets which are polarised to push the magnetic flux in sympathy with the field generated by the conductors. This leads to a torque being produced as the rotor is being pushed away by the first pair of magnets while simultaneously being attracted by the adjacent pair of magnets [86]. The magnitude of the produced torque depends on the magnetic loading as well as electric loading of the machine. Some of the major advantages of transverse flux machines are listed below [84, 85, 87]:

- Better utilization of active materials than in standard machines for the same cooling system (i.e. higher torque density)
- Less winding and ferromagnetic core materials for the same torque
- Simple stator winding consisting of a single ring-shaped coil
- A higher number of poles leads to a higher torque, a lower torque ripple and better power factor
- A three phase TFM can be fed from a standard three phase inverter
- Ideal to use as a low speed generator
- Toroidal nature of the field winding means that the circumferential path it follows around the machine is the most economical route, this is especially important for superconductors due to the high capital cost.
- TFMs do need to make a compromise between electric loading and magnetic loading

Whereas some disadvantages are [84, 85, 87]:

- In general, TFMs have a lower power factor, due to large leakage flux between poles [88], which forces the relating power electronics equipment to be rated for a higher apparent power rating
- The power factor further reduces as the load increases
- Cogging torque can be a problem due to the mostly iron-cored structures
- More difficult to manufacture since components often deviate from standard rotating machines

For the application of superconductors, one type of transverse flux machine in particular is a promising candidate, the claw pole machine. Claw pole machines are widely being used, especially for car alternators [89]. The principle of the claw pole machine is similar to the transverse flux machine discussed previously. The machine consists of large toroidal armature winding, which produces a rotating magnetic field. The magnetic flux is modulated with claw poles, which are oriented around the armature winding. The rotor consists of a set of surface mounted permanent magnets. The resultant flux path is three dimensional, with the flux going up one claw pole and travelling downwards over the next adjacent claw pole [90]. The general structure of such a claw pole machine is shown in figure 4.6.

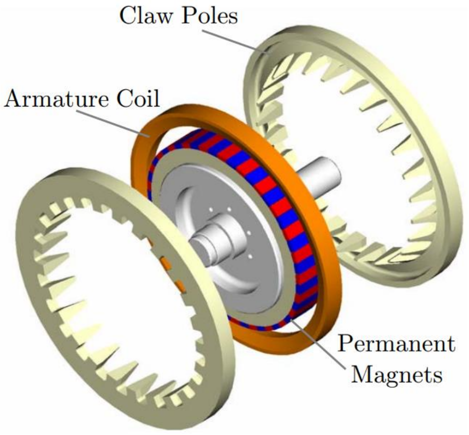

Figure 4.6. Claw pole machine with permanents magnets structure [87].

This structure offers the opportunity to apply a superconducting winding to produce the required MMF. The copper armature winding is replaced with a superconducting field winding, which carries a direct current. The permanent magnets are replaced with concentrated stator coils. While the claw poles for the previous design were stationary, the claw poles are now rotating around the field winding to produce the required flux variation along the stator coils. The concept of this design is highlighted in figure 4.7

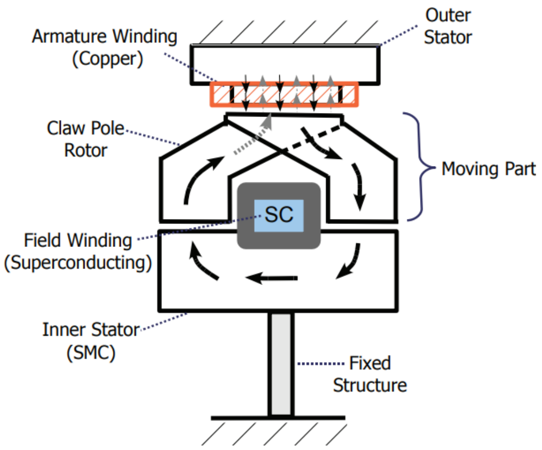

Figure 4.7. Axial view of the transverse flux superconducting claw pole generator concept [91].

The outer stator is similar to conventional stators. It is laminated in the axial direction and consists of concentrated copper stator coils. Since the superconducting field winding produces a unidirectional rotating magnetic field, the claw poles a magnetised in one direction only, i.e. the flux travels upwards through the left claw pole and downwards through the right claw pole as can be seen in figure 4.7. Due to the unidirectional magnetic flux the claw poles can be constructed with laminated electrical steel. The inner stator consists of soft magnetic composite (SMC) materials, since the flux path through the inner stator is both into the axial as well as radial direction resulting in a three-dimensional magnetic flux path. While this concept is very promising, there are still a number of flaws, which make it unsuitable for large diameter high-torque machines. The main issues with this design come from a mechanical point of view. Firstly, SMC materials have lower mechanical strength than laminated electrical steel, hence it is unclear whether the inner stator structure can support the resulting mechanical stresses for large diameter machines. Secondly, the air gap closing forces for the inner and outer air gaps are not equivalent to each other. F_1, which is the outer air gap closing force, is approximately half of F_2, which is the inner air gap closing force. Hence, a net force inward is acting on the claw poles. Additionally, the air gap forces are not perfectly aligned, resulting in a pivoting force acting on the claw poles. These issues make the assembly of a large diameter machine very challenging. However, this design offers the possibility of turning it into an axial flux machine, which will be discussed in the next section in further detail.

4.1.4 Double Claw Pole Superconducting Generator

This section will highlight the design of the double claw pole superconducting generator, which served as the basis of the research that was done during this research work. A schematic of the machine concept is highlighted in figure 4.8. As can be seen the design of the transverse flux machine is taken as the basis. This machine concept is rotated by 90° to essentially turn it into an axial flux machine. This axial flux concept is then mirrored over the vertical axis and combined together. The resulting machine is the double claw pole generator concept. The design features a stator on each side. The claw poles consist of a set of smaller claw poles and a set of large claw poles. The inner stator of the previous design is turned into the field core, which provides structural support and access to the superconducting field winding. This design eliminates many of the mechanical issues that existed previous. SMC materials are not required anymore, since the 3D-flux path that existed within the inner stator previously, was eliminated. Additionally, the forces acting on the claw poles are now balanced, which simplifies the design of the mechanical support structure for the rotor. In addition to the improved mechanical design of the generator, the modularity of the generator was significantly improved as well. The stators on either side of the claw poles can operate independently, hence even if there is a fault, the generator can keep operating under partial load. In addition, the field winding can be wound into separate loops, again providing further modularity in case of a fault.

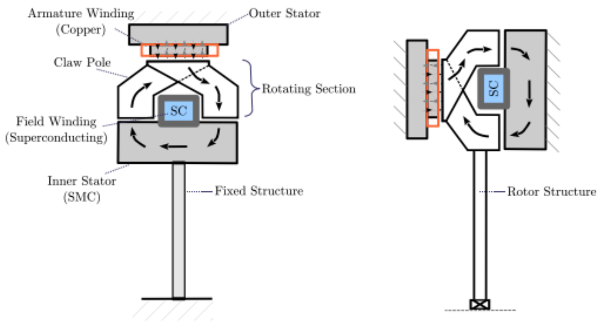

(a) Radial claw pole.

(b) Axial claw pole.

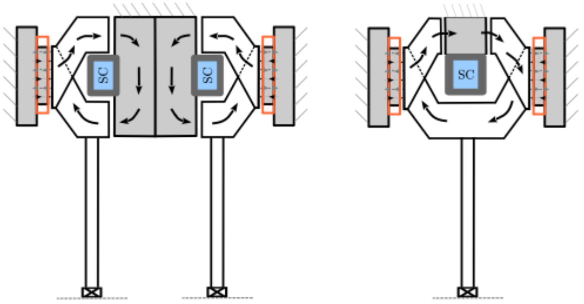

(c) Combined axial claw pole.

(d) Double-sided claw pole.

Figure 4.8. Double claw pole generator development [15].

A genetic algorithm was run to optimize the design of the generator for a power rating of 10 MW [50]. The objective function of the algorithm was to find the lowest mass of the generator, while maintaining an as small as possible diameter. The final design specifications of the optimized double claw pole generator are summarized in table 4.2.

Table 4.2. Optimized double claw pole generator design

Rated power	10	MW
Rated speed	10	RPM
Outer diameter	6.63	m
Number of poles	88	/
Number of coils	66	/
Electrical frequency	7.33	Hz
Operating temperature	65	K
Efficiency	94.5	%
Length of SC wire	13.5	km
Active mass	57.9	tonnes
Total mass	184.2	tonnes

With a total mass of 184 tonnes, the design was found to be significantly lighter than conventional permanent magnet generators. In addition, due to its high modularity, the design was considered an ideal candidate for offshore wind turbines. The HTS tape requirements of the design are considerably lower than other superconducting generators designs due to its iron cored structure and claw pole design itself, which benefits from a large toroidal coil. Overall, the proposed design was found to be a suitable option to initiate the use of superconducting tapes in direct-drive wind turbine generators due to its modularity and cost-effectiveness. This final design served as the basis over the course of the conducted research work. To investigate the machine design in further detail, modelling tools had to be developed and verified. Analytical as well as numerical modelling methods were applied to validate and then improve the existing design. These modelling methods will be introduced and discussed in the next section.

4.2 Machine Modelling Methods

In the previous section, the evolution of the double claw pole generator was introduced. The optimized design of the double claw pole generator was found to offer a high torque-density, low HTS tape requirements and a high modularity. These properties made the design an ideal candidate for the application in large direct-drive off-shore wind turbines.

In this chapter, the modelling methods that were used during the course of this research work will be introduced and discussed. The modelling methods will be compared to the original design to validate the correctness of the models. The introduced methods will serve as the basis for investigating and improving the double claw pole generator design.

4.2.1 Reluctance Network Modelling

The first modelling method that will be introduced is an analytical approach for modelling electrical machines. The analytical approach is based on the reluctance network modelling, which uses the magnetic equivalent circuit as its basis. The magnetic equivalent circuit technique is a powerful analysis and design tool for electric machines. It combines low computational effort with relatively high accuracy to quickly assess the electromagnetic performance of electrical machine designs. The basis behind the reluctance network modelling comes from electric circuits with the resistances being represented by reluctances and voltage source being represented by the magneto-motive force. Two formulations of the magnetic equivalent circuit technique exist, the nodal-based formulation and the mesh-based formulation. For the nodal based system, Kirchhoff’s current law (KCL) is applied to the circuit, creating a set off nodal equations to be solved. For the mesh-based system Kirchhoff's voltage law (KVL) is used, which allows to setup flux loop equations and solving for the magnetic flux in the circuit. The two systems have been compared and it is widely regarded that the mesh-based magnetic equivalent circuits are computationally more efficient, especially in non-linear models [92]. This advantage is attributed to the Jacobian matrix in the Kirchhoff's voltage law configuration as well as the shape of the residual function [93]. Since the KVL method offers better convergence, this formulation was used to assess the electromagnetic performance of the machine designs. The general form of the KVL equations is shown in equation 4.4.

$$\boldsymbol{R\phi} - \boldsymbol{F} = 0 \tag{4.4}$$

where $\boldsymbol{R}$ is the reluctance matrix, $\boldsymbol{\phi}$ is the magnetic flux vector and $\boldsymbol{F}$ is the magneto-motive force vector.

Each reluctance is calculated according to the dimensions of the machine section it represents using equation 4.5.

$$R = \frac{l_\mathrm{e}}{\mu_0 \mu_\mathrm{r} A} \tag{4.5}$$

where l_e is the equivalent length through the component, μ_0 is the permeability of air, μ_r is the relative permeability of iron and A is the cross-sectional area of the component.

The relative permeability of iron follows a non-linear curve, which is dependent on the flux density of the component. Since the relative permeability of iron is non-linear, the resulting reluctance is also non-linear. Figure 4.9 highlights the variation of μ_r with flux density for Vacoflux50, which is a cobalt iron manufactured by Vacuumschmelze. The iron offers a very high saturation limit of 2.32 T [94], which allows to take advantage of the high current density of superconductors. In addition, it can be manufactured in laminations, which simplifies the assembly of the large generator components.

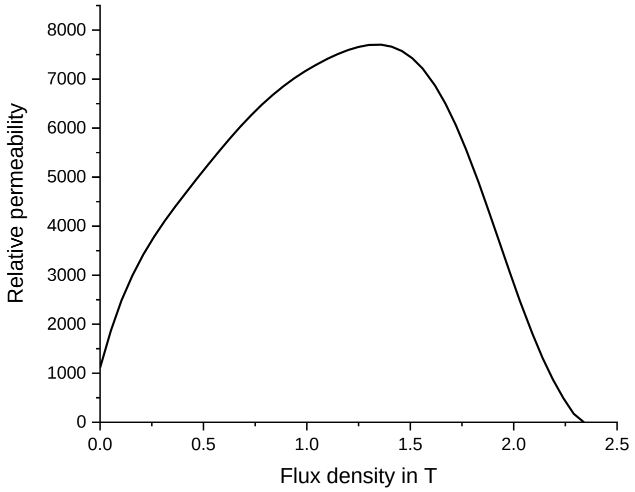

Figure 4.9. Relative permeability variation with flux density for Vacoflux50 [94].

Due to the non-linearity of the flux loop equations a root-finding algorithm is required. The Newton-Raphson algorithm is a popular method for solving non-linear equations. The basic Newton-Raphson equation is highlighted in equation 4.6.

$$x_{\mathrm{n}+1} = x_{\mathrm{n}} - \frac{f(x_{\mathrm{n}})}{f'(x_{\mathrm{n}})} \tag{4.6}$$

where $f(x_{\mathrm{n}})$ is an arbitrary function, $f'(x_{\mathrm{n}})$ is the derivative of that function, x_{n} is the previous value and $x_{\mathrm{n+1}}$ is the newly calculated value. The algorithm runs until a sufficiently precise value for x_{n} is reached. One issue with this method is that the derivative of $f(x_{\mathrm{n}})$ is required. To avoid this, an approximation can be used to represent the derivative such as shown in equation 4.7.

$$f'(x_{\mathrm{n}}) \approx \frac{f(x_{\mathrm{n}} + \Delta x) + f(x_{\mathrm{n}})}{\Delta x} \tag{4.7}$$

Hence, this method needs to solve two functions per iteration. Another popular algorithm exists, the secant method, which can be considered as a finite-difference approximation of the Newton-Raphson method. The secant method is shown in equation 4.8.

$$x_{\mathrm{n}+1} = \mathrm{x_n} - \frac{f(x_{\mathrm{n}})}{\frac{f(x_{\mathrm{n}}) - \mathrm{f}(x_{\mathrm{n}-1})}{x_{\mathrm{n}} - x_{\mathrm{n}-1}}} \tag{4.8}$$

This algorithm requires two initial values to start off, x_{n} and $x_{\mathrm{n-1}}$, however it only needs to solve one function per iteration. This makes the secant method a faster converging algorithm than the Newton-Raphson method. One disadvantage is that the initial values to start of the algorithm need be in the relative vicinity of the solution to guarantee convergence.

Since the secant method was found to be fastest converging algorithm it was decided to use this algorithm to solve the non-linear flux loop equations. Figure 4.10 highlights the secant method algorithm flow chart. The algorithm was coded using MATLAB.

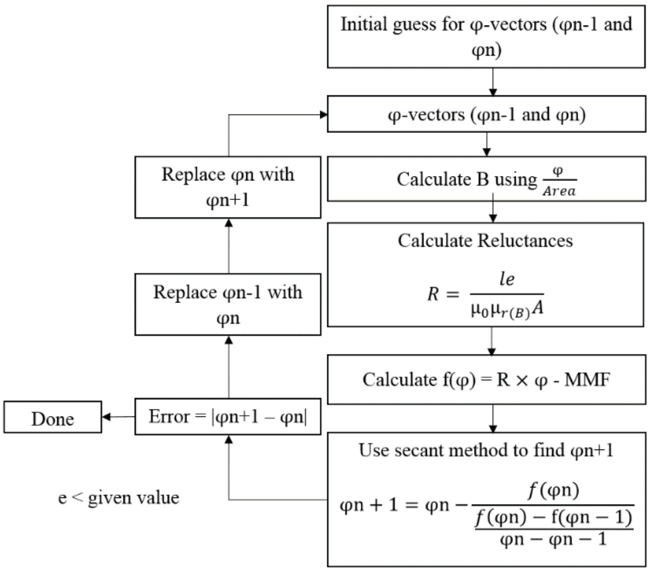

Figure 4.10. Secant method algorithm [16].

Through applying this algorithm to solve the non-linear flux loop equations, the flux density in each component of the electrical machine as well as the air gap flux density can be calculated. The power output can hence be determined through the stator tooth flux, which is directly related to the air gap flux density. The power output is calculated according to equation 4.9.

$$P_{\text{out}} = N_{\text{coil}}\left(E_{\text{RMS}} I_{\text{RMS}} - {I_{\text{RMS}}}^2 R_{\text{coil}}\right) \tag{4.9}$$

where P_{out} is the output power, N_{coil} is the number of coils per stator, E_{RMS} is the induced voltage for one coil, I_{RMS} is the stator current and R_{coil} is the stator coil resistance. The coil resistance is determined through the coil cross-sectional area A_{coil}, the mean turn length and the number of turns. The second part of the equation essentially denotes the copper loss in the stator. E_{RMS} is calculated according to Faraday's law using equation 4.10 and I_{RMS} is calculated according to equation 4.11.

$$E_{\text{RMS}} = \frac{N_{\text{turn}} \phi_{\text{peak}} f}{\sqrt{2}} \tag{4.10}$$

where N_{turn} is the number of turns per coil, ϕ_{peak} is the peak stator tooth flux density and f is the electrical frequency in radians.

$$I_{\text{RMS}} = J_{RMS}A_{\text{coil}} \tag{4.11}$$

where J_{RMS} is the current density of copper, which is assumed to be $5\times 10^{6}\,\text{A/m}^2$ and A_{coil} is the cross-sectional area of the coil, which is determined by machine dimensions. A fill factor of 0.75 is assumed for the coils. In [95], the different manufacturing methods for concentrated coils is discussed. Fill factors as high as 0.78 can achieved by using rectangular conductors, making a fill factor of 0.75 a reasonable choice to achieve a high power density.

In addition to calculating the electromagnetic performance of the generator designs, the active mass may also be calculated since the machine component dimensions are known. The analytical method hence allows to quickly assess different generator designs in terms of electromagnetic performance and power density. Since the analytical method is also computationally very efficient, optimization of different designs is very quick and effective.

4.2.2 Reluctance Network of the Original Design

To validate the analytical model, the original double claw pole generator design was modelled and compared to FEA results. The reluctance network for the original design of the double claw pole generator is shown in figure 4.11. The reluctance network was adapted from [50] and [96].

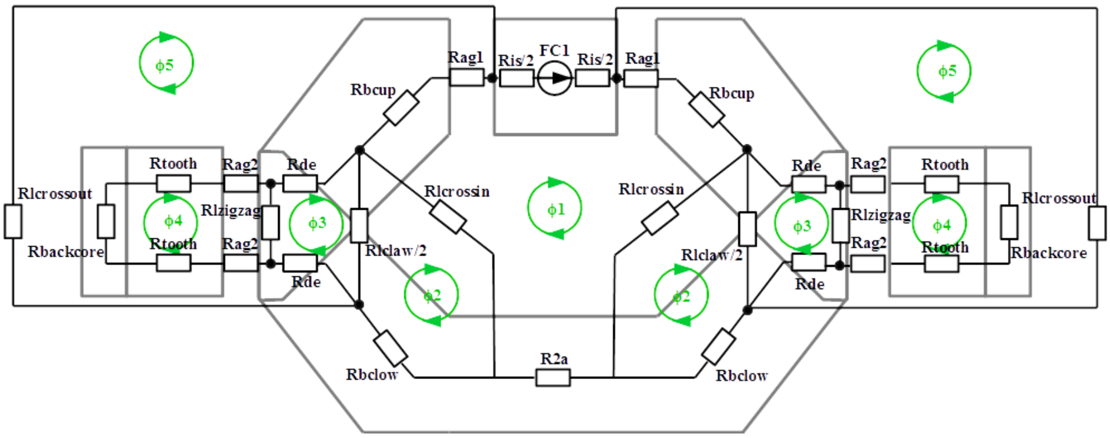

Figure 4.11. Double claw pole generator reluctance network [97].

As can be seen each component of the design is represented by several reluctances. In addition, leakage reluctances were also added, to model leakage flux in between claw poles and stator teeth. It can be seen that five different flux loops can be identified in the reluctance network. Equation 4.12 shows the resulting reluctance network equation.

$$\begin{bmatrix} 2 \times (R_{iag} + R_{bup} + R_{lcrossin}) + R_{2a} + R_{is} & -2 \times R_{lcrossin} & 0 & 0 & -2 \times (R_{iag} + R_{bup}) \\ -2 \times R_{lcrossin} & 2 \times (0.5 \times R_{lclaw} + R_{blow} + R_{lcrossin}) & -R_{lclaw} & 0 & -2 \times R_{blow} \\ 0 & -R_{lclaw} & 2 \times (0.5 \times R_{lclaw} + 2 \times R_{de} + R_{zigzag}) & -2 \times R_{zigzag} & -4 \times R_{de} \\ 0 & 0 & -2 \times R_{zigzag} & 2 \times (R_{zigzag} + 2 \times R_{oag} + R_{os1} + R_{os2}) & -2 \times (2 \times R_{oag} + R_{os1} + R_{os2}) \\ -2 \times (R_{iag} + R_{bup}) & -2 \times R_{blow} & -4 \times R_{de} & -2 \times (2 \times R_{oag} + R_{os1} + R_{os2}) & 2 \times (R_{lcrossout} + R_{blow} + 2 \times R_{de} + 2 \times R_{oag} + R_{iag} + R_{os1} + R_{os2} + R_{bup}) \end{bmatrix} \begin{bmatrix} \phi_1 \\ \phi_2 \\ \phi_3 \\ \phi_4 \\ \phi_5 \end{bmatrix} = \begin{bmatrix} MMF \\ 0 \\ 0 \\ 0 \\ 0 \end{bmatrix} \tag{4.12}$$

The structure of the double claw pole generator concept is shown in figure 4.12, with the main dimensions highlighted. The figure shows a cross-section into the radial direction of the machine. The shown dimensions are used to calculate the respective reluctances depicted in figure 4.11.

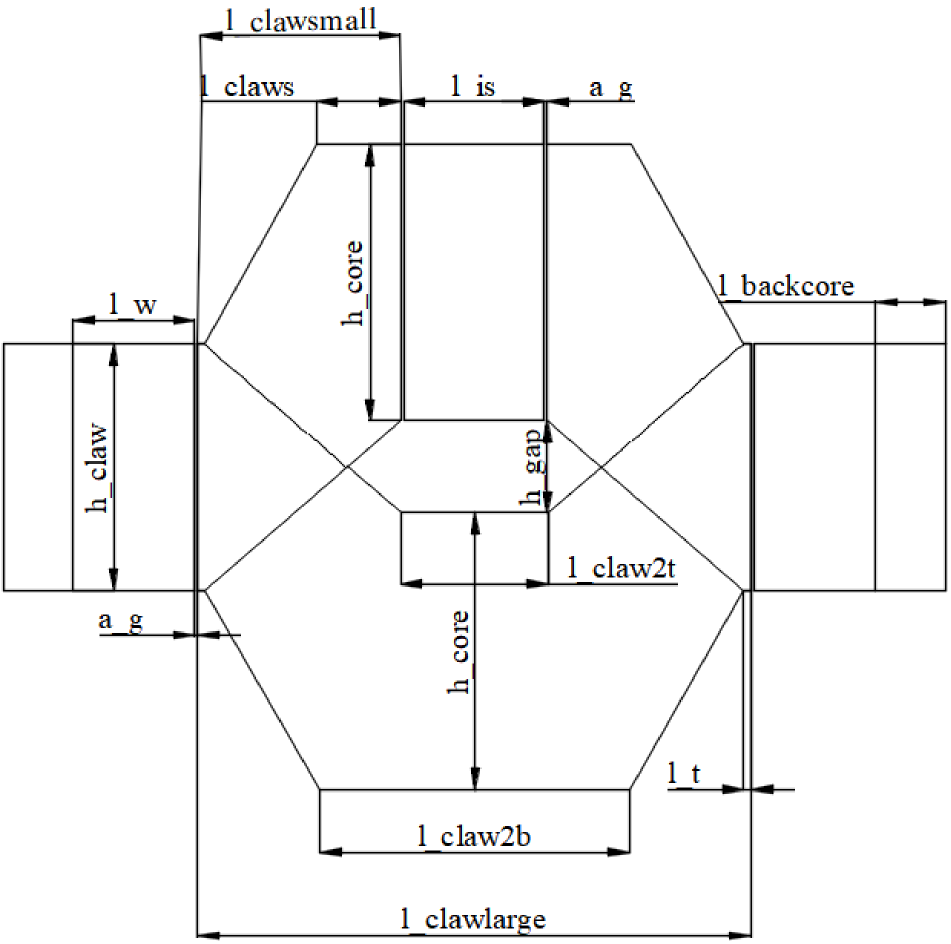

Figure 4.12. Double claw pole generator parameters.

The parameters needed to establish the reluctance network of the generator components are listed in table 4.3. To determine the thickness of the claw poles and stator teeth, the core to pole and tooth to coil ratios are used. The respective pole pitch and coil pitch can be determined through the number of poles and coils. In conjunction with the respective radii, the width of the components can be determined. The dimensions listed in the table are the same as given in [15], a genetic algorithm was used to optimize the generator design and find the optimal dimension to achieve the lowest active mass for a 10 MW output power design.

Table 4.3 Main component parameters

Variable	Value (mm)
R_{in}	2288
N_{pole}	88
N_{coil}	66
N_{turn}	96
ag	4.5
Core to pole ratio	0.85
Tooth to coil ratio	0.5
$l_{\text{clawlarge}}$	789
l_{claw2t}	210
l_{claw2b}	440
$\text{l}_{\text{clawsmall}}$	283
l_{claws}	120
l_{t}	10
h_{core}	393
h_{claw}	351
l_{w}	172
l_{backcore}	100
h_{gap}	121
l_{is}	200

As was shown in equation 4.5, to calculate the respective reluctances, the equivalent length and cross-sectional area of each component need to be known. The following equations will highlight how the equivalent length and cross-sectional area were calculated for each reluctance component.

- **Field core**

$$l_{\text{is}} = l_{\text{claw2t}} - 2ag \tag{4.13}$$

where l_{is} is the equivalent length through the field core, l_{claw2t} is the length of the straight part of the large claw pole as depicted in figure 4.12 and ag is the air gap. The air gap is defined as 1/1000 of the air gap diameter, which is a common machine design choice [13, 98]

$$A_{\mathrm{is}} = h_{\mathrm{core}} * T_{\mathrm{core}} * k_{\mathrm{fring\_is}} \tag{4.14}$$

where A_{is} is the equivalent cross-sectional area of the field core, h_{core} is the height, T_{core} is the width of the claw as determined by the pole pitch and core to pole ratio. As the magnetic flux crosses from one claw pole to the other through the field core it fringes throughout the width of the field core, to model this behaviour, $k_{\mathrm{fring\_is}}$ was added, which is a fringing constant.

- **Inner air gap**

$$l_{\mathrm{iag}} = ag \tag{4.15}$$

where the equivalent length l_{iag} is simply the length through the air gap, which is given as *ag*.

$$A_{\mathrm{iag}} = h_{\mathrm{core}} * T_{\mathrm{core}} * k_{\mathrm{fring}} \tag{4.16}$$

where A_{iag} is the equivalent cross-sectional area for the inner air gap. A fringing constant was added since, when the magnetic flux crosses the air gap it fringes out on the edges of the air gap, this phenomenon is highlighted in figure 4.13.

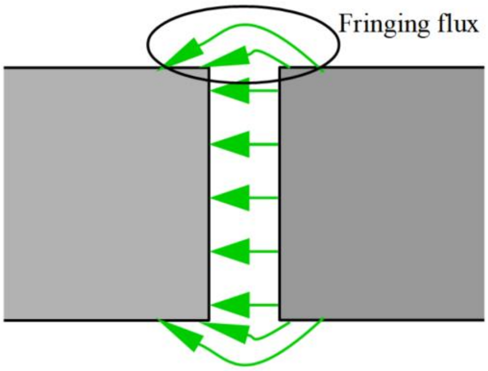

Figure 4.13. Fringing flux in the air gap.

- **Small claw pole**

The small claw pole is broken up into two reluctances as shown in figure 4.11 to improve the accuracy in the model, where R_{de} represents the lower part of the claw pole and R_{bcup} represents the upper part of the claw pole.

$$l_{\mathrm{de}} = 0.5 * h_{\mathrm{claw}} * \cos(\alpha) + l_{\mathrm{t}} \tag{4.17}$$

where l_{de} is the equivalent length through the bottom part, h_{claw} is the claw pole height near the stator teeth, α is the angle of the claw pole bend at the elbow and l_{t} is the short straight section.

$$A_{\mathrm{de}} = h_{\mathrm{claw}} * T_{\mathrm{core}} \tag{4.18}$$

where A_{de} is the equivalent cross-sectional area for the bottom section.

The next equations describe the upper part of the small claw pole.

$$l_{\mathrm{bcup}} = \left(\frac{\pi}{2} - \alpha\right) * 0.5 * h_{\mathrm{core}} \tag{4.19}$$

where l_{bcup} is the equivalent length for the upper part of the claw pole.

The cross-sectional area of the claw pole changes as the flux passes through it. However, the most important cross-section is the smallest area, since that part of the claw pole will saturate first and hence limit the electromagnetic performance of the machine. The shortest height and hence cross-sectional area are highlighted in figure 4.14. It will be shown from the reluctance network modelling and the FEA models that it is this area, which approaches saturation for both the small as well as large claw poles.

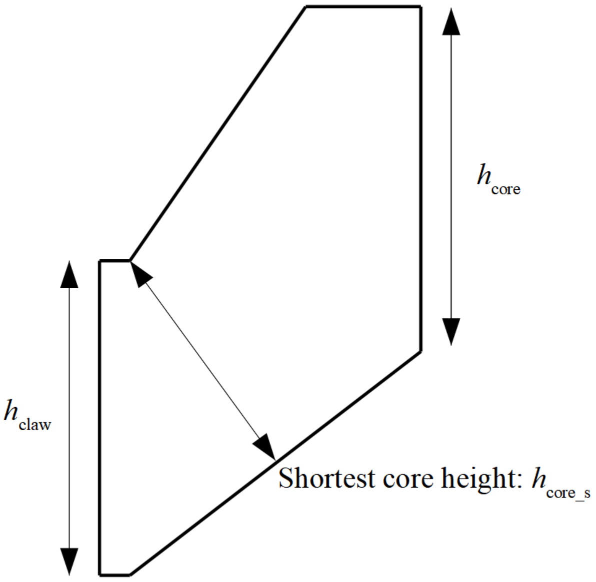

Figure 4.14. Shortest height for the small claw pole.

Equation 4.20 is used with the shortest height as defined in figure 4.14 to calculate the cross-sectional area.

$$A_{\mathrm{bcup}} = h_{\mathrm{core\_s}} * T_{\mathrm{core}} \tag{4.20}$$

where A_{bcup} is the equivalent cross-sectional area and $h_{\mathrm{core\_s}}$ is the shortest height as defined in figure 4.14.

- **Large claw pole**

For the large claw pole, the parameters are calculated with the same equations as for the small claw poles. This is because the large claw pole essentially consists of the same dimensions as two small claw poles with straight section in between added to connect both halves. The additional reluctance, $R_{2\mathrm{a}}$, was added to represent that straight section of the large claw pole.

$$l_{2\mathrm{a}} = 2 * l_{\mathrm{clawl}} \tag{4.21}$$

where $l_{2\mathrm{a}}$ is the equivalent length and l_{clawl} is the length of the straight section from the elbow to the middle.

$$A_{2\mathrm{a}} = h_{\mathrm{core}} * T_{\mathrm{core}} \tag{4.22}$$

where $A_{2\mathrm{a}}$ is the equivalent cross-sectional area.

- **Outer air gap**

The outer air gap is calculated in the same fashion as the inner air gap, where the equivalent length is equal to the air gap length and the cross-sectional area is equivalent to the claw pole height h_{claw} and pole thickness T_{core}. Similarly, to the inner air gap, a fringing constant was added to account for the magnetic flux fringing outwards on the edges of the air gap.

- **Stator**

The stator is split into 3 reluctances, one reluctance for each stator tooth and one reluctance for the back iron. The following equations describe the parameters for the stator:

$$l_{\mathrm{tooth}} = l_{\mathrm{w}} * \frac{l_{\mathrm{backcore}}}{2} \tag{4.23}$$

where l_{tooth} is the equivalent length from the stator tooth to half the back iron thickness, l_{w} is the stator tooth length and l_{backcore} is the back iron thickness.

$$A_{\mathrm{tooth}} = h_{\mathrm{claw}} * T_{\mathrm{tooth}} \tag{4.24}$$

where A_{tooth} is the cross-sectional area of a stator tooth and T_{tooth} is the thickness of the tooth, which is dependent on the number of coils, coil to tooth ratio and the stator diameter.

$$l_{\mathrm{tooth\ to\ tooth}} = T_{\mathrm{coil}} \tag{4.25}$$

where T_{coil} is the coil pitch, *i.e.*, the distance between each stator coil.

$$A_{\mathrm{backcore}} = h_{\mathrm{claw}} * l_{\mathrm{backcore}} \tag{4.26}$$

where A_{backcore} is the cross-sectional area of the back core.

- **Leakage flux**

In addition to modelling the active mass, it is necessary to also account for leakage flux that occurs in between claw poles and stator teeth to accurately model the electromagnetic performance of the machine. The zigzag flux, R_{zigzag}, which is magnetic flux that travels to neighbouring stator teeth instead of straight ahead is represented by the following equations [99]:

$$l_{\mathrm{zigzag}} = 2 * \sqrt{ag^2 + \frac{T_{\mathrm{coil}}}{2}^2} \tag{4.27}$$

where l_{zigzag} is the equivalent length from one claw pole to neighbouring stator teeth.

$$A_{\mathrm{zigzag}} = h_{\mathrm{claw}} * T_{\mathrm{core}} \tag{4.28}$$

Flux leakage between adjacent claw poles is modelled through R_{lclaw}. This flux leakage can be significant depending on the number or poles and the core to pole ratio, since these parameters reduce the distance between neighbouring poles. The distance between the claw poles can be described as:

$$l_{lclaw} = \left(R_{\mathrm{in}} + h_{\mathrm{core}} + \frac{h_{\mathrm{gap}}}{2}\right) * \theta_{pole} * (1 - core\ to\ pole\ ratio) \tag{4.29}$$

where R_{lclaw} is the equivalent length from one pole to the adjacent pole, R_{in} is the inner diameter, h_{core} is the core height, h_{gap} is the field winding gap height, θ_{pole} is the pole pitch and the *core to pole ratio* is the pole thickness as compared to the pole pitch.

The equivalent cross-sectional area in between the claw pole surfaces can be described as follows:

$$A_{lclaw} = l_{\mathrm{t}} * h_{\mathrm{claw}} + \frac{h_{\mathrm{claw}}^{2} * \tan(\alpha)}{4} \tag{4.30}$$

where A_{lclaw} is the equivalent cross-sectional area. The first part of the equation represents the overlapping short straight section at the beginning of the claw poles. The second represents the overlapping area as the claw poles deviate from each other at the angle α.

The final leakage paths that exist within the machine are from the inner stator downwards to the large claw pole, defined as $R_{\mathrm{lcrossout}}$ and flux leakage between the small claw pole and large claw pole inner surfaces defined as R_{lcrossin}. Both reluctances are essentially equivalent to each other, however, to avoid the flux paths crossing over each other, complicating the reluctance network model, one of the reluctances was moved outwards, which simplifies the model. The equivalent length and area can be defined as follows:

$$l_{\mathrm{crossin}} = l_{\mathrm{crossout}} = \sqrt{(0.5 * (h_{\mathrm{core}} + h_{\mathrm{gap}}))^2 + (0.75 * l_{\mathrm{claw}})^2} \quad (4.31)$$

$$A_{\mathrm{crossin}} = A_{\mathrm{crossout}} = \frac{h_{\mathrm{claw}}}{2 * \cos(\alpha) + l_{\mathrm{t}}} * T_{\mathrm{core}} \quad (4.32)$$

The next subsection will show the results of the reluctance network model in combination with the original design of the double claw pole machine.

4.2.3 Reluctance Network Results

Figure 4.15 shows the iteration process for equation 4.12, solving the equations as shown in equation 4.4. As can be seen the algorithm trends towards 0, indicating that the correct reluctance and flux values were found. The algorithm runs for approximately 2000 iterations, which are completed within a couple of seconds.

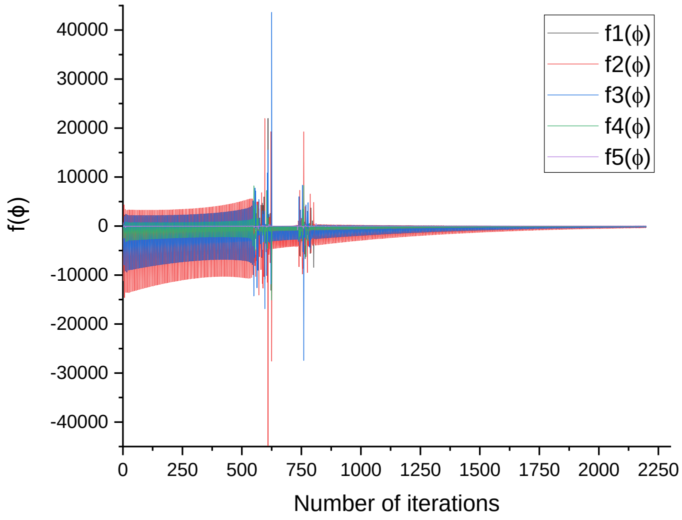

Figure 4.15. Secant method algorithm solving procedure.

Figure 4.16 shows the calculated flux density distribution in the active mass of the generator component for increasing MMF from 0 to 42 kA·turns. The operating MMF was chosen to be 32.4 kA·turns. Each component is split into several reluctances, which are represented by the different colours. Figure 4.11 shows the location of each reluctance component. As can be seen, the iron in the machine starts saturating as the MMF is increased beyond the operating point. The highest flux density occurs in the elbow of the claw poles as was discussed in equation 4.20 and highlighted in figure 4.14.

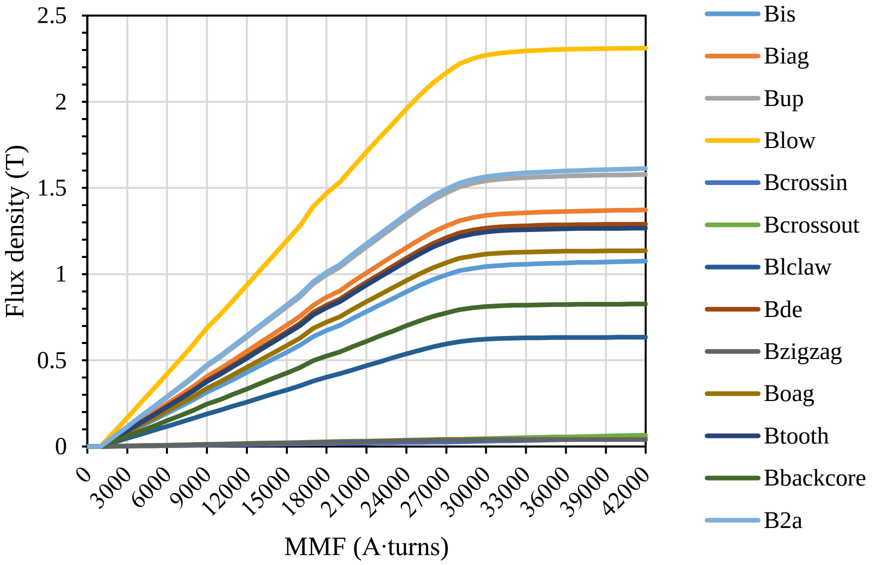

Figure 4.16. Generator component flux density results for increasing MMF.

The stator tooth flux in particular is important in order to calculate the induced voltage in the stator coils. Figure 4.17 shows the stator tooth flux with increasing MMF. At the operating MMF of 32.4 kA·turns, the stator tooth flux is equivalent to approximately 57.2 mWb.

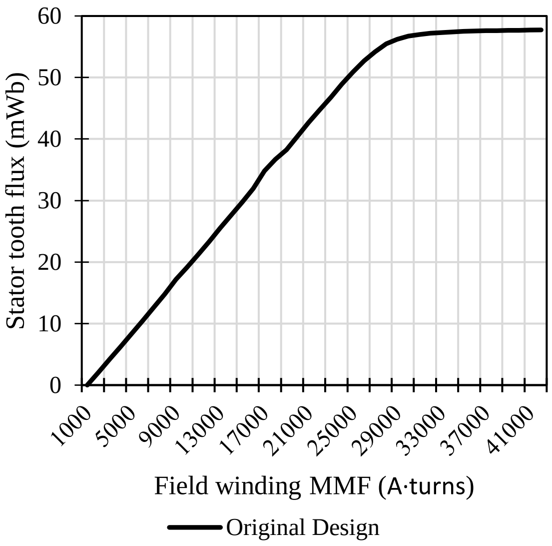

Figure 4.17. Stator tooth flux density with increasing MMF.

Using equations 4.9 to 4.11, the resultant induced voltage per coil can be calculated to be 179 V RMS. The power output can hence be calculated to be 10 MW. Results show that the reluctance network is in excellent agreement with the original double claw pole generator design highlighted in [100].

As was mentioned previously, the double claw pole generator design was optimized using a genetic algorithm, to verify the optimization, some further investigation was done. Figure 4.18 shows power output and efficiency variation with increasing pole number. It can be seen that the power output increases with number of poles to a peak and then starts declining due to the increased leakage flux between poles. While the peak in power output occurs at a lower pole number than 88, the efficiency only peaks for a higher number of poles. According to the reluctance network results the efficiency peaks at approximately 72 poles. However, for simulation purposes a different number of poles was chosen. The number of poles and number of slots together dictate the level of symmetry within the machine geometry, a high level of symmetry enables to only model a small portion of the complete generator design by applying the appropriate symmetry boundaries. The symmetry of a rotational machine is defined by the number of poles and coils such as that [101]:

$$\theta_{\text{symmetry}} = \frac{360^\circ}{GCD\left(N_{\text{pole}}, N_{\text{coil}}\right)} \tag{4.33}$$

where θ_{symmetry} is the angle of symmetry, GCD is a greatest common divider function, N_{pole} is the number of poles and N_{coil} is the number of stator coils.

For a pole number of 72, the angle of symmetry would be 60˚ assuming the same number of slots is maintained. On the other hand, with a pole number of 88, which is the pole number chosen for the original design of the double claw pole machine, the angle of symmetry is 16.36˚, drastically reducing the computational time for the required numerical modelling. To benefit of the reduced computational time, 88 poles are maintained throughout this thesis.

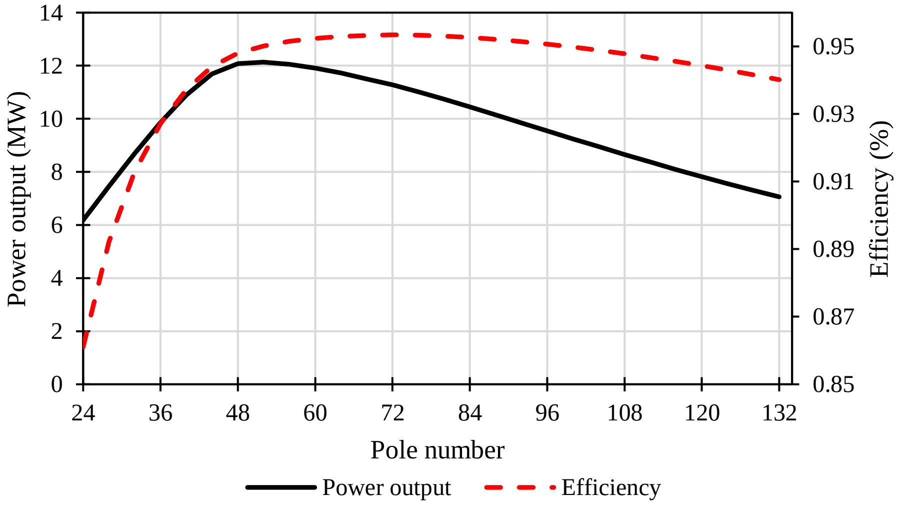

Figure 4.18. Power output and efficiency with pole number.

Figure 4.19. shows the power output and efficiency variation with *core to pole ratio*. The power output increases with the *core to pole ratio* since the claw poles can carry more flux and hence saturate later. Beyond a *core to pole ratio* of approximately 0.85, the power output starts to decrease due to the increased leakage flux between claw poles. The efficiency follows the same trend, with it peaking at a core to pole ratio of approximately 0.85, which is the design value, again indicating that the *core to pole ratio* of 0.85 was chosen adequately.

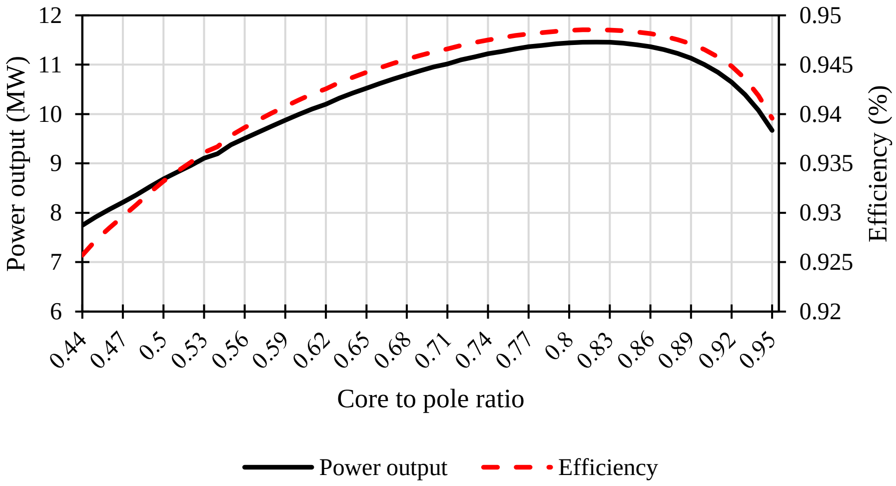

Figure 4.19. Power output and efficiency with core to pole ratio.

Results show that the original design of the double claw pole machine was optimized well and that the machine dimensions chosen give the highest power output at the highest efficiency, while still offering a high level of symmetry for efficient numerical modelling.

4.3 Numerical Model of the Original Design

In this section the numerical modelling of the double claw pole machine will be introduced and the FEA results will be compared to the reluctance network results. Furthermore, the voltage and torque characteristics of the double claw pole generator are investigated for the first time.

4.3.1 Magnetostatic Analysis of the Original Design

To further verify the results produced by the reluctance network model, a FEA model of the original double claw generator design was created in MagNet. For this model, the stator coils were excluded since the simulation served to only investigate the flux density distribution in the machine due to the field winding. The dimensions of the generator components are equivalent to the dimensions in the reluctance network model. The MMF is set to 32.4 kA·turns. A flux tangential boundary was added around the active mass, to contain the magnetic flux within the simulation area. A finer mesh was used in the air gap region and for the claw poles to improve the accuracy. The solution mesh is shown in figure 4.20, as can be seen the mesh is finer in the air gap region, i.e., on the faces of the field core, claw poles and stator teeth.

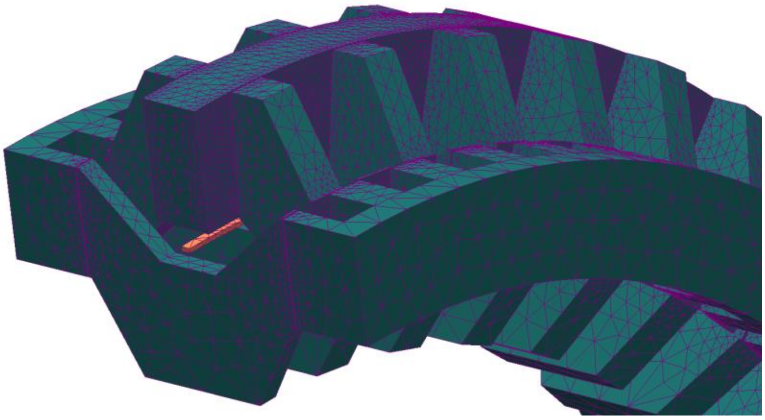

Figure 4.20. Solution mesh in the *MagNet* model.

Figure 4.21 shows the resultant flux density distribution in the active mass of the machine. As can be seen, the elbows of the claw poles are beginning to saturate.

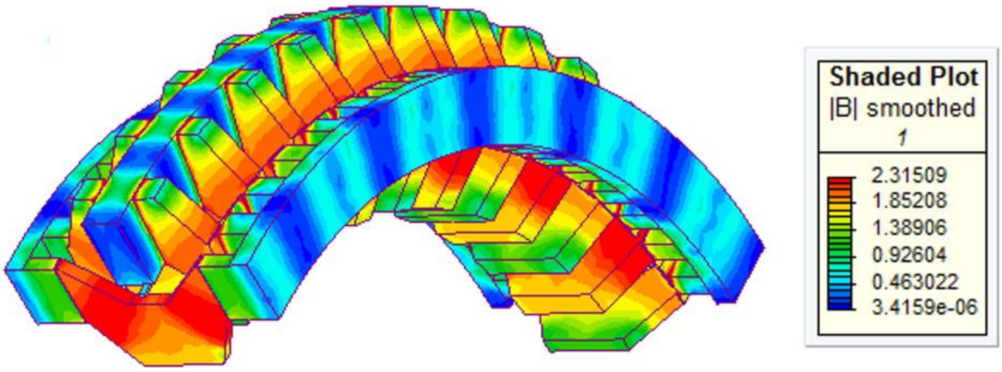

Figure 4.21. 3D FEA results for the original double claw pole generator design [16].

Figure 4.22 highlights the stator tooth flux density in the z-direction, *i.e.* into and out of the page, halfway through the stator teeth. The left side shows the flux density when the large claw pole is aligned with the middle tooth, the right side shows the case when the small claw pole is aligned instead.

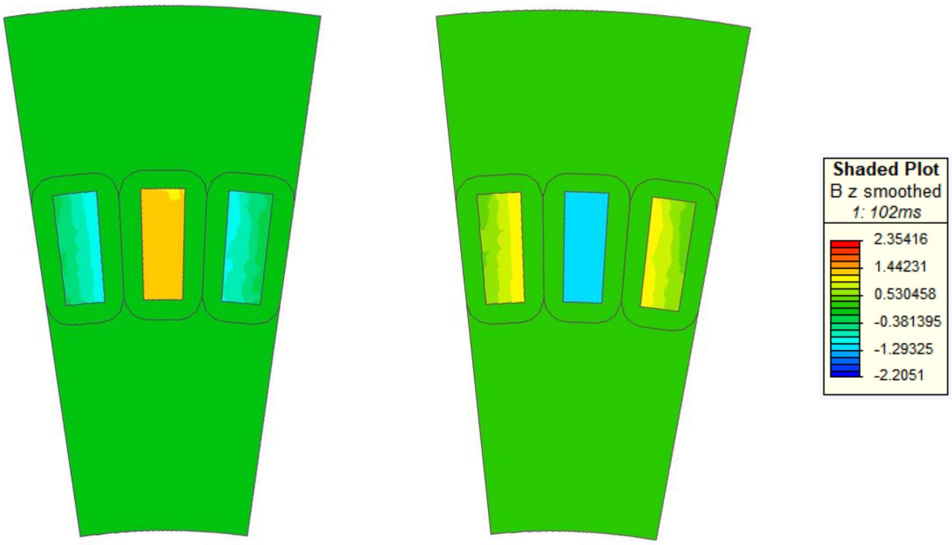

Figure 4.22. Flux density into the z-direction (into/out of the page) halfway through the stator teeth. Left shows the flux density distribution when the large claw pole is aligned and right shows the case when the small claw pole is aligned.

The z-direction stator tooth flux, for the case when the large claw pole is aligned, was found to be 57 mWb, which is in exact agreement with the peak stator flux stated in [100]. In addition, when investigating the flux density distribution throughout the machine components, there is an excellent agreement between the flux densities produced by the FEA and the flux densities produced by the reluctance network, which was shown in figure 4.11.

The results show that both the reluctance network model and the FEA model produce results, which are in agreement with each other. With the working models the work done on the double claw pole generator design can be further expanded. In particular, the voltage and torque characteristics are of importance, these were investigated by expanding the FEA model to enable a transient analysis with the claw poles in motion.

4.3.2 Transient Analysis with Motion for the Original Design

Since the magnetostatic analysis produced very good results, the model was further expanded by including a transient analysis with rotational motion of the claw poles. This model includes the stator coils to investigate the no load voltage waveform and cogging torque characteristics. To create a model with motion in *MagNet*, it needs to be setup in a specific manner. First off, while the previous model featured one quarter of the machine, the model for the transient analysis was reduced down to 1/22. This allows to make use of the symmetry of the machine and reduces the computational time significantly, this is especially important for transient analyses since these types of simulations involve a multitude of time steps. A side perspective of the model is shown in figure 4.23. The model consists of 3 stator coils on each side and 4 poles. Even-periodic boundaries are applied to the cross-sectional surfaces of the model. The arc length of the model is equivalent to 16.36˚, which is the angle of symmetry.

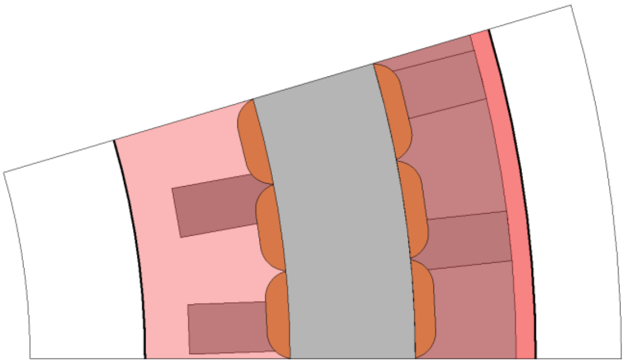

Figure 4.23. Side view of the transient model with motion in MagNet.

In order to set up the rotational motion of the model, the rotating components need to be selected and a re-mesh region for the mesh needs to be defined. This is done by breaking the air gap up into 4 different layers as shown in figure 4.24. The part of the model shaded in red are the components in motion, *i.e.* the claw poles, the claw poles are surrounded by a separate boundary, which is defined as the rotor boundary. The claw poles rotate past the stator coils along with the rotor boundary. The motion domain is separated from the stationary domain by 4 mesh layers as shown in the figure, where the two layers in the middle are the re-mesh region, the mesh in this region is re-meshed for each new time step as the rotor rotates.

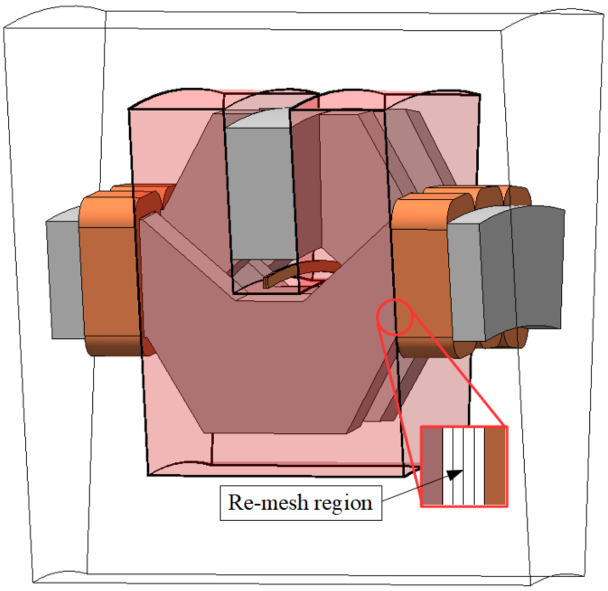

Figure 4.24. Model in MagNet with the motion domain shaded in red and the re-mesh region definition.

Since a transient analysis involves a multitude of time steps, it is computationally much more time consuming. While the previous magnetostatic simulations had a very fine mesh for all components, the mesh for the transient model is less dense to save computational time. For the simulations, the simulation time was chosen as 140 ms with 2 ms time steps, resulting in 70 simulation steps. Figure 4.25 shows the solution mesh for the first time step of the simulation. As can be seen when comparing the mesh to the previous model shown in figure 4.20, a rougher mesh is used. Except for the air gap region and re-mesh region, where a very fine mesh was maintained. A fine mesh is required in the re-mesh region to assure convergence.

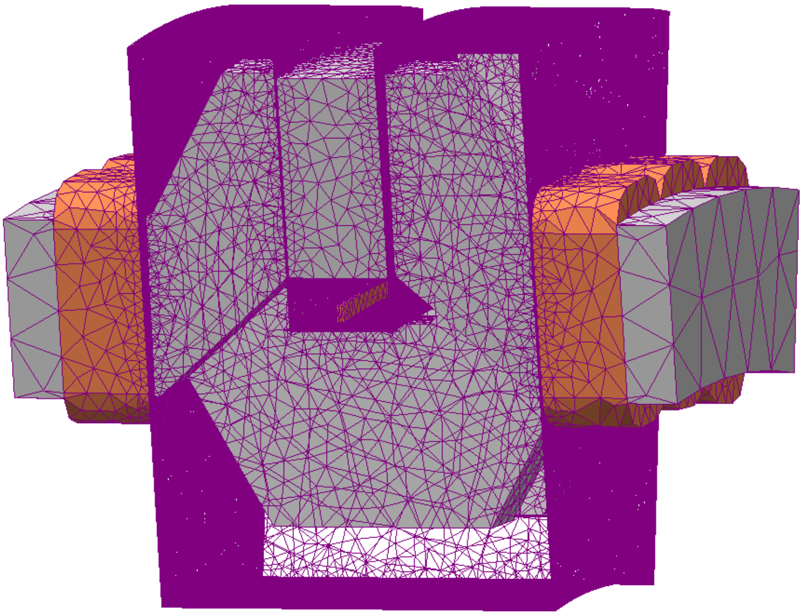

Figure 4.25. Solution mesh for the first time step of the transient analysis.

To verify the correctness of the model, the time step where the large claw poles are aligned with the stator teeth is investigated and compared to the magnetostatic model. Figure 4.26 shows the flux density distribution in the machine, it can be seen that it is identical to the flux density distribution of the magnetostatic model shown in figure 4.21.

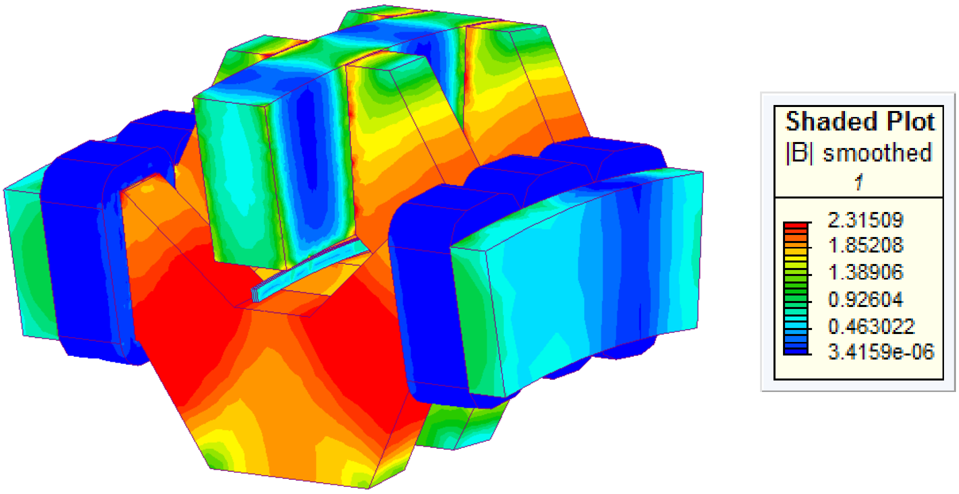

Figure 4.26. Flux density distribution when the large claw poles are aligned with the stator teeth.

With the correctness of the model verified, the voltage and torque characteristics of the design can be investigated. To examine the no-load conditions, the stator coils are open-circuited by connecting a very large load, this is shown in figure 4.27. Coils 1, 2 and 3 are located on the same stator, similar to coils 4, 5 and 6, which share the stator on the opposite side. The coils that are located opposite of each other are placed in parallel and share the same phase. The load is connected in star configuration

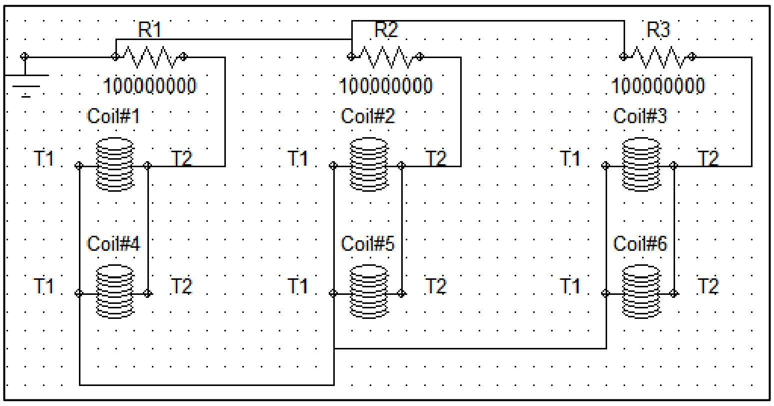

Figure 4.27. Open-circuit configuration for the stator coils.

The open-circuit voltage is shown in figure 4.28. It can be seen that a 3-phase voltage is being generated. The electrical frequency of the generator is 7.33 Hz at 10 rpm, which is equivalent to a time period of 136.4 ms. The peak induced coil voltage is approximately 250 V, giving an RMS voltage of 176 V. The voltage waveforms are slightly offset into the negative direction, *i.e.* the negative peak is bigger in magnitude than the positive peak. This is due to the larger claw pole carrying a higher amount of flux than the small claw poles since there are no air gaps in the flux path throughout the large claw poles. Furthermore, it can be seen that the waveforms are not perfectly sinusoidal, which is due to the interaction between the stator slots and the claw poles.

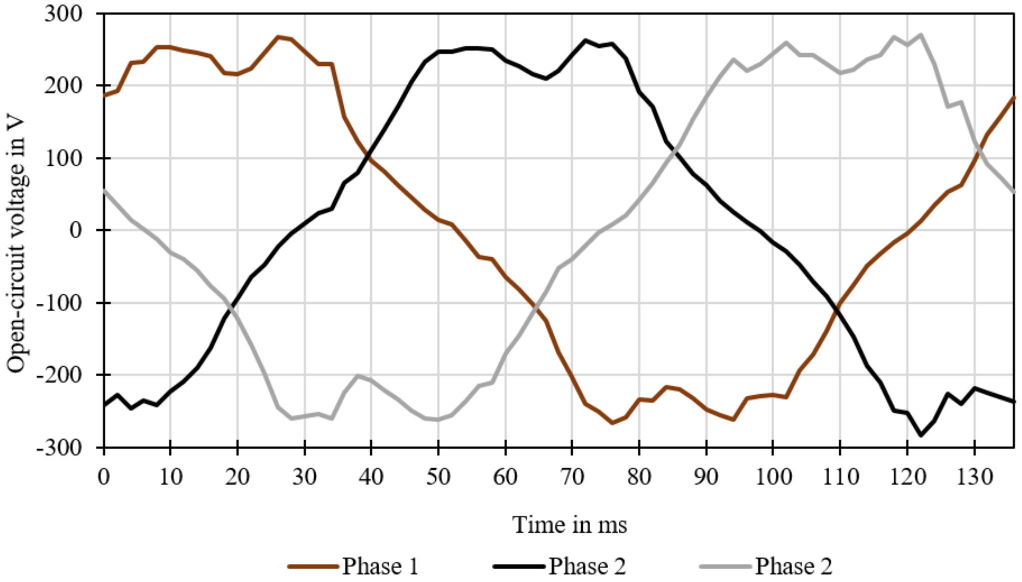

Figure 4.28. Open-circuit voltage for the double claw pole machine with an angled stator concept.

This interaction becomes especially evident when investigating the cogging torque of the machine, which is the torque required to rotate the rotor at the rated RPM without a load being connected. The cogging torque is essentially the manifestation of the rotor poles trying to align with the stator teeth. The cogging torque is an important characteristic for rotating electrical machines since it does not contribute towards the net effective torque but causes speed ripples and vibrations. This is especially important when considering low-speed applications such as in direct-drive wind turbine generators [102]. The reduction of cogging torque in rotating machines is one of the major design goals. To analyse the cogging torque, the same open-circuit configuration as shown in figure 4.27 was used. To obtain the forces between the rotor and stator as the rotor is in motion, the Maxwell stress tensor method is applied to the rotor. This torque calculation method is readily available in the FEA software that was used throughout this research work.

Figure 4.29 shows the resulting cogging torque for the double claw pole machine. Considering the power output of 10 MW and the rotational speed of 10 RPM, the rated torque can be calculated to be 9.55 MNm. The peak-to-peak cogging torque is approximately 96 kNm, which is 1% of the rated torque.

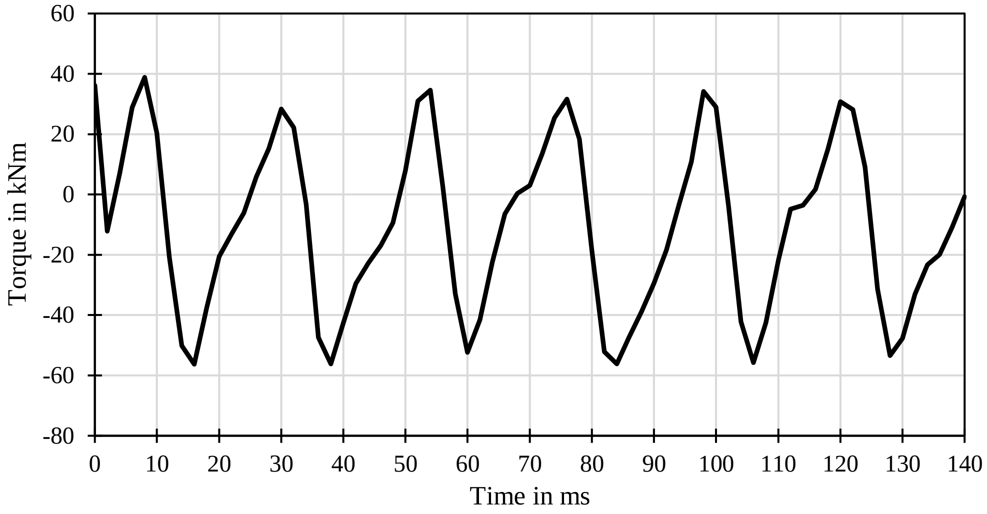

Figure 4.29. Cogging torque characteristics.

The model can be further expanded to investigate the torque ripple, which similar to the cogging torque leads to vibrations and speed ripples, which should be minimized when operating at low rotational speeds. Figure 4.30 shows the torque ripple at rated power output. The magnitude of the peak-to-peak torque ripple was found to be approximately 763 kNm, which is approximately 8 % of the rated torque. As was discussed, the pole and slot numbers selected result in a high common divider, enabling a high level of symmetry to reduce the computational time required. However, this combination of poles and slots also results in a higher cogging torque and torque ripple [101, 103]. Both the cogging torque and torque ripple could be further reduced by choosing a more appropriate combination of poles and slots.

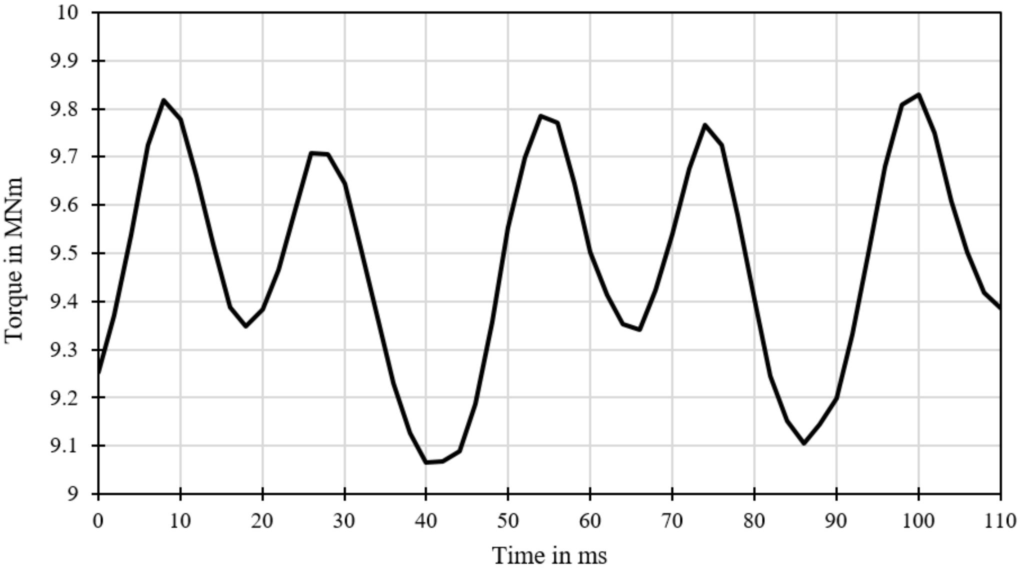

Figure 4.30. Torque ripple at rated power.

Overall, it was shown in this section that the finite element analysis models developed produce the same results as stated in previously published works [100]. Additionally, the models were further expanded to show the voltage and torque characteristics of the double claw pole generator, giving a more detailed insight into the operation of the double claw pole machine than the previously done research work, Suggestions were given to improve the torque characteristics, such as choosing a more appropriate combination of poles and slots, at the cost of increased computational time. With the working reluctance network and FEA models a good basis was developed to investigate the double claw pole machine design in further detail.

4.4 Chapter Summary

This chapter described the evolution of the double claw pole machine and the modelling methods used to design and assess machine concepts. Firstly, the reluctance network model was introduced. It is an analytical approach to modelling electric machines, which offers reasonably high accuracy at very low computational power. In addition to the reluctance network model, finite element analysis using the simulation software *MagNet* was introduced, to further verify the reluctance network modelling results and to offer more detailed results in terms of machine performance. The results produced by the reluctance network and the FEA for the original design of the double claw pole generator were shown and compared to previous publications. Results confirmed that both the reluctance network model and the FEA models produce accurate results, which are well in agreement with the results of previous publications of the double claw pole generator. Furthermore, the FEA models were expanded to highlight the transient performance of the generator such as the open-circuit voltage, cogging torque and torque ripple, giving a deeper insight into the double claw pole machine performance.

With the established working models, it is possible to further investigate the design of the double claw pole generator, and to further improve upon it. These new designs will be highlighted and discussed in the following chapters.

Chapter 5 Novel Stator Design for Axial Flux Machines

This chapter introduces a novel stator design for axial flux machines. The new stator design deviates the air gap closing forces partially into the concentric direction, reducing the axial air gap closing forces and hence simplifying the design of the support structure. Reluctance network and FEA modelling results are shown for the novel design. The newly introduced design is compared to the original design of the double claw pole generator to highlight the increased power density that was achieved. The design and results shown in this chapter have been published in *Superconductor Science and Technology* as “Novel model of stator design to reduce the mass of superconducting generators, *Superconductor Science and Technology,* vol. 31 no. 5, p. 1-8, 2018.”

5.1 Axial Flux Machines with Novel Stator Design

A multitude of different topologies of electrical machines exist. One clear difference between the various topologies is the direction of the magnetic flux. In an axial flux machine, the magnetic flux travels axially across the air gap. The main advantage of axial flux machines is that they offer higher torque to volume ratios than other topologies, due to their short axial length, which make them an attractive option where space or transportation becomes an issue [104]. Axial flux machines in particular have attracted a lot of attention where high power densities are required such as motors for electric vehicles [105, 106, 107]. However, since the flux crosses the air gap in the axial direction there are large axial forces acting on the machine components leading to structural instability, this especially becomes an issue for very large diameter machines. To counter this, axial flux machines require a rigid support structure, which in turn leads to a lower torque to mass ratio [108]. In addition, with the large magnetomotive force (MMF) produced by superconductors, this issue is further amplified and further complicates the mechanical support structure to main the air gap clearance at all times. To highlight the impact of the air gap closing forces, equation 5.1 is shown.

$$F = \frac{B^2 A}{2\mu_0} \tag{5.1}$$

where B is the air gap flux density, A is the cross-sectional area of the air gap and μ_0 is the magnetic permeability of air.

Conventional machines tend to only operate with an air gap flux density of 0.6 T~0.8 T. Superconducting machines on the other hand can easily reach and exceed 1 T leading to very high air gap closing forces. Since the air gap closing force increases with the square of the flux density, it becomes clear that the mechanical support structure becomes a key issue, especially when using superconducting wire to provide the MMF. Figure 5.1 shows the air gap closing force for increasing air gap flux densities. The cross-sectional area in-between an overlapping claw pole and stator tooth for the original design of the double claw pole machine was used to calculate the force. As is shown, the air gap closing force increases significantly with the air gap flux density.

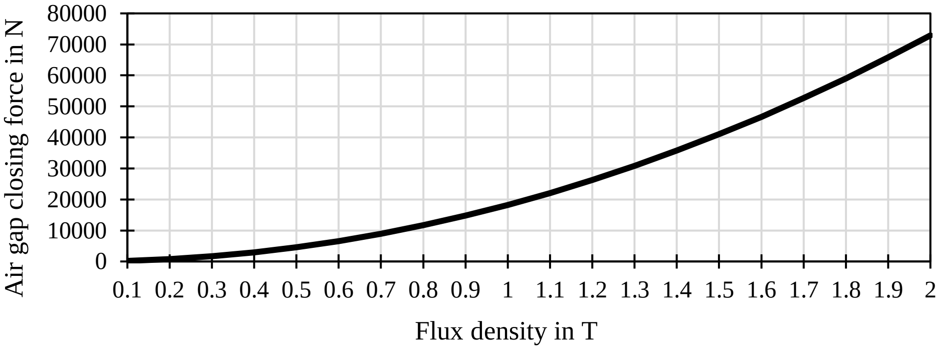

Figure 5.1. Air gap closing force with increasing flux density.

These issues in conjunction with superconductors make the design of axial flux machines very challenging. Figure 5.2 shows a schematic of an axial flux machine with double slotted stators and a single rotor.

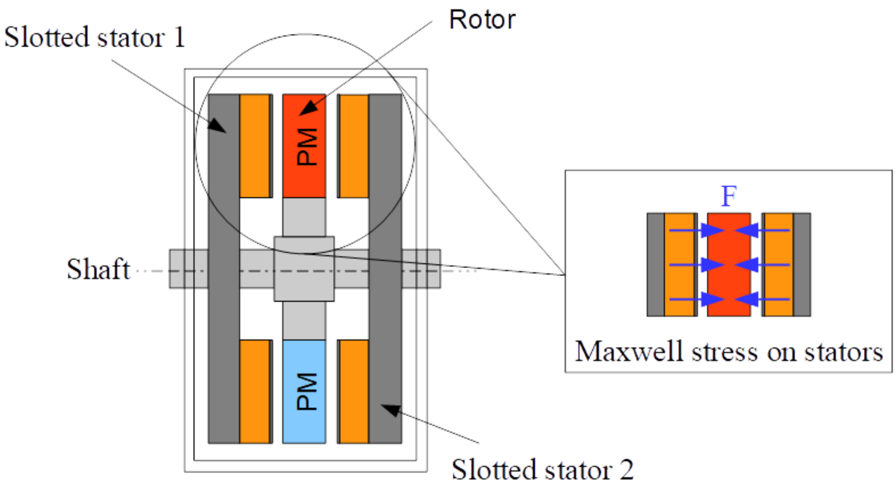

Figure 5.2. Axial flux permanent magnet machine schematic.

It is one of the most common types of axial flux machines next to variation with double rotors and a single stator [108]. The Maxwell stress on the machine components is highlighted. While the forces on the rotor are balanced, the forces on the stator sides are not and they only act in the axial direction. In conjunction with very large diameter machines, it is challenging to maintain the air gap clearance, which is further worsened with high air gap flux densities. A high air gap flux density is however required in order to achieve a high power density. For convenience, the basic machine equation is highlighted again below. It can be seen that the power output of a machine is proportional to the air gap flux density.

$$P = BA_{\mathrm{E}}\frac{\pi}{2}D^2L\omega \tag{5.2}$$

where B is the air gap flux density, A_{E} is the electric loading, D is the machine air gap diameter, L is axial length of the machine and ω is the rotational speed.

For conventional machines, the flux density B and the electrical loading A_{E} are essentially fixed, hence the dimension of a machine can roughly be estimated by considering the required output power and rotational speed. With superconductors, the magnetic loading B is no longer limited by the current carrying capabilities of copper or the flux density of permanent magnets. Hence the size of the machine can be significantly reduced with a higher magnetic loading. However, as was discussed previously, the high air gap flux density leads to high air gap closing forces. To avoid this issue, slotless and air-cored machine topologies exist, but these come with the disadvantage of increasing the amount of superconducting tape required, which increases the capital cost significantly. To avoid using an excessive amount of superconducting material, an iron-cored structure is desirable. Clearly, the air gap closing force itself cannot be reduced without negatively impacting the machine performance. However, the direction of the force can be diverted, which is achievable by designing the stator at an angle. Figure 5.3 shows a schematic of the concept. The stator teeth are angled outwards by an angle α deviating the air gap closing forces. The angle α is used to adjust the axial and radial forces to attempt to reduce structural mass. The optimal angle depends on the structure of the machine that the concept is being applied to.

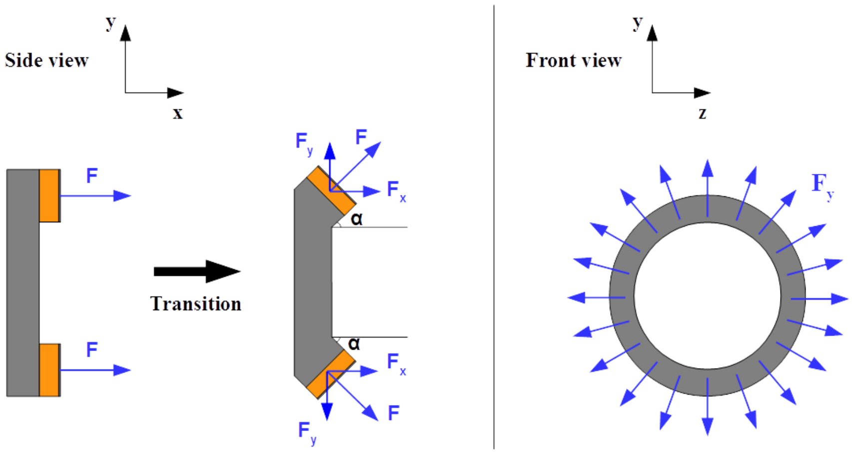

Figure 5.3. Transition from normal axial stator to an angled stator with the air gap closing forces highlighted: side view of the stator (left) and front view of the stator (right) [16].

With the angled stator, the total air gap closing force can be separated into its x- and y-components as shown in the following equations.

$$F_x = Fcos(\alpha) \tag{5.3}$$

$$F_y = Fsin(\alpha) \tag{5.4}$$

Through applying an angle to the stator, the axial forces can be reduced and hence the structural stability can be improved. A portion of the air gap closing force now acts into the radial direction, but this force essentially cancels out due to the rotational symmetric of the machine. This force can be compared to the air gap closing forces that exist within radial machines. Radial flux machines are the most common machines, hence the structural support and ball bearings for this topology are well developed. To further highlight the concept, figure 5.4 shows the previous schematic of the axial flux machine with an angled stator.

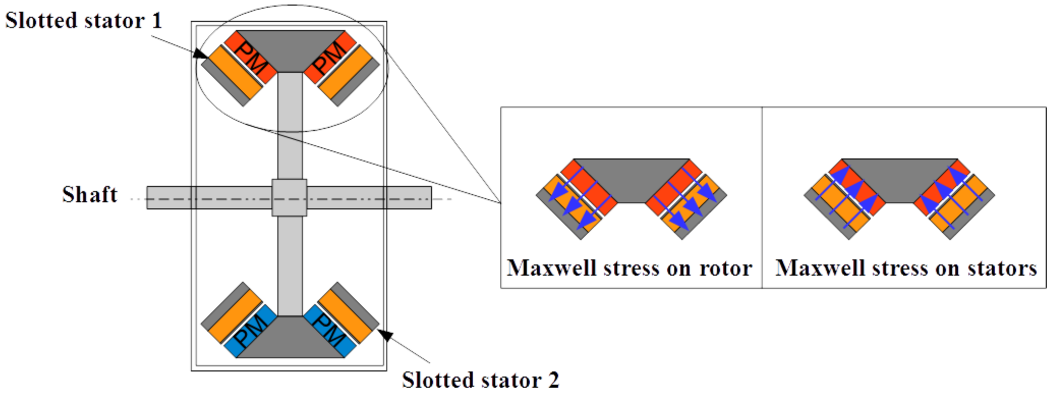

Figure 5.4. Slotted axial flux machine with an angled stator [16].

In order to verify the idea, the concept is applied to the double claw pole machine to reduce its structural mass.

5.2 Design of the Double Claw Pole Generator with an Angled Stator

This section will cover the design of the double claw pole generator with an angled stator. First of the concept is described in conjunction with the double claw pole machine design. The first iteration of the design is then investigated using a reluctance network model. The design is then further improved upon by reducing the active mass required, while increasing the electromagnetic performance. With the reluctance network model producing satisfactory results, the next section investigates the design in further detail with the use of numerical models.

5.2.1 First Iteration of the Design

To start applying the angled stator concept to the double claw pole machine, it is necessary to define the size of the components. It was discussed and shown in chapter 4 that the design of the original double claw pole machine was optimized for the lowest active mass, hence it was decided to maintain most of the machine dimensions. Maintaining the majority of the dimensions allows to easily compare the original design and the new design of the double claw pole machine in terms of their power densities. Some critical parameters to maintain for a meaningful comparison between the two designs were: the inner diameter R_{in}, the number of poles N_{pole}, the number of stator coils N_{coil} and turn number N_{turn}, the same MMF and the same rotational speed. The main attributes of the original design of the double claw pole generator are highlighted in table 5.1.

Table 5.1: Original design of the double claw pole generator

Attribute	Value
Total mass	188 tonnes
Outer diameter	6.37 m
Power output	10 MW
Rotational speed	10 rpm
Power density	53.19 W/kg
HTS requirement at 30 K	3.3 km

Particular attention had to be paid to the dimensions of the claw poles in order to avoid saturation. Another important parameter was to maintain the space in between the claw poles where the superconducting winding and its cryostat are located. Figure 5.5 shows a schematic of the transition from the original double claw pole machine design to the variation with the angled stator. The concept of the double claw pole machine remains the same, the stationary superconducting field winding is supplied with a DC current hence it produces a magnetic field. Upper and lower claw poles are oriented around the field winding. These are oriented in an alternating fashion in order to create a North-South pole flux variation across the stator coils. The stationary field core offers support and access to the superconducting field winding and its cryostat.

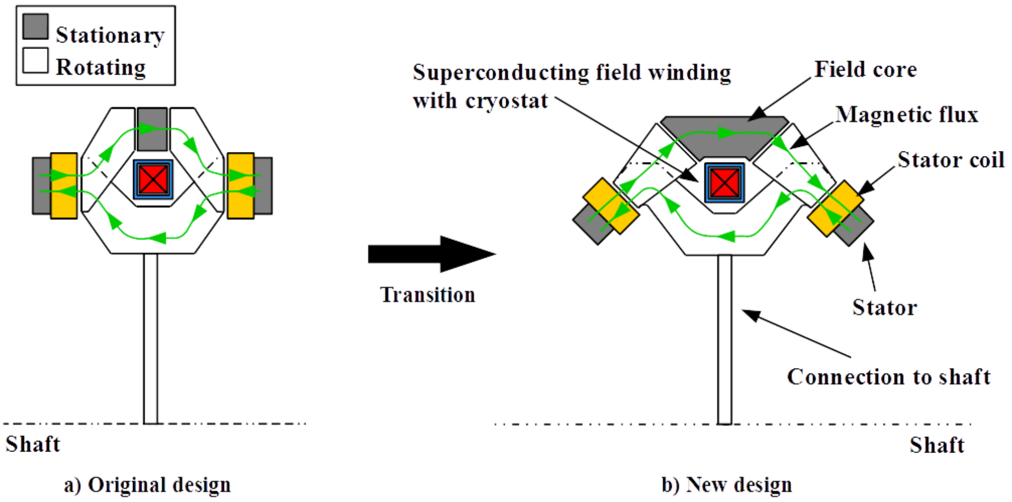

Figure 5.5. The transition from a) the original design to b) the new design [16].

From Figure 5.5 it can be seen that for the new design the flux travels axially as well as transversely across the air gaps leading to the forces being diverted. The new directions of the forces acting on the machine components are shown in Figure 5.6.

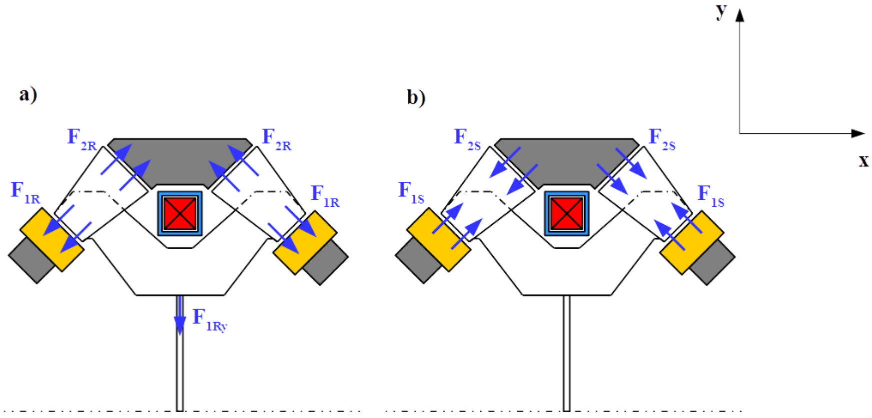

Figure 5.6. a) Forces acting on the rotor (claw poles) and b) forces acting on the stator [16].

For the original design, the shape of the claw poles was optimized using a genetic algorithm. The cross-sectional areas of the claw poles were increased near the field core to balance the forces F_1 and F_2. This is due to the flux density being higher in the inner air gap than in the outer air gap. As was shown in equation 5.1, the air gap closing force depends on the flux density and the cross-sectional area. Since the flux density is higher in the inner air gap, the cross-sectional area was increased to balance the forces F_1 and F_2. These dimensions were taken over for the new design to keep the same balance of forces. There is a net force inwards from the large claw poles towards the shaft. However, due to the rotational symmetry of the machine these forces are balanced in relation to the shaft leading to no resultant net force. This inward force is similar to the forces present in radial flux machines. The x-component of F_1 is smaller in magnitude than the axial force of the original design. Hence the axial forces acting on the stator sides were reduced, improving the structural stability of the machine. Considering the structure of the double claw pole machine, setting the stator sides at an angle of 45° was found to be a good compromise between reducing the axial forces and viability of the design. Increasing the angle further leads to difficulty in maintaining the required space in between the claw poles for the superconducting field winding and its cryostat. In addition, a higher angle would also lead to a stronger bend of the lower claw poles and stator sides, which would increase the manufacturing complexity of the generator components. With the 45˚ angle, the axial air gap closing force can be reduced by 30 %.

To model the newly introduced machine concept, the reluctance network model highlighted in the previous chapter was adjusted. Figure 5.7 shows the new reluctance network. The machine components were broken up into new reluctances. Equation 5.5 shows the resultant reluctance network matrix.

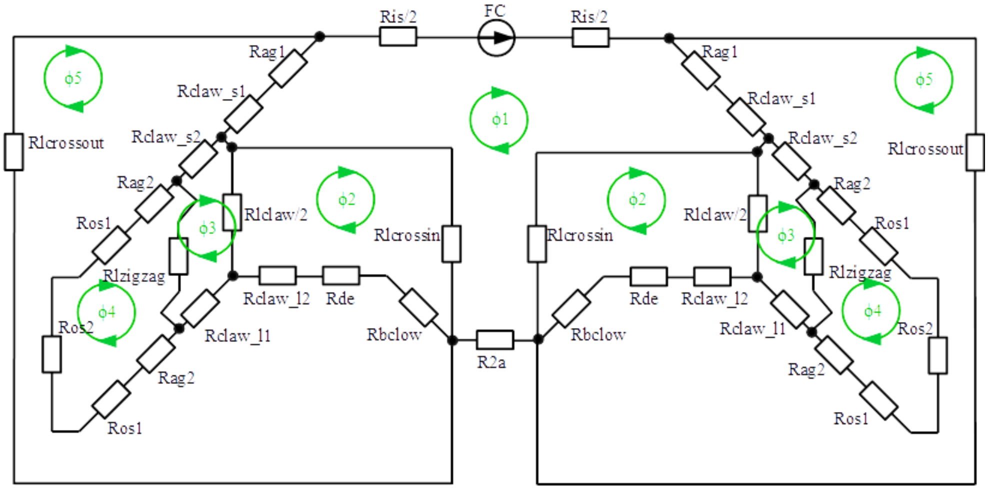

Figure 5.7. Reluctance network of the double claw pole machine with angled stator sides [16].

$$\begin{bmatrix} \begin{array}{c} 2(R_{iag}+R_{claws1}+R_{lcrossin}) \\ +R_{2a}+R_{is}+R_{is2} \end{array} & -R_{lcrossin} & 0 & 0 & -2(R_{iag}+R_{lclaws1}) \\ -2R_{lcrossin} & \begin{array}{c} 2(0.5R_{lclaw}+R_{blow}+R_{de} \\ +R_{clawl2}+R_{lcrossin}) \end{array} & -R_{lclaw} & 0 & -2(R_{blow}+R_{de}+R_{clawl2}) \\ 0 & -2R_{lclaw} & \begin{array}{c} 2(0.5R_{lclaw}+R_{claws2}+R_{clawl1} \\ +R_{zigzag}) \end{array} & -2R_{zigzag} & -2(R_{claws2}+R_{clawl1}) \\ 0 & 0 & -2R_{zigzag} & \begin{array}{c} 2(R_{zigzag}+2R_{oag}+R_{os1} \\ +R_{os2}) \end{array} & -2(2R_{oag}+2R_{os1}+R_{os2}) \\ -2(R_{iag}+R_{claws1}) & -2(R_{blow}+R_{de}+R_{clawl2}) & -2*(R_{claws2}+R_{clawl1}) & -2(2R_{oag}+R_{os1}+R_{os2}) & \begin{array}{c} 2(R_{lcrossout}+R_{blow}+R_{de} \\ +R_{clawl2}+R_{clawl1}+2R_{oag} \\ +R_{iag}+2R_{os1}+R_{os2}+R_{claws1} \end{array} \end{bmatrix} \begin{bmatrix} \Phi_1 \\ \Phi_2 \\ \Phi_3 \\ \Phi_4 \\ \Phi_5 \end{bmatrix} = \begin{bmatrix} MMF \\ 0 \\ 0 \\ 0 \\ 0 \end{bmatrix} \tag{5.5}$$

Figure 5.8 shows the first iteration of the machine design and table 5.2 highlights the main machine dimensions.

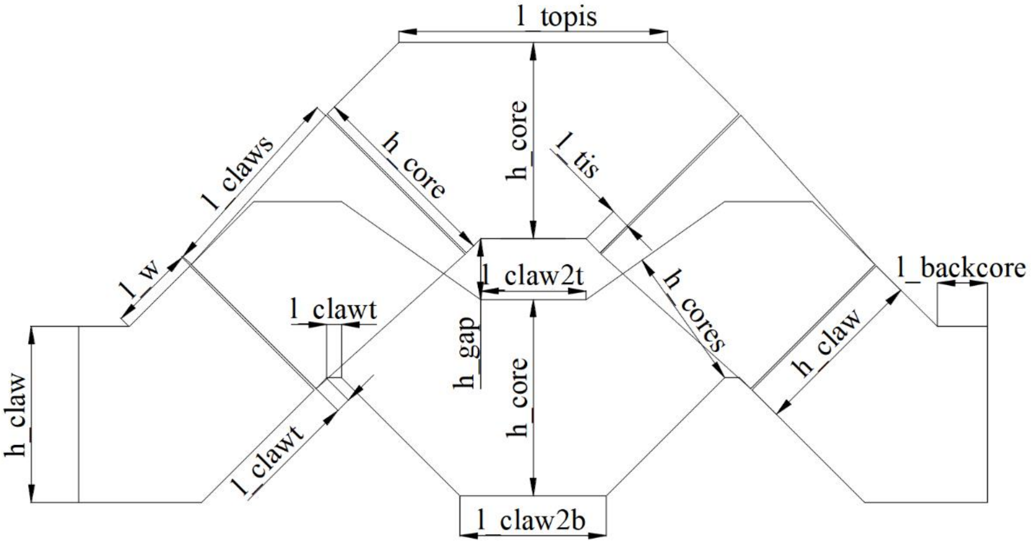

Figure 5.8. First iteration of the double claw pole machine with an angled stator.

Table 5.2. Main component parameters for the first iteration of the design

Variable	Value (mm)
R_{in}	2288
N_{pole}	88
N_{coil}	66
ag	4.5
l_{claw2t}	210
l_{claw2b}	292
l_{claws}	400
l_{clawt}	30
h_{core}	393
h_{cores}	287
h_{claw}	351
l_{w}	172
l_{backcore}	100
h_{gap}	121
l_{istop}	535
l_{ist}	40

As was mentioned previously, the main parameters were largely kept the same as the for the original double claw pole machine to simplify the comparison between the two concepts and since the original concept was already optimized for lowest mass. Especially the dimensions of the claw poles were mainly maintained such as the core heights to avoid saturation. From figure 5.8, it can be seen that the large claw pole consists of the essentially the same geometry as in the original design, with the addition of the end parts, which were adjusted to comply with the angled stator concept. The small claw pole was completely changed, it is now shaped similar to a trapezoid. The field core was also adjusted to align with the stator angle. The equations for the new equivalent lengths and areas for the new components are highlighted below. For the field core, equations 5.6 to 5.9 define the equivalent length and equivalent cross-sectional area. It was broken up into two reluctances, where the first reluctance represents the straight section on either side of the tooth and the second reluctance the horizontal section from one side to the other side of the machine.

$$l_{\mathrm{is}} = 2l_{\mathrm{tis}} + \frac{\left(l_{\mathrm{gap}} + l_{\mathrm{isup}}\right)}{2} \tag{5.6}$$

where l_{is} is the equivalent length through the claw pole, the first part of the equation defines the straight sections on either side and the second part describes the straight section from one side of the field core to the other.

$$A_{\mathrm{tis}} = h_{\mathrm{core}} * T_{\mathrm{core}} * k_{\mathrm{fringis}} \tag{5.7}$$

where A_{tis} is the cross-sectional area for either side of the field core.

$$A_{\mathrm{is}} = h_{\mathrm{coreis}} * T_{\mathrm{core}} * k_{\mathrm{fringis}} \tag{5.8}$$

where A_{is} cross-sectional area for the middle of the field core.

For the outer stator the equivalent length from the beginning of the stator tooth to the middle of the back core is defined by equation 5.9 and the cross-sectional area is defined by equation 5.10.

$$l_{\mathrm{os1}} = l_{\mathrm{w}} + 0.5 * l_{\mathrm{backcore}} + 0.5 * h_{\mathrm{claw}} * \alpha \tag{5.9}$$

$$A_{\mathrm{os1}} = h_{\mathrm{claw}} * t_{\mathrm{tooth}} \tag{5.10}$$

The length from one stator tooth to the other is represented by equation 5.11 and the cross-sectional area through the back core is defined in equation 5.12.

$$l_{\mathrm{os2}} = T_{\mathrm{pole}} \tag{5.11}$$

$$A_{\mathrm{os1}} = h_{\mathrm{claw}} * l_{\mathrm{backcore}} \tag{5.12}$$

The small claw poles were broken up into two reluctances with the equivalent lengths for each part being the same as shown in equation 5.13.

$$l_{\mathrm{claws1}} = l_{\mathrm{claws2}} = \frac{l_{\mathrm{claws}}}{2} \tag{5.13}$$

Equation 5.14 gives the cross-sectional area for the lower power of the small claw pole, the shortest height of the section is taken for simplicity.

$$A_{\mathrm{claws1}} = h_{\mathrm{claw}} * T_{\mathrm{core}} \tag{5.14}$$

Equation 5.15 gives the cross-sectional area for the upper part of the claw pole.

$$A_{\mathrm{claws2}} = h_{\mathrm{core}} * T_{\mathrm{core}} \tag{5.15}$$

Since the large claw pole mainly consists of the same dimensions are for the original design, only the new parts introduced are highlighted in this section. Equation 5.16 defines the path through the two straight sections on either side of the claw pole.

$$l_{\mathrm{clawl1}} = 2l_{\mathrm{t2}} \tag{5.16}$$

Equation 5.17 gives the path through the 45° bend introduced in the claw pole, where α is given in radians.

$$l_{\mathrm{clawl2}} = \frac{h_{\mathrm{claw}}}{2} * \alpha \tag{5.17}$$

Equation 5.18 gives the cross-sectional area for the new parts introduced.

$$A_{\mathrm{clawl1}} = A_{clawl2} = h_{\mathrm{claw}} * T_{\mathrm{core}} \tag{5.18}$$

The dimensions for the other parts of the large claw pole remain the same as for the original design and can be found in the second chapter of this thesis.

Applying the reluctance network to the machine design the generator performance can be assessed. Figure 5.9 shows the flux density distribution in the generator components for an increasing MMF.

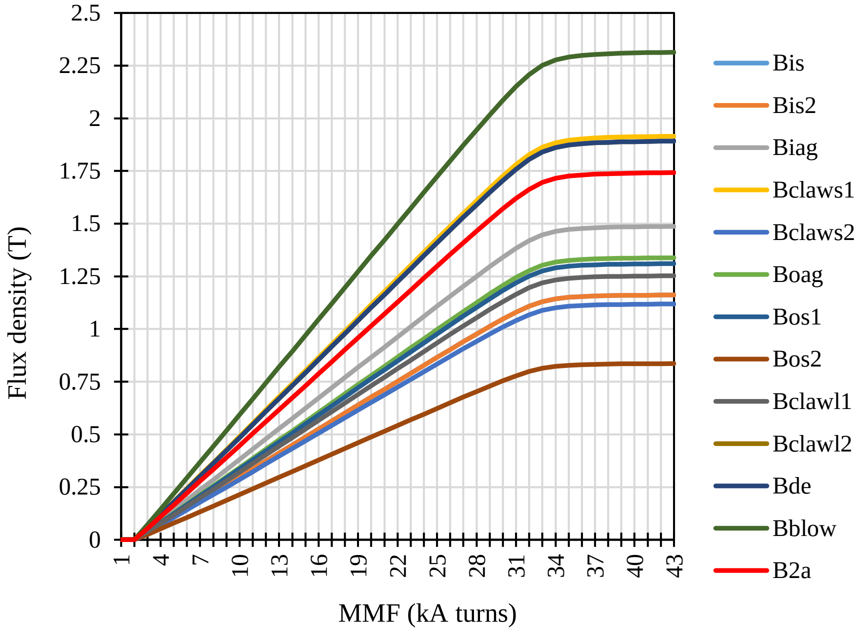

Figure 5.9. Flux density distribution in the first iteration of the design with increasing MMF.

It can be seen that the machine components already approach saturation before 32 kA·turns. This is due to the large claw pole saturating around the elbow. The elbow is defined as B_{blow} in figure 5.9, it can be seen that it has saturated at a flux density of approximately 2.3 T, the shortest height of the large claw pole in the elbow was defined in figure 5.8 as h_{cores}. A further issue with this iteration of the design is the new active mass, which considerably increased. The active mass of the original and the newly introduced design are summarized in table 5.3.

Table 5.3. Active mass comparison

Component	**Original mass (kg)**	**New mass (kg)**
Small claw poles	262	316
Large claw pole	349	471
Stator cores and coils	21,140	50,131
Field core	11,354	38,382
Total rotor mass	26,884	34,628
Total active mass	**59,378**	**123,141**

As can be seen the active mass increased significantly, especially the stator and field core are considerably heavier than for the original design. Due to the significantly increased active mass, any reduction in structural mass is expected to be too low to be beneficial for the over all mass of the generator design. To further improve upon the design to avoid early saturation and reduce the active mass, the machine components need to be optimized. The reduction of active mass will be addressed in the following sub-section.

5.2.2 Optimisation of the Design

With the aim to reduce the active mass, the stators are investigated at first, figure 5.10 shows a comparison of the cross sectional view of the two stator designs. For the original design the stator simply consists of the backcore with length l_{backcore} and the stator tooth length l_{w}. For the new design an angle was introduced in the stator tooth, this bend introduces a significant amount of additional mass. The added mass serves no purpose and only leads to the design being heavier. Since the introduced bend in the stator tooth leads to unnecessary mass, the best option to lighten design is to eliminate the bend. This is done by rotating the back core and stator teeth by the angle α.With this method the mass of the stator essentially remains the same as for the original design and the active mass of the design is reduced.

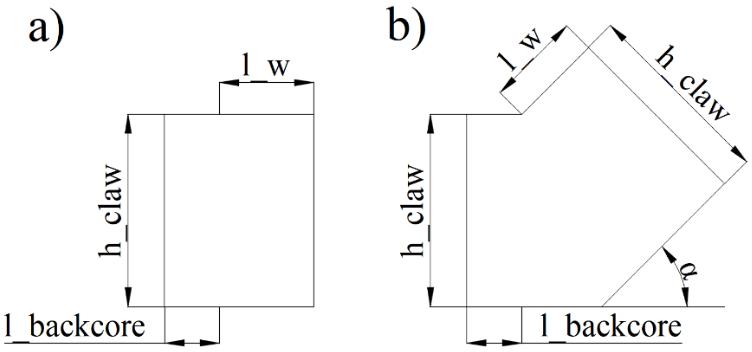

Figure 5.10. Stator cross-section comparison for a) original design and b) angled stator design.

Following the stator, the mass of the new field core was found to be much higher as well. This is due to a similar issue as for the stator teeth, the bend in the field core that was necessary to adjust for the stator angle, increased the size of the field core considerably. When investigating the resultant flux density in the field core, B_{is1} and B_{is2}, from figure 5.9, it can be seen that the iron is far from saturating. This indicates that the size of the field core can be reduced without negatively impacing the machine performance. The size is reduced by decreasing the height of the core h_{core} in the middle of the field core. The height near the inner air gap on the other hand remains the same, as to avoid impacting the balance of air gap closing forces for the inner and outer air gaps. Additionally, the straight sections defined by l_{tis} in figure 5.8 were shortened, to further reduce that mass. Lastly the claw poles were investigated. Since the elbows of the large claw poles were found to saturate too quickly, the geometry was adjusted to increase the elbow height h_{cores}. Additionally, unnecessary straight sections were removed to further reduce the mass. The final design of the double claw pole machine with an angled stator is shown in figure 5.11 with the the main parameters summarized in table 5.4.

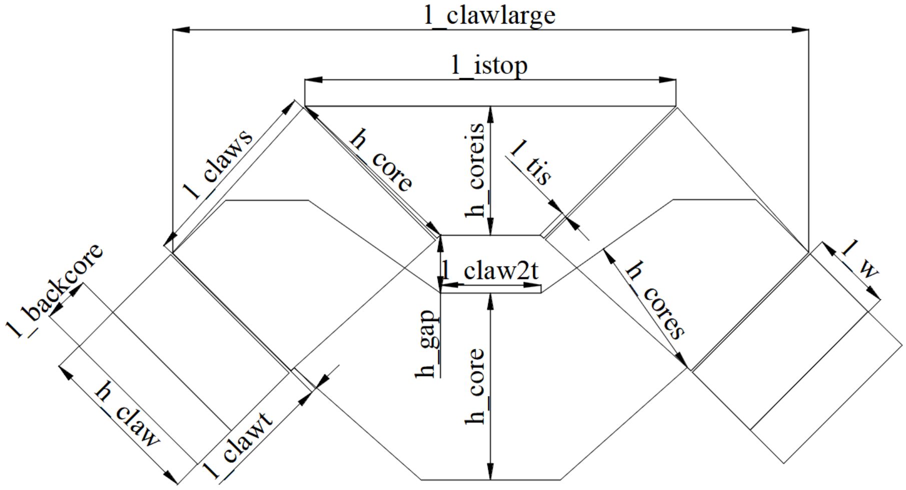

Figure 5.11. Final design of the double claw pole machine with angled stator.

Table 5.4 Main component parameters for the final design

Variable	Value (mm)
R_{in}	2288
N_{pole}	88
N_{coil}	66
ag	4.5
l_{claw2t}	210
l_{claw2b}	292
l_{claws}	410
l_{clawt}	10
h_{core}	393
h_{cores}	306
h_{claw}	351
l_{w}	172
l_{backcore}	100
h_{gap}	121
h_{coreis}	270
l_{istop}	764
l_{ist}	10

With the new dimensions, the active mass was reduced considerably, table 5.5 compares the new active mass to the previous designs. The active mass was reduced from 123 tonnes to approximately 73 tonnes.

Table 5.5. Active mass comparison

Component	Original mass (kg)	First iteration mass (kg)	Final design mass (kg)
Small claw poles	262	316	318
Large claw pole	349	471	461
Stator cores and coils	21,140	50,131	19,156
Field core	11,354	38,382	19,447
Total rotor mass	26,884	34,628	34,276
Total active mass	**59,378**	**123,141**	**72,879**

In addition to the reduced active mass, the electromagnetic performance of the generator was improved as well. Figure 5.12 shows the flux density distribution in the machine for the new dimensions with increasing MMF. It can be seen that machine components now saturate at a later stage at approximately 35 kA·turns, which indicates that the operating MMF of 32.4 kA∗turns was chosen adequately.

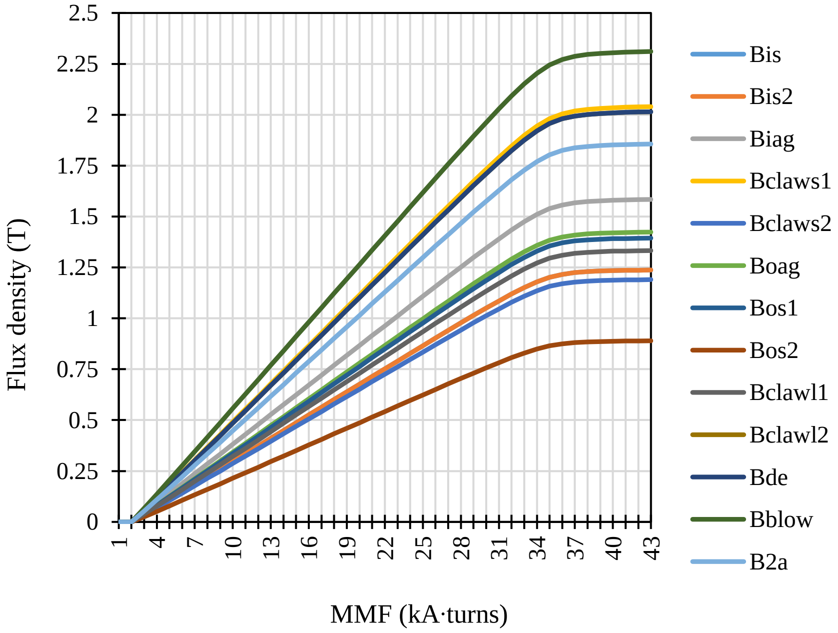

Figure 5.12. Flux density distribution in the machine with increasing MMF.

From the figure it can also be seen that the highest flux density still occurs in the elbow of the large claw pole, similar to the original design. To investigate the machine performance, the stator tooth needs to be investigated it further detail. Figure 5.13 shows the stator tooth flux variation with MMF for the original design of the double claw pole machine and the new design. It can be seen that the stator tooth flux was increased due to the new shape of the claw poles.

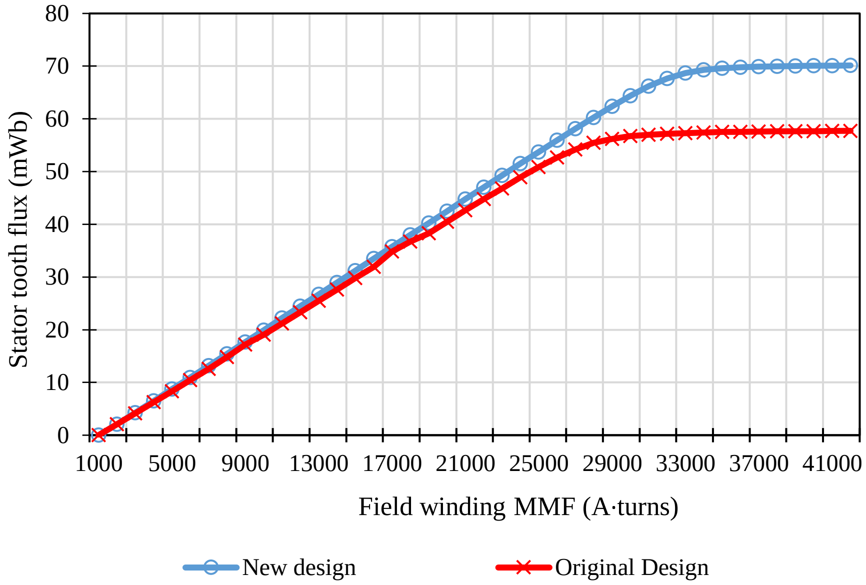

Figure 5.13. Stator tooth flux variation with MMF for the original and new design [16].

The machine was designed for a field winding MMF of 32.4 kA·turns . Since the design of the machine was changed, the magnetic environment of the superconducting coil needs to be investigated to ensure the operating current is within its limitations. Taking the 4 mm wide GdBCO-based superconducting tape model FYSC-SCH04 manufactured by Fujikura as an example, the required number of turns to supply the MMF is dependent on the temperature and magnetic field environment the superconducting tape is located in. The superconducting tape data was received from Fujikura from personal correspondence. Table 5.6 shows the required number of turns in conjunction with the operating temperature assuming no external field is applied to the tape, a safety margin of 30 % is applied to account for the critical current reduction of the tape in the machine environment.

Table 5.6. Number of turns required at different operating temperatures (Data from [109])

Temperature (K)	Critical current in self field (A)	Field current (A)	# of turns	Length (km)
77	230	161	202	3.62
65	469	329	99	1.77
50	783	549	60	1.07
40	1061	743	44	0.79
30	1347	943	35	0.63
20	1721	1205	27	0.48

Three coils are placed next to each other and assuming an operating temperature of 65 K, the required conductor area can be approximated to be 15 mm by 32 mm. Similar to the original design, the field winding can be wound into 4 separate loops with separate cryostats in order to improve the modularity of the machine [15]. For this configuration the required amount of tape is equivalent to 4.03 km.

It should be noted that the HTS length requirements calculated here are much lower than the ones presented by Keysan in [50]. This is due to using the most up to date data provided by Fujikura on the performance of their superconducting tape. In [50], the self-field critical current of YBCO-coated conductors was assumed to only be 125 A at 65 K. The actual critical current is higher than 300 A as shown in table 5.6.

The magnetic field environment of the field winding will be investigated in the next section in further detail using numerical modelling tools to account for the critical current reduction of the tape in the machine environment.

For a field winding MMF of 32.4 $\text{kA} \cdot \text{turns}$, the peak stator tooth flux for the original design is equivalent to 57 mWb. For the same MMF the stator tooth flux with the new design was increased to 69 mWb. With the increased stator tooth flux density, the induced stator coil voltage was increased from 180 V to 206 V. The new output power can hence be calculated to be equivalent to 11.7 MW using the procedure and equations highlighted in the previous chapter. To further validate the results produced by the reluctance network, the next section covers the magnetostatic and transient analyses on the design that were done using the simulation software *MagNet* by *Mentor Graphics*.

5.3 Numerical Modelling of the Generator

In this section the reluctance network model results are verified, and the design of the machine is investigated in further detail. Firstly, a magnetostatic analysis is done and compared to the reluctance network results. This section then moves on to investigating the electromagnetic performance of the design by examining the voltage and torque characteristics. Finally, the electromagnetic environment of the superconducting field winding is examined.

5.3.1 Magnetostatic Analysis

Firstly, a magnetostatic analysis is performed to validate the reluctance network results. In the model, the stator coils were omitted since only the flux density due to the field winding was to be investigated. The dimensions are equivalent to the ones stated in table 5.4. Figure 5.14 shows the solution mesh that was used. The mesh density was increased for the claw poles and stators. In addition, the mesh density in the air gaps was further refined to further improve the accuracy of the model.

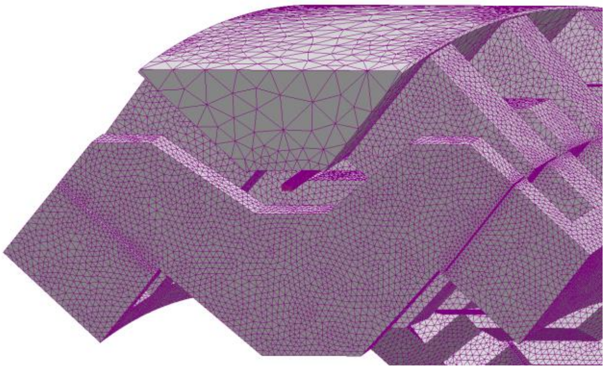

Figure 5.14. Solution mesh for the double claw pole machine design with an angled stator.

Figure 5.15 shows the flux density distribution in the machine for the original and new design. It can be seen that for both designs the highest flux density occurs in the elbows of the claw poles. Furthermore, it can be seen that the flux density in the field core for the new design is now higher than for the original design. This is due to the reduced core height to eliminate unnecessary active mass.

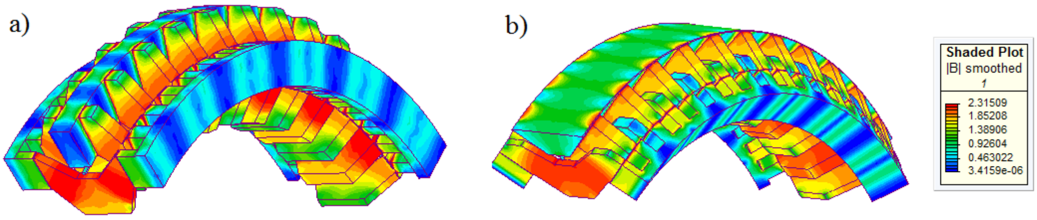

Figure 5.15. Flux density distribution for a) the original design and b) the new design [16].

Overall, there is a very good agreement between the flux density results produced by the reluctance network model and the numerical model. To further validate the results, the stator tooth flux is investigated in more detail in the next figure. Figure 5.16 highlights the stator tooth flux density for the original design and the new design for the case when the large claw pole overlaps with the stator teeth.

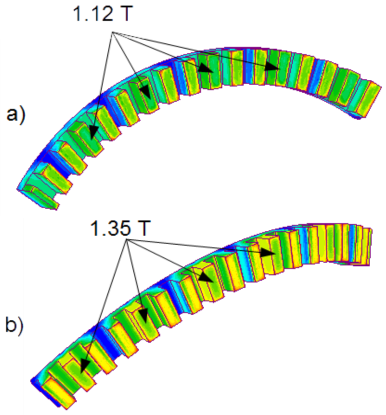

Figure 5.16. Air gap flux density for a) the original design and b) the new design [16].

It can be seen that the flux density for the new design was increased from approximately 1.12 T to 1.35 T. These results are in excellent agreement with the reluctance network model results shown in figure 5.13. In the figure the stator tooth flux is defined as B_{os1}, which is equivalent to 1.35 T at approximately 32 kA·turns. Since both the reluctance network model and the magnetostatic analysis produced very good results, this design offers an interesting novel approach for the design of the stator of axial flux machines. For this design in particular, the novel design approach allowed to redesign the component shapes to further improve the electromagnetic performance. To investigate the design in further detail the next sub-section will investigate the machine performance with the rotor in motion.

5.3.2 Transient Analysis with Motion

Since the magnetostatic analysis produced very good results, the model was further expanded by including a transient analysis with rotational motion of the claw poles. This model includes the stator coils to investigate the no load voltage waveform and cogging torque characteristics. Figure 5.17 shows a side perspective of the transient model of the machine. The model is setup with the same procedure as for the original design discussed in the previous chapter. The design still features the same angle of symmetry; hence the model consists of 1/22th of the full the design.

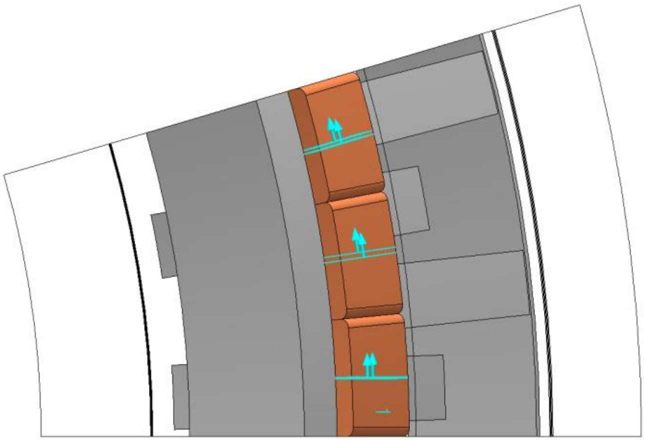

Figure 5.17. Side view of the transient model with motion in MagNet.

Similarly, in order to set up the rotational motion of the model, the rotating components were selected and a re-mesh region for the mesh was defined. Figure 5.18 shows the model with the defined motion components and re-mesh region.

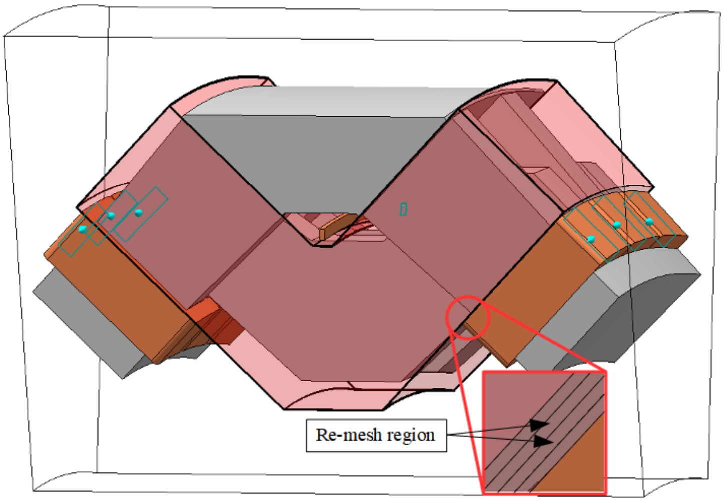

Figure 5.18. Model in MagNet with the motion domain shaded in red and the re-mesh region definition.

To save computational time, the mesh for the transient model was reduced similar to the original model described in chapter 4. Figure 5.19 shows the solution mesh for the first time step of the simulation. As can be seen when comparing the mesh to the previous model shown in figure 5.15, a rougher mesh is used. Except for the air gap region and re-mesh region, where a very fine mesh was maintained. The solution time and time steps are equivalent to the model in the previous chapter, *i.e.* 140 ms with 2 ms steps.

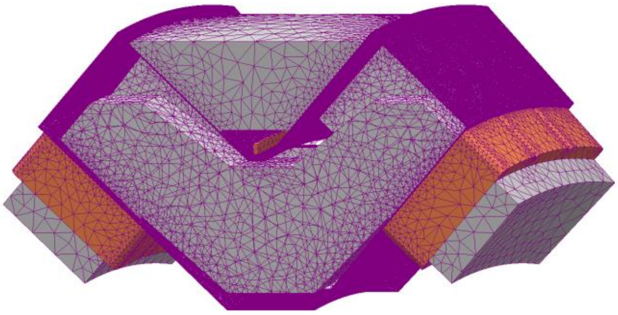

Figure 5.19. Solution mesh for the first time step of the transient analysis.

To verify the correctness of the model, the time step where the large claw poles are aligned with the stator teeth is investigated and compared to the magnetostatic model. Figure 5.20 shows the flux density distribution in the machine, it can be seen that it is identical to the flux density distribution of the magnetostatic model shown in figure 5.15.

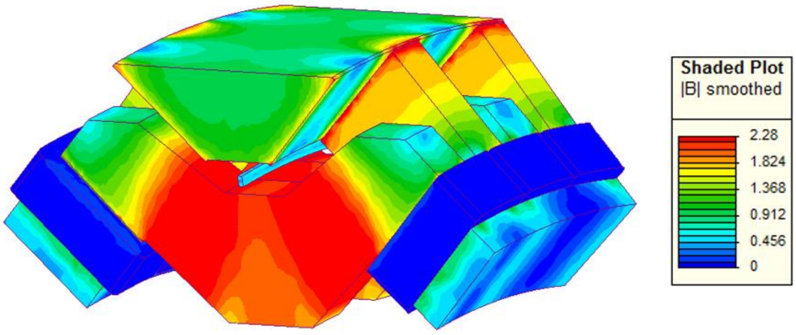

Figure 5.20. Flux density distribution when the large claw poles are aligned with the stator teeth [110].

With the correctness of the model verified, the voltage and torque characteristics of the design can be investigated. To examine the no-load conditions, the stator coils are open-circuited by connecting them to a very large load as was introduced in the previous chapter. The open-circuit voltage is shown in figure 5.21. It can be seen that a 3-phase voltage is being generated. The electrical frequency of the generator is 7.33 Hz at 10 rpm, which is equivalent to a time period of 136.4 ms. The peak induced coil voltage is approximately 280 V, giving an RMS voltage of 198 V. The coil voltage was increased from 176 V RMS to 198 V RMS due to the increased stator tooth flux. Similar to the original design, the induced voltages are not perfectly sinusoidal due to the iron-cored structure of the generator.

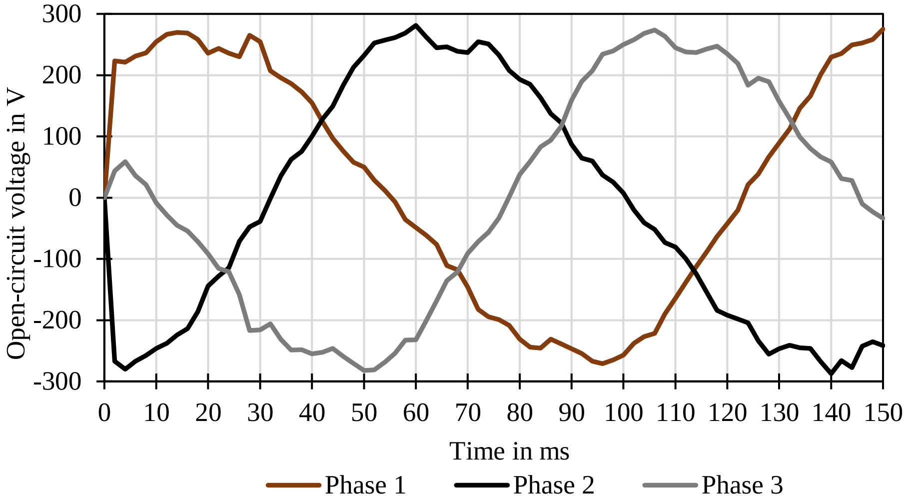

Figure 5.21. Open-circuit voltage for the double claw pole machine with an angled stator concept [110].

Figure 5.22 shows the cogging torque for the original design and the design with the angled stator. For the original design of the double claw pole machine the cogging torque was found to be 1 % of the rated torque. For the new design, the cogging torque was slightly increased, due to the increased air gap flux density as was shown in figure 5.16, to 1.15 % of the rated torque for 11.7 MW. While the cogging torque was found to be higher than for the original design, it should be noted that this design was not optimized with the use of an optimization algorithm, a reduction in cogging torque should be possible with a further optimization process such as by using a genetic algorithm. Additionally, the skewing of the stator teeth can be considered to further improve the torque characteristics.

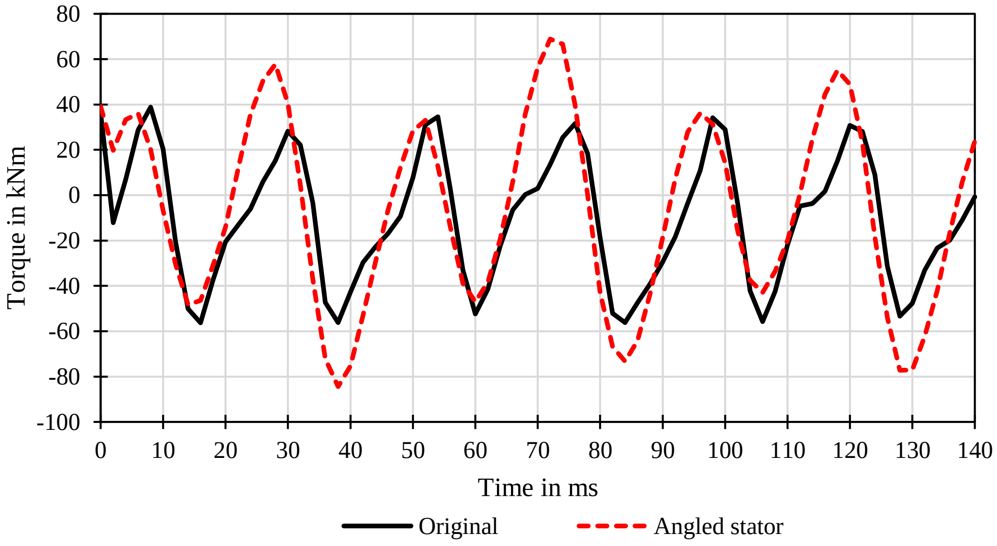

Figure 5.22. Cogging torque characteristics for the original design and the angled stator design.

When considering superconducting machines, another aspect is of high importance. As was discussed in the second chapter, the performance of superconducting tapes, namely the current carrying ability, is highly affected by the electromagnetic field the superconductor is located in. In particular, the perpendicular flux density to the surface of the tape reduces the critical current density significantly. To investigate the flux density that occurs on the field windings, several points along its circumference were investigated. Figure 5.23 shows a cross-section of the field winding and the examined points with the resultant perpendicular to the tape flux density distribution. The field winding consists of 3 coils placed next to each other. The coils on the side experience the highest flux density, with point 2 along the field winding having the peak flux density. The field current produces a rotating magnetic field, hence the flux density magnitudes at points 1, 2 and 3 also occur on the opposite side coil but into the opposite direction, *i.e.* with a negative value. The values along point 5 were multiplied by -1 to highlight that the magnitude on either side is equivalent. The lowest flux density magnitude occurs for the coil in the middle, this is due to a shielding effect of the two side coils. The purpose of this study was to find the peak flux density at the field winding to determine the critical current and hence the required number of turns for the coils. A less refined mesh was used to speed up the computational time, which explains the high variation in flux density along the winding circumference.

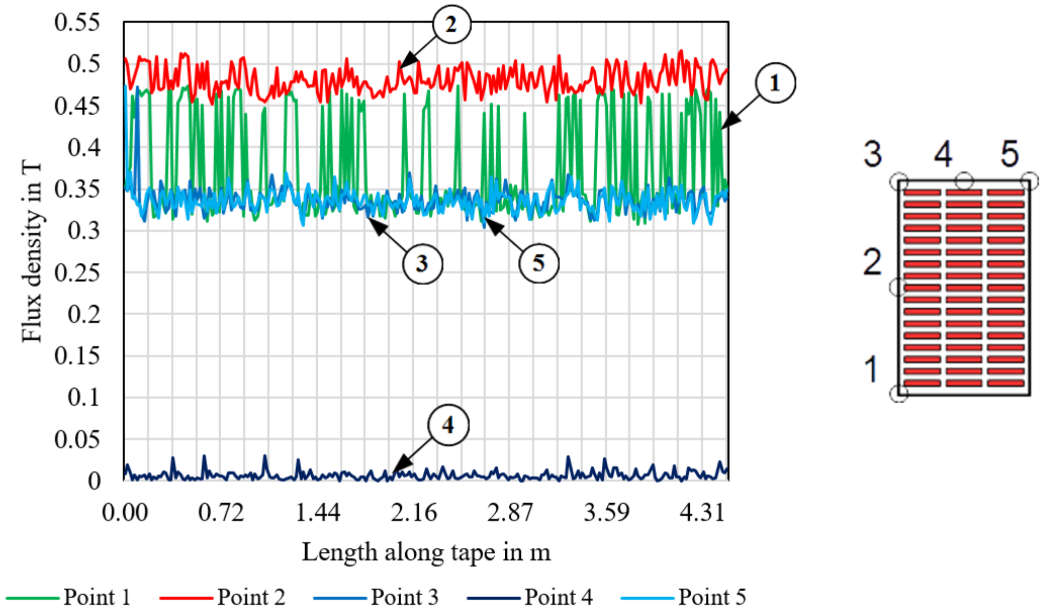

Figure 5.23. Flux density distribution along tape (left) and cross-section of field winding with investigated points highlighted [16].

A more detailed study on the field winding flux density is done with a finer mesh in the superconductor modelling chapter, to investigate the time varying flux density along the tape in order to calculate the resultant field winding loss. Taking into account the flux density distribution along the field winding, the required number of turns and superconductor length needed has to be re-adjusted. For 65 K, the field current was assumed to be equivalent to 329 A, but due to the high flux density that occurs on the edges of the side coils, the critical current was lowered to approximately 300 A. Applying a safety margin of 70 %, the new field current for the side coils is chosen to be 210 A. The current for the middle coil remains at 329 A. The new required number of turns for the side coils is 51 and for the middle coil 33 turns, giving a total of 135 turns. For the 135 turns, a length of 2.42 km is required for the single toroidal field winding design.

In [111], the possibility of rearranging the field winding is discussed to minimize the tape length required. The authors suggest taking advantage of the flux density distribution along the winding to redistribute the number of turns to the locations where the lowest flux density exists. This allows to reduce the overall number of turns by enabling more turns to carry a higher amount of current. Optimizing the layout of the field winding could lead to a decrease in the number of turns required.

Overall, it was shown that electromagnetic performance of the double claw pole generator was improved at the cost of a slightly increased active mass. With the improved electromagnetic performance of the generator, the next section will investigate the mechanical structure to maintain the air gap clearance and discuss the possible reduction in structural mass and the improved torque and power density of the new design.

5.3.3 Structural Mass of the Generator

As was mentioned in the beginning of the chapter, the structural mass required to maintain the air gap clearance in electrical machines can be very substantial. The structural mass required increases with the power and torque rating. For a 2 MW, 3 MW and 5 MW DD (direct drive) double stator, single rotor, iron-cored axial PMSG (permanent magnet synchronous generator), the structural mass makes up 23 %, 40 % and 65 % respectively [112]. Especially for iron-cored axial flux machines with a large diameter, a very stiff structure is required, this is due to the large normal component of the Maxwell stress in the air gap, which leads to the facing iron surfaces being attracted towards one another [112]. The forces in the air gap can essentially be broken down into 2 parts, the shear stress and the normal component. The shear stress is defined as the useful force in electrical machines as it creates the machine torque. The normal component is defined as the air gap closing force. For high air gap flux densities ($B >$

0.8 T), the normal stress is approximately ten times larger than the shear stress [112]. Figure 5.24 highlights the shear stress defined as σ and the normal stress defined as q, for the double claw pole machine.

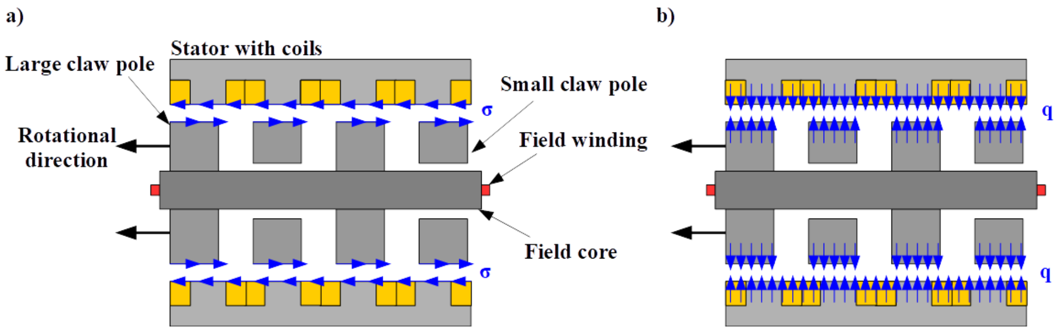

Figure 5.24. Top view for a section of the double claw pole machine for a) shear stress and b) normal stress.

To deal with these forces in electrical machines a multitude of variations of machine structures are used. Analytical methods exist, which allow to give reasonable indications of structure size and weight. However, in the design process of the support structure, finite element stress analysis packages are ultimately required [112]. Since the structural design of direct-drive generators was not the main aim of this thesis, an analytical model is used to approximate the structural mass required to maintain the air gap clearance. The analytical model, which was applied to the machine design to find the air gap deflection, is based on a transverse flux machine, developed by Zavvos *et al* [113]. While the topology of the machine in the analytical model is different to the double claw pole machine, the forces acting on the stator sides are very similar for both machines. Figure 5.25 shows the structure of the stator and the forces acting on the stator cores. It can be seen that the stator structure features five torque arms on either side and cylindrical shells that connect the two stator sides to each other. Through an optimization process done by Zavvos, the optimal number of torque arms was found to be five, for lowest structural mass. The analytical model calculates the radial bending of the cylinder shells and the axial deflection of the stator due to the normal stress q. The analytical model was compared to FEA simulation results and the difference between the two models for all investigated cases was less than 20 % with a mean error of 15.3 % [113]. A detailed description of the analytical model can be found in [113].

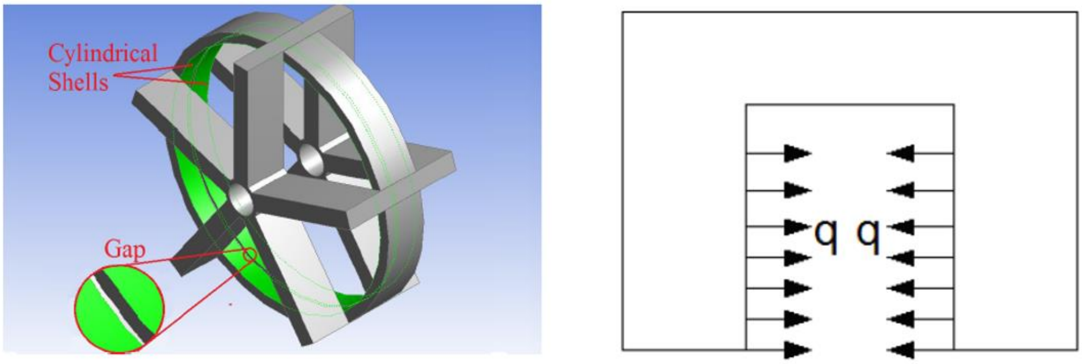

Figure 5.25. (Left) Stator structure and (right) forces acting on the stator core [113].

In [5] a detailed structural analysis of the original design of the double claw pole machine was done, the resultant mechanical structure is shown in figure 5.26. As can be seen the structure features the same cylindrical shells, connecting either side of the mechanical structure for further support. It should be noted that the investigated design in this case is for the radial configuration of the double claw pole machine, which can be thought of as the axial design rotated by 90˚ [5].

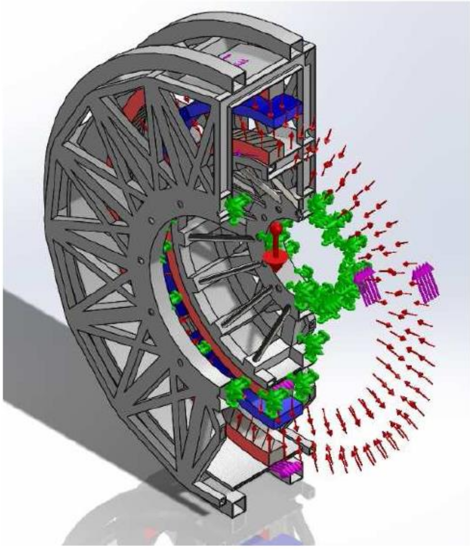

Figure 5.26. Mechanical structure for the original design of the double claw pole machine [5].

Using the analytical model developed by Zavvos, the structural mass required to maintain the air gap clearance for the double claw pole machine was calculated to be 42.8 t for the rotor and 82.6 t for the stator. In [5], the structural mass was calculated through structural FEA packages to be equal to 50 t for the rotor and 60 t for the stator. There is an excellent agreement for the structural mass of the claw poles since the orientation of the claw poles does not influence the forces acting between them. The calculated structural mass for the stator is higher for the analytical model since the air gap closing forces act in the axial direction, whereas for the radial configuration used in the FEA model, they act in the radial direction. Overall, it can be assumed that the analytical model can give a good estimation for the structural mass for the double claw pole machine. Figure 5.27 shows the structural mass increase with air gap flux density for the original design of the double claw pole machine.

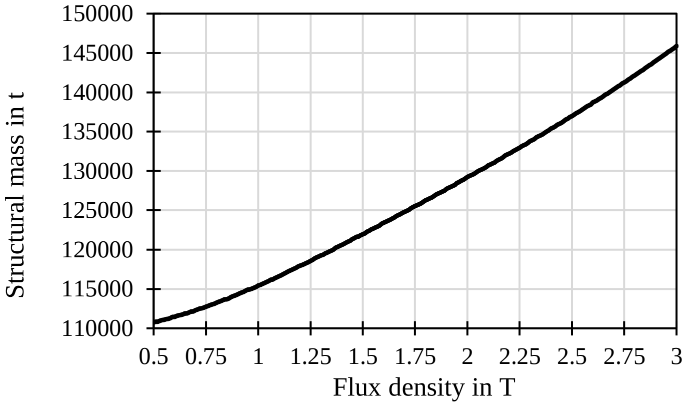

Figure 5.27. Structural mass required to maintain air gap clearance for the original double claw pole machine.

For the analytical model, 1.8 T was chosen as the air gap flux density to provide a safety margin, this results in a required structural mass of 126.3 t to maintain the air gap clearance. As was mentioned in the beginning of the chapter, the axial forces acting on the stator structure lead to the highest deflection in the air gap, creating the need for a very stiff mechanical structure, which in turn makes the structure extremely heavy. To investigate the structural mass for the newly suggested design, only the forces in the axial direction are considered for the calculation, to simplify the analytical model. The assumption is made that, since the overall structure has to be very stiff to begin with, it is assumed that the concentric forces created by the angle will not incur a significant increase in additional mass. Hence, for a stator angle of 45°, the axial component of the normal stress in the air gap is 70% of the total air gap closing force. The axial component of the normal stress is used as the input in the analytical model to calculate the structural mass. With the reduced axial closing force, the structural mass for the new design was estimated to be 115 t. It should be noted that with a detailed structural analysis the structural mass could be further reduced. In particular, the structural design of the rotor could be significantly simplified for the new design. In the original design, there was a momentum acting on the small claw poles since the forces did not act on the same plane, the air gap closing forces for the original design are shown in figure 5.28 to highlight this issue. As can be seen, the forces on the smaller claw poles are not acting on the same plane, resulting in a pivoting force acting them. For the new design this momentum was eliminated which simplifies the structural design of the rotor. The air gap closing forces acting on the angled stator machine components was highlighted in figure 5.6.

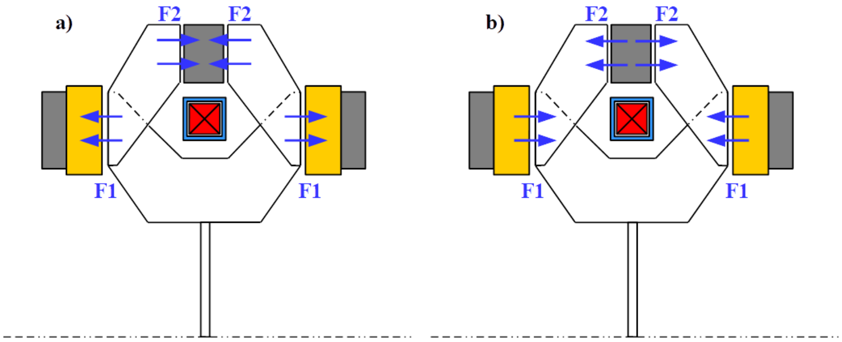

Figure 5.28. Air gap closing forces for the original design for a) rotor normal force and b) stator normal force.

Overall, it was shown that the structural mass was reduced through applying the novel stator design to the double claw pole machine. While only an analytical model was used to calculate the structural mass, it gives a good indication about the mass reduction that can be achieved. In the future a more detailed investigation of this design could be done to study the mechanical structure in further detail. Figure 5.29 shows the dimensions of the final design of the generator.

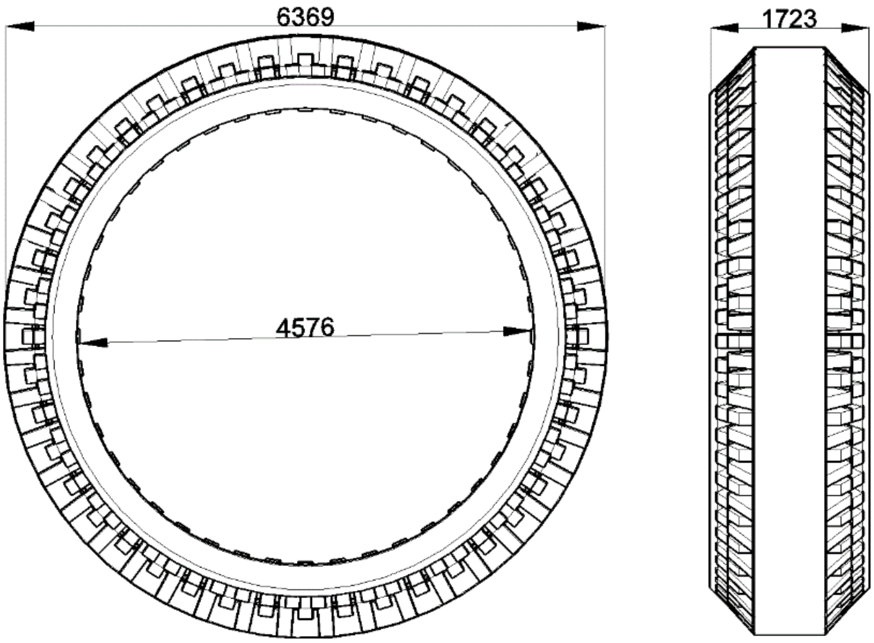

Figure 5.29. 11.7 MW design dimensions of the double claw pole generator with an angled stator.

Table 5.7 compares the main aspects of the original and new design. The structural mass was reduced from 126 tonnes down to 115 tonnes due to the deviated air gap closing forces. The power density of the generator was increased from 53.19 W/kg to 61.90 W/kg while maintaining the same HTS tape requirements.

Table 5.7. Design comparison [16].

Attribute	Components	Original	New
MMF	HTS field winding	Identical	
Mass	Active mass	62 tonnes	74 tonnes
	Structural mass	126 tonnes	115 tonnes
	Total Generator	188 tonnes	189 tonnes
Dimensions	Outer diameter	6.37 m	6.14 m
	Axial length	1.34 m	1.72 m
Performance	Power output	10 MW	11.7 MW
	Rotational speed	10 rpm	10 rpm
	Power density	53.19 W/kg	61.90 W/kg

5.4 Chapter Summary

In this chapter, a novel stator design to reduce the structural mass of axial flux machines was introduced. It was suggested to design the stator at an angle in order to deviate the forces in both the horizontal as well as concentric directions. By reducing the axial forces, the structural design is simplified. The design was applied to the double claw pole machine to reduce the structural mass. Further improvements could be made such as eliminating the pivoting force that existed previously on the small claw poles. Through these steps the structural mass was reduced from 126 tonnes to 115 tonnes. Additionally, to the new stator concept, new claw pole shapes were designed. The claw poles saturate later due to a bigger cross-sectional area and hence can carry more flux. A reluctance network was developed and FEA models were created in order to determine the electromagnetic performance of the machine. From the simulations the stator tooth flux was found to increase from 57 mWb to 71.4 mWb increasing the power output of the generator from 10 MW to 11.7 MW. One of the major disadvantages of the double claw pole machine was its weight. Through the new design the power density of the generator was further increased from 53.19 W/kg to 61.90 W/kg making it more competitive while still maintaining the same superconducting wire requirements and its modularity. It is believed that the double claw pole machine in conjunction with the new design and further work can lead to a cost-effective power generator for 10 MW and even higher rated wind turbines. Further work in regard to the structural design is required to investigate potential reduction in mass that can be achieved in further detail.

Chapter 6 Double Claw Pole Generator with Inner Stator

In this chapter, one short-coming of the original design is identified and investigated. The field core, which gives support and access to the superconducting field winding and its cryostat, increases the active mass significantly without offering additional benefits. In this chapter the field core is replaced by an additional inner stator, since a homopolar field can be seen to cross the field core. The inner stator increases the electric loading of the machine and hence further increases the shear stress in the air gap, which results in a higher power and torque density of the machine. The concept is investigated through a reluctance network model and verified with FEA simulations. The work discussed in this chapter was partially addressed in the following publication: ‘Kails K. *et al*, “Mass reduction of superconducting generators for large wind turbines”, *Journal of Engineering,* vol. 2019, no. 17, p. 3972 – 3975, 2019’.

6.1 Inner Stator Concept

The power density and hence torque density of electrical machines is determined by the shear stress in the air gap. The shear stress depends on the electrical loading and the magnetic loading of the machine [114]. For the double claw pole machine, which was introduced in detail in the previous chapter, the magnetic loading as compared to conventional machines was increased, by employing a superconducting field winding. The machine design features a conventional copper stator, hence leading to the design having a similar electrical loading as conventional machines. The electrical loading of rotating electrical machines can essentially be determined by the space, *i.e.* how much copper can be fitted into the stator, and the cooling system, *i.e.* how much heat can be removed to maintain safe operation [114]. When examining the structure of the double claw pole machine, it becomes clear that a novel design approach can be introduced to reduce the mass per kW of the machine. The field core in between the small claw poles is required in order to give mechanical support and access to the stationary superconducting field winding, it does not serve any other purpose. However, a homopolar field crosses the field core similar to the field in the homopolar machine described in [83]. The homopolar field can be seen from figure 6.1, which shows a side perspective of the original design of the double claw pole machine with the flux density distribution highlighted. It can be seen that the flux density in between the small claw poles is close to 0 T and where the small claw poles overlap it is approximately 1 T.

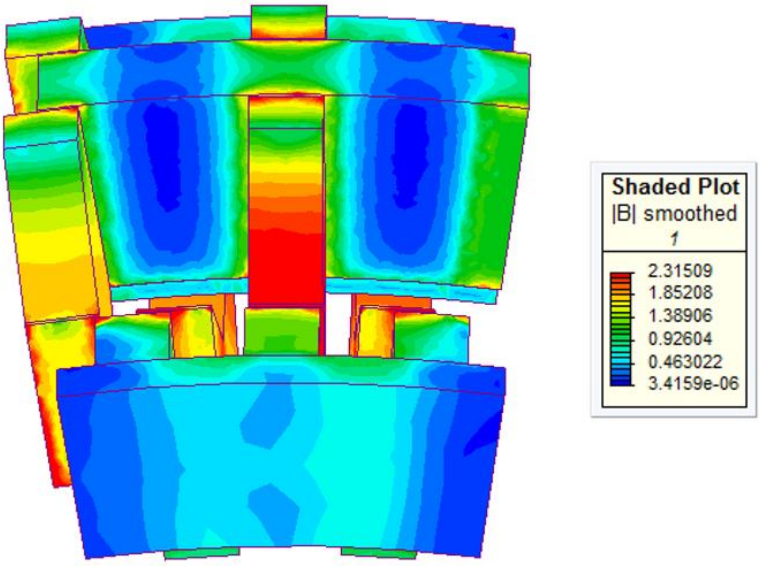

Figure 6.1. Side perspective of the double claw pole machine, with the flux density distribution highlighted.

Figure 6.2 shows a more detailed analysis of the flux density in the inner air gap. The figure shows the z-direction flux density distribution, *i.e.* out of the claw poles and into the field core over the mechanical angle of the machine.

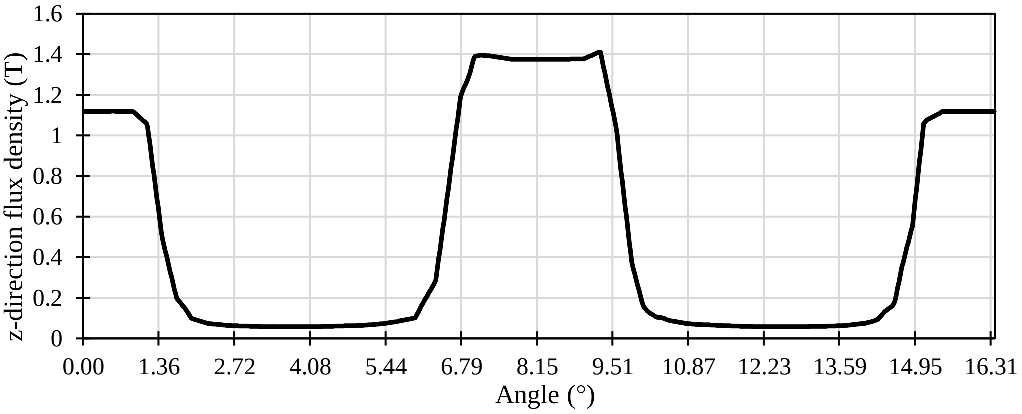

Figure 6.2. z-direction flux density distribution in-between the claw poles and field core.

It can be clearly seen that a homopolar field is present in the air gap. The minimum flux density does not reach 0 T due to the flux leakage that is present between claw poles and the fringing flux inside of the field core. The flux density peaks in the middle since the small claw pole is perfectly aligned with the adjacent outer stator teeth as shown in figure 6.1. The peak flux density for the neighbouring small claw poles is slightly lower since they only partially overlap with the outer stator teeth.

From investigating the flux density in the inner air gap, it becomes clear that additional power can be extracted from the generator by replacing the field core with copper coils and hence increasing the electric loading of the machine. Figure 6.3 shows the how the field core can be modified to accommodate the new inner stator coils.

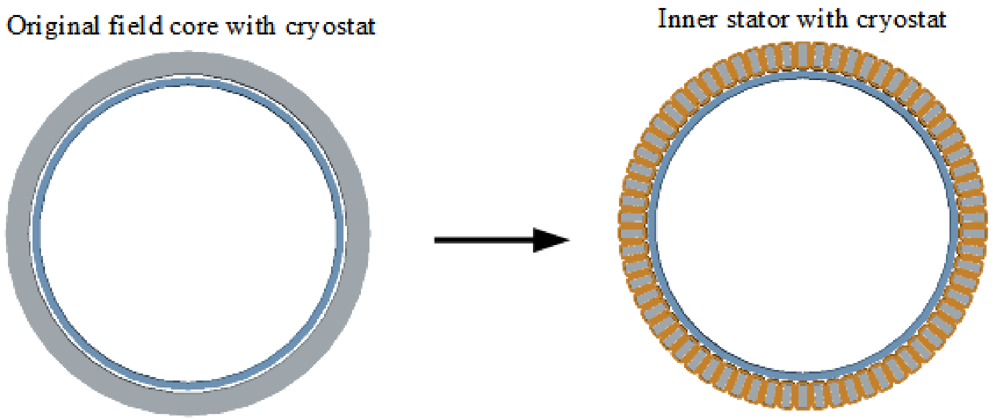

Figure 6.3. Concept for the new design [97].

The small claw poles overlap the inner stator coils on either side equally, leading to the forces acting on the coils in the axial direction being balanced and hence there is no net force acting in either direction. Similar to another design of an axial flux machine, the C-GEN concept, the stator coils can be immersed in epoxy resin, which are then held in place by an aluminium band for mechanical support [115]. Similar to the outer stators, the new inner stator also consists of 66 coils. The stator teeth of the three stators are aligned with each other. This ensures that the overlapping area between the small claw poles and the stator teeth is always equal for all four air gap, hence leading to the air gap closing forces acting on the claw poles also still being balanced for the outer and inner air gaps. To investigate the potential increase in power output, a reluctance network model is applied to the design in the next section.

6.2 Reluctance Network Modelling with the Inner Stator

The reluctance network, which was introduced in chapter 4, can easily be modified to study the stator tooth flux for the newly created inner stator. Maintaining the same dimensions for the machine and simply replacing the field core by the stator coils as shown in figure 6.3, the equivalent length through the inner stator coils is unchanged with respect to the original design and is given by equation 6.1.

$$l_{\mathrm{is}} = l_{\mathrm{claw2t}} - 2ag \tag{6.1}$$

where, as previously, l_{is} is the equivalent length through the inner stator, l_{claw2t} is the length of the straight part of the large claw pole as depicted in figure 4.12 and *ag* is the air gap.

The equivalent cross-sectional area for the inner stator teeth is given in equation 6.2.

$$A_{\mathrm{is}} = h_{\mathrm{core}} * T_{\mathrm{core}} * k_{\mathrm{fring_{is}}} \tag{6.2}$$

where A_{is} is the equivalent cross-sectional area of the inner stator, h_{core} is the height, T_{core} is the width of the claw pole as determined by the pole pitch and core to pole ratio. $k_{\mathrm{fring_{is}}}$ is a fringing constant, which accounts for the magnetic flux fringing outwards in the air gap. Maintaining the other machine dimensions the same then allows to make a meaningful comparison between the original design and the new concept with the additional inner stator.

From the reluctance network model, the peak flux for the outer stator teeth was hence found to be 57.8 mWb and for the inner stator teeth 81.3 mWb. When comparing the stator tooth flux for the outer stator for the original design of the double claw pole machine and for this design, it can be seen that it is unchanged. This is because the reluctance path throughout the machine components is essentially the same as for the original design, due to the stators being aligned. Figure 6.4 shows the flux variation for the outer and inner stators with the assumption made that the flux variation is perfectly sinusoidal.

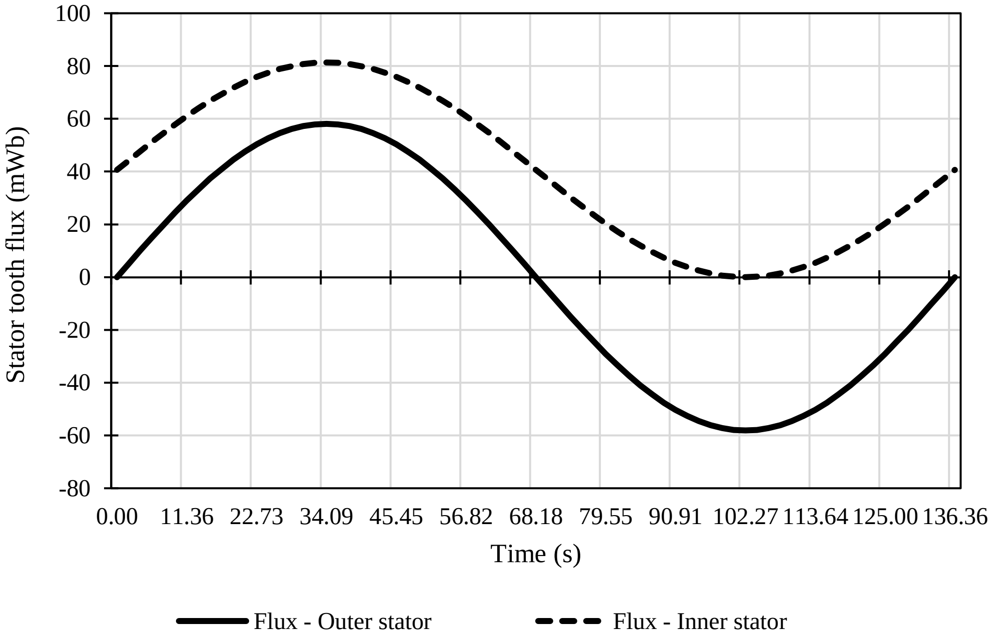

Figure 6.4. Stator tooth flux variation for the outer and inner stator.

It can be seen that the flux variation for the inner stator is homopolar since it only varies between 0 and ϕ_{max}. In the reluctance network, the leakage flux between the inner stator teeth is ignored, hence the minimum flux is assumed to be equal to 0 T.

In [97] it was assumed that the frequency for the inner stator would be half of the frequency of the outer stator, since the inner stator only sees half the number of poles of the outer stators.

Hence, assuming half the frequency the induced voltage in the inner stator was calculated to be 58 V and hence the power output was calculated to be 1.16 MW for the inner stator alone. However, through further investigation it was determined that both stators, the inner as well as the outer stator, operate at the same frequency. This can be explained as follows, the outer stator essentially sees a flux variation from $\phi_{\max}$ to $\phi_{\min}$, whereas the inner stator sees a flux variation from $\phi_{\max}$ to 0, but both flux variations occur at the same time, hence giving the same frequency. Further details on the flux linkages in the machine and the induced voltages can be found in section 6.2, which covers the transient analysis of the generator using 3D FEA analysis.

To calculate the potential power output from the reluctance network, the flux variation from figure 6.4 is used. To determine the power output and efficiency two different approaches exist. The first approach is to assume the same current density for the inner stator as for the outer stators, which results in the highest potential power density that can be achieved for the given machine dimensions. Another approach would be to maintain the power output at 10 MW but make use of the additional copper volume available through the inner stator to reduce the rated current per stator, leading to reduced copper losses and hence an increased efficiency. Starting with the first approach, the current density in all stators is set to be equivalent to each other. Taking the same number of turns for the inner stator coils as for the outer stator coils, *i.e.* 96 turns, since they both have roughly the same dimensions, the induced voltages for the outer stator coils and inner stator coils can be calculated to be 180.9 V and 128 V respectively. To find the rated power output, the rated current needs to be defined, which is dependent on the stator coil dimensions. Figure 6.5 depicts a drawing of a stator coil.

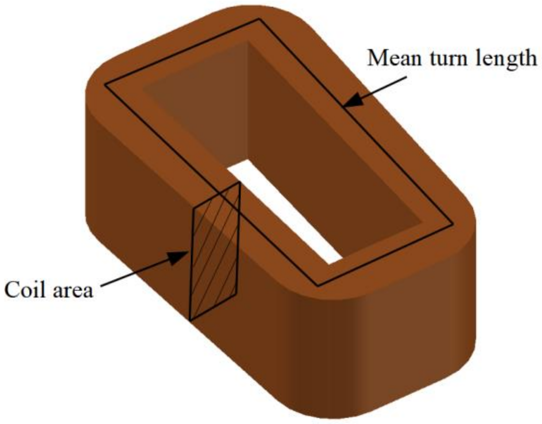

Figure 6.5. Stator coil geometry.

The available coil area is defined by the stator design through the stator tooth length and the coil pitch with the tooth to coil ratio. For the outer stator coils the rated RMS current can be calculated to be equivalent to 438 A for 96 turns, assuming a current density of $5 \cdot 10^6$ A/m^2 and a fill factor of 75 %. The inner stator coils are slightly bigger, due to the bigger mean radius as compared to the outer stator, and hence offer an increased coil area. Assuming the same current density, the rated RMS current for the inner stator is hence higher than for the outer stator coils and can be calculated to be equivalent to 554 A.

The power output for the inner stator can hence be calculated to be equivalent to 4 MW, using the same procedure as described in chapter 4. This is assuming that the rotational speed is kept at 10 rpm to allow for a meaningful comparison between the new design and the original concept. Hence, an additional 4 MW of output power can be achieved while maintaining essentially the same active mass, raising the total output power to 14 MW. The field winding is identical to the original design hence the required length of superconducting tape is unchanged.

One disadvantage of increasing the electrical loading is that it also leads to an increase in copper losses, hence reducing the overall efficiency. The copper losses are calculated according to the dimensions of the copper wire and the number of turns for each coil. Due to the very low operating frequency, the copper losses can essentially be determined solely from the DC coil resistance of the coils and the rated current squared. To find the efficiency with the addition of the new stator, the coil resistance of the inner stator coils has to be calculated. From the coil dimensions, the outer stator coil resistance can be calculated to be 0.02 Ω and the inner stator coil resistance is 0.0167 Ω. Table 6.1 summarizes the coil design for both stators.

Table 6.1. Coil design

Parameter	Outer stator coil	Inner stator coil
Turns	96	96
Wire length (m)	104	118
Wire diameter (mm)	10.6	11.9
Coil resistance (ohm)	0.02	0.0167
Rated current (A)	438	554

For the original 10 MW design, the copper losses are equivalent to 510 kW. With the addition of the inner stator the total copper losses are increased to 873 kW. When only considering the copper loss in the machine the efficiency can be calculated to be 95.13 % for the original design and 94.19 % with the inner stator. The big drop in efficiency is due to the homopolar field of the inner stator. The induced voltage for the inner stator is significantly lower than for the outer stators, hence the produced power output is much lower as well. The additional copper losses in combination with the relatively low additional power output results in an overall drop in efficiency.

Hence for this design approach, a significant increase in power density was achieved but at the cost of the reduced efficiency. However, efficiency is a critical parameter when designing electrical machines. While a lighter generator can reduce the levelized cost of energy of the wind turbine due to the potentially reduced capital cost and ease of installation, a lower efficiency could completely negate this benefit. An efficiency of 95 % for example, is a common target efficiency for large direct-drive wind turbine generators [5]. To achieve a higher efficiency another design approach can be applied. As has been discussed, the generator design was optimized for the lowest total mass. To maintain this benefit, the generator dimensions are fixed. The fixed generator dimensions in turn lead to a fixed volume for the stator coils and hence a fixed copper loss when considering a fixed fill factor. This can be explained through figure 6.5, which shows one stator coil. The depicted coil area is fixed due to the stator design. Taking the extreme example of a single turn coil, we can calculate the rated current by simply assuming a fixed current density and hence calculate the copper losses through the coil geometry using equation 6.3.

$$P_{\mathrm{copper1}} = I^2 * \frac{\rho * l_{\mathrm{mean}} * N}{A_{\mathrm{wire1}}} = I^2 * \frac{\rho * l_{\mathrm{mean}}}{A_{\mathrm{wire1}}} \qquad (6.3)$$

where ρ is the copper resistivity, l_{mean} is the mean turn length, N is the number of turns and A_{wire} is the cross-sectional area of the copper wire.

To show that the copper loss is fixed, we can increase the number of turns to $N = 2$ and substitute the variables in equation 6.4.

$$P_{\mathrm{copper2}} = \left(\frac{I}{2}\right)^2 * \frac{\rho * l_{\mathrm{mean}} * N}{\frac{A_{\mathrm{wire1}}}{2}} = \frac{I^2}{4} * \frac{\rho * l_{\mathrm{mean}} * 4}{A_{\mathrm{wire1}}} = P_{\mathrm{copper1}} \qquad (6.4)$$

From this example it becomes clear that for the original design, the only way to improve the efficiency is to change the machine dimensions, which could result in an increased total mass.

However, with the addition of the new inner stator, the available copper volume in the machine was increased. The first approach to take advantage of this was to assume the same current density for the inner stator and for the outer stators, hence achieving a significantly increased power density, while ending up with a lower efficiency. Another approach that can be taken, is to reduce the overall current density in the stators while still maintaining the target 10 MW power output. The reduced current per coil, reduces the overall copper losses and hence a higher efficiency can be achieved. Through testing of different combinations of stator currents, the lowest possible copper loss while still maintaining a power output of 10 MW was found to be 392 kW with a rated outer stator current of 340 A and an inner stator current of 270 A. Hence, when only considering the copper losses the efficiency was increased to 96.2 % at 10 MW. To calculate the overall efficiency, the copper losses, iron losses, cooling power for the superconducting winding and air blowers for the armature were considered. The iron losses are calculated using the Vacoflux50 datasheet and using the operating frequency in the machine, which is 7.33 Hz at 10 rpm. The required cooling power was adapted from [50] with some minor changes. The required power input for the air blowers to cool down the stator coils was estimated to be 40 kW for 510 kW of heat produced in the stators. Since the copper loss were reduced by approximately 23 %, the required input power for the air blowers was reduced down to 31 kW. The overall efficiency is however still dominated by the copper losses in the stators. With all losses considered the overall efficiency for this design approach can be calculated to be 95.63 %. Taking 95 % as the target efficiency, the electric loading can be further increased at the cost of the efficiency to increase the power density of the design. A power output of 11.57 MW can be achieved at an efficiency of 95 % with a rated RMS current of 400 A for the outer stators and 310 A for the inner stator. A comparison between the original design and the designs with an additional stator are shown in table 6.2.

Table 6.2. Design comparison

Parameter	Original	Highest power density	Highest efficiency	95% Target efficiency
Total mass	184.2 tonnes	236.5 tonnes	184.2 tonnes	201.2 tonnes
Outer diameter	6.37 m	6.37 m	6.37 m	6.37 m
Power output	10 MW	14 MW	10 MW	11.5 MW
Rotational speed	10 rpm	10 rpm	10 rpm	10 rpm
Rated torque	9.54 MNm	13.27 MNm	9.54 MNm	10.98 MNm
Power density	54.29 W/kg	59.11 W/kg	54.29 W/kg	57.5 W/kg
Efficiency	94.50%	93.75%	95.63%	95%

For the design iterations with a higher power output, the structural mass was recalculated to account for the new rated torque using the analytical model that was described in chapter 4. At 13.98 MW and 10 RPM, the rated torque can be calculated to be 13.27 MNm. Applying the new torque with the analytical model the new structural mass for the generator was calculated to be 61.37 tonnes for the rotor and 119.15 tonnes for the stators, giving a total structural mass of 180.5 tonnes. For 11.5 MW, the rated torque can be calculated to be 10.98 MNm, giving a structural mass of 49.3 tonnes for the rotor and 95.9 tonnes for the stators. The active mass was recalculated to be 56 tonnes, which is slightly lower than for the original design. This is due to the copper partially replacing the solid iron of the field core.

While a significant increase in power density was achieved in terms of mass, it should be noted that the outer diameter and axial length of the machine are identical to the original design. Hence, a substantial increase in power density was achieved when considering the machine volume as well. As was discussed in the first chapter, the size of the machine, in addition to the weight, plays a crucial role in the transportation and installation of the generator. In addition to the increased power density, the modularity of the machine was even further increased. For the original design, the two outer stators can operate independently from each other, if there is a fault the generator can continue operating under partial load. Since the inner stator generates power at a lower voltage magnitude, a separate power converter is required. The additional power converter raises the capital cost of the design, however, it also introduces further redundancy in the system. With the second power converter, similar to the outer stators, the inner stator can also operate independently in case of a fault, hence further increasing the modularity of the design. Assuming that the two converters operate at the same efficiency as a single converter, there would be no impact on the overall system efficiency.

Since according to the reluctance network, an increase in power density and efficiency can be achieved, it is necessary to verify the results using finite element analysis and important to investigate the machine performance in further detail such as the voltage and torque characteristics. The design meeting the 95 % target efficiency was taken for this purpose and the FEA results will be addressed in the next section.

6.3 FEA Analysis with the Inner Stator

6.3.1 Magnetostatic Analysis with the Inner Stator

In order to verify the results, a 3D magnetostatic analysis using the simulation software *MagNet*, was performed. Figure 6.6 shows the magnetic flux density distribution when the large claw poles are aligned with the outer stator teeth. Figure 6.7 shows the flux density distribution when the small claw poles are aligned with the inner and outer stator teeth. It can be seen that the overall flux density distribution throughout the machine is very similar to the flux density distribution in the original design of the double claw pole machine as shown in figures 4.21 and 4.26. This is a good indication that the original flux path throughout the new machine was maintained as compared to the original design, as was the assumption when setting up the reluctance network model.

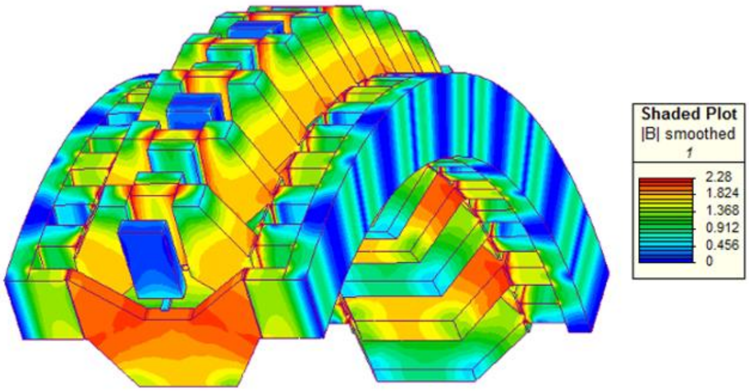

Figure 6.6. Flux density distribution for large claw poles aligned with outer stator teeth [97].

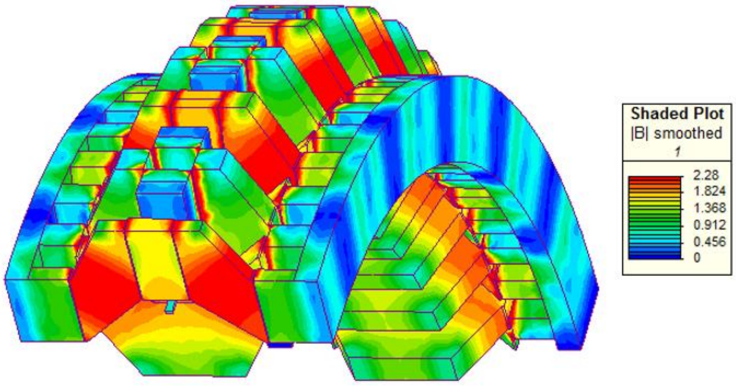

Figure 6.7. Flux density distribution for small claw poles aligned with stator teeth [97].

Similar to the previous chapters, to analyse the machine performance in further detail, a transient analysis is setup in the next subsection.

6.3.2 Transient Analysis with the Inner Stator

With the flux densities in the machine verified using the reluctance network model and the magnetostatic FEA, it is important to further analyse the machine performance when the rotor is in motion to study the induced voltages and torque characteristics. The model is setup in the same fashion as introduced in chapter 4 and 5. The *MagNet* model is shown in figure 6.8, with the motion components shaded in red. Figure 6.9 shows the solution mesh for the first time step of the transient analysis. The same mesh is used as for the original model, with a very dense mesh being applied to the mesh layers in the air gap. The final solution mesh features 850,751 elements with approximately half of the elements located in the re-mesh region. The time step for the simulation is set to 2 ms and the end time is set to 140 ms.

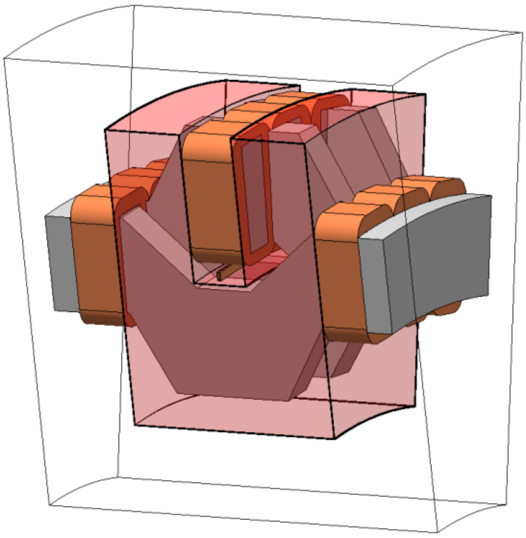

Figure 6.8. MagNet model of the double claw pole machine with an inner stator.

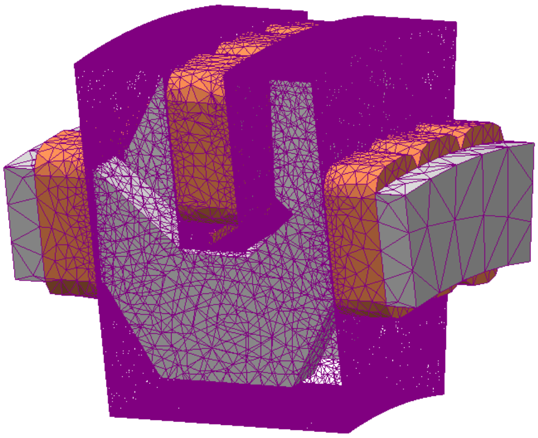

Figure 6.9. Solution mesh for the first time step.

With the transient model setup, the machine performance can be further studied. The stator tooth flux is of particular importance. Figure 6.10 shows the z-direction flux density distribution for the outer stator and the inner stator coils, midway through the coil, when the small claw pole is aligned with the middle tooth. It can be seen that the flux direction is in the positive as well as negative direction for the outer stator, while the flux for the inner stator is only into one direction.

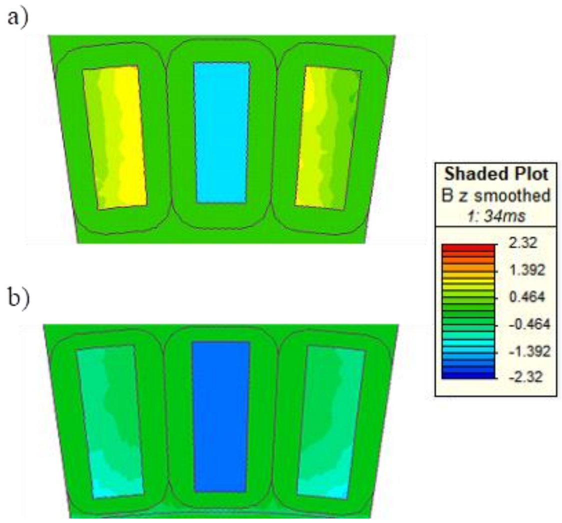

Figure 6.10. z-direction stator tooth flux density when the small claw pole is aligned with the middle tooth for a) the outer stator and b) for the inner stator.

Figure 6.11 shows the stator tooth flux variation for one of the outer stator coils and one of the adjacent inner stator coils as the rotor is in motion.

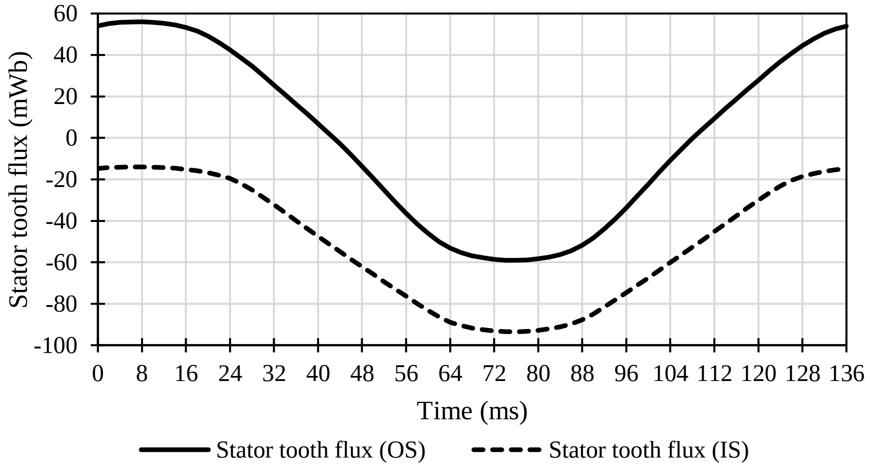

Figure 6.11. Stator tooth flux variation for adjacent outer and inner stator coils as the rotor is in motion.

From the figure, it can be seen that the peak stator tooth flux for the outer stator, depicted as OS, is approximately -59 mWb, which is well in agreement with the calculated flux shown in section 6.2. For the inner stator tooth flux, depicted as IS, it can be seen that the peak flux is approximately 93.5 mWb. This is higher than the calculated flux in section 6.2, which was given as 81.3 mWb. However, the minimum flux for the inner stator tooth is approximately -14 mWb as opposed to 0 mWb, which was assumed in the reluctance network model. Taking the difference between the maximum and minimum flux for the inner stator results in a flux variation of 79.5 mWb, which again is well in agreement with the results of the reluctance network model.

To investigate the open-circuit voltage, similar to the previous models, a very large resistive load is connected to the stator coils. The resultant open-circuit voltage is shown in figure 6.12. For each phase, two waveforms are shown. One waveform corresponds to the induced voltage of the outer stator depicted as ‘OS’ and the other waveform to the induced voltage of the inner stator depicted as ‘IS’. It can be seen that the induced voltage for the outer stator has remained the same for the original design, the RMS voltage of a single coil was calculated to be equal to 182 V, which also agrees with the result from the reluctance network shown in section 6.2. The RMS voltage of the inner stator coils can be calculated to be 125 V, which again is well in agreement with the reluctance network results.

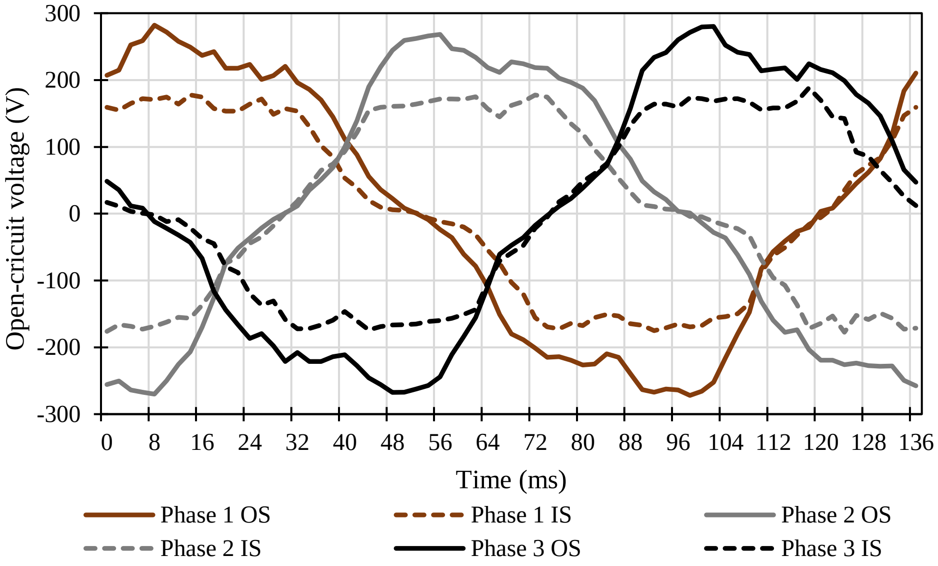

Figure 6.12. Open-circuit voltage for the outer (OS) and inner stator (IS) coils.

In addition to the voltage characteristics it is important to investigate the torque characteristics. As was mentioned in the previous chapter, the cogging torque leads to vibrations, which should be minimized to maintain smooth operation of the generator. The cogging torque comparison between the original design and the design with an inner stator is shown in figure 6.13.

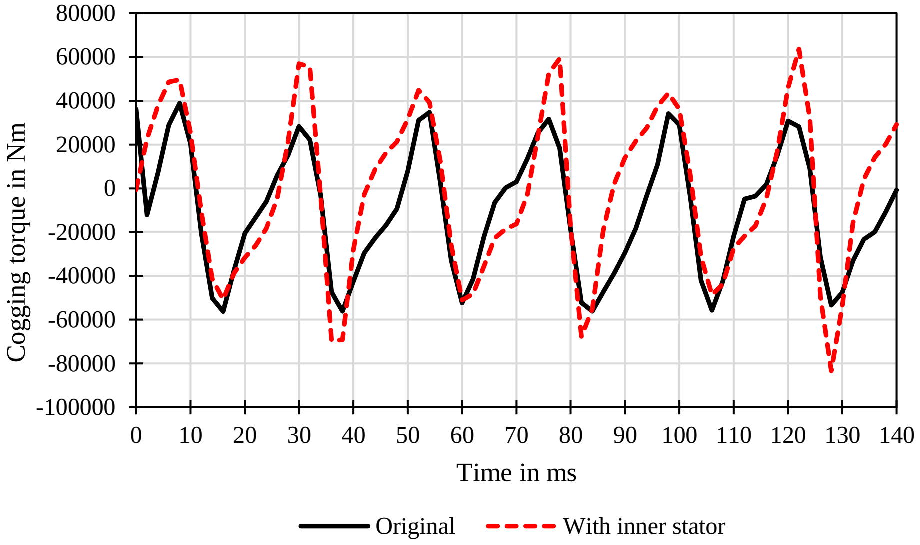

Figure 6.13. Cogging torque comparison between the original design and the design with an inner stator.

From the figure it can be seen that the cogging torque was increased as compared to the original design. For the original design, interaction between the claw poles and the field core did not lead to any cogging torque, since the field core was a continuous solid piece of iron. The only source of cogging torque came from the interaction of the claw poles with the outer stator teeth. With the introduction of the inner stator, which has additional iron stator teeth, a further increase in cogging torque can be observed since the small claw poles now interact with the inner stator teeth as the rotor is in motion. The peak-to-peak cogging for the original design is approximately 96 kNm, which is equivalent to 1 % of the rated torque. With the inner stator the peak-to-peak cogging torque was increased to 146 kNm, which is 1.33 % of the rated torque at 11.5 MW. As was shown, the additional inner stator had only minor effects on the torque characteristics of the generator. It should be highlighted again that the combination of slots and poles by nature leads to a higher cogging torque and torque ripple, both attributes can be further improved by choosing a more appropriate combination of pole and slot numbers.

6.3.3 Flux Density Distribution of the Superconducting Field Winding

One further concern in regard to the inner stator is the effect of the inner stator coils on the superconducting field winding. As has been discussed, the performance of the superconducting tape strongly depends on the magnetic field environment the superconductor is located in. The outer stator coils are located at the distance from the superconducting field winding, hence their effect on the field winding is relatively low. The inner stator coils on the other hand are located just above the field winding. The hypothesis is made that the magnetic flux produced by the inner stator coils will mainly be parallel in relation to the superconducting tape in the field winding, hence the effect is expected to be relatively low. To confirm the effect of the inner stator coils on the magnetic field distribution on the tape, the inner stator coils are supplied with the rated current and the flux density distribution along the tape is recorded. To increase the accuracy of the field distribution on the field winding, the mesh density for the winding was increased significantly.

Figure 6.14 shows the perpendicular and parallel to the tape flux density distributions for the case when the rated current is applied to the inner stator coils and for the case when no current is applied. The high variance that is present in the field distributions is due to the relatively small size of the field winding in comparison to the generator dimensions, requiring a very fine mesh size. However, the main point of interest in regard to the flux density distribution is the change in magnitude.

Firstly, considering the perpendicular flux density distribution, it can be seen that the current in the inner stator coils has a negligible effect on the perpendicular flux density, both flux density distributions are nearly identical.

When considering the parallel flux density, it can be seen it was approximately doubled when supplying the stator coils with a current. However, as was mentioned before, a parallel field penetrating the superconducting tapes has little effect on the critical current density and induced losses, hence this effect is negligible as well. It can be concluded that the inner stator coils have little to no effect on the field winding since the produced magnetic field mainly penetrates the superconducting tapes in a parallel fashion. More detailed discussions on the loss mechanisms of HTS tapes in the machine environment are discussed in the superconductor modelling chapter later on.

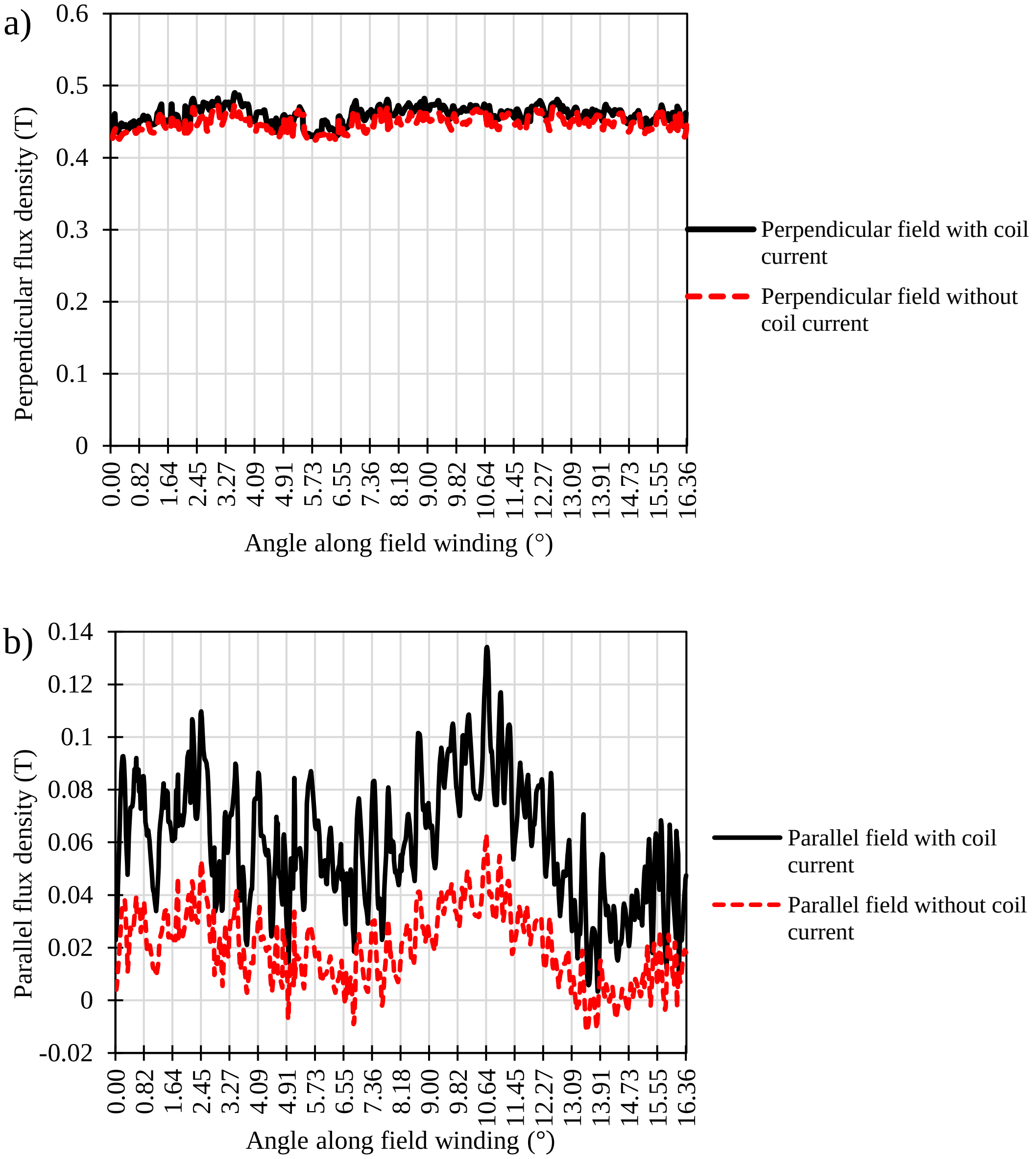

Figure 6.14. a) Perpendicular flux density distribution and b) parallel flux density distribution along the field winding with and without a current in the inner stator coils.

6.4 Chapter Summary

In this chapter, one short-coming of the original design of the double claw pole machine was identified and addressed. The field core in the double claw pome machine is required for mechanical support and to provide access to the superconducting field winding, it however serves no other purpose and adds a significant amount of active mass. When investigating the magnetic field crossing the field core as the rotor is in motion, it can be seen that a homopolar field exists, which crosses the field core through the small claw poles from one side to the other. By replacing the field core with an inner stator with copper coils, the electric loading of the machine can be further increased, which leads to an increased shear stress in the air gaps and hence additional torque and power. The machine with the inner stator was modelled using a reluctance network and through finite element analysis, with both methods producing results which are well in agreement with each other. The additional power that can be extracted from the inner stator was found to be equivalent to 4 MW, assuming the same rotational speed as for the original design. Hence, a 14 MW machine was created, using approximately the same active mass and covering the same machine volume. However, this method significantly reduced the machine efficiency due to increased copper losses. A second approach was applied, which reduced the electric loading of the machine, which in turn reduced the copper losses. With a target efficiency of 95 %, a power output of 11.5 MW can be achieved, while again maintaining the generator mass and volume. With the additional stator, the resultant cogging torque increased from 1 % of the rated torque to 1.33 % of the rated torque. Another important aspect for machines employing superconducting field windings is their magnetic environment. However, the effect of the new stator coils, which are located in close vicinity of the field winding, was found to be negligible. Overall, the inner stator increased the power output, efficiency and modularity of the double claw pole machine.

Chapter 7 Modular and Stackable Power Generators

This chapter investigates the opportunity of increasing the power density of machines by stacking smaller generator modules, instead of designing one big machine. How to identify an effective way of stacking modules is however necessary and requires new knowledge for future guidance. In this chapter, both possibilities of stacking modules concentrically and axially are explored and compared. For this purpose, a 5 MW module of the double claw pole machine was designed and the stacking methods were explored. Results show that stacking modules concentrically leads to a significant increase in power density, both in terms of mass and volume, while also further increasing the modularity. The chapter continues to verify the reluctance network model results through FEA simulations and gives further details on the voltage and torque characteristics of the generator in combination with the different stacking methods. Finally, the chapter addresses the mechanical issues that arise in particular when considering the concentric stacking method and gives guidance on how to alleviate some of the structural design issues. The work introduced in this chapter has been published in *IET Renewable Power Generation* as “Modular and Stackable Power Generators for Efficient Renewable Power Generation”, vol. 13, no. 15, 2019.”

7.1 Machine Module Stacking

One option when trying to avoid a very large and heavy machine is to design smaller machines and have them share the same shaft. Axial flux generators in particular offer the possibility of stacking modules axially, several examples of multistage axial flux machines have been discussed in literature [116, 117] . Stacking the modules results in a NS-type machine, the flux for this machine travels mainly axially. Through this option, the possibility arises to reduce the active mass of the machine and maintain a smaller diameter generator at the cost of an increased axial length. However, another stacking option is available. Modules can be stacked concentrically on top of each other, which allows to have a large diameter machine with modular components. The two stacking options are applied to the double claw pole generator design to find the best stacking method for axial flux machines to further increase their power density.

7.2 Design of the 5 MW Module

To investigate the stacking methods a design of a generator module is required. The size of the module and the power rating are of particular importance. Since the aim is to study direct-drive generators in the 10 MW range, it was decided to design a 5 MW module. Hence, stacking two modules either axially or concentrically is expected to lead to the desired power output. For the sizing of the module, it is assumed that the rotational speed is 10 rpm, to account for the rated rotational speed of a 10 MW direct-drive generator. However, a 5 MW direct-drive wind turbine generator generally operates at a rotational speed of 12.1 rpm. Hence, to compare the 5 MW module design, it is investigated at a rotational speed of 12.1 rpm as well as 10 rpm. The double claw pole reluctance network that was discussed in the second chapter was used to the design the 5 MW module. The machine components were scaled down and adjusted, while maintaining the same aspect ratio, until the desired power output of 5 MW was reached. The dimensions of the claw poles were chosen such as that iron saturation is avoided at rated MMF while minimizing active mass. Through this approach it is expected that the active mass stays relatively close to the optimal mass that was calculated for the full 10 MW design, since the relative size of the components with respect to each other was maintained. Figure 7.1 shows the stator tooth flux variation with MMF, as can be seen the machine starts saturating at approximately 23 kA·turns. The optimal MMF for a power output of 5 MW was found to be 22.4 kA·turns. With a transport current of 100 A, the field winding results in 3 separately wound superconducting coils, connected in series and placed next to each other. Each coil consists of 75 turns, giving a total number of turns of 225 for the superconducting field winding. It should be noted that the same transport current is chosen here as in [15] to make the comparison between the two designs simpler. However, as was shown in chapter 5, the transport current at 65 K can actually be chosen to be higher.

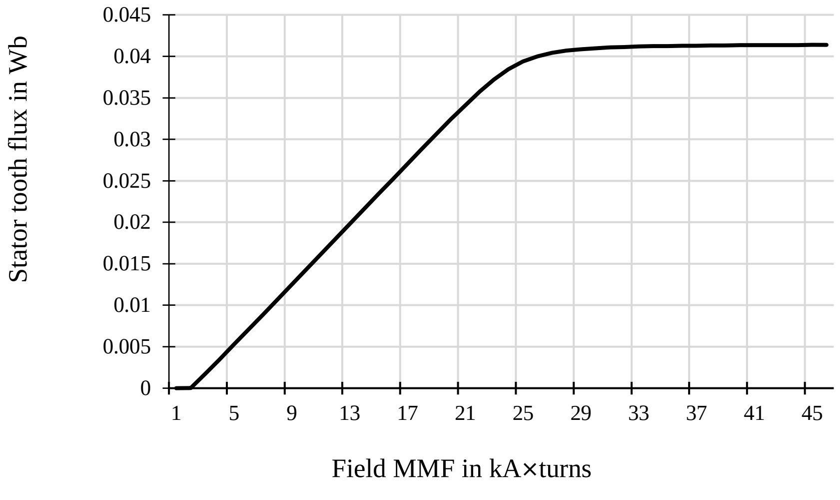

Figure 7.1. Stator tooth flux variation with MMF for the 5 MW module [118].

Table 7.1 shows a comparison between the 5 MW module at 10 rpm and 12.1 rpm and the full 10 MW double claw pole generator described in the previous chapters.

Table 7.1. Comparison between 5MW module and full 10MW design.

Power	**5 MW**	**6.1 MW**	**10 MW**
Efficiency	93.75%	94.73%	94.50%
RPM	10 rpm	12.1 rpm	10 rpm
Number of poles	88	88	88
Coils per stator	66	88	66
Active mass	36 t	36 t	58 t
Inner radius	1.91 m	1.91 m	2.29 m
Outer radius	2.66 m	2.66 m	3.19 m
Axial length	1.15 m	1.15 m	1.38 m
MMF	22400 A	22400 A	32400 A
HTS tape length at 65K	7.56 km	7.56 km	13.5 km

As was mentioned in the previous paragraphs, the 5 MW design was investigated at two rotational speeds, 12.1 rpm and 10 rpm. The active mass was calculated to be approximately 36 tonnes. The efficiency was calculated to be equal to 93.75 % at 10 rpm using the same methods described in the previous chapters.

When comparing the efficiency to the original design, it can be seen that the efficiency of the 5 MW module is lower. The lower efficiency can be explained through the rotational speed, the induced coil voltage is lower due to the lower rpm, which in combination with the smaller machine diameter and lower output power results in a lower efficiency. When setting the rotational speed to 12.1 rpm, which is the rated speed for 5 MW direct-drive wind turbine generators, the power output increases to 6 MW and the efficiency to 94.73 %.

In [70] the main design requirements of a 5 MW superconducting wind turbine generator are discussed. To be economically as well as technically viable the target weight of the active mass of the generator was suggested to be below 40 tons to be competitive against permanent magnet technology. The maximum allowed HTS tape was calculated to be 228 km of AMSC 348C that has a critical current of 95 A at 77 K, or 206 km of Superpower tape 4050 with a critical current of 125 A at 77 K, to be economically feasible. These requirements were determined for a generator rotational speed of 12.1 rpm.

As can be seen the 5 MW module satisfies both requirements, for 12.1 rpm and even for 10 rpm. At 65 K the generator design requires 7.56 km of superconducting tape at an operating current of 100 A. This can be further reduced by lowering the operating temperature to 20 K which reduces the tape requirements to 1.89 km with an operating current of 400 A. The required cooling power for both temperatures can be estimated to be approximately 125 W

[15]. Since it is more challenging to remove heat at a lower temperature, the required input power to the cooling system is significantly larger for 20 K as compared to 65 K [119]. In addition, operating at low temperatures such as 20 K or even 10 K requires a large number of cooling heads making these designs impractical [120, 121]. To maintain a higher efficiency and a simplified cooling system, 65 K was chosen as the operating temperature, similar to the 10 MW design, at the cost of increased superconducting tape requirements. Since the generator design fit the target design criteria it was deemed suitable to investigate the different stacking methods and hence determine the best options for stacking machine modules.

To further validate the 5 MW design of the double claw pole machine module, a 3D finite element analysis was performed using the simulation software *MagNet*. The simulations were performed at 10 rpm. The total flux density distribution in the machine is shown in figure 7.2. The air gap flux density distribution is shown in figure 7.3, the figure shows the distribution for cases, when the large claw pole (lower claw pole) and when the small claw pole (upper claw pole) are aligned with the middle stator tooth.

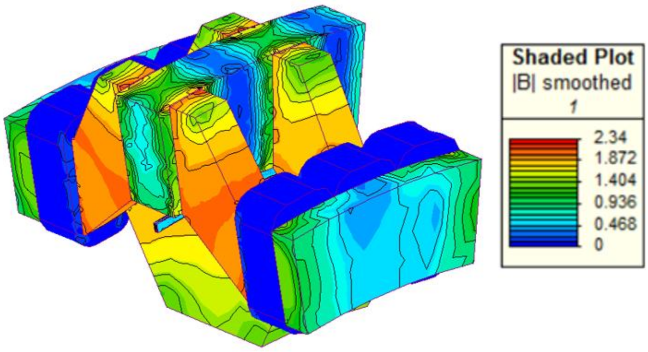

Figure 7.2. Total flux density distribution for the 5 MW module [118].

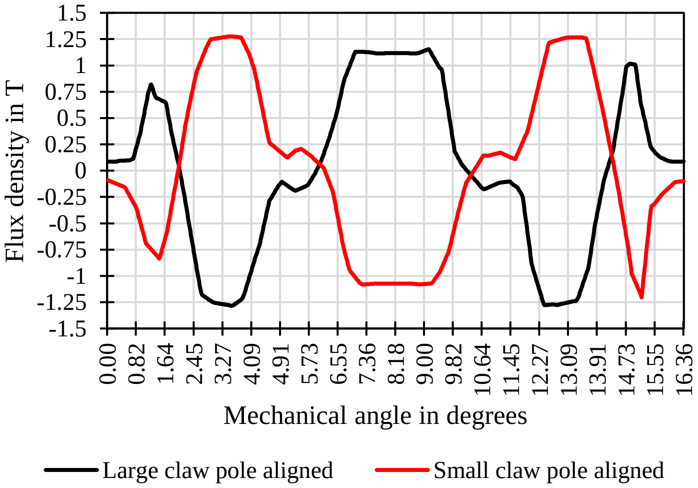

Figure 7.3. Air gap flux density distribution for large and small claw poles aligned with middle stator tooth [118].

The stator tooth flux was calculated to be equal to 0.038 Wb, which is in good agreement with the reluctance network model, which found the flux to be equal to 0.037 Wb. Figure 7.4 highlights the open-circuit voltage of the 5 MW generator design for 6 stator coils. An in-phase voltage is induced in the coils that are oriented opposite of each other, hence there are always 2 curves overlapping each other. The period of the voltage is 136.36 ms, which gives an electrical frequency of 7.33 Hz at 10 rpm. There are 66 coils in total per stator, each coil has 96 turns. Each phase consists of two parallel branches of 11 coils in series. Hence, the stator design and winding configuration is similar to the original design of the double claw pole machine.

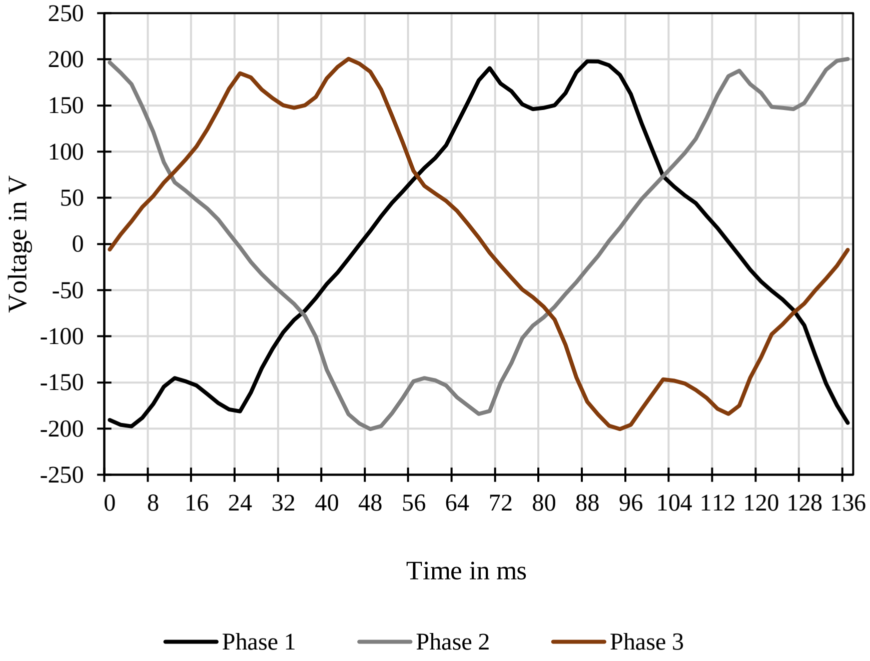

Figure 7.4. Open-circuit voltage for the 5 MW module [118].

7.2.1 Steppingstone Towards 10 MW

The scaled generator design introduced in this chapter can serve another purpose in addition to investigating the possibility of stacking machine modules. In [17], a geared generator, a conventional PMDD generator and a HTSDD generator are compared for 3.1 MW, 6 MW and 10 MW wind turbines. It was concluded that HTS generators offer significant advantages over conventional generators. However, due to the potentially high capital costs in combination with a lot of uncertainty, it was determined that the incurred risk was too high to enter the market with a 10 MW HTS generator design. In turn, the authors suggest deploying a 3 to 6 MW HTSDD generator, and to use the experience gained from this to move on towards higher power rated HTS machines. In fact, a similar approach was taken in the EcoSwing project, which was introduced in the first chapter, where a 3.6 MW HTSDD generator was commissioned. One of the major benefits in designing a lower rated HTS generator, is that it can be compared to existing conventional machines, to actually gauge the benefit of applying superconductors. In [17], the power density of a 6 MW PMDD generator is given as approximately 29 kg kW^{-1}. The 6 MW generator proposed here has an active mass of 36 tonnes. The structural mass was calculated to be 90 tonnes using the analytical method described in chapter 5. Hence, with a total weight of 126 tonnes, the power density was calculated to be 20.65 kg kW^{-1}. In [10], the diameter of a 6 MW PMDD generator was given as 7 m, the proposed design here is only 5.32 m. Hence, the proposed 6 MW HTSDD generator is significantly lighter and smaller. Additionally, the efficiency for the PMDD generator at rated load was given as only 90 % [17]. Whereas, for the proposed design here, the efficiency at rated load is 94.88 %. Hence, even in the 6 MW range, the double claw pole generator offers a significant competitive advantage over conventional machines. To calculate the required superconductor length, the transport current used in chapter 5 for the 65 K case is used, giving a length of approximately 1.35 km, potentially making the proposed generator design very cost-effective as well.

Hence, by first conducting tests with the proposed 6 MW design, the incurred risk due to uncertainty is reduced. Valuable experience could be gained during the operation of the machine, which could in turn directly translate into the research into the stacking of machine modules to further increase the power density and modularity.

The next section will discuss the different stacking options and how they can be applied in conjunction with the double claw pole generator design.

7.3 Stacking Methods

7.3.1 Axial Stacking

Since the double claw pole machine is an axial flux machine, the possibility of stacking modules axially is available. Through this option, the possibility arises to reduce the active mass of the machine by partially eliminating the stator back iron that is shared between connecting modules. This is highlighted in Figure 7.5. The figure shows a cross-section of the generator design, looking at one pole pair.

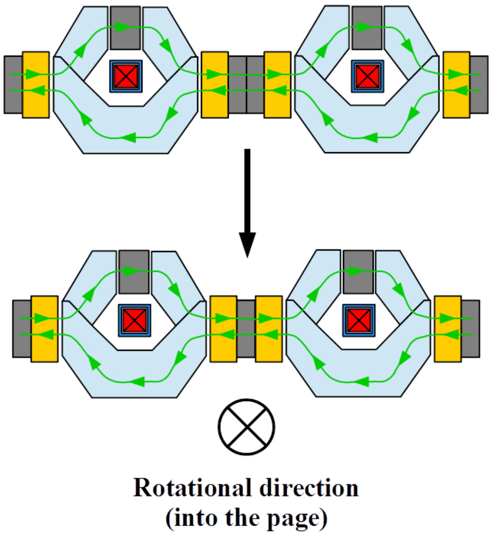

Figure 7.5. Axial stacking of the double claw pole machines, and structural optimization [118].

As shown, two modules share the same stator back iron in the middle. Hence the active mass is reduced. Figure 7.6 shows the full machine for stacking two modules axially [118].

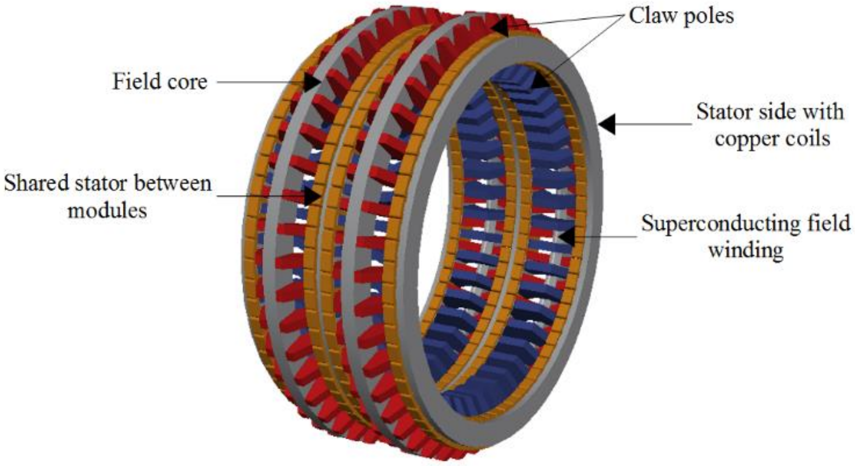

Figure 7.6. Full machine for stacking two modules axially [118].

Figure 7.7 shows the reluctance network for 2 modules for the axial stacking method. It is a combination of the original reluctance network with a shared stator in between the two modules. It can be seen that, from the middle stator point of view, each side is simply mirrored over. To simplify the reluctance network, the original reluctance network can be used while simply multiplying variables by the number of modules.

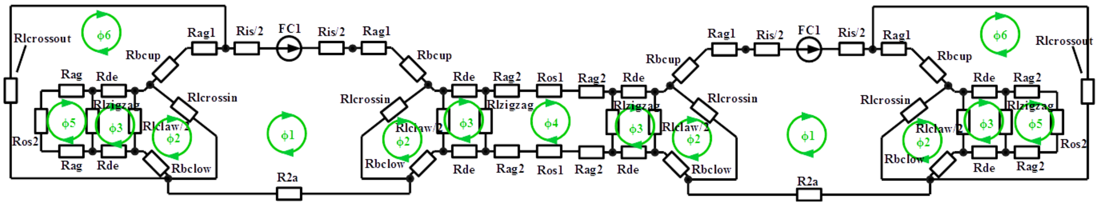

Figure 7.7. Reluctance network for axial stacking [118].

7.3.2 Concentric Stacking

Due to the structure of the double claw pole machine another stacking option is available. Modules can be attached concentrically on top of each other, as shown in figure 7.8.

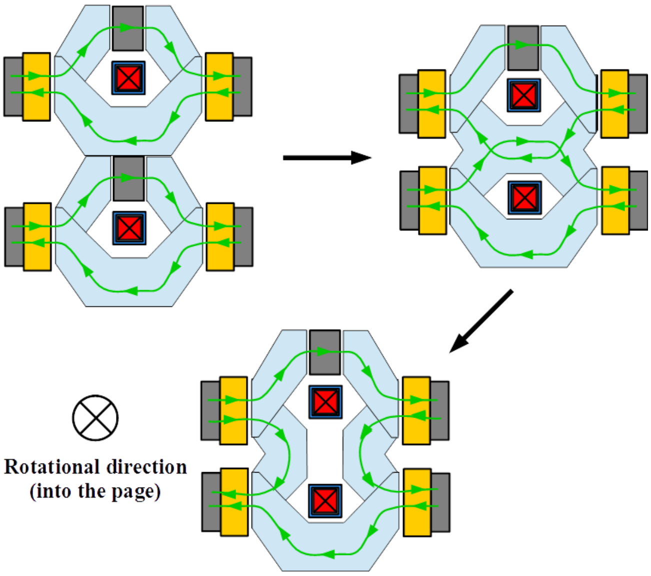

Figure 7.8. Concentric stacking of the double claw pole machines, and structural optimization [118].

As can be seen, the middle section of the larger claw poles was eliminated since the magnetic fields produced by the field windings cancel each other in between them. A mass reduction of the claw poles is achieved. In addition, the air gap diameter of the machine increases with each additional module hence the power density is expected to increase significantly for this stacking method.

For concentric stacking, essentially several air gap diameters exist, where the innermost air gap diameter would be D_1 and the outermost air gap diameter would be D_2 for a two-module machine design.

Another advantage that the concentric stacking option offers over the axial method is that it reduces the number of air gaps. For the original concept shown in figure 7.2, the magnetic flux crosses 6 air gaps before the loop is closed. Stacking the modules axially essentially doubles the original machine hence two axially stacked modules have 12 air gaps. Stacking the modules concentrically however eliminates one of the field cores. For 2 modules, the number of air gaps is reduced down to 10. Hence, the machine can be designed for a lower magnetomotive force (MMF), which reduces the amount of HTS tape that is required.

The flux path for this configuration can be described as follows. The magnetic flux travels from the first stator (bottom left) upwards over the middle claw pole into the upper stator. It then travels radially through the stator back iron. The flux then flows axially over the upper small claw poles and the field core to the right-hand side stator. It is then again guided downwards over the middle claw pole. The magnetic flux loop is closed over the bottom large claw pole. The middle claw pole was designed taking advantage of the existing geometry of the original machine. Two small claw poles were taken and overlapped with each other, creating the new middle claw pole, this is shown in figure 7.9.

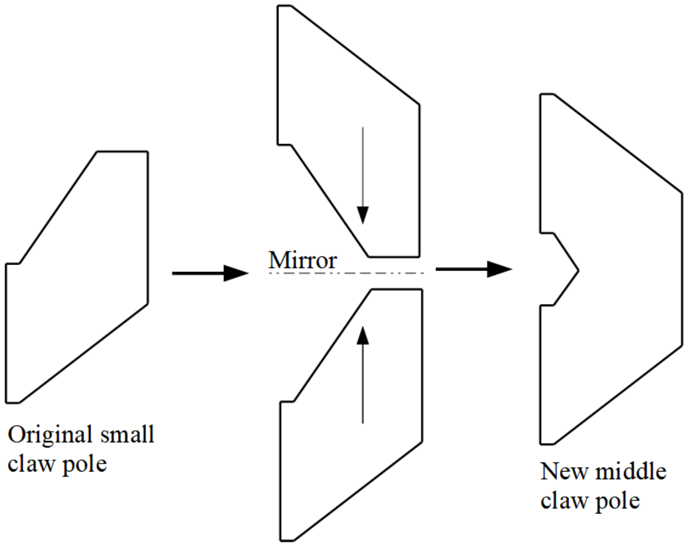

Figure 7.9. Design of the middle claw pole connecting the lower and upper stators.

Figure 7.10 shows the full machine for this stacking option.

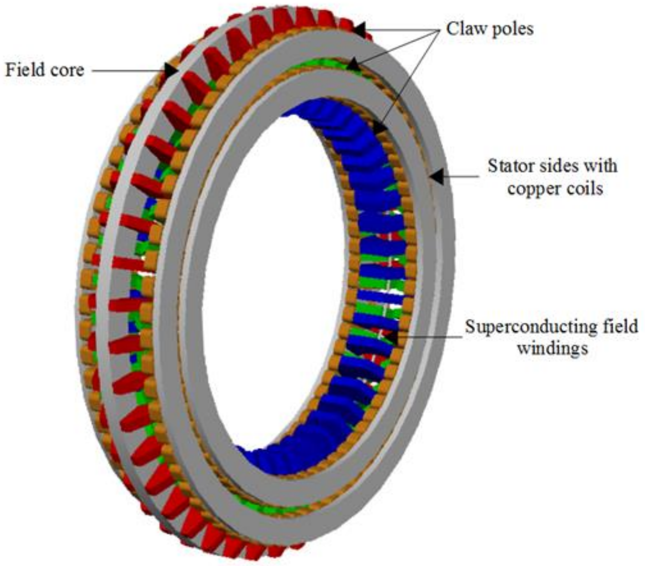

Figure 7.10. Full machine for stacking two modules concentrically [118].

Figure 7.11 shows the reluctance network for 2 modules for the concentric stacking method. The original reluctance network was adjusted to include the middle claw poles, which connect the lower and upper stators.

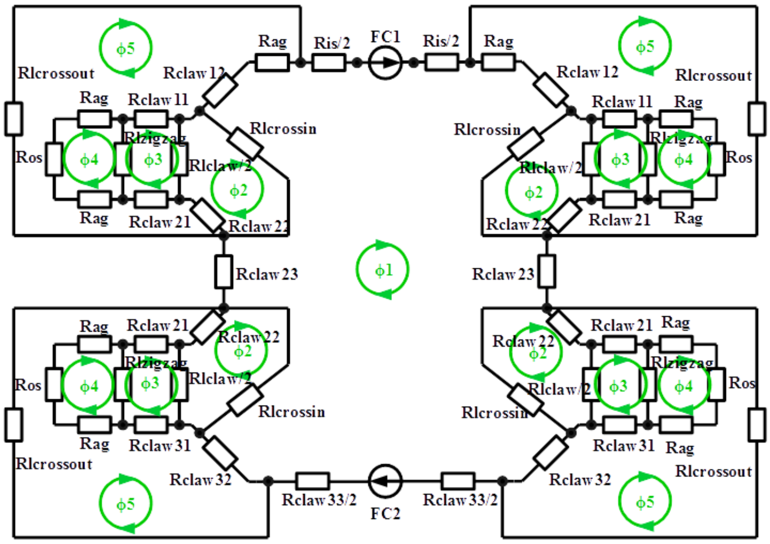

Figure 7.11. Reluctance network used for concentric stacking [118].

To model several stacks, the reluctance network is simplified back to the original network that was introduced in the beginning of the chapter, essentially taking advantage of the modularity of the machine. Each stack can essentially be thought off as a separate machine. To calculate the performance of a concentrically stacked machine, the power output and efficiency of each module is taken separately. This is done using the different air gap diameters of the different stators. The total power output is then simply the summation of the individual module power outputs.

7.4 Stacking Methods Comparison

Similar to the previous chapter, there are two approaches to design the machine when stacking modules. The first approach maximizes the power output by maximizing the electric loading of the machine, which can in turn negatively impact the overall efficiency due to the increased copper losses. The second approach would be to make use of the additional stator space to reduce the current in each stator, while maintaining the required electric loading to achieve a 10 MW power output.

Since the main purpose of this study was to investigate the potential power density increase from stacking modules, mainly the first approach is investigated, giving the highest power output for the two stacking methods, at the cost of a potentially lower efficiency.

It will be shown that the efficiency can be increased with the number of modules, hence giving one possibility to increase the efficiency while also having a significantly increased power density. However, due to the importance of generator efficiency, a case study for stacking two modules is also shown, to find the highest efficiency achievable while maintaining a power output of 10 MW with a target efficiency of 95 %.

Figure 7.12 shows the performance comparison between the two stacking methods, aiming for the highest power density. It should be noted that for this case only the active mass was considered. Due to the relatively complicated generator structure, it is difficult to estimate the structural mass required to maintain the air gap clearance using analytical methods. However, it can be assumed that stacking a high number of modules concentrically becomes unrealistic due to the increased air gap diameter with each module resulting in the need for a very stiff mechanical structural. The structural issues of the concentric stacking method are discussed in further detail in section 7.7 of this chapter.

For the axial stacking method, the power density in terms of mass and volume does not change significantly since only a small proportion of the active mass is eliminated. Stacking the modules concentrically however increases the power density considerably in both aspects since the air gap diameter increases with every new module. Especially in terms of power to volume ratio, a very high power density machine can be assembled by stacking modules on top of each other. For instance, stacking two modules concentrically creates a 12.1 MW machine with an outer diameter of 6.2 m, which is smaller than the 10 MW machine, which has an outer diameter of 6.38 m. This makes the concentric modules an attractive option for high power density applications and applications where space is an issue.

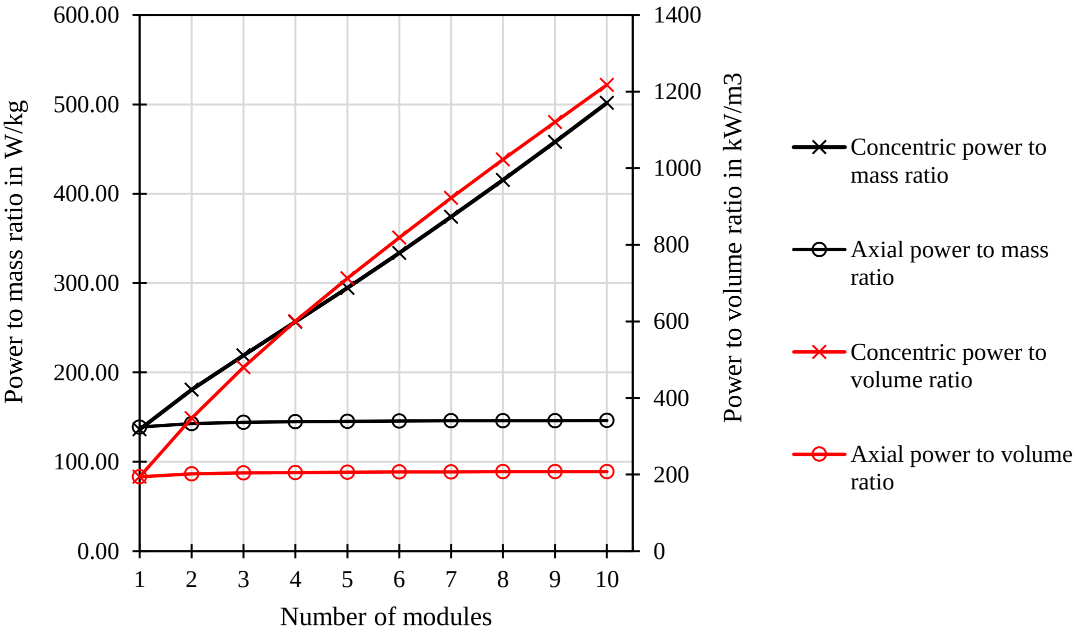

Figure 7.12. Power density comparison between concentric and axial stacking [118].

Another important aspect for generators is their efficiency. The main losses such as the cooling power for the superconductor cryostat, iron losses and copper losses were considered. Due to the low frequency the iron losses are relatively low, and the overall efficiency is dominated by the copper losses in the stators. For the superconducting field winding the following losses were considered, suspension straps fixing the winding within the cryostat, radiation, current leads, cold-head sleeve and eddy currents. Figure 7.13 shows the efficiency variation for the two stacking options.

For the axial stacking method, the efficiency is constant since each module produces power at the set efficiency of 93.75 %. When stacking the modules concentrically the efficiency changes since the power output for each additional module varies, giving a higher efficiency with a higher number of modules. The efficiency is calculated separately for each module and by using the contribution towards the total power output from each module the overall efficiency of the whole generator is calculated. An additional benefit of the concentric stacking method is the cryostat design. The axial option requires two separate cryostats, which increases the total surface area of the cryostat and hence leads to increased heat loss. The vertical stacking option allows to use one cryostat for both superconducting field windings with a lower total surface area.

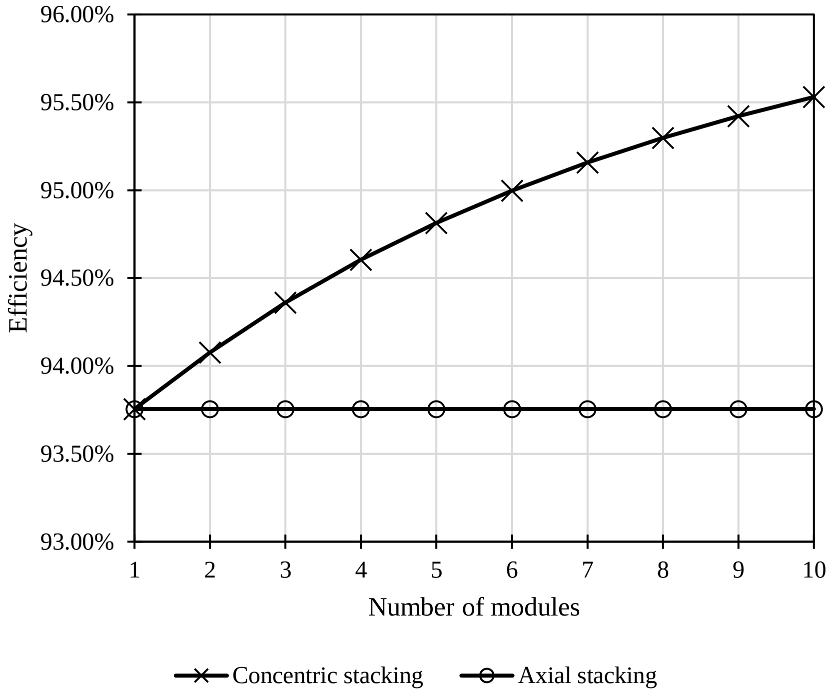

Figure 7.13. Efficiency for stacking modules axially and concentrically [118].

Table 7.2. Comparison between stacking methods and original 10 MW design [118].

Design	Concentric stack	Axial stack	Original
Power	12.1 MW	10 MW	10 MW
Power density (mass)	183.3 W/kg	142.9 W/kg	172.4 W/kg
Power density (volume)	348.5 kW/m^3	203.5 kW/m^3	226.7 kW/m^3
Efficiency	94.03%	93.76%	94.50%
Active mass per 10 MW	54.5 t	70 t	58 t
Inner radius	1.91 m	1.91 m	2.29 m
Outer radius	3.10 m	2.66 m	3.19 m
Axial length	1.15 m	2.21 m	1.38 m
MMF	36,600 A	44,800 A	32,400 A
HTS tape length at 65K	13 km	15.12 km	13.5 km

Table 7.2 shows a comparison between the two stacking methods for two modules and the original 10 MW design of the double claw pole machine. Each design has 88 poles and runs at 10 rpm. When stacking the modules concentrically the generator offers better performance. The power density in terms of mass as well as volume was improved in comparison to the original 10 MW design while maintaining approximately the same HTS tape requirements. One disadvantage of the stacking methods is that the efficiency is lower than for the original generator. The next subsection will address the efficiency for stacking two modules concentrically and how it can be improved.

7.4.1 Improved Efficiency

The method used in the previous section of this chapter tried to maximize the electric loading to maximize the power density. However, this approach leads to high copper losses, which in turn lead to a lower efficiency. To improve the efficiency, a similar approach to the one introduced in the previous chapter can be applied. The electric loading can be reduced to maintain a higher efficiency at the cost of a lower power density. In this section a design of the concentrically stacked machine is introduced, which meets the 95 % target efficiency while still offering a higher power density than the original double claw pole machine design. When maximizing the electric loading, the rated RMS current for the lower and upper stators are 305 A and 362 A, resulting in a power output of 12.1 MW and an efficiency of 94 %. To achieve the target efficiency of 95 %. the rated RMS current for the lower and upper stators can be reduced down to 260 A and 310 respectively. The resulting power output for this case is 10.6 MW.

7.5 Stacking FEA Validation

To confirm the results from the reluctance models, a 3D finite element analysis (FEA) for each stacking method was performed using the simulation software *MagNet*. Since the flux travels three-dimensionally it is essential to use 3D FEA in order to simulate the machine accurately. One quarter symmetry was applied in order to reduce the computational time. The mesh size was reduced in the air gaps of the generator in order to improve the accuracy of the results. Figure 7.14 and 7.15 show the flux density distributions for the stacking options. Figure 7.14 highlights the total flux density in the machine for axial stacking. Evidently, the claw poles start saturating around the elbows, this indicates that the MMF was chosen adequately.

The figure also shows the z-direction flux density, i.e. the flux in and out of the stator teeth, when the bottom larger claw pole is aligned. The z-direction flux density for the stator teeth was found to be equal to 1.14 T when the large claw pole overlaps. The stator tooth flux density from the reluctance network model was calculated to be 1.12 T for the same scenario, showing a good correlation between the FEA and the reluctance model.

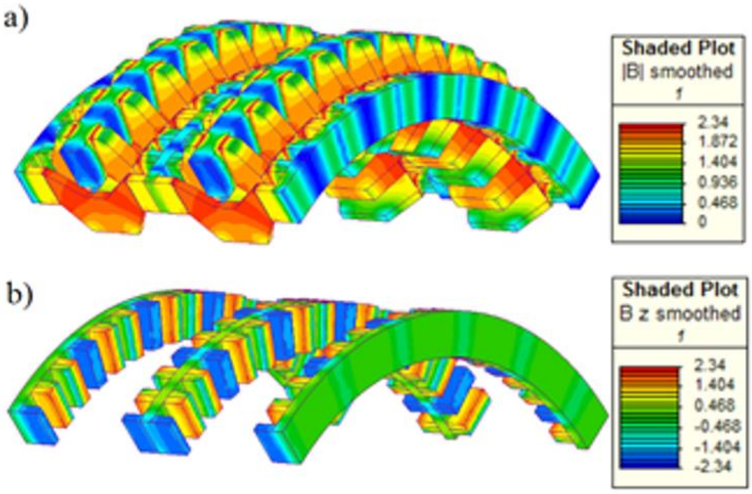

Figure 7.14. a) Total flux density distribution and b) z-direction flux density distribution in the stator teeth for axial stacking (*i.e.* out/into the stator teeth) [118].

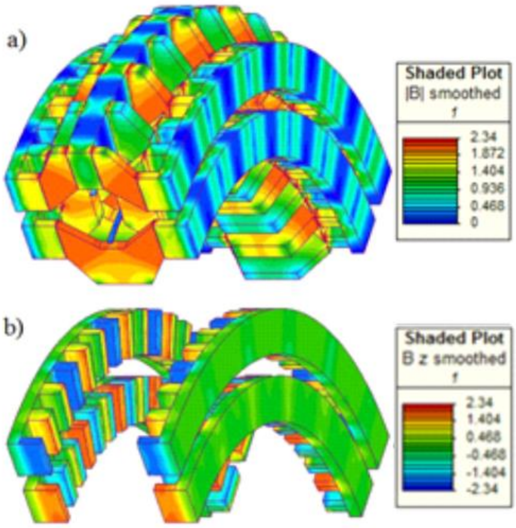

Figure 7.15. a) Total flux density distribution and b) z-direction flux density distribution in the stator teeth for concentric stacking (*i.e.* out/into the stator teeth) [118].

Figure 7.15 shows the total flux density distribution when stacking modules concentrically, similarly to the axial stacking method, the elbows of the claw poles are approaching saturation. The figure also shows the z-direction flux density. The stator tooth flux density for the stators were found to be equal to 1.15 T when overlapping with the claw poles. From the reluctance model, the stator tooth flux for both stators was found to be equal to 1.2T again showing a relatively good correlation between the two models.

Additionally, it is important to analyse the machine performance under no load and load conditions. Figure 7.16 shows a cogging torque comparison for the original design and the two stacking methods over one period. For 10 MW and 10 RPM the rated torque for the generator is 9.55 MNm. The original design has the lowest cogging with a peak of -56 kNm, the concentric stacking method has a peak of -61 kNm and the axial stacking method results in the highest cogging torque with a peak of -94 kNm.

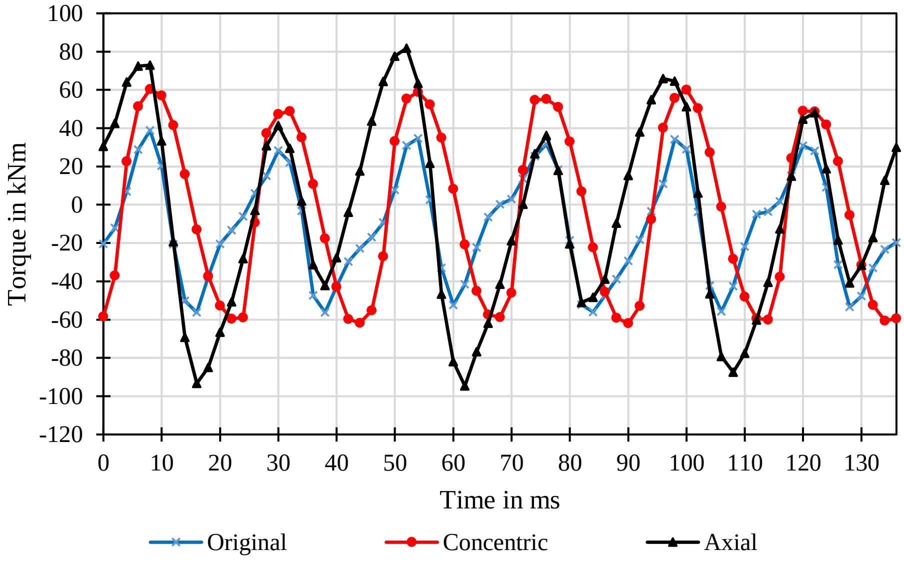

Figure 7.16. Cogging torque over one cycle for the original design and both stacking methods [118].

The cogging torque for the concentric stacking method is lower than for the axial stacking method since the concentric method results in only 10 air gaps instead of 12 as mentioned in section 2.3. While both stacking methods resulted in a higher cogging torque, it should be noted that the original design was optimized through a genetic algorithm optimization tool [100]. The cogging torque for both stacking methods could be further decreased through applying optimization tools.

Under rated load conditions the torque ripple was found to be 8 % for the original design, 9.75 % for the concentric design and 14.8 % for the axial stacking method. The torque ripple for the concentric design is shown in figure 7.17.

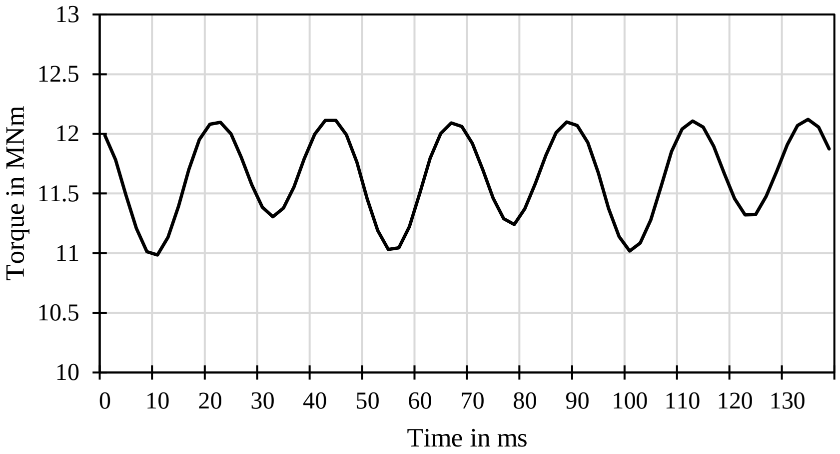

Figure 7.17. Torque ripple for the concentrically stacked generator design.

The torque ripple can be studied in further detail through applying a fast Fourier transform (FFT) to identify the main harmonics in the signal. The main harmonics in the torque ripple can be identified as the 6th, 12th and 18th, where the 6th harmonic is the most dominant. The 6th harmonic in the torque ripple is a result of the fundamental and 5th harmonics in the EMF waveform. The 5th harmonic in the EMF waveform occurs due to saturation of the iron core and leakage flux [122]. From the original design to the introduced stacked designs, the 6th harmonic in the torque ripple increases further, resulting in a higher torque ripple. From this, it can be deduced that the designed 5 MW module has some iron saturation issues, which result in worse torque characteristics. The torque profile of the introduced stacked designs can be improved through further optimizing the claw pole shapes.

Additionally, the stacking designs maintained the same combination of number of poles and stator slots as the original design, which inherently results in a higher cogging torque and torque ripple as has been discussed in chapter 4. A better combination of pole and slot numbers can further improve the torque characteristics. In addition, the torque characteristics can be further improved by skewing the stator teeth as suggested in [5, 50]. One further measure to reduce the torque ripple is to change to non-magnetic stator teeth, which would almost completely eliminate the torque ripple, at the cost of increased HTS tape requirements.

Figure 7.18 shows the open-circuit voltages. For the axial design, one power converter can be used since the phase voltages are of the same magnitude and phase. For the concentric method potentially two power converters are required since the voltages produced by the bottom and top modules are of different magnitudes and phase. This can be explained through examining figure 7.15. When comparing the magnetic flux in and out of the stator teeth for the upper and low stator stators, it can be seen that the flux is in the opposite directions for top and bottom teeth. This leads to the 180°-degree phase shift that can be observed between the voltage waveforms for each phase.

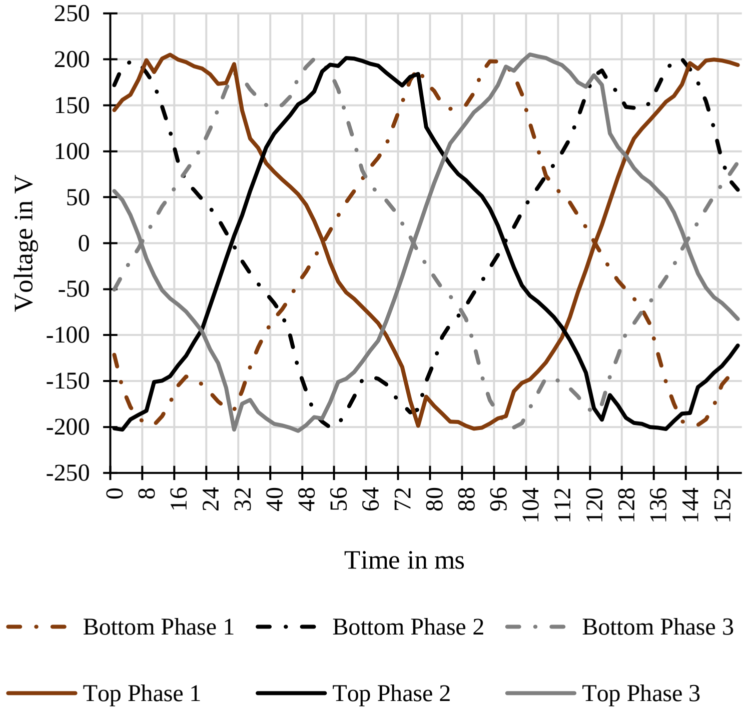

a) Concentric design open-circuit voltage

b) Axial design open-circuit voltage

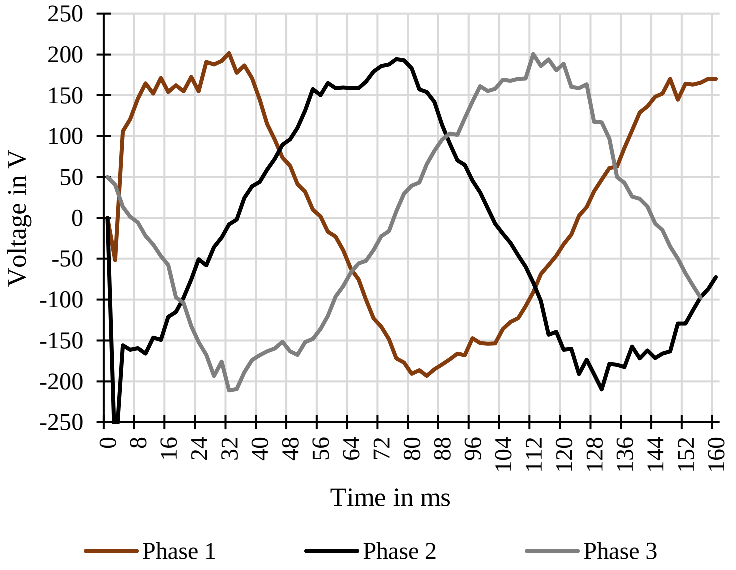

Figure 7.18. Open circuit voltages for a) concentric design and b) axial design [118].

7.6 Modularity and Size Advantages

It was shown that two stacking options can be applied to an axial flux machine. Both options further increase the modularity and power density of the machine without compromising the torque characteristics of the generator. From a manufacturing point of view, there are significant advantages to be gained by manufacturing standardized modules. The manufacturer only needs to produce a certain set of components that can then be assembled to create a machine with the desired power output. The machine components are more compact and easier to handle than if one big machine was developed. The smaller machine components also reduce the construction costs of the generator when compared to conventional generators.

In [10] the cost of a 6 MW permanent magnet generator for large wind turbines is discussed for different drive-train configurations such as, direct-drive, single-stage and multi-stage gearboxes. The direct-drive generator discussed in the paper has a stator radius of 3.5 m. The generator with a single-stage gearbox has a stator radius of 2.5 m. The active material and constructions costs for the smaller generator were shown to be significantly less than for the bigger DD generator. The concentric DD 12 MW design proposed here has an outer radius of 3.1 m, making it smaller than a conventional direct-drive generator of half the power rating. Due to the smaller machine dimensions the construction cost of the proposed design is expected to be significantly lower than that of a conventional generator and in combination with the small amount of HTS tape required, the proposed design is considered a very competitive option in terms of cost and performance.

The smaller and lighter components also simplify the transportation of the machine, this is especially important for offshore renewable energy applications [123, 124]. Another advantage of the modular setup is that an existing machine can be upgraded to a higher power rating by adding another module without the need of investing in a completely new machine. Stacking several modules on top of each other however results in very large diameter machines. For 5 modules the outer diameter is 8.76 m with a power rating of 49.5 MW. Here the possibility arises to lay out the machine horizontally. This is especially interesting for hydro power plants.

7.7 Concentric Stack Structural Design

The concentric stacking method was found to offer the best increase in power density, however there are also challenges that arise. Due to the new claw pole structure, the forces acting on the machine components have changed. This is highlighted in figure 7.19.

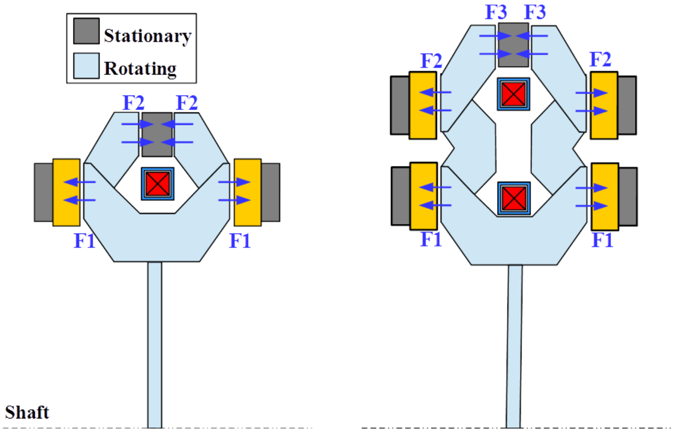

Figure 7.19. Air gap closing forces comparison.

There are now 10 forces acting on the claw poles instead of only 6 since the magnetic flux crosses the air gap 10 times before the magnetic flux loop is closed. Clearly this issue becomes worse with every additional module that is stacked concentrically on top. In particular, the balance of forces acting on the claw poles was disturbed. For the original design the forces F_1 and F_2 are equal to each other and act in opposite directions, hence essentially cancelling out. Only a rotational momentum exists for the small claw poles due to the misalignment of the air gap closing forces, this issue was discussed in chapter 5. With the concentrically stacked design, the forces acting on the middle claw poles do not balance out. It can be seen that both forces F_1 and F_2 act in the same direction with respect to the middle claw poles. To counter act this further research into the optimization of the machine is required with the aim to balance out the forces so that force F_3, which occurs in the inner air gap, is equal in magnitude to the forces F1 and F2 to again balance the magnetic forces acting on the claw poles. As was discussed in chapter 5, the air gap closing force is a function of the cross-sectional area of the surfaces the magnetic flux transverses. Hence, a balance of forces could be achieved through varying the size of the claw poles while avoiding iron saturation.

Another method to avoid issues with air gap closing forces and hence the structural design could be to design the generator with non-magnetic stator teeth. With non-magnetic teeth, the air gap closing forces are significantly reduced or even completely eliminated. This would enable the stacking of several machine modules to achieve very high power densities. One disadvantage of this method would be the increased HTS tape requirements to account for the increased reluctance due to the increased air gap lengths. Another benefit that non-magnetic teeth would bring is the reduction of the cogging torque and torque ripple.

Clearly, special care is required in the mechanical support structure of the machine in order to ensure the air gap clearance is kept constant. While a detailed mechanical structure analysis was out of the scope of this research work, further research into the mechanical design of the generator is required.

7.8 Chapter Summary

In this chapter a 5 MW of the double claw pole machine was introduced, with the aim to explore different methods of stacking machine modules to increase the power density. Stacking the modules concentrically was found to offer significant advantages. The power density, both in terms of mass and volume, was increased while essentially maintaining the same field winding requirements. Additionally, the modularity of the machine was further improved, which makes it easier to manufacture and transport and also provides additional fault tolerance. One disadvantage when stacking machine modules concentrically, is the complication of the structural design. The air gap closing forces on the claw poles are not balanced anymore for this configuration, leading to the need for a very stiff mechanical structure. Further research into the mechanical design and structural optimization is required. Furthermore, the scaled design allows to test the generator performance and reliability at a reduced capital cost, hence the opportunity arises to use it as a steppingstone towards 10 MW and higher rated generators.

Chapter 8 Superconductor Modelling

This chapter introduces the superconductor modelling that was done during this research work. Firstly, the 2D ***H***-formulation based numerical model is introduced in detail. The chapter then moves on to showing the simulation results for dynamic loss in superconducting tapes for different magnetic field environments. Particularly focusing on AC fields with a large DC background field as found in superconducting machines. Using the introduced models, the dynamic loss for the superconducting field winding of the double claw pole machine is calculated for the first time. The chapter then moves on to quantifying the dynamic loss and total loss in superconducting tapes in the magnetic field environment of very fast spinning machines, such as in superconducting motors for aircraft propulsion. Finally, the experimental setups that have been setup during this research work, to enable AC and dynamic loss experiments, will be introduced. The research introduced in this chapter has been published in the following journal papers:

- Kails K. *et al.*, "Dynamic loss of HTS field windings in rotating electric machines", *Superconductor Science and Technology,* vol. 33, no. 4, 2020

- Kails K. *et al.*, "Loss characteristics of HTS coated conductors in field windings of electric aircraft propulsion motors", *Superconductor Science and Technology,* vol. 33, no. 6, 2020.

- Kails K. *et al.*, "T - formulation based numerical modelling of dynamic loss with a DC background field", *Journal of Physics: Conference Series*, vol. 1559, EUCAS 2019, 2020.

8.1 2D *H*-formulation Model

The two-dimensional model layout for a single tape is shown in figure 8.1. The model is drawn in the x - y plane, the z-direction is assumed to be infinitely long. The superconductor is surrounded by air and enclosed by a Dirichlet boundary. The Dirichlet boundary allows to set a value that the partial differential equation solution needs to take along the boundary. Hence, this boundary can be used to apply magnetic fields to the superconducting tape by setting the value of the Dirichlet boundary appropriately. The Dirichlet boundary can also be referred to as a fixed boundary condition. In this model, the current J_z can only flow in the z – direction, hence J_x and J_y are equal to 0. Since the current can only flow in the z – direction, it follows that the electric field E_z is also only in the z – direction as well [125].

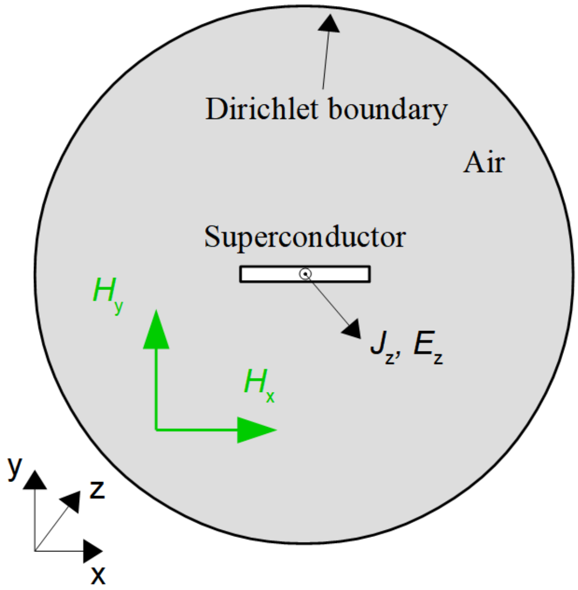

Figure 8.1. ***H***-formulation based 2D model.

Hence, in the 2D model, Ampere's law can be expressed as:

$$J_z = \frac{\partial H_y}{\partial x} - \frac{\partial H_x}{\partial y} \tag{8.1}$$

Substituting $H = \begin{bmatrix} H_x \\ H_y \end{bmatrix}$ into Faraday's law (equation 2.18), results in:

$$\begin{bmatrix} \frac{\partial E_z}{\delta y} \\ -\frac{\partial E_z}{\partial x} \end{bmatrix} = -\mu_0 \mu_r \begin{bmatrix} \frac{\partial H_x}{\delta t} \\ \frac{\partial H_y}{\partial t} \end{bmatrix} \tag{8.2}$$

The electrical behaviour of the superconducting layer is modelled with the *E*-*J* power law (equation 2.16):

$$E_z = E_0 \left(\frac{J_z}{J_c(B)} \right)^n \tag{8.3}$$

Substituting equation 8.1 and 8.3 into 8.2 yields [125]:

$$\begin{bmatrix} \dfrac{\delta\left(E_0\left(\dfrac{\dfrac{\partial H_\mathrm{y}}{\partial x}-\dfrac{\partial H_\mathrm{x}}{\partial y}}{J_\mathrm{c}(B)}\right)^n\right)}{\delta y} \\ -\dfrac{\delta\left(E_0\left(\dfrac{\dfrac{\partial H_\mathrm{y}}{\partial x}-\dfrac{\partial H_\mathrm{x}}{\partial y}}{J_\mathrm{c}(B)}\right)^n\right)}{\partial x} \end{bmatrix} = -\mu_0\mu_\mathrm{r}\begin{bmatrix} \dfrac{\partial H_\mathrm{x}}{\partial t} \\ \dfrac{\partial H_\mathrm{y}}{\partial t} \end{bmatrix} \quad (8.4)$$

where J_c(B) is the critical current, which is dependent on the magnetic field as was shown in equation 2.15.

Equation 8.3 includes two partial differential equations (PDEs) and two dependent variables H_x and H_y, with suitable boundary conditions it can be solved through FEM software [125]. In this case, the commercial software COMSOL was used. To solve for the non-superconducting regions in the model, the same equations are used but in combination with a linear Ohm's law. With the equations set up, the model geometry and boundaries need to be defined. A Dirichlet boundary is applied on the outer boundary of the model to apply magnetic fields. A point wise constraint for the current is applied to the tape, which forces the applied current to flow within the tape geometry. As was discussed in chapter 2, YBCO-coated conductors consist of several layers of different materials, usually two copper layers, one silver layer and the substrate, giving a total of 5 layers. Figure 8.2 shows the general layout of the different layers.

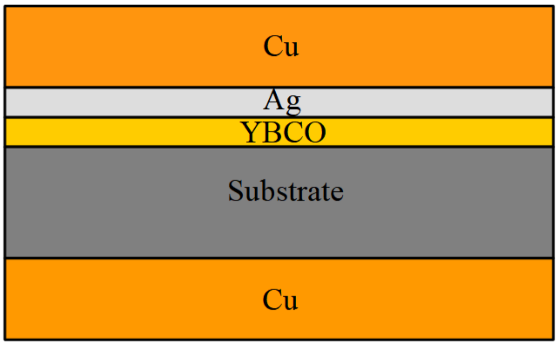

Figure 8.2. YBCO-coated conductor structure.

As can be seen from the figure, the superconducting layer is essentially sandwiched in between other layers. When every layer of the superconductor is accounted for in the model, this is called multi-layer modelling. For the non-superconducting layers, a resistivity needs to be defined. The resistivity of each layer at 77 K is given in table 8.1 along with common thicknesses for the various layers. It should be noted that a resistivity of 1 Ωm needs to be defined for the surrounding air for COMSOL to run. The relative permeability of all the materials is assumed to be equal to 1. If a magnetic substrate is used, a relative permeability needs to be defined for it. The width of the various tapes varies greatly, in general the tape width can be between 2 mm and 12 mm.

Table 8.1. Layer parameters [126].

YBCO layer thickness	h_{HTS}	1 µm
Total copper thickness	h_{Cu}	40 µm
Silver thickness	h_{Ag}	2 µm
Substrate thickness	h_{Subs}	50 µm
Copper resistivity (77 K)	ρ_{Cu}	$1.97\mathrm{x}10^{-9}$ Ωm
Silver resistivity (77 K)	ρ_{Ag}	$2.7\mathrm{x}10^{-9}$ Ωm
Substrate resistivity (77 K)	ρ_{Subs}	$1.25\mathrm{x}10^{-6}$ Ωm

The current in each layer can be defined as [127]:

$$I_{\mathrm{n}} = I(t) = \int_{S_{\mathrm{n}}} \boldsymbol{J}\, dS_n \tag{8.5}$$

where n ranges from 1 to 5, I_{n} is the transport current in the nth layer, $I(t)$ is an arbitrary function for the transport current and S_{n} is defined as the cross-sectional area of the nth layer of the coated conductor.

The average AC loss in each layer over one cycle can be found through integrating the power density over the cross-sectional area S_{n} and the second half of the cycle. Only the second half of the cycle is taken to reject transients that could result in the beginning of the simulation cycle, the loss in the second half is simply multiplied by two to get the full cycle loss.

$$Q_{\mathrm{total-n}} = \frac{2}{T}\int_{0.5T}^{T}\int_{S_{\mathrm{n}}} \boldsymbol{E}\cdot\boldsymbol{J}\, dS_{\mathrm{n}}dt \tag{8.6}$$

The total loss in the conductor is then given as the summation of the losses in each layer:

$$Q_{\mathrm{total}} = \sum_{n=1}^{5} Q_{\mathrm{total-n}} \tag{8.7}$$

To generate good results, a good mesh is required. A mapped mesh is used for the superconductor geometry where the number of vertical and horizontal elements can be predefined. For the two copper layers, 4 vertical elements are defined and for the rest of the geometry 2 vertical elements. The horizontal number of elements was fixed at 100. Outside of the geometry, a free triangular mesh is used. The generated mesh for a single tape is shown in figure 8.3. These mesh settings are maintained throughout the simulation work presented.

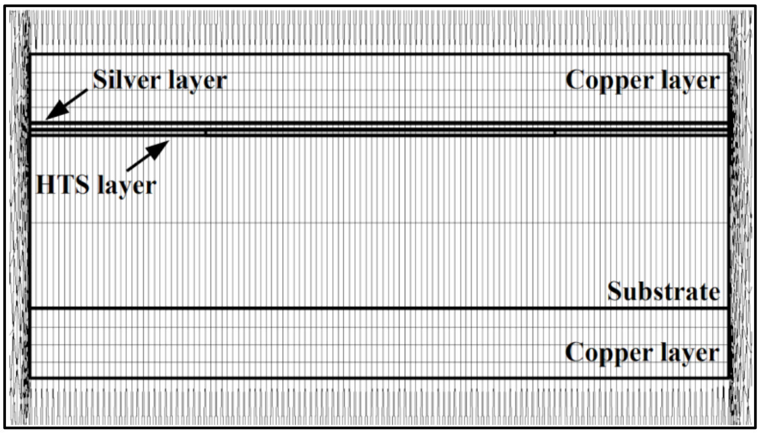

Figure 8.3. Mesh for a multi-layer simulation of a single tape [127].

8.2 Single Tape AC Loss

In this section the AC loss simulation results for a single tape are shown and compared to the analytical equations and experiments. The purpose of this is to validate that the introduced model is working correctly.

8.2.1 Transport Current Loss

In this section, the transport current loss of a single tape is shown. The loss was calculated according to the methods discussed in section 8.1. The parameters of the tape are summarised in table 8.2.

Table 8.2. SuperPower SCS12050 tape [32]

Parameter	Variable	Value
Critical current	J_{c0}	$2.5 \cdot 10^{10}$ A/m^2
n-value	n	30
Magnetic field constant	B_0	0.426 T
Anisotropy factor	k	0.186
Tape width	$2a$	12 mm
YBCO layer thickness	h_{HTS}	1 µm
Substrate thickness	h_{Subs}	50 µm
Silver thickness	h_{Ag}	2 µm
Total copper thickness	h_{Cu}	40 µm

The transport current frequency was set to 100 Hz. The experimental data was taken from [32]. The loss per cycle results are shown in Figure 8.4.

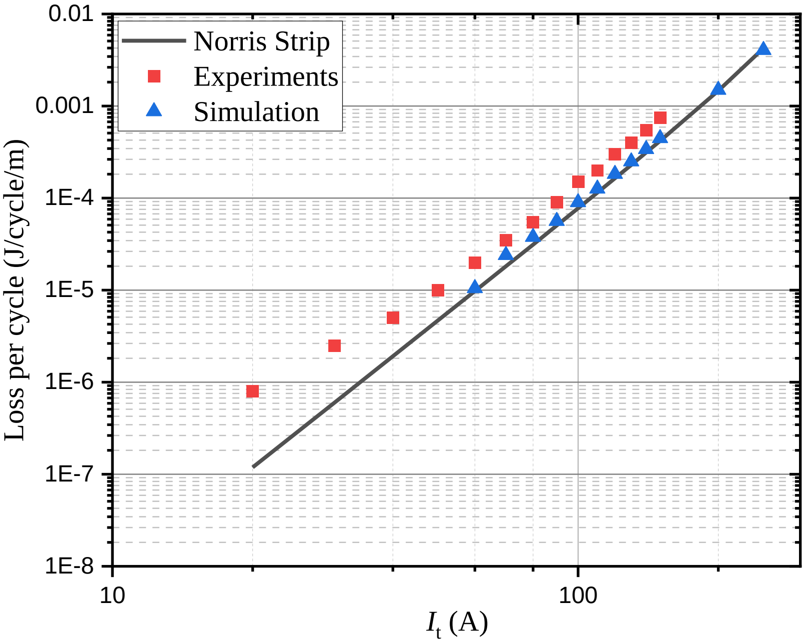

Figure 8.4. Transport current loss with increasing current at 100 Hz for Norris equation, experiments and simulations. The experimental results were taken from [32].

It can be seen that the loss per cycle increases with the transport current. There is a very good agreement between the numerical model, the analytical equation and the experimental results. AC loss is particularly important for fully superconducting machines since the current in the stator is AC.

The next subsection highlights the magnetisation loss.

8.2.2 Magnetisation Loss

In this section, the magnetisation loss of a single tape is shown and compared to the Brandt equation. The magnetic field is applied perpendicular to the long surface of the tape. For this simulation, a different tape was used than in the previous section, hence the parameters are different. Table 8.3 shows the parameters used in this simulation.

Table 8.3. SuperPower SCS12050 tape [32].

Parameter	Variable	Value
Critical current	J_{c0}	$1.91 \cdot 10^{10}$ A/m^2
n-value	n	25
Magnetic field constant	B_0	0.035 T
Anisotropy factor	k	0.25
Tape width	$2a$	6 mm
YBCO layer thickness	h_{HTS}	1 µm
Substrate thickness	h_{Subs}	50 µm
Silver thickness	h_{Ag}	2 µm
Total copper thickness	h_{Cu}	40 µm

The frequency was set to 50 Hz. The magnetisation loss results are shown in figure 8.5.

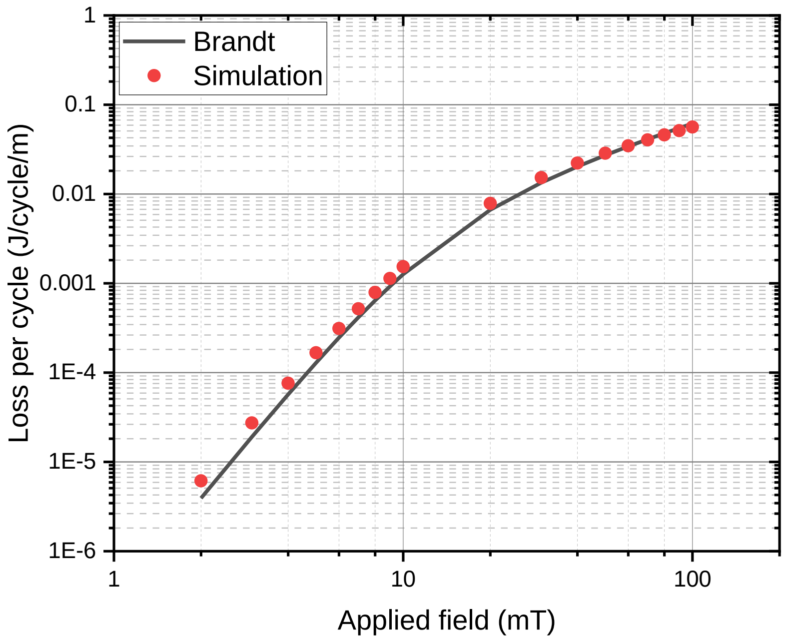

Figure 8.5. Magnetisation loss for 50 Hz from 2 mT to 100 mT applied field.

Again, it can be seen that there is a very good correlation between the two calculation methods. It can be seen that the loss increases with the applied magnetic field magnitude as expected. In rotating electrical machines, magnetisation loss can occur in both the superconducting field winding and superconducting stator windings, hence the accurate modelling of magnetisation loss is key to understand superconductor loss in the electromagnetic environment of machines.

The next section will address the calculation of dynamic loss, which occurs in the superconducting field windings of rotating machines.

8.3 Single Tape Dynamic Loss with Pure AC Field

Superconductors carrying a DC current are assumed to be lossless however, when the superconductor is placed in a alternating magnetic field while carrying a direct current, it starts exhibiting loss [128, 129]. This is particularly important when considering superconducting field windings. As the field winding rotates in the machine, it will be subject to changing magnetic fields, the resultant loss is called dynamic loss. Clearly it is an important loss that needs to be well understood, in order to design the associated cooling systems for superconducting field windings. In this section, the dynamic loss in a tape over a wide range of applied fields and load factors is calculated and presented. To calculate the loss, the introduced superconductor model in section 8.1 needs to be slightly adjusted.

For a coated conductor carrying a DC transport current I_t under an AC magnetic field B, it was shown that the transport current occupies the superconducting layer with width $2ia$ in the centre, leaving the rest of the width $(1 - i)2a$ free on both sides, where a is defined as half the width of the HTS tape and i is the load factor [ref me [130]]. This region is defined as the dynamic region, of which the concept is illustrated in figure 8.6.

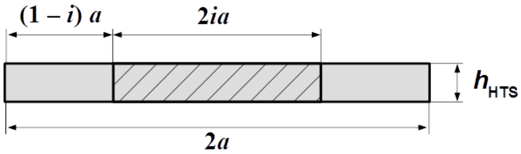

Figure 8.6. Dynamic region definition [64].

To define a DC current in COMSOL, it needs to be ramped up, since COMSOL expects all initial values to be equal to zero at the start of the simulation. Hence, the current is defined as shown in equation 8.4, where I(t) is a ramp function, which ramps up the current to the required value defined by the load factor within the first half of the first cycle. Simulations are run over two cycles and only the loss in the second cycle considered to reject possible transients that may be present in the first cycle from the ramping of the current.

To highlight the existence of the dynamic region and its dependence on the load factor, two simulations were performed. A magnetic field of 20 mT was applied to a superconducting tape carrying a DC transport current of 30 % and 70 % of its critical current. The simulations were done at an applied magnetic field frequency of 26.62 Hz and the tape parameters used are summarised in table 8.4.

Table 8.4. SuperPower YBCO-coated conductor [130].

Parameter	Variable	Value
Critical current	J_{c0}	2.63×10^{10} A/m^2
n-value	n	22.5
Magnetic field constant	B_0	0.135 T
Tape width	$2a$	4 mm
YBCO layer thickness	h_{HTS}	1 µm
Substrate thickness	h_{Subs}	50 µm
Silver thickness	h_{Ag}	2 µm
Total copper thickness	h_{Cu}	40 µm

Figure 8.7 shows the current density and the magnetic field distribution profiles for the two cases when the applied field is at its maximum and when it’s at its minimum. From the figure,

it can be seen that the DC transport current occupies the centre of the tape and that the DC transport current region becomes wider with a higher load factor.

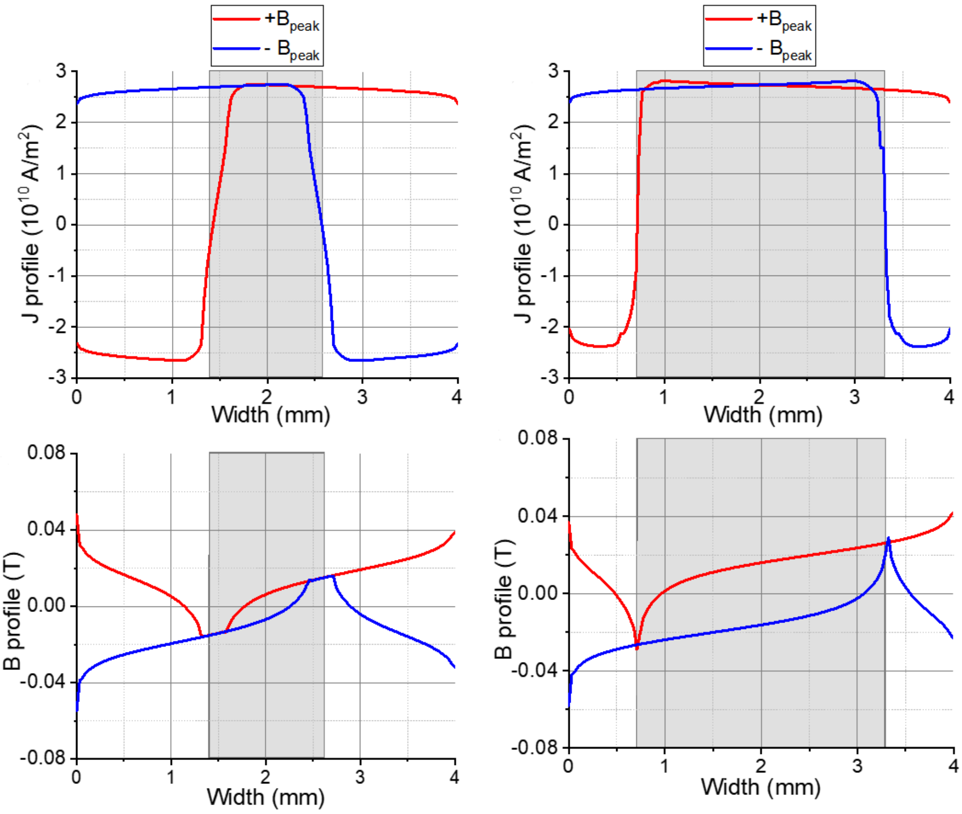

Figure 8.7. Dynamic region for 30 % load factor (left) and 70 % load factor (right) for an applied field of 20 mT at a frequency of 26.62 Hz.

The origin of dynamic loss is due to the occurrence of dynamic resistance, which is caused by a net flow of flux across that DC current-carrying region defined in figure 8.4 and shown in figure 8.5 [131]. Additionally, it was shown that it is the perpendicular component of the applied field, which induces the majority of the loss [132], hence during the conducted simulations only perpendicular fields were applied. Since only perpendicular fields are applied the $J_c(B)$ dependence shown in equation 2.14 is used. Dynamic loss is in fact a well understood loss mechanism and the dynamic resistance in superconducting tapes has been measurement in multiple experimental setups [133, 130, 134, 135].

Since the transport current region can easily be defined from the load factor, the average dynamic loss in the dynamic region per unit time can be calculated as [64]:

$$Q_{\text{dyn}} = \frac{1}{T}\int_0^T \int_{S_{\text{dyn}}} \boldsymbol{E}\cdot\boldsymbol{J}\, dS_{\text{dyn}} dt \tag{8.8}$$

where T is the period of the applied magnetic field and S_{dyn} is the dynamic region, which is dependent on the load factor as defined in figure 8.4.

A second method exists to calculate the dynamic loss in addition to defining the dynamic region. Ainslie proposed in [133] to calculate the average electric field E_{ave} across the tape cross-section, such as that:

$$E_{\mathrm{ave}}(t) = \frac{\int_S \boldsymbol{E}(t)\, dS}{S} \tag{8.9}$$

and hence the instantaneous loss can be calculated with

$$P_{\mathrm{dyn}} = E_{\mathrm{ave}} \cdot I_{\mathrm{t}} \tag{8.10}$$

The average dynamic loss per unit time (W/m) can be given as:

$$Q_{\mathrm{dyn}} = \frac{I_{\mathrm{t}}}{T} \int_0^T E_{\mathrm{ave}}(t) dt \tag{8.11}$$

The two methods are used together to calculate the dynamic loss and are compared to experimental results.

The experiment results were provided by researchers of the Robinson Research Institute at the Victoria University of Wellington. Their experimental setup is shown in figure 8.8. An approximately 10 cm long sample is fixed in between two AC powered coils, which produce a uniform magnetic field up to 100 mT. A 10 cm long tape sample, allows for a 5 cm distance between voltage taps and 2 cm between the voltage taps and the current leads, leaving 0.5 cm for the soldering of the current leads onto the tape. A Keithley 2182 nanovoltmeter is used to measure the voltage drop across the superconducting tape sample, the voltage taps are arranged in spiral loop to cancel introduced induction. The voltmeter time averaged function is used; hence the dynamic loss can simply be calculated from the DC transport current and the time-averaged measured voltage. Further details on the experimental setup may be found in [130] and [131].

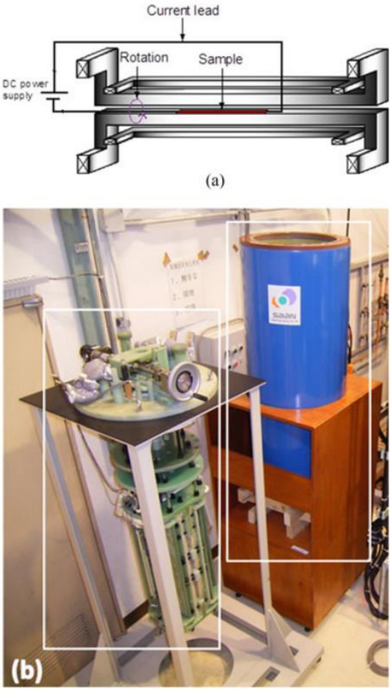

Figure 8.8. a) Experimental setup schematic and b) AC magnet (left) and cryogenic vessel (right) [130].

The dynamic loss results for applying a perpendicular AC field to the tape are shown in figure 8.9 for both methods and validated with experimental results. The frequency is set to 26.62 Hz and the respective load ratios are 0.3, 0.5, 0.7 and 0.9. The peak applied magnetic field ranges from 0 mT to 100 mT in 10 mT steps. As can be seen there is a very good correlation between the two methods and the experimental results. The dynamic loss is in positive correlation with the applied field as well as with the load factor. There is no loss when the applied field is below the threshold field, after the applied field is greater than the threshold field, dynamic loss occurs and increases linearly with the applied field. The threshold field B_{th} is defined as [130]:

$$B_{\mathrm{th}} = B_{\mathrm{p}}\left(1 - \frac{I_{\mathrm{t}}}{I_{\mathrm{c}}}\right) \tag{8.12}$$

where B_{p} is the effective penetration field of the HTS-coated conductor and can be given as [130]:

$$B_{\mathrm{th}} = 2.4642\left(\frac{\mu_0 J_{\mathrm{c}} t_s}{\pi}\right) \tag{8.13}$$

where J_{c} is the current density of the tape and t_{s} is the thickness of the superconducting layer. As the applied field increases, there is a slight lift-off for a load factor of 0.7 and applied fields beyond 80 mT and a rapid increase in dynamic loss at a load factor of 0.9 for applied AC fields beyond 40 mT. The nonlinear behavior arises due to the field dependence of the critical current, which leads to $I_{\mathrm{c}}(B)$ dropping below the transport current for short periods of time for each cycle leading to flux-flow loss [130, 131].

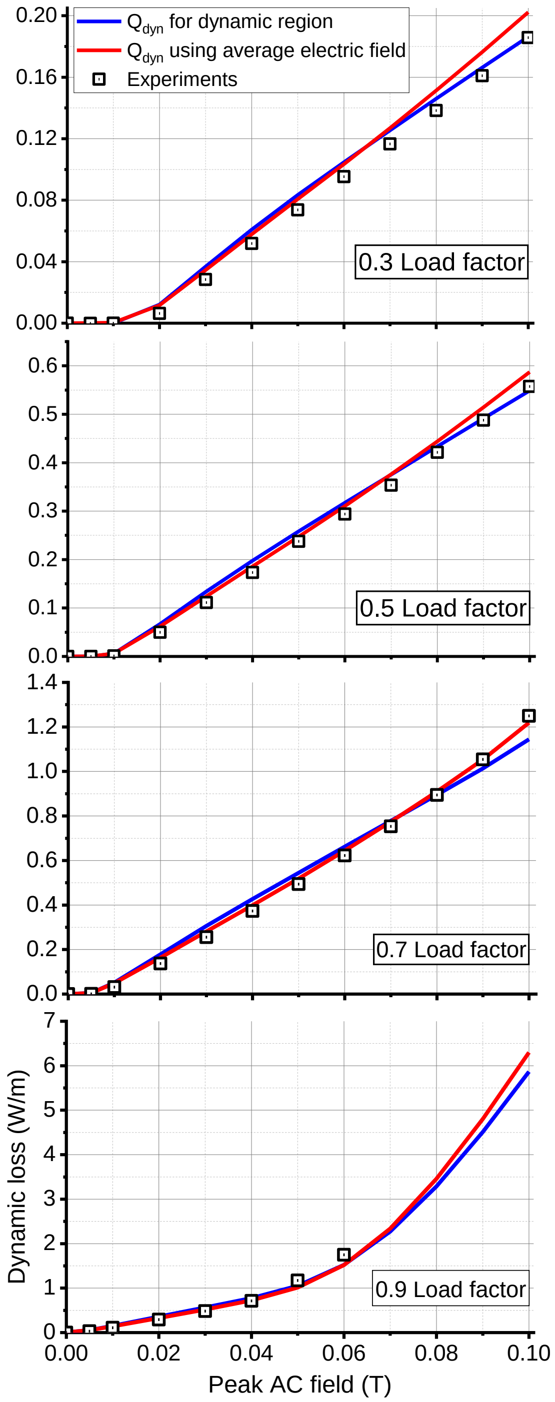

Figure 8.9. Dynamic loss results for a load factor of 0.3, 0.5, 0.7 and 0.9 for the dynamic region and average electric field methods with experimental results. The applied field ranges from 0 mT to 100 mT in 10 mT increments. The frequency is 26.62 Hz [64].

8.4 Dynamic Loss with Combined AC and DC Field

In the previous section, dynamic loss results were shown and validated with experimental results. The dynamic loss was investigated under a purely AC applied field. However, when considering the magnetic field environment field windings of rotating machines operate in, it becomes clear that the field is not a pure AC field, but rather a combination of an AC field with a large DC background field, which is produced by the field windings in the machine. The majority of research so far has only focused on applying pure AC fields leaving a lack of knowledge in regard to the loss behaviour of superconductors in the magnetic field environment of a rotating machine. In this section, the dynamic loss results for combined AC and DC magnetic fields will be shown, giving further insight into the superconductor loss behaviour in machines.

8.4.1 Dynamic Loss Results

In this section the dynamic loss results for the combined applied fields will be shown. The same simulation parameters as in the previous section were used, *i.e.*, the same tape parameters and the same magnetic field frequency.

Figure 8.10 shows the dynamic loss results for load factors of 0.3, 0.5, 0.7 and 0.9 for a combination of different applied fields. It can be seen that for a low load factor, the DC background field only has a minor effect on the dynamic loss, since the transport current is relatively low, hence the reduced critical current, due to the field dependence, does not strongly affect the overall losses. As the load ratio increases, the dynamic loss increases significantly with the DC background field, due to the decreased critical current. While for the previous case, where no DC background field was applied, the non-linear region for the dynamic loss only occurred for very high load factors and applied fields. When applying a DC background field of 50 mT, the non-linear region already occurs for a load factor of 70 %. Furthermore, in the previous case the rapid increase in dynamic loss only occurred for short periods of time each cycle when the AC field was in the vicinity of its peak, reducing the critical current temporarily below the transport current. Applying a DC background in conjunction with an AC field leads to the critical current being below the transport current for longer periods of time during each cycle, leading to a quicker and more rapid increase in dynamic loss. This becomes especially clear when comparing the loss results for the two cases where only a 100 mT AC field is applied and the case when only a 100 mT DC field is applied, both cases for a load ratio of 0.9. The dynamic loss result for the DC field case is significantly higher since the transport current is above the critical current for the whole cycle instead of only short periods of time as is the case for the 100 mT AC field example.

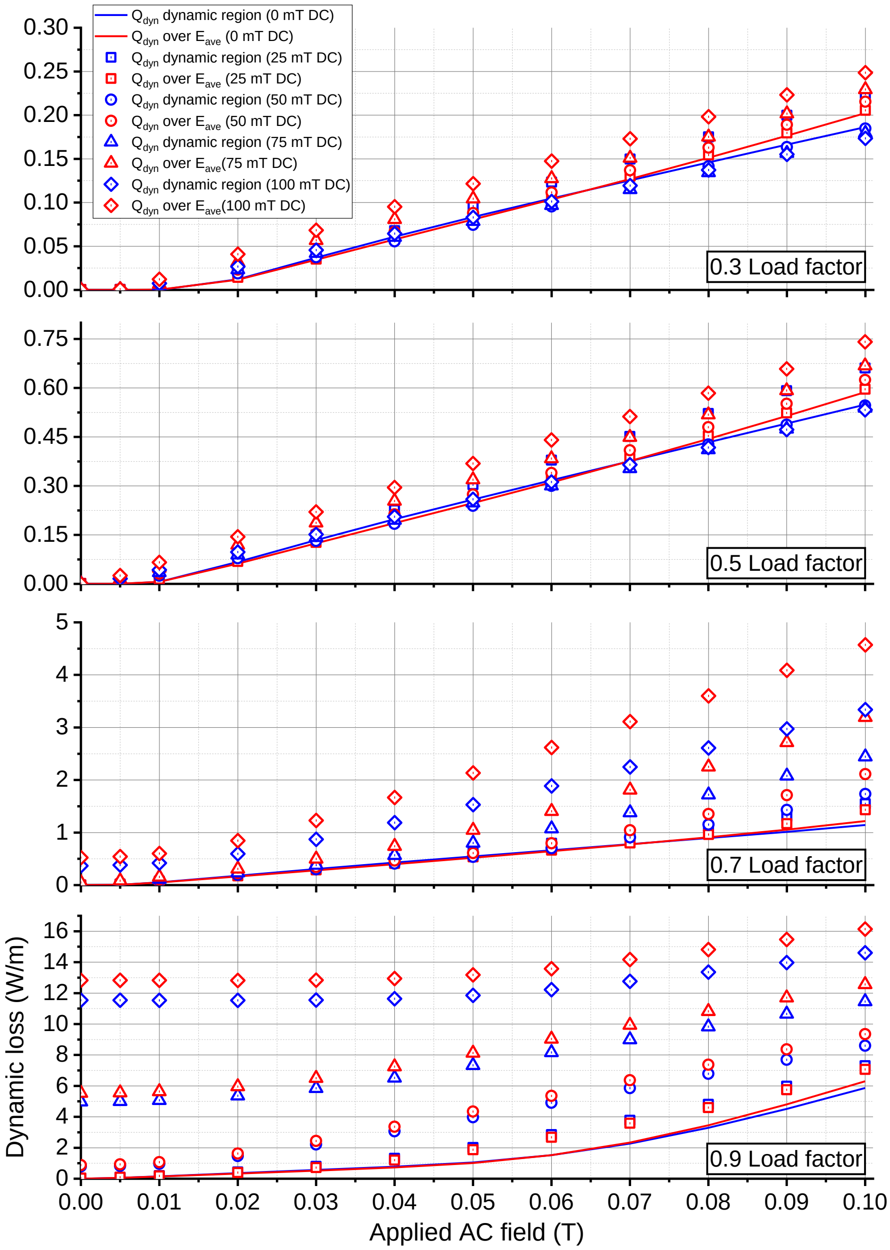

Figure 8.10. Dynamic loss results for a load factor of 0.3, 0.5, 0.7 and 0.9 for the dynamic region and average electric field method. The applied AC field ranges from 0 mT to 100 mT in 10 mT increments with a DC background of 25 mT, 50 mT, 75 mT and 100 mT. The frequency of the applied AC field is 26.62 Hz [64].

While the two methods for calculating the dynamic loss show a similar trend, the method of defining the dynamic region as a function of the load factor leads to consistently lower results. This is due to the DC background field reducing the critical current, and hence, increasing the area that the DC transport current occupies. For a high load ratio of 90%, this effect is slightly mitigated since most of the cross-sectional area of the coated conductor is considered for calculating the dynamic loss. In addition, since the DC field direction does not change *i.e.* top to bottom, flux weakening and flux strengthening occurs on the edges of the tape, skewing the current and field distributions in the coated conductor.

This is highlighted in figure 8.11, which shows the current density and magnetic field profiles for a 50 % load factor, with an AC applied field of 20 mT, with and without a DC background field of 50 mT.

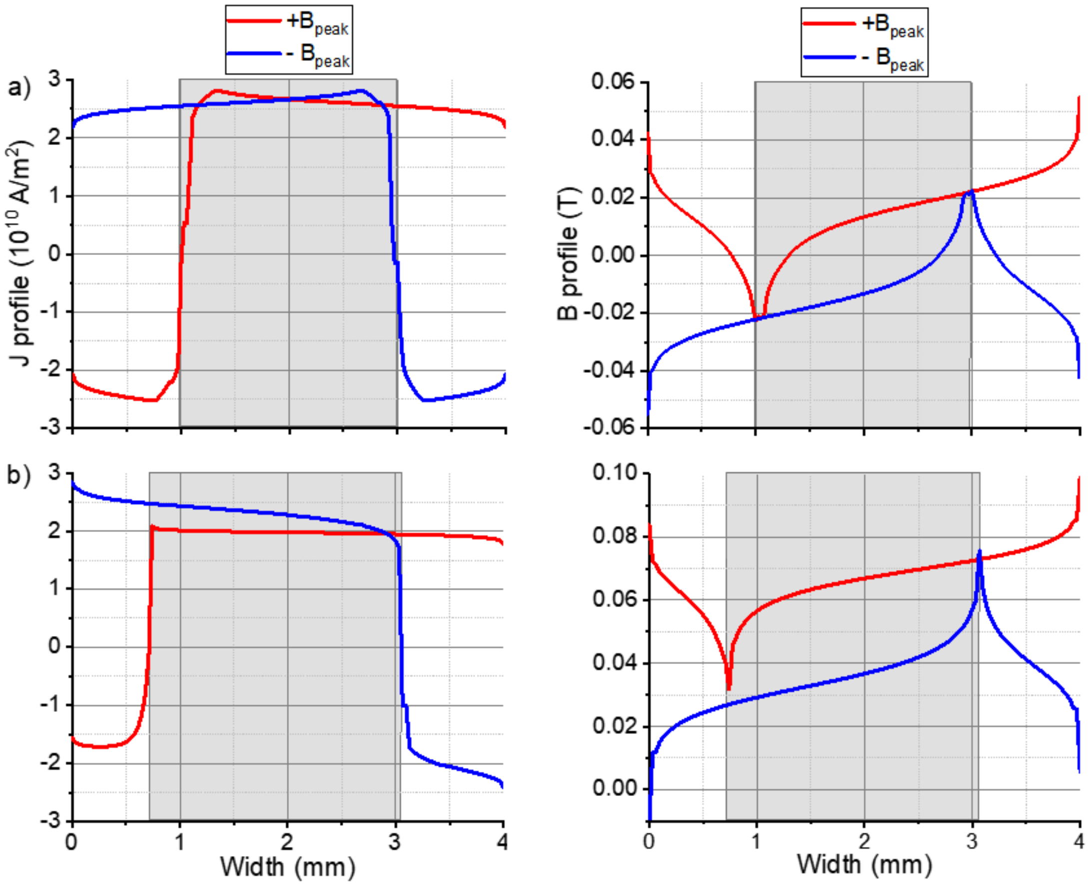

Figure 8.11. B and J profiles for a load factor of 50% and 20 mT applied AC field for a) without DC background and b) with a DC background field of 50 mT. The shadowed area is defined as the dynamic region [64].

For no applied DC field, the current density and magnetic field profiles are symmetrical, and the dynamic region can be clearly defined as a function of the load ratio. With the applied DC background field, flux strengthening occurs on the right-hand side of the tape and flux weakening on the left-hand side, skewing the profiles towards the left. Hence, for more complex applied magnetic fields, it becomes more challenging to define the dynamic loss region accurately. Calculating the dynamic loss through the average electric field avoids this issue and leads to more accurate results. The simulation results show that a DC background field such as present in superconducting rotating machine environments can play a vital role in the calculation of dynamic losses in superconducting tapes since it pushes the conductor into the non-linear loss region for longer periods of time each cycle, leading to significantly higher losses. This is especially important to consider when operating with load factors beyond 70 %.

With the dynamic loss modelling methods developed, it is now possible to calculate the dynamic loss in the field winding of the double claw pole machine design for the first time. This will be addressed in the next section.

8.4.1 DCPG Dynamic Loss at 77 K (*H*-formulation)

To further study the proposed double claw pole generator design, the dynamic losses within the field winding need to be considered. For this purpose, a 3D transient finite element analysis was done using the simulation software MagNet to find the applied magnetic fields that occur on the surfaces of the field winding while the claw poles are rotating. The double claw pole machine variation with the angled stator was used for this case study, however the magnetic field environment for the original machine is almost identical, hence the loss results also apply to the original design. The 2D HTS model introduced in this paper is then used to apply the resultant magnetic fields to the superconducting tapes, and hence determine the dynamic loss. This method allows to estimate the dynamic loss for the field winding without the need to build a complex 3D model of the whole generator, which includes the HTS properties, since the actual resultant magnetic fields in the generator are taken and applied to the superconducting tapes. This methodology also avoids the issue of the large aspect ratio of the field winding diameter (5.5 m) to the HTS layer thickness. Due to the very large size of the coil, the 2D model is expected to be a good approximation to a full 3D model. To estimate the total dynamic loss for the field winding, the loss of each tape is then taken and multiplied by the required length depending on the location of the tape in the coil. Figure 8.12 shows a schematic of the field winding and the main points that were investigated are highlighted. As can be seen, the field winding consists of 3 coils that are placed next to each other. Splitting the field winding into several coils enables the generator to continue operating under partial load even if one field winding coil is damaged. In table 8.5 the superconducting tape parameters are summarized. The simulations were run assuming an operating temperature of 77 K since this model has only been validated with experiments, which were done at 77 K.

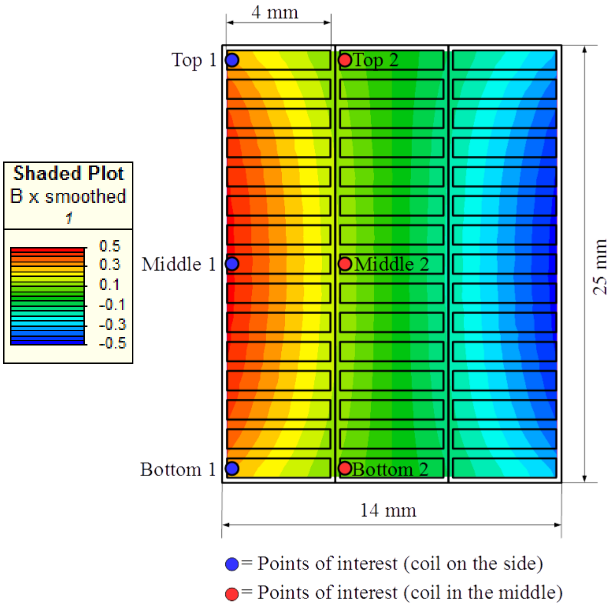

Figure 8.12. Cross-section of the superconducting field coil with highlighted points of interested [110].

Table 8.5. Fujikura FYSC-SCH04 tape parameters [109].

Temperature	77 K
I_C (self-field)	230 A
n-value	23
B_0	0.2 T
Tape width	4 mm
Superconducting layer thickness	1.9 µm
Substrate thickness	75 µm
Silver thickness	2 µm
Copper thickness	40 µm

The perpendicular flux density variations over one period for the investigated locations are shown in figure 8.13.

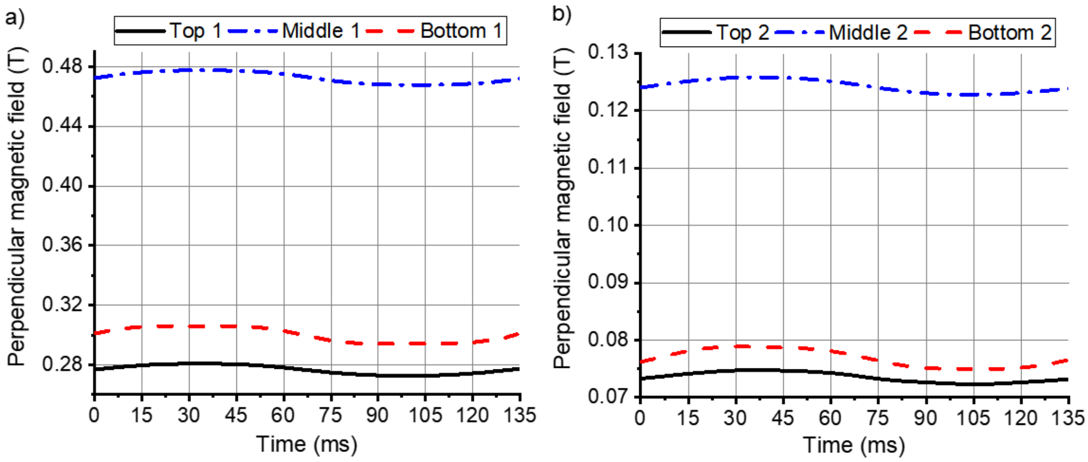

Figure 8.13. Perpendicular flux density variation for the investigated points on the field winding for a) coil 1 and b) coil 2 [64].

The generator design features 88 poles and rotates at 10 rpm, which results in an electrical frequency of 7.33 Hz. The peak flux densities occur on the edges of the coils, these values are taken and applied over the whole width of the relevant tapes to estimate the dynamic losses. Considering the reduced critical current due to the DC background field on the field winding, the transport current for the side coils (*i.e.* coil 1 and coil 3) is chosen as 52 A and 122 A for the middle coil (coil 2), giving a load factor of approximately 0.7 for each coil. Figure 8.14 shows the dynamic loss results for the investigated coil locations.

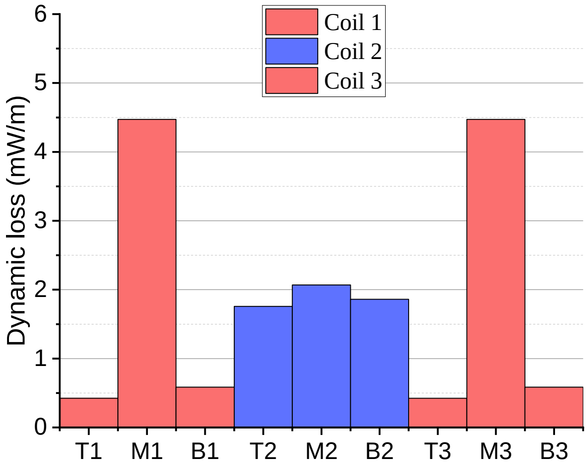

Figure 8.14. Dynamic loss for investigated points in the field winding [64].

It can be seen that the tapes in the middle of each coil have the highest loss due to seeing the highest magnetic fields. Since coil 3 sees the same magnetic field magnitude as coil 1, it is assumed that both coils exhibit the same dynamic loss. The loss for coil 2, *i.e.* the coil in the middle, is the lowest due to the shielding effect from the outer coils, it is affected by the lowest DC background field and only a small AC ripple. The total dynamic loss of the field winding may be estimated by multiplying the loss for each location by the required length of YBCO tape. The total current needed in the field winding is 32,400 A·turns, considering the transport currents, the middle coil is given 148 turns at 122 A, and the side coils 138 turns at 52 A. Hence, the side coils each require approximately 2.3 km of tape and the middle coil 2.5 km, giving a total of 7.1 km at 77 K. The dynamic loss of the field winding can be roughly estimated to be 13.3 W, by multiplying the loss in each location of the coil by one third of the required length. Overall, the dynamic loss was found to be relatively low, since the rotational speed is low and hence frequency is very low. In addition, due to the design of the generator, the field winding coils only see small magnetic field variations, since they are located at a distance from the air gap and armature coils, which further reduces the dynamic loss. In [50], the thermal budget was estimated to be approximately 157 W, it was decided to use four cryocoolers providing 50 W of cooling power each, leaving a large safety margin of approximately 25 %. With the additional calculated dynamic loss, the new thermal budget becomes approximately 170 W, which can still easily be provided by the four cryocoolers, operating at a safety margin of 15 %. Hence, even with taking into account the loss of the field winding, the efficiency of the generator is unchanged.

While the dynamic loss model was verified through experiments for applying a purely AC magnetic field, no experiments are available for a combination of DC and AC fields. To further increase the confidence in the modelling methods and adding to the understanding of dynamic loss mechanisms and the dynamic region, experiments are required. In section 8.7, an experimental setup is proposed to conduct experiments with a combined DC and AC field.

8.4.2 DCPG Dynamic Loss at 65 K (*T*-formulation)

In addition to ***H***-formulation based numerical modelling, ***T***-formulation based modelling was performed as well. The ***T***-formulation was briefly introduced in the second chapter. In this formulation a current vector potential is defined such as was shown in equation 2.21. It is an in-house superconductor model coded in FORTAN90, it was first introduced by Amemiya in 1998 [47], and further studied by Yao at the University of Edinburgh [23].

The governing equation of the electromagnetic field in the HTS tape is derived from Faraday's law as [23, 130]:

$$-\frac{\partial}{\partial y}\frac{1}{\sigma_{sc}}\frac{\partial T}{\partial y} = -\frac{\partial}{\partial t}\left(\frac{\mu_0 t_s}{2\pi}\int \frac{1}{y-y'}\cdot\frac{\partial T}{\partial y}dy'\right) - \frac{\partial B_\perp}{\partial y} \tag{8.14}$$

where y is the coordinate in the lateral direction of the HTS tape, σ_{sc} is the conductivity of the superconducting layer and $B_\perp$ is the perpendicular component of the external magnetic field. Figure 8.15 shows a schematic of the superconducting layer in a magnetic field, where $2w$ is the width of the tape and t_s is the thickness of the superconducting layer.

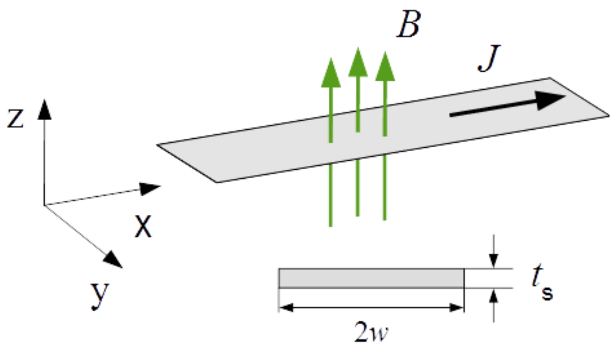

Figure 8.15. Schematic of a superconducting tape carrying the transport current *J* in a magnetic field *B* [110].

The superconducting property is determined using the $E - J$ power law characteristic, where the equivalent conductivity of the HTS tape is defined as [23, 130]:

$$\sigma_{\mathrm{sc}} = \frac{J}{E} = \frac{J_{\mathrm{c}}^{n}}{E_{\mathrm{c}}} J^{1-n} = \frac{J_{\mathrm{c}}^{n}}{E_{\mathrm{c}}} (\nabla \times T)^{1-n} \tag{8.15}$$

where $E_{\mathrm{c}} = 1 \times 10^{-4}$ Vm^{-1}. In this formulation, a dynamic region is defined for calculation the dynamic loss, similar to the first calculation method described in section 8.3. The dynamic loss in the dynamic region can hence be calculated by [23, 130]:

$$Q = \int_{(1-i)w}^{(1+i)w} J E t_s \, dy = \int_{(1-i)w}^{(1+i)w} \frac{J^2}{\sigma_{\mathrm{sc}}} t_s \, dy \tag{8.16}$$

where i is the ratio between transport current I_{t} and critical current I_{c}. The model has been validated with a multitude of experiments [23].

For the simulations, the same magnetic fields were applied to the tape as in the previous section, but the operating temperature was reduced to 65 K from 77 K. The lower operating temperature changes the superconducting tape parameters. The new parameters are summarized in table 8.6.

Table 8.6. FYSC-SCH04 tape parameters [109].

Temperature	65 K
I_{C}	469 A
n-value	24
B_0	0.8 T
k	0.88
α	0.6
Tape width	4 mm
Superconducting layer thickness	1.9 µm

The same coil layout as described in the previous section is used, where three coils are placed next to each other. With the operating temperature set to 65 K, the self-field critical for a single tape is given as 469 A. To achieve the necessary MMF, each coil has 49 turns, giving a total number of turns of 147.

For this simulation, the self-field critical current of the field winding was calculated using the following method which was proposed by Zermeño in [136]:

The E-J power law serves as the basis of the model:

$$E = E_{\mathrm{c}} \frac{J}{J_{\mathrm{c}}(B)} \left| \frac{J}{J_{\mathrm{c}}(B)} \right|^{n-1} \tag{8.17}$$

This relationship is inverted to yield:

$$J = J_{\mathrm{c}}(B) P \tag{8.18}$$

where

$$P = \frac{E}{E_{\mathrm{c}}} \left| \frac{E}{E_{\mathrm{c}}} \right|^{\frac{1}{n}-1} \tag{8.19}$$

When the transport current I_{t} reaches the critical current I_{c}, $P = 1$ and $E = E_{\mathrm{c}}$, hence I_{c} can be determined. The variable P allows for avoiding the direct solution of the nonlinear $E - J$ relationship, simplifying the problem and hence making it easier to solve.

The critical current of the coil was calculated to be 310 A. Applying a load factor of approximately 70 %, the transport current can be calculated to be equal to 220 A. The total length of superconducting tape required is 2.64 km. Hence, all simulation parameters have been defined. The simulations were run for three cycles. Different ways of analyzing the results were available. Firstly, normally only the results of the last cycle of the simulation are taken, similar to the COMSOL model, to reject possible transients. The results for this case are shown in table 8.7.

Table 8.7. Dynamic loss results for one cycle.

Location	Dynamic loss (mW/m)
Top 1	4.29
Middle 1	4.14
Bottom 1	4.47
Top 2	2.98
Middle 2	4.72
Bottom 2	3.19

It can be seen that the values are relatively close to the results produced by the ***H***-formulation based numerical model, but with a different distribution of the loss. From figure 8.13, the expected loss distribution should be as shown in figure 8.14, with the dynamic loss peaking at the point “Middle 1”, since this point sees the highest DC background field and AC ripple field. However, in the results produced by the ***T***-formulation model, “Middle 2” has the highest loss, even though its DC background field and AC field are much lower.

When taking all three cycles, but rejecting the very first time steps, and dividing by three to average over the three cycle, the loss results are shown in table 8.8.

Table 8.8. Dynamic loss results for three cycles [110].

Location	Dynamic loss (mW/m)
Top 1	27.2
Middle 1	24.9
Bottom 1	27.8
Top 2	12.2
Middle 2	24.1
Bottom 2	13.6

For the results in this case, it can be seen that the dynamic loss distribution matches better. “Middle 1” is now the highest dynamic loss but the loss for “Middle 2” is still very high. However, the magnitudes of the losses are much higher now due to including potential transients form the previous cycles. The main reason for the discrepancy between the two models comes down to the dynamic region. As was shown in the previous section, the dynamic region is strongly affected by the DC background field. In the ***T***-formulation based numerical model, the dynamic loss is however calculated over the dynamic region definition. Hence, for more complicated magnetic fields, the ***T***-formulation based model needs to be further improved and a better understanding of the dynamic region needs to be gained.

Furthermore, since these simulations were run assuming an operating temperature of 65 K, there is additional uncertainty introduced by the change in temperature, experimental results are lower temperature than 77 K could help to further understand dynamic loss properties.

One of the major advantages of the ***T***-formulation based model is that it is much faster than the ***H***-formulation, hence the results produced by the model can still serve as a rough guidance for the estimation of the dynamic loss in field windings.

8.5 Total and Dynamic Loss in High Frequency Magnetic Fields

In the previous sections, the dynamic loss results were shown for very low frequencies such as present in low RPM direct-drive generators. The dynamic loss results were found to be relatively low due to the low frequency. In this section, the loss in YBCO-coated conductors when subject to high frequency magnetic fields such as present in fast-spinning superconducting machines is investigated. Superconducting motors in particular are considered vital to enable all-electric propulsion systems. These motors are high-speed rotational machines, with some designs considering rotational speeds of up to 12,000 rpm. The resulting frequency is directly linked to the rotational speed and the number of pole pairs, hence high RPM machines lead to high frequencies. A summary of some prominent superconducting motor designs for aircraft propulsion are highlighted in table 8.9.

Table 8.9. HTS motor designs for aircraft propulsion [127].

Ref	Power rating	RPM	Poles	Field frequency
[137]	150 kW	2700	8	720 Hz
[138]	450 kW	3000	6	600 Hz
[139]	1 MW	12000	4	1600 Hz
[140]	5 MW	5000	2	333 Hz
[141]	2 MW	3000	2	200 Hz
[142]	200 kW	4000	6	800 Hz

In [57] the overall frequency range for aircraft propulsion motors is considered to be between 225 Hz to 750 Hz.

Most research so far has focused on lower frequencies (i.e. power frequency range), using thin film approximations or homogenized models to calculate the losses [130, 133, 143]. In [144] it was shown that for frequencies above approximately 100 Hz, homogenized models consistently underestimate AC magnetisation loss since they only consider the loss in the HTS layer.

8.5.1 Dynamic Loss in High Frequency Magnetic Fields

In this section the 2D multi-layer model, based on the ***H***-formulation, is used to quantify the total loss, *i.e.* dynamic and magnetisation loss, for superconducting tapes subject to magnetic fields up to 800 Hz. Only a pure AC field is applied to investigate the impact of the frequency alone. The loss in each layer, i.e. copper, silver, HTS and substrate are calculated using the methods described in section 8.1. The same tape parameters as shown in table 8.4 were used. The two calculation methods for quantifying the dynamic loss, which were introduced in section 8.3, are again used together. To validate the models at a higher frequency, the loss results are compared to experiments at a frequency of 112.5 Hz. The experimental results were again provided by researchers of the Robinson Research Institute at the Victoria University of Wellington [131]. The loss results compared to the experiments are shown in figure 8.16. Similar to before, the applied magnetic field ranges from 0 mT to 100 mT in 10 mT steps and the investigated load factors are 0.3, 0.5, 0.7 and 0.9. The two methods are in good agreement with each other and match well with the experiments. When comparing the loss results to figure 8.9, it can be seen that the loss at a higher frequency is much larger. The non-linear region also still takes effect for large load factors and large applied fields as was described in section 8.3.

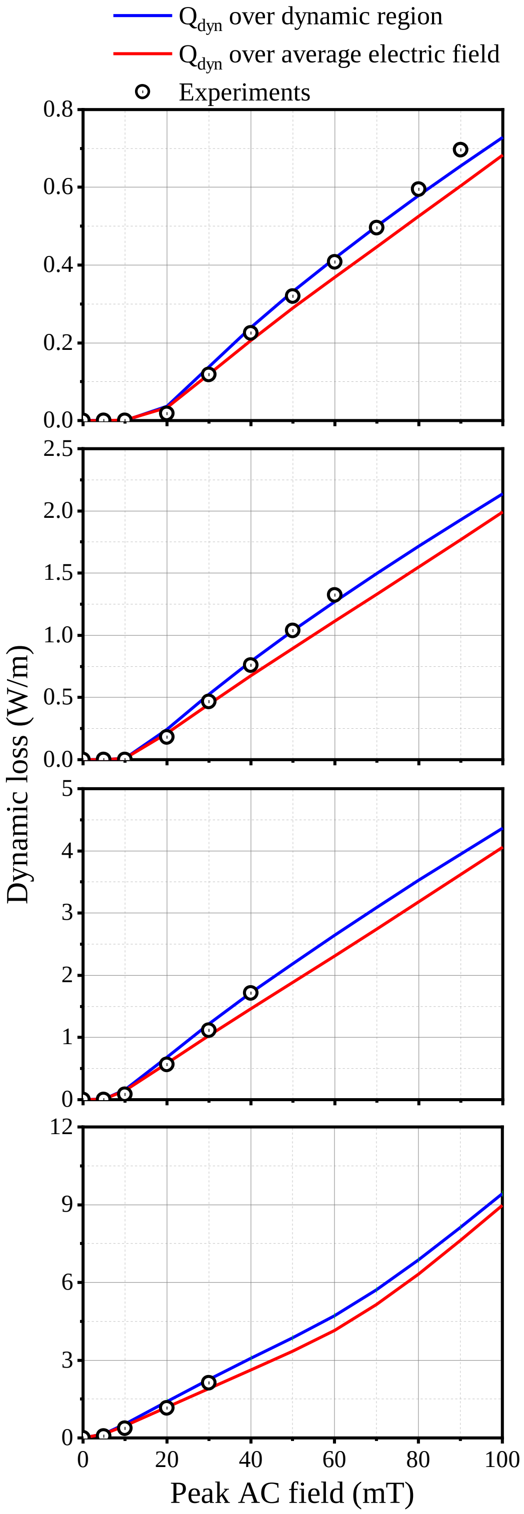

Figure 8.16. Total dynamic loss results with experiments for load factors of 0.3, 0.5, 0.7 and 0.9 with an AC applied field of 0 mT to 100 mT in 10 mT steps [127].

With the two numerical model validated with experiments for a higher frequency, the dynamic loss results were investigated for an applied field frequency up to 800 Hz. The applied field magnitude was chosen as 50 mT. Again, load factor of 0.3, 0.5, 0.7 and 0.9 were investigated. The results are shown in figure 8.17.

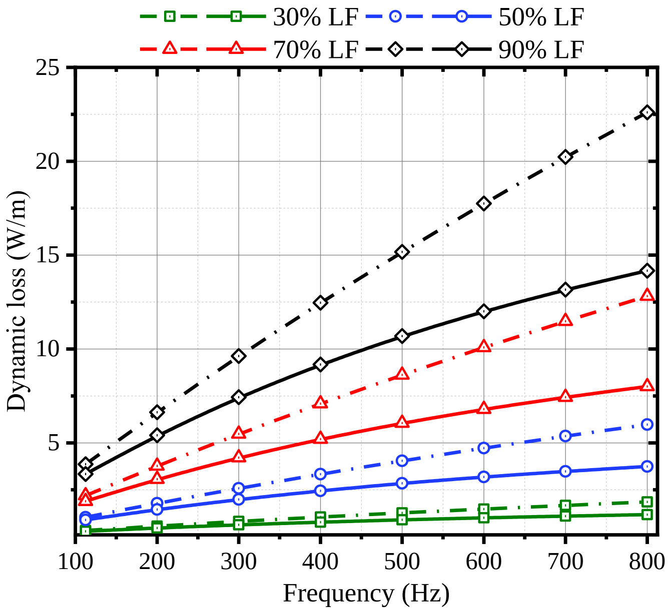

Figure 8.17. Dynamic loss over a frequency range of 112.5 Hz to 800 Hz for a load factor of 0.3, 0.5, 0.7 and 0.9 and an applied field of 50 mT. The dash – dot line uses the dynamic region method and the simple line uses the average electric field to calculate the dynamic loss [127].

For a low frequency the two methods agree well with each other, but as the frequency increases, the dynamic loss results calculated from either method start to deviate. For a load factor of 0.3, the calculated loss from either method stays in relatively good agreement. The difference in the calculated results from the two methods can be explained through investigating the current density and magnetic field distributions in the tape.

Figure 8.18 highlights the current density and magnetic field profiles for a frequency of 112.5 Hz, 400 Hz and 800 Hz, at a load factor of 50 % and an external AC field of 50 mT. For a frequency of approximately 100 Hz and below, the dynamic region can be clearly defined as a function of the load factor. However, as the frequency increases, a higher magnetisation current is induced around the edges of the tape, which pushes the transport current further into the centre reducing the transport current area, and hence the size of the dynamic region. Due to the reduced area, the transport current density in the dynamic region increases.

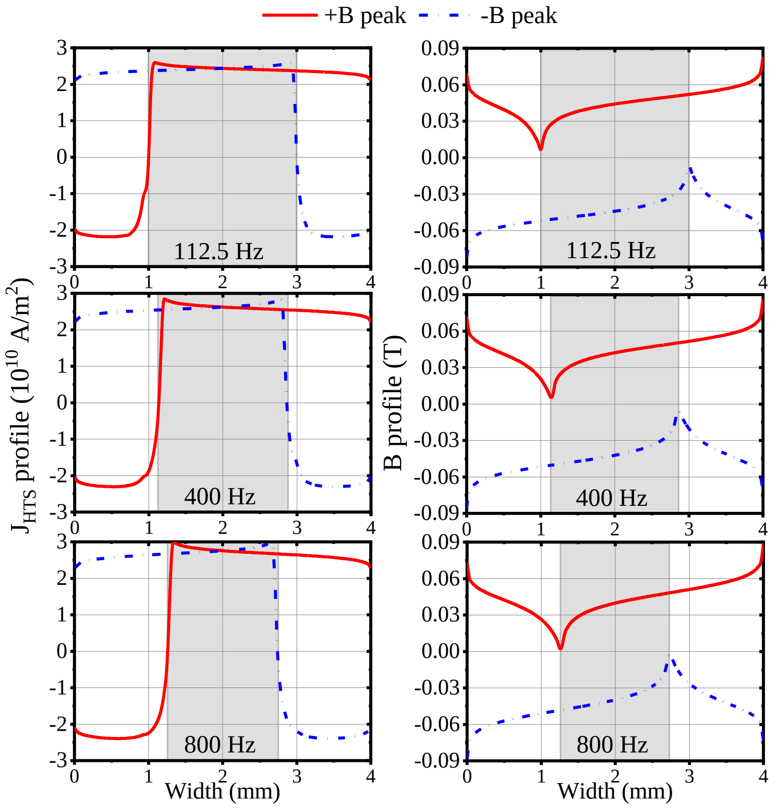

Figure 8.18. Current density and magnetic field profiles for the HTS layer for a load factor of 0.5 and an applied field of 50 mT and frequencies of 112.5 Hz, 400 Hz and 800 Hz [127].

For 112.5 Hz, the peak current density in the transport current region is approximately $2.5{\cdot}10^{10}$ A/m^2, for 800 Hz the peak current density increases to $3{\cdot}10^{10}$ A/m^2. However, overall, the area under the curve decreases as the frequency increases. Since for a load factor of 0.3 the transport current already only occupies a small area of the tape, the increased magnetisation current has little effect on the dynamic region and hence, the calculated loss for either method stays in relatively good agreement.

From the results it can be seen that the dynamic loss (W/m) increases with frequency, however, as the frequency increases the dynamic loss per cycle (J/cycle/m) decreases. This is partly due to the reduced transport current region, but another phenomenon takes place. As the frequency increases, the penetration depth of the magnetic field decreases, and the magnetic field becomes weaker the further it travels into the HTS tape according to the Beer-Lambert law. This results in a lower net flow of flux across the DC current carrying region, reducing the dynamic loss per cycle.

Since the penetration depth of the magnetic field decreases, this poses the question of how the current density distribution in the copper stabilizers, which are the outermost layers of the tape, change with frequency. Figure 8.19 shows the current density distribution within the copper stabilizers for load factors of 0 %, 30 % and 90 % for an applied field of 50 mT with a frequency of 112.5 Hz and 800 Hz.

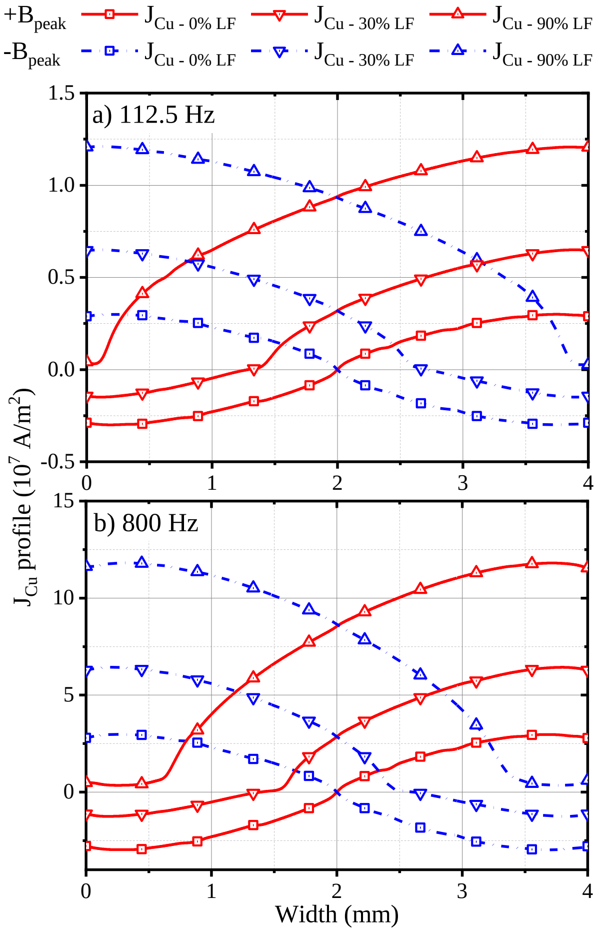

Figure 8.19. Current density profiles in the copper layer for no current, 0.3 load factor and 0.9 load factor with an applied field of 50 mT and a frequency of a) 112.5 Hz and b) 800 Hz [127].

For the cases where solely an AC field is applied, the current density distribution is symmetrical. It increases by a factor of 10 from 112.5 Hz to 800 Hz. When the HTS tape is also carrying a DC current, the current distribution in the copper is shifted upwards into the positive direction, indicating that a portion of the DC current is now flowing in the copper layers. This phenomenon can be explained through figure 8.18. The increased current density in the transport current region leads to a lower conductivity of the HTS layer due to its dependence on the critical current and transport current densities. The reduced conductivity causes a small proportion of the transport current to flow in the copper layer, since the HTS and copper layers form a parallel electric circuit. A higher load factor leads to a further shift of the copper current distribution and further increases the current density in the copper.

Since the current density distribution in the copper and HTS layer significantly change with frequency and load factor, it becomes essential to consider the total loss in the HTS tape to accurately study and understand the loss characteristics of field windings in very high RPM machines.

8.5.2 Total Loss in High Frequency Magnetic Fields

This section will discuss the total loss in the HTS tape in regard to dynamic loss and magnetisation loss as well as the loss in the various layers for the investigated frequency range. The total loss is defined as the magnetisation loss as well as the dynamic loss. To compare the effect of the DC transport current on the total loss, the loss in a HTS-coated conductor carrying a DC transport current is also compared to a HTS tape, which is only subject to an applied magnetic field (*i.e.* 0% LF), hence exhibiting solely magnetisation loss. It was shown in [144] that the ***H***-formulation based numerical model can reliably be used to determine the magnetisation loss over a wide frequency range. Figure 8.20 shows the total loss, the dynamic loss, the difference between the two losses and the magnetisation loss of a tape subject to solely an AC field as a reference.

It can be seen that overall, the total loss for an HTS tape carrying a DC current with an AC applied field is the summation of the magnetisation loss and the dynamic loss. This holds true for a load factor up to 0.7 and a frequency up to approximately 400 Hz. As the frequency increases beyond 400 Hz, the magnetisation loss for the case with a DC transport current becomes greater than the magnetisation loss for solely an AC applied field. This can be explained through the current density profiles in the copper, which were highlighted in figure 8.19. As the frequency increases, more current is induced in the copper stabilizers, this phenomenon is further reinforced by the transport current, due to the reduced conductivity of the HTS layer. The higher the load factor, the higher the current in the copper, hence additional loss is generated in the copper layer as compared to the 0 % load factor magnetisation case. For a load factor of 0.9, almost the whole width of the HTS layer is occupied by the transport current, hence the total loss is dominated by the dynamic loss. After a frequency of approximately 500 Hz, the magnetisation loss starts to become greater than the dynamic loss due to the reduced penetration depth of the applied field and the reduced dynamic region. Overall, it was shown that for low load factors, the magnetisation loss dominates the contribution towards the total loss. At a load factor of 0.7, which is a common load factor for field windings to ensure safe operation, the dynamic loss and magnetisation loss are comparable up to approximately 300 Hz to 400 Hz, as the frequency increases further, the magnetisation loss becomes dominant.

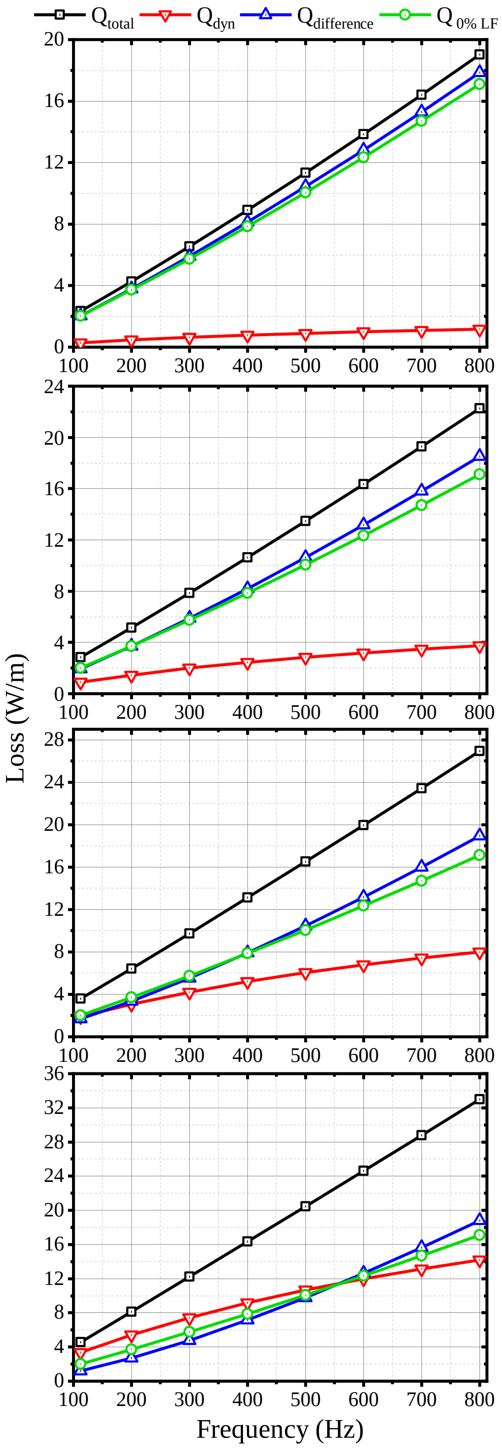

Figure 8.20. Loss components of an HTS tape subject to an AC field of 50 mT for a frequency range of 112.5 Hz to 800 Hz for load factors of 0.3, 0.5, 0.7 and 0.9 [127].

While for fully superconducting machines most studies only consider the AC loss in the stator, results show that the induced loss in the rotor field windings can become significant as well depending on the frequency and magnetic field environment within the machine.

Since the loss distribution in each layer is highly dependent on the applied frequency, it is also important to investigate the total loss contributions from each layer under the investigated frequency and magnetic field amplitude ranges. Figure 8.21 shows the loss ratio, which is the loss in each layer of the tape divided by the total loss in the tape, for the HTS, copper, silver, and substrate layers as the frequency increases from 112.5 Hz to 800 Hz using an applied field of 100 mT.

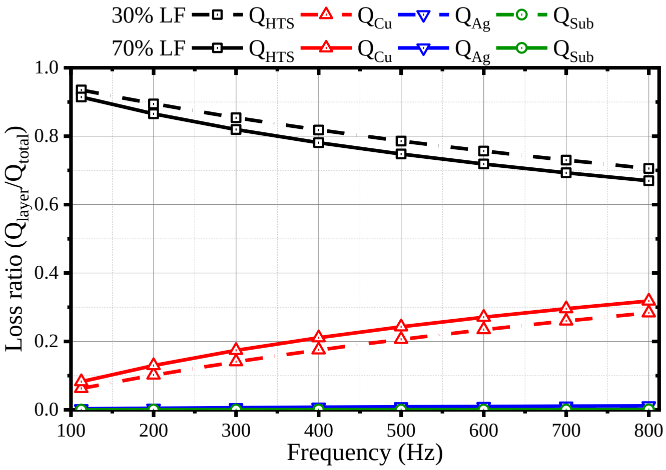

Figure 8.21. Contribution to the total loss of each layer over a frequency range of 112.5 Hz to 800 Hz for an applied AC field of 100 mT [127].

It can be seen that virtually no loss occurs in the silver and substrate layers over the investigated frequency range. For a frequency of approximately 100 Hz and below, the vast majority of the loss occurs in the HTS layer. As the frequency increases, the contribution to the overall loss by the copper layer increases significantly. At 800 Hz, approximately 30 % of the total loss occurs in the copper layers. From the figure it can also be seen that the loss ratio is dependent on the load factor, a higher load factor leads to more loss occurring in the copper layer, which agrees well with the results highlighted in figure 8.19.

Since the field magnitude itself also strongly influences the loss distribution in the HTS tape, it is also worth investigating the loss ratios for different applied field magnitudes. In figure 8.22, the loss ratios for the HTS and copper layers are shown for an AC applied field of 0 mT to 100 mT. The losses in the silver and substrate layers were omitted since they were found to be virtually zero as was shown in figure 8.21. It can be seen that the higher the applied magnetic field, the higher the contribution of the copper loss towards the total loss. Already at frequencies below 400 Hz, up to 20 % of the loss can occur in the copper layer depending on the resulting magnetic field magnitude in the machine.

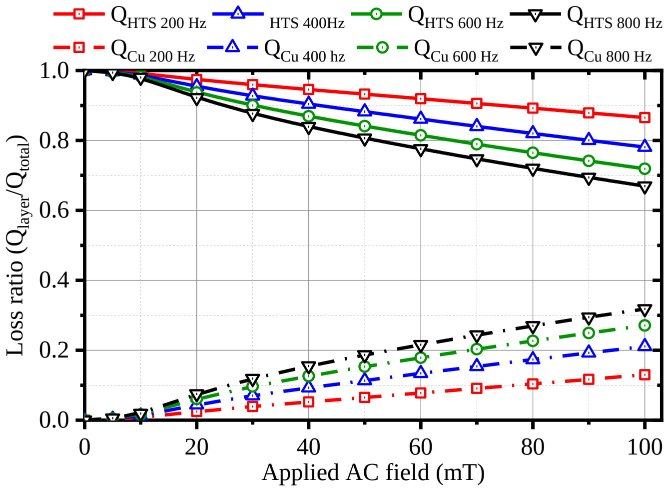

Figure 8.22. Contributing ratio to the total loss for the HTS and copper layers for an applied AC field of 0 mT to 100 mT for a frequency of 200 Hz, 400 Hz, 600 Hz and 800 Hz and a load factor of 0.7 [127].

Overall, results show that for frequencies above 100 Hz it becomes essential to use multi-layer models to accurately predict the losses in HTS field windings. Using homogenized or single layer models could lead to underestimating the loss by more than 30 % depending on the rotational speed of the machine and the magnetic field environment. It was shown that not only the AC loss in the stator of high speed machines is of importance, but also the loss that could occur in the field windings, and that it is essential to consider this loss in the design of the rotor cooling system.

8.5.3 Field Winding Loss Mitigation

It was shown in the previous section that high frequency fields can lead to very high losses. Hence methods need to be developed to mitigate this loss. For the reduction of AC loss several methods are being considered, one approach which has been shown to work very well, is the striation of tapes. In [145], tapes are cut into narrower strips and stacked on top of each other creating a ‘soldered-stacked-square’ 2G HTS conductor. It was shown that this approach can reduce AC losses by up to 80 %. The striation can also be done before ReBCO synthesis through laser scribing and oxidisation [37]. However, these methods involve additional complicated manufacturing steps. In rotating machines, often an electromagnetic shield is placed in the air gap to provide some shielding to the superconducting field windings. However, as was discussed in Chapter 3, one major issue with most superconducting machines is that the mechanical air gap in the machine is not equal to the electromagnetic air gap. This is in part due to the field windings requiring a cryostat and in combination with an electromagnetic shield, the problem is further worsened. The larger electromagnetic air gap leads to higher HTS tape requirements. Figure 8.23 shows a schematic of a synchronous machine with EM shields. In the figure it can be seen that two electromagnetic shields were placed in the air gap, according to [146], this is one of the most common configurations. The mechanical air gap is also highlighted and as can be seen, the mechanical air gap is much smaller than the electromagnetic air gap.

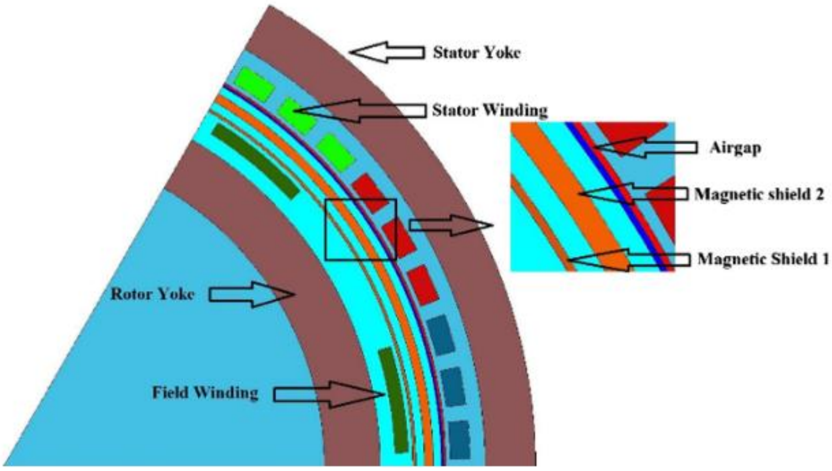

Figure 8.23. Schematic of a radial flux HTS synchronous machine [146].

To reduce the loss in superconductors, another method exists, which does not influence the air gap length or requires complicated manufacturing processes. In [36], it was shown that placing magnetic flux diverters at the edges of tapes reduces the AC transport current loss. The loss is reduced because the flux diverters reduce the perpendicular penetrating flux to the tape's long surface. The concept is illustrated in figure 8.24.

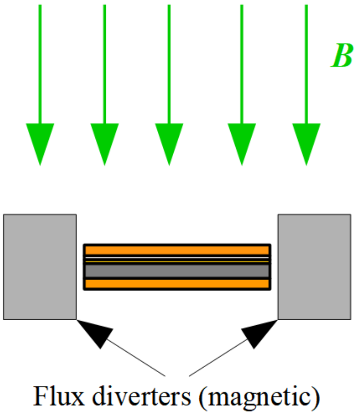

Figure 8.24. Superconducting tape with flux diverters

To investigate the potential of using flux diverters to reduce the dynamic and magnetisation loss, the same tape model as discussed in the previous sections is used with flux diverters placed 200 µm from the edges of the tape on either side. In [36], it is stated that the flux diverter in particular works very well for high load factors since the HTS loss becomes very high and the iron losses are very small when compared to the HTS loss. Hence for the simulations a load factor of 70 % was chosen. To simplify the model, the iron losses are ignored and a constant permeability for the iron was used. Different values of μ_r were tested and the influence on the loss was found to be minimal. The height and width of the diverters are 2 mm, in [36] it was shown that the loss is at its minimum for a flux diverter height of 1.67 to 2 mm.

Figure 8.25 shows the results for dynamic loss and magnetisation loss with and without a flux diverter when applying a field of 50 mT. The loss results without a flux diverter are the same as presented in figure 8.20. As can be seen, a significant decrease in loss could be achieved, especially in regard to the total loss. It can be seen that the reduction in dynamic loss is not as effective, which is due to the flux diverters mainly diverting the magnetic flux near the edges of the tape. Dynamic loss however occurs due to the magnetic flux penetrating the dynamic region in the centre of the tape, which is less affected by the flux diverters. Nevertheless, flux diverters can be identified as a promising solution to the reduce loss in field windings without affecting the magnetic air gap length.

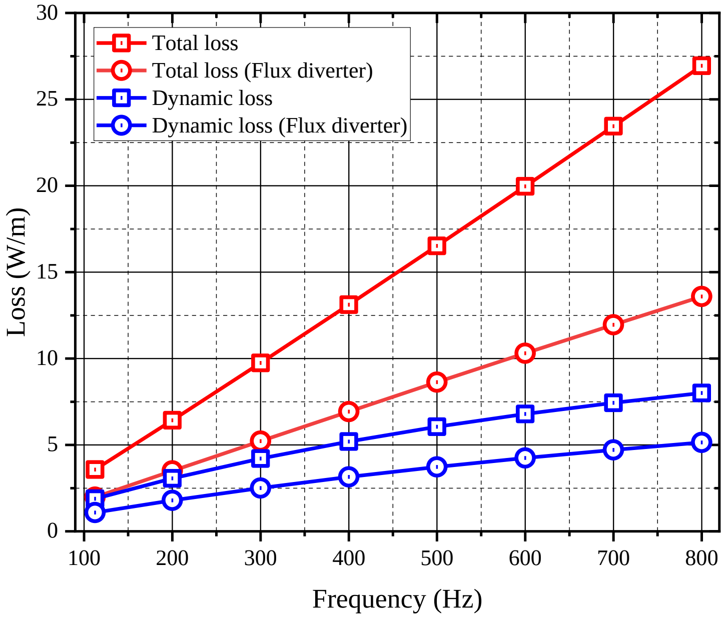

Figure 8.25. Total loss and dynamic loss with and without a flux diverter for an applied field of 50 mT and a load factor of 70 %.

8.6 2D Axisymmetric Model

In this section simulation results with a 2D axisymmetric model for a double pancake coil will be introduced. The simulations are performed in the frequency range relevant to electrical machines. The lowest frequency was chosen as 20 Hz, such as in low RPM machines and the highest frequency is 1 kHz such as in very fast spinning machines. The 2D axisymmetric model layout is shown in figure 8.26.

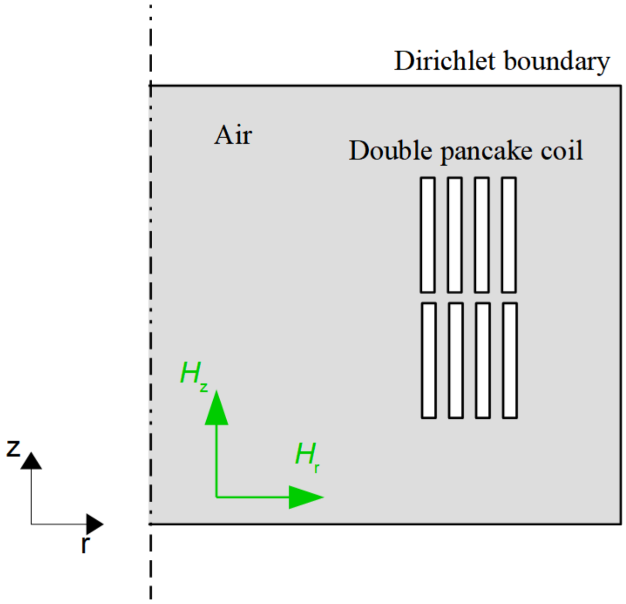

Figure 8.26. 2D axisymmetric model layout.

Similar to the previous model, there is only one component for the electric field E_θ and the current density J_θ. To change to a 2D axisymmetric model equations 8.1, 8.2 and 8.3 need to be changed into cylindrical coordinates such as that [55, 147]:

$$J_\theta = -\frac{\partial H_z}{\partial r} + \frac{\partial H_r}{\partial z} \tag{8.20}$$

$$\begin{bmatrix} -\dfrac{\partial E_\theta}{\partial z} \\ \dfrac{1}{r}\dfrac{\partial (rE_\theta)}{\partial r} \end{bmatrix} = -\mu_0\mu_r \begin{bmatrix} \dfrac{\partial H_r}{\partial t} \\ \dfrac{\partial H_y}{\partial t} \end{bmatrix} \tag{8.21}$$

$$E_\theta = E_0 \left(\frac{J_\theta}{J_c(B)}\right)^n \tag{8.22}$$

Substituting 8.20 and 8.22 into 8.21 results in an equation similar to equation 8.4 but in cylindrical coordinates. With the equations changed to cylindrical coordinates the 2D axisymmetric model is set up in the same fashion as described in section 8.1. For the geometry it was decided to model an 8 turn double pancake coil (DPC) with an inner diameter of 0.0625 m. This coil geometry matches the coil which was manufactured during the course of this research work. The wound coil is shown in figure 8.27. The coil was wound with 4 mm wide tape and each turn was insulated with Kapton tape.

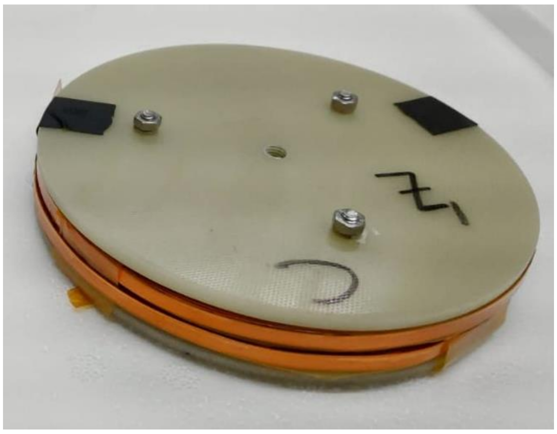

Figure 8.27. 8-turn double pancake HTS coil

Due to the COVID-19 pandemic it was not possible to conduct any experiments with the coil. However, the simulation results for the same coil geometry are given in this section, which can be used by future researchers in conjunction with possible experiments. A spacing of 200 µm between turns was assumed in the simulations to account for the Kapton tape thickness. The tape parameters used in the model are shown in table 8.10.

Table 8.10. Fujikura FYSC-SCH04 tape parameters.

Temperature	77 K
I_C (self-field)	230 A
n-value	23
B_0	0.2 T
k	0.67
α	0.6
Tape width	4 mm
Superconducting layer thickness	1.9 µm
Substrate thickness	75 µm
Silver thickness	2 µm
Copper thickness	40 µm

8.6.1 Coil AC Transport Current Loss

In this section the coil AC transport current loss is shown for load factors of 0.3, 0.5, 0.7 and 0.9 for a frequency of 20 Hz to 1 kHz. Figure 8.28 shows the total transport current loss, *i.e.* loss in all layers, for the different load factors over the investigated frequency range. To get the total loss of the coil, the loss in W/m can be multiplied by the circumference of the coil and the number of turns.

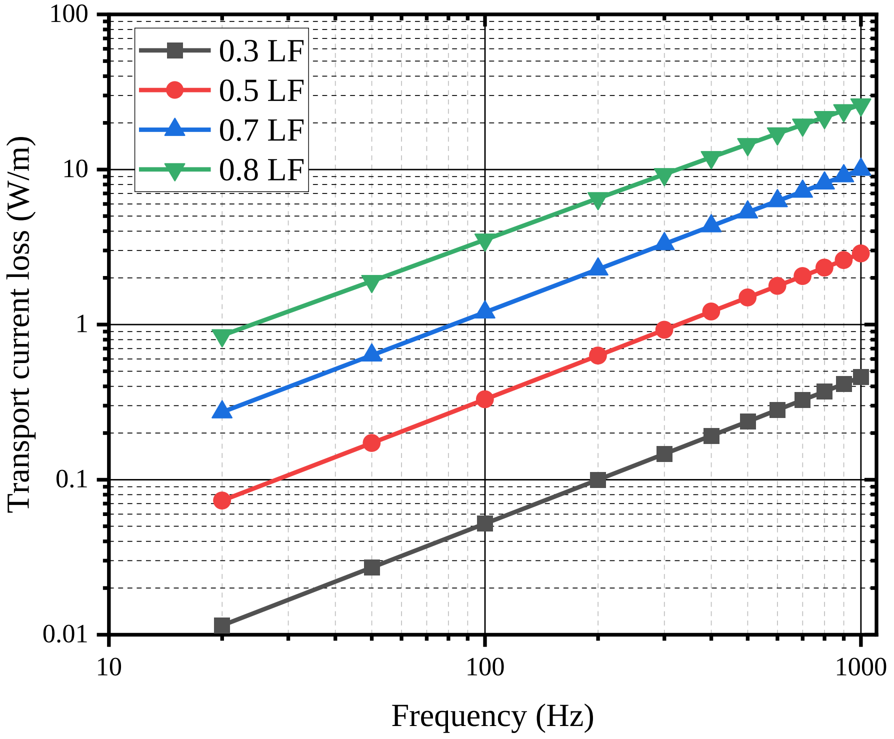

Figure 8.28. Total AC transport current loss for 8-turn double pancake coil from 20 Hz to 1 kHz for load factors of 0.3, 0.5, 0.7 and 0.9.

8.6.2 Coil Magnetisation Loss

In this section the magnetisation loss of the coil is introduced. The simulations were done in the same frequency range as for the transport current loss. The investigated applied magnetic fields were 50 mT and 100 mT. Figure 8.29. shows the resultant loss in W/m.

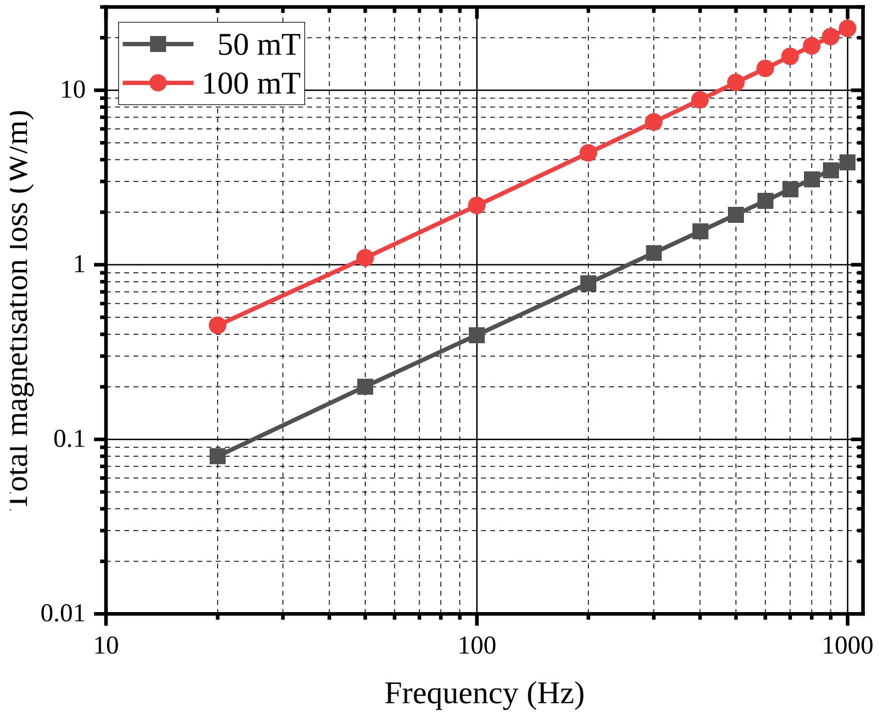

Figure 8.29. Magnetisation loss for the 8-turn double pancake coil for a frequency range of 20 Hz to 1 kHz for applied perpendicular fields of 50 mT and 100 mT.

8.6.3 Coil Dynamic Loss

In this section the dynamic loss results are shown, the average electric field method is used to calculate the loss. To adjust this method for the 2D axisymmetric model, the average electric fields needs to be calculated over the volume of the coil as shown in equation 8.23.

$$E_{\text{ave}}(t) = \frac{\int_V \boldsymbol{E}(t)\, dV}{V} \tag{8.23}$$

The resultant dynamic loss per cycle can then be calculated according to equation 8.10.

Figure 8.30 shows the total loss and dynamic loss of the 8-turn coil for an applied field of 50 mT at load factors of 30 % and 50 % over a frequency range of 100 Hz to 1 k Hz. Similar to the results shown in figure 8.20, it can be seen that the loss per cycle of the dynamic loss decreases, hence leading to a slower increase in dynamic loss as the frequency increases.

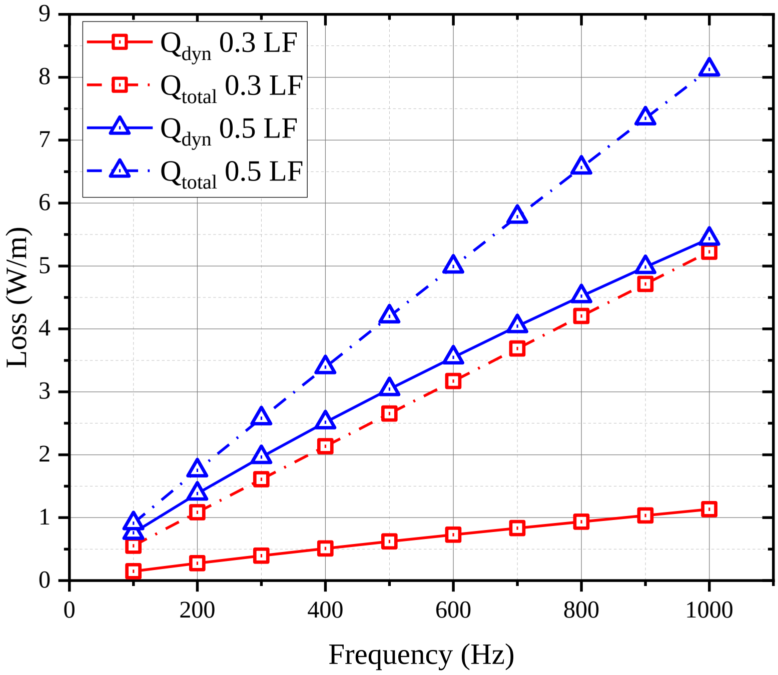

Figure 8.30. Dynamic loss and total loss from 100 Hz to 1 kHz for an applied magnetic field of 50 mT and a load factor of 30 % and 50 %.

The next section discusses the potential experimental setups for measuring transport current loss and dynamic loss.

8.7 University of Edinburgh Applied Superconductivity Laboratory

At the University of Edinburgh, a new purpose-built laboratory was established for applied superconductivity research. However, due to the COVID-19 pandemic, no actual tests with superconducting coils could be conducted. This section was still added to this thesis to provide valuable insights on the laboratory equipment and superconductor loss experimental setups. The hope is to enable future researchers to setup experiments with relative ease and potentially conduct experiments to further verify the simulations results presented in this thesis.

8.7.1 Small Cryostat

The laboratory features a small custom-built cryostat manufactured by A.S. Scientific Products Ltd. In combination with a Trivac E2 vacuum pump and a Turbovac50 turbomolecular pump, an operational pressure of ~10^{-8} mbar can be reached, minimizing the heat loss through convection. The pressure is monitored over an analogue pressure gauge and a PTR90 digital pressure gauge. The vacuum system is shown in figure 8.31. Since the turbomolecular pump can only operate once a rough vacuum has been established a valve was added in its path, once a pressure of 10^{-1} mbar is reached, the Turbovac valve can be opened and the turbomolecular pump may be switched on.

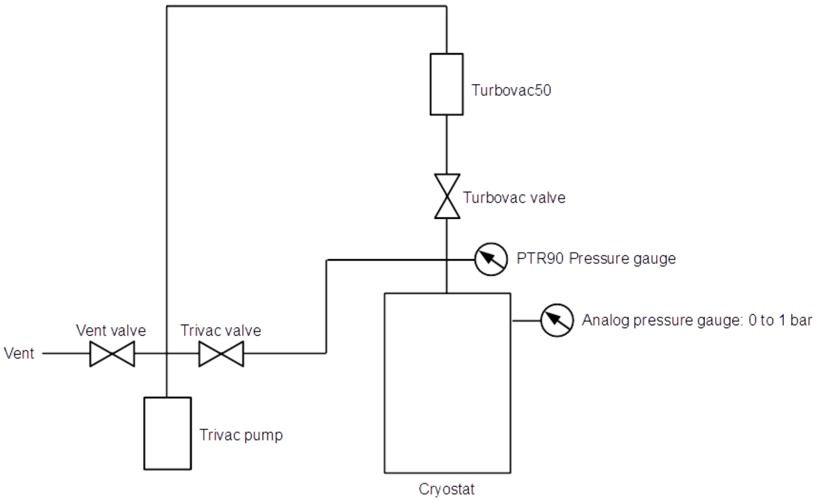

Figure 8.31. Vacuum system schematic.

A Cryomech AL330 cooling head is connected to the cryostat over a CP970 compressor. The base temperature of the cooling head is 12 K (no load). As the temperature increases the available cooling power increases as well, for instance at 20 K the cooling head can provide

33 W of cooling power. At 50 K, the available cooling power increases to 141 W. The cooling head is based on the Gifford-McMahon cooling cycle; hence it features a compression and expansion space, a regenerator and a displacer. As was discussed in chapter 3, GM coolers are the most wide-spread cryocoolers. A picture of the experimental setup is shown in figure 8.32.

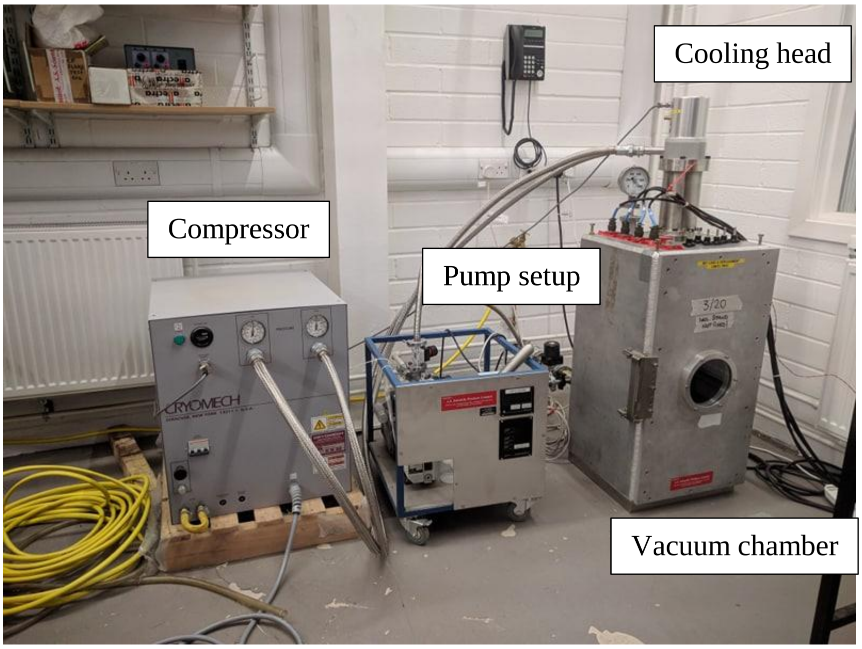

Figure 8.32. Small cryostat experimental setup.

The cooling head temperature is controlled over a Lakeshore 336 temperature controller, a heating plate is connected to cooling head, which is used to regulate the temperature through the temperature controller. The laboratory features several Lakeshore 218 temperature monitors to observe the temperature at various locations on the superconducting test subject. Cernox CX-1050AA temperature sensors, which have a temperature range of 4.2 K to 420 K, are used.

The complete setup was built and tested, to confirm the operation of the cooling head, during the conducted research work, however, due to the COVID-19 pandemic, no superconductor tests were conducted. To enable future researchers at the University of Edinburgh to use the system with ease, a detailed manual for the experimental setup is attached in the appendix.

8.7.2 Superconductor Loss Measurement Setups

The required equipment for superconductor loss measurements were acquired during the conducted research and the loss measurement setups were established. However, again due to the COVID-19 pandemic, no superconductor loss results could be recorded. To provide future students and researchers with some guidance, the established measurement systems have been added to this thesis.

- **AC loss measurements**

To measure the AC loss of an HTS coil, the resistive voltage needs to be known, such as that the loss can be expressed as:

$$P_{\mathrm{loss}} = I_{\mathrm{RMS}} \cdot V_{\mathrm{R-RMS}} \tag{8.24}$$

The voltage drop measured across an HTS coil consists of two components:

$$V_{\mathrm{coil}} = V_{\mathrm{R}} + jV_{\mathrm{L}} \tag{8.25}$$

Since the resistance of an HTS coil is extremely low, the inductive voltage component dominates the measured voltage across the coil. It is however only the resistive component which results in heating loss being produced. Whereas for a normal conductor the resistance can simply be measured, the resistance of HTS tapes is highly non-linear and depends on its operating conditions. To measure solely the resistive voltage drop across the HTS coil, the inductive voltage component needs to be cancelled out. This is achieved by adding a cancelling coil to the circuit. The cancelling coil costs of two separate coils which are wound around the same former. The distance between the two coils can be varied to change the mutual inductance. Setting the mutual inductance to be equal to L_{HTS} results in an induced voltage in the cancelling coil which is equivalent to jV_{L}. Hence the resistive voltage across the HTS coil can be indirectly measured by subtracting the induced voltage in the cancelling coil from the voltage drop across the HTS coil:

$$V_{\mathrm{coil}} = V_{\mathrm{R}} + jV_{\mathrm{L}} - jV_{\mathrm{M}} \tag{8.26}$$

To set the correct mutual inductance two possible methods were identified. The first method is through a magnetics analyser. Firstly, the inductance of the test subject has to be measured. Once the inductance L_{HTS} is known, the mutual inductance M of the cancelling coil can be set.

The mutual inductance is defined as:

$$M = k\sqrt{L_{\mathrm{C1}}L_{\mathrm{C2}}} \tag{8.27}$$

where k is defined as the coupling factor and L_{C1} and L_{C2} are the self-inductances of the cancelling coils.

Since L_{C1}, L_{C2} and L_{HTS} are known and M is equal to L_{HTS}, the equation can be rearranged to give the required coupling factor such as that

$$k = \frac{L_{\mathrm{HTS}}}{\sqrt{L_{\mathrm{C1}}L_{\mathrm{C2}}}} \tag{8.28}$$

The coupling factor k can be measured indirectly by measuring the short-circuit and open-circuit inductance of the cancelling coil. This is done by connecting the analyser to the coil with the highest inductance of the two, to increase the accuracy, and measuring the inductance when the secondary coil is short-circuited and open-circuit. The coupling factor can then be defined as:

$$k = \sqrt{1 - \frac{L_{\mathrm{SC}}}{L_{\mathrm{OC}}}} \tag{8.29}$$

Where L_{SC} is the short-circuit inductance and $\mathrm{L_{OC}}$ is the open-circuit inductance. The distance between the cancelling coil is varied until the required coupling factor is reached.

The second method would be to send a known current I (for example 1 A) through one of the coils of the cancelling coil setup and to measure the open-circuit output voltage at the other coil. The measured voltage will be equal to:

$$V_2 = \omega M I \tag{8.30}$$

The distance between coils is then varied until $V_2 = V_{\mathrm{L\text{-}HTS}}$, which implies that $M = L_{\mathrm{HTS}}$.

Figure 8.33 shows the experimental setup for AC loss measurement of superconductors. The experimental setup consists of a power source, in this case a signal generator in conjunction with a power amplifier, to provide the required current to the superconducting coil. A current transducer is used to measure the current. The voltage drop across the test subject is measured using two oscilloscope channels and the induced voltage in the cancelling coil is measured using the remaining channel.

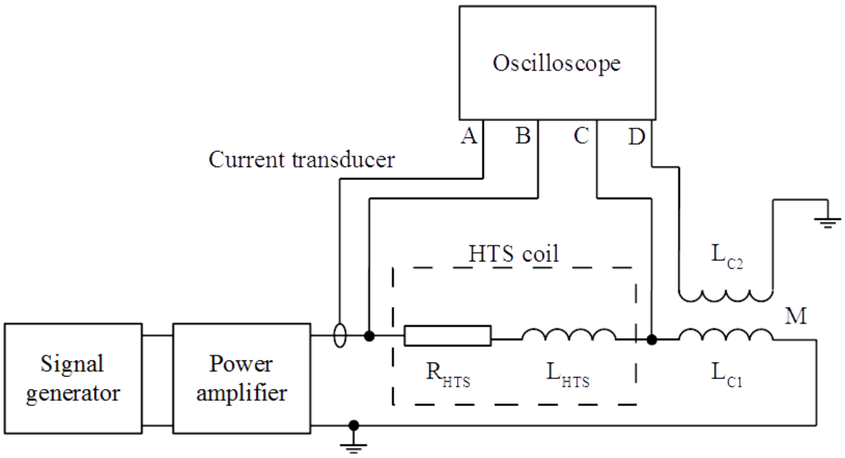

Figure 8.33. Experimental setup

With the correct mutual inductance, the circuit as shown in figure 8.33 can be used to cancel out the inductive part of the HTS coil and determine the AC loss. To test the setup, the circuit was tested with a simple copper coil as an example. Figure 8.34 shows the cancelling coil with the copper coil, Litz wire is used for the copper coil and the primary coil of the cancelling coils, 1.6 mm diameter copper wire is used for the secondary coil. The test copper coil has 8 turns, which is equivalent to the HTS coil that was wound. Both copper and HTS coils have a diameter of 125 mm.

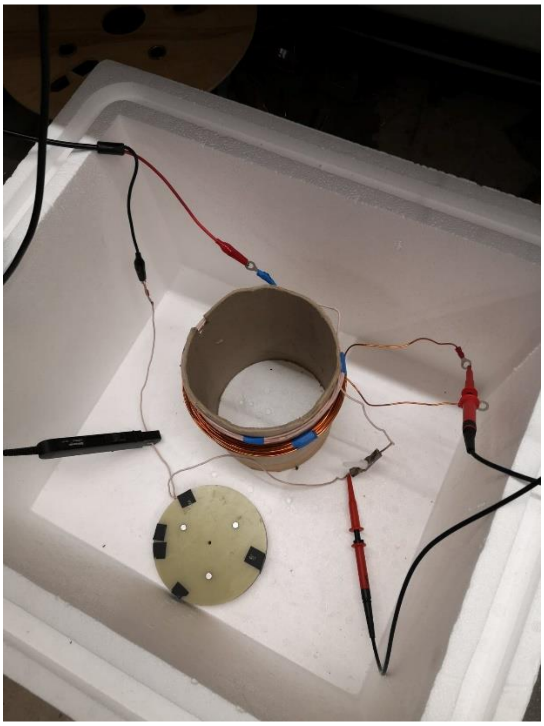

Figure 8.34. Copper coil and cancelling coil

Table 8.11. Setup parameters

Parameter	Value	Unit
L_{copper}	15.588	μH
R_{copper}	130	mΩ
L_{c1}	16.65	μH
L_{c2}	143.92	μH
k_{required}	0.318436	/
k_{actual}	0.31826	/

The resistance of the copper coil is 130 mΩ with an inductance of 15.588 μH. The mutual inductance of the cancelling coil is setup to give a value of 15.557 μH. Figure 8.35 shows the oscilloscope waveforms. The voltage drop along the copper, the cancelling coil voltage and the current are shown. Table 8.12 shows the RMS values of each parameter.

Table 8.12. Setup parameters

Parameter	Value	Unit
$V_{\text{coil RMS}}$	5.22	V
$V_{\text{cancel RMS}}$	5.3	V
I_{RMS}	0.501	A
$R_{\text{resultant}}$	82.5	mΩ

From the parameters the resultant resistance of the coil can be estimated to be 82.5 mΩ. While this value is not exactly the resistance of the copper coil, it is expected to reach the actual value through further adjusting the mutual inductance. A similar setup was used at the University of Manchester [148].

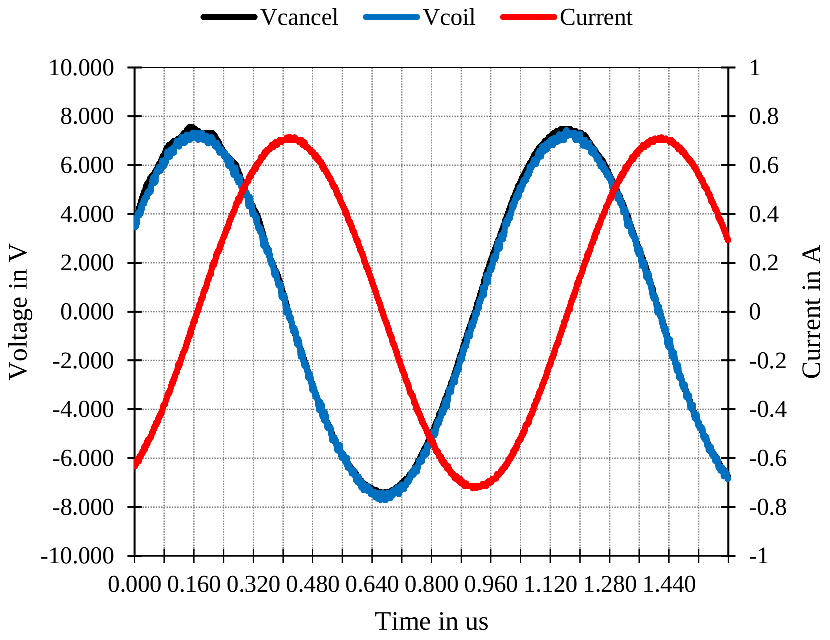

Figure 8.35. Oscilloscope waveforms for 100 kHz.

Another widely used method is to use a lock-in amplifier. The lock-in amplifier removes a lot of the calibration that is required when simply using an oscilloscope. The lock-in amplifier takes the phase and frequency from the current as a reference, and only measures voltages in reference to that signal. A SR830 lock-in amplifier manufactured by Stanford Research Systems was used for initial tests with copper coils. To further improve the accuracy, the lock-in amplifier is still used in combination with the cancelling coil set up, where the mutual inductance of the cancelling coil is set to be equal to the inductance of the test subject. The experimental setup schematic is shown in figure 3.36. The lock-in amplifier is set to measure the differential voltage (A – B), which includes the loss voltage. The reference signal is provided by the current transducer, once the lock-in amplifier has locked its frequency to the reference signal, the amplifier ‘Auto Phase’ function can be used to measure the voltages in phase to the reference signal, which is the pure loss voltage. Figure 8.37 shows the experimental setup. The oscilloscope is used to measure the current, the current signal is then also relayed as the reference signal to the lock-in amplifier. When the lock-in amplifier has locked into the reference signal, the distance between the two cancelling coils can be changed and the Y-channel output voltage remains 0. The X-channel output voltage reads out the loss voltage, in this case the loss voltage is 111.7 mV at 1 A, hence giving a closer result to the actual resistance of the copper coil, but further calibration was required. Initial tests were done to setup the experiments but due to the COVID-19 pandemic, the continuation of the tests was made impossible.

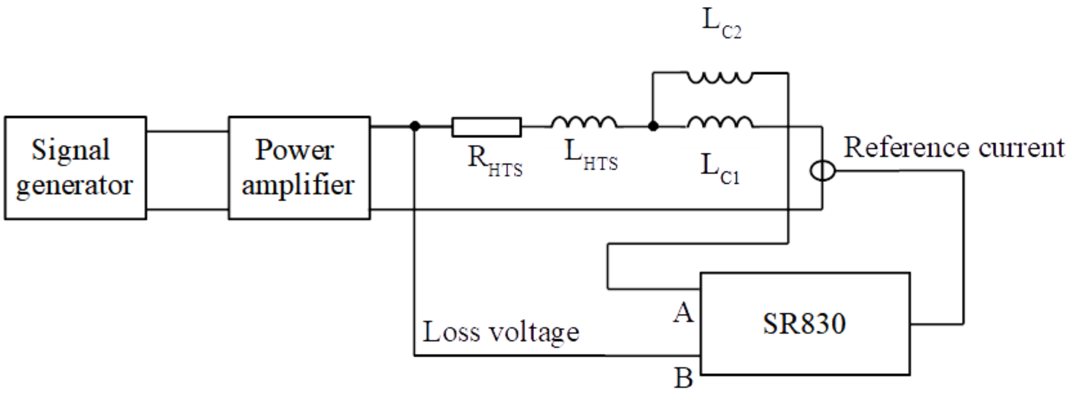

Figure 8.36. AC loss measurement setup with lock-in amplifier

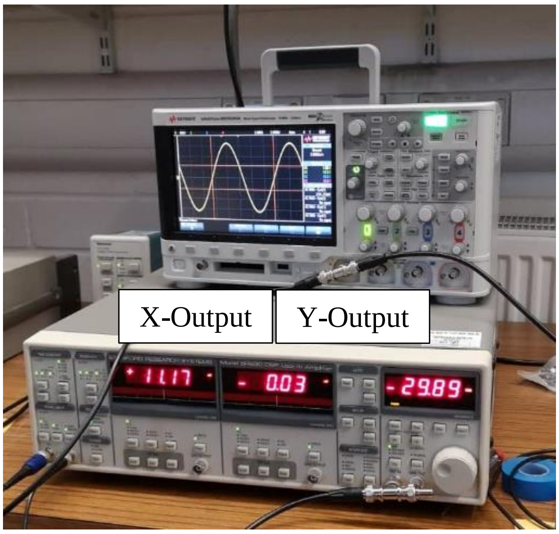

Figure 8.37. Lock-in amplifier and oscilloscope

Similar setups have been described in [149] and [150]. In [150] it is suggested to use two lock-in amplifiers to simplify the calibration of the phase and frequency references.

This section described the AC loss measurement setups and work that has been done during the research project. It is the hope that with the provided information, future researchers can continue the loss measurements.

- **Dynamic loss**

Almost all research so far in regard to dynamic loss has focused on a purely AC field being applied. However as has been discussed in the previous sections, in a machine environment, a large DC background field is present, which has a significant impact on dynamic loss. A new electromagnet setup was designed to apply magnetic fields over a wide range of frequencies and magnitudes. The electromagnet has two coils, one coil is operated with a DC current to set the DC background field, the second coil is operated with an AC current to set the AC field. While usually an air-cored setup is used, this magnet features an iron core to reach higher magnetic fields such as present in superconducting rotating machines. Figure 8.38 shows a schematic of the electromagnet and table 8.13 summarizes the dimensions and parameters. The electromagnetic was designed in conjunction with Fountain Design Ltd. to ensure the manufacturability of the proposed the design. The dimensions were chosen to ensure that iron saturation is avoided. The number of turns for each coil were chosen such as that existing equipment at the University of Edinburgh can be used to provide the necessary current. For performing the superconducting experiments, the complete electromagnet is submerged in liquid nitrogen. Single superconducting tapes and stacks of tapes can be placed in the centre of the middle leg to apply magnetic fields.

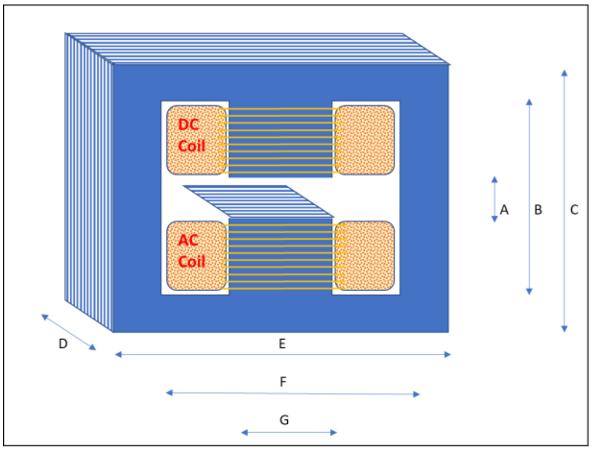

Figure 8.38. Electromagnet design.

Table 8.13. Electromagnet design

Parameter	Value	Unit
A	30	mm
B	120	mm
C	170	mm
D	150	mm
E	210	mm
F	160	mm
G	60	mm
Turns (DC)	955	/
Turns (AC)	153	
Max B_{dc}	0.4	T
Max B_{ac}	0.13	T
Max Frequency	250	Hz

One issue when using an iron core is that the iron can change the magnetic flux distribution on the superconducting tape, which changes the current density distribution and hence the loss. 2D FEA simulations were run for a range of air gap lengths, to find the minimal air gap length, which does not change the flux density distribution when the tape is carrying a DC current. A transport current of 45 A was chosen since that is the maximum current the available DC power source (Magnapower TSA1000-45) at the University of Edinburgh can supply.

Figure 8.39 shows the flux density distribution along the long surface of the tape when placed in the air gap of the electromagnet and when simply surrounded by air. The air gap length is 30 mm.

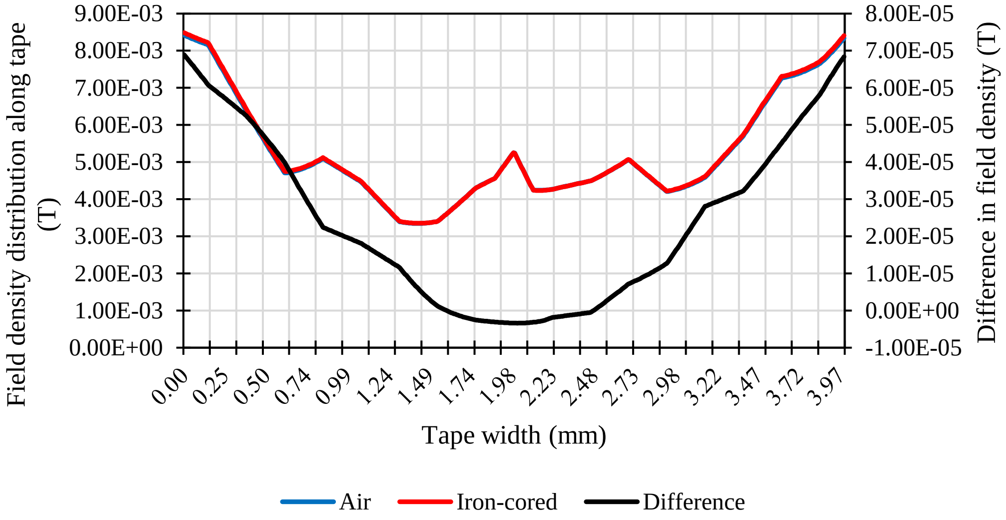

Figure 8.39. Flux density distribution along tape with and without the electromagnet when carrying a transport current of 50 A.

It can be seen that there is virtually no difference in the flux density distribution in the middle of the tape. The maximum difference occurs around the edges of the tape, which is approximately 70 μT. Hence, a 30 mm air gap length was deemed suitable for dynamic loss experiments. The length of the magnet was chosen to be 15 cm, which allows for the testing of tape samples of 10 cm length, maintaining an even magnetic field distribution along the length of the tape. A 10 cm length allows for a 5 cm distance between voltage taps and 2 cm between the voltage taps and the current leads, leaving 0.5 cm for the soldering of the current leads onto the tape [131]. Figure 8.40. shows the experimental setup schematic.

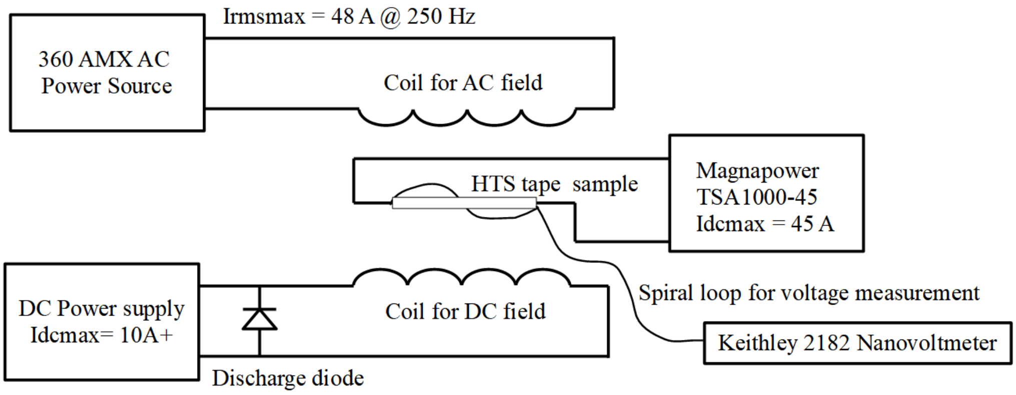

Figure 8.40. Dynamic loss measurement setup

A Keithley 2182 nanovoltmeter is used to measure the voltage drop across the superconducting tape sample, the voltage taps are arranged in spiral loop to cancel introduced induction. The voltmeter time averaged function is used; hence the dynamic loss can simply be calculated from the DC transport current and the time-averaged measured voltage. A similar measurement setup with an air-cored magnet was used at the Robinson Research Institute at the University of Wellington [131].

As has been mentioned before, due to COVID-19, no dynamic loss measurements have been conducted and the electromagnet has not been manufactured. However, with the provided information and electromagnet design, it is possible for future researchers to perform dynamic loss experiments at the University of Edinburgh.

8.8 Chapter summary

In this chapter extensive modelling results were shown with particular focus on dynamic loss in YBOC-coated conductors. The ***H***-formulation based numerical model was introduced and validated with experiments for AC transport current loss and dynamic loss.

Modelling results were shown for dynamic loss in superconducting tapes in the electromagnetic environment relevant to rotating machines. This was done by applying a combined AC and DC magnetic field to tapes while carrying a DC current. The dynamic loss is calculated over two different methods, the first method uses the definition of the dynamic region, the second method calculates the loss over the average electric field.

It was shown that the DC transport current region, or dynamic region, is strongly affected by the DC background field, leading to the results calculated over the dynamic region definition being less accurate than using the average electric field method. Hence, the dynamic region definition needs to be further improved when considering more complication magnetic field.

With the established dynamic loss model, the dynamic loss in the field winding of the double claw pole generator was calculated for the first time. It was calculated to be approximately 13 W. It was found to be relatively low due to the low RPM of the machine and hence low frequency magnetic field environment. Due to the large safety margin of the cryocooling system, the additional dynamic loss does not have an impact on the overall efficiency of the generator.

To investigate the impact of the magnetic field frequency on the dynamic loss, dynamic loss modelling results up to 800 Hz were shown. This frequency range was identified as the operating range of high-speed superconducting machines for electric aircraft propulsion. It was shown that the dynamic region shrinks as the applied field frequency increases, causing the dynamic loss per cycle to decrease as well. It was shown that for low frequencies, dynamic loss makes up the majority of the total loss. As the frequency increases, the dynamic loss contribution to the total loss decreases and magnetisation loss becomes the dominant loss contributor. In addition, the importance of using multi-layer models when operating in a high frequency was shown. A significant proportion of the loss starts occurring in the copper stabilizers as the frequency increases.

Finally, the University of Edinburgh applied superconductivity laboratory was introduced. The different AC and dynamic loss measurement setups were shown. Additionally, a new design of an electromagnet capable of applying combined AC and DC fields to superconducting tapes and stacks was proposed. The electromagnet can be used to perform dynamic loss experiments in magnetic fields similar to the electromagnetic environment in superconducting machines.

Chapter 9 Summary and Conclusion

The main outcomes of the thesis and proposed future work are here summarised and discussed.

9.1 Contribution to Knowledge

9.1.1 Modelling of Electrical Machines

Extensive modelling methods were developed to research electrical machines. Analytical methods were successfully used to investigate design concepts. Numerical models were established to validate the analytically developed designs and provide more detailed insights into the machine performance. The original design of the double claw pole generator was systematically investigated, and shortcomings were identified and addressed, which resulted in developing machine concepts applicable to a multitude of rotating electrical machine topologies.

9.1.2 Novel Stator Design for Axial Flux Machines

One major disadvantage of the double claw pole generator was the heavy structural mass. To simplify the mechanical structure of the double claw pole machine, a novel stator design was introduced. It was proposed to design the stator at an angle, which deviates a part of the air gap closing forces into the radial direction. The reduced axial air gap closing forces lead to a simplified and lighter mechanical structure. The novel stator design is expected to be applicable to several other axial flux machine designs with the potential to further increase their power density.

9.1.3 Improved Electric Loading

After detailed investigation of the double claw pole generator design, the potential to further increase its electric loading was identified. An additional inner stator was created, which takes advantage of the existence of a homopolar field crossing in between the small claw poles. The inner stator improves the machine power density and, while maintaining the same machine diameter and volume. Furthermore, through the inner stator, the modularity of the design was further improved, resulting in a more fault-tolerant machine, which was identified as a major requirement for off-shore wind turbines.

9.1.4 Stacking Machine Modules

With the aim to further increase the modularity and power density of machines, for the first time the possibility of stacking machine modules concentrically was investigated. It was shown that a significant increase in power density, both in terms of machine mass and volume, can be achieved. Additionally, the increased modularity of the machine greatly simplifies the transportation and installation of the generator due to smaller standardised machine components. The structural mass for this design concept was identified as a possible bottleneck however, non-magnetic stator teeth were identified as a possible solution.

9.1.5 Dynamic Loss Modelling

Extensive superconductor modelling was done during this research work and several novelties were discovered. A lack of research into dynamic loss mechanisms in the electromagnetic environment of electrical machines was identified. Superconductor loss was modelled with a combined AC and DC applied electromagnetic field, mimicking the electromagnetic environment in a machine. It was shown that the definition of the dynamic region breaks down when the superconductor is exposed to a DC background field, the dynamic region does not cover the exact centre of the tape anymore, it instead shifts and expands, leading to an increase in dynamic loss.

With the gained knowledge, the dynamic loss of the field winding in the double claw pole generator was calculated to the first time. It was calculated to be approximately 16 W adding further details for the design requirements of the cooling system for the double claw pole machine, the loss was found to be relatively low, due to the low operating frequency of the generator.

To research dynamic loss properties under high frequency conditions, the model was expanded to investigate HTS loss characteristics in the magnetic field environment relevant to high-speed superconducting machines. For the first time, it was shown that the dynamic region shrinks as the magnetic field frequency increases. This results in the dynamic loss per cycle decreasing while the magnetisation loss increases significantly. In was shown that magnetisation loss becomes the dominant loss in superconducting field windings operating in a high frequency environment.

9.2 Recommendations and Future Work

9.2.1 Combining Non-Magnetic and Magnetic components

As the cost of YBCO-coated conductors comes down, it becomes more attractive to investigate a combination of magnetic and non-magnetic materials in the machine design. The large air gap closing forces of the double claw pole generator were identified as one of the major reasons for the high structural mass. The stator teeth could be replaced by non-magnetic materials, which would result in a reduction of the air gap closing forces and improved torque characteristics, at the cost of increased HTS requirements.

9.2.2 Combining the Proposed Designs

The opportunity exists to combine some of the proposed designs in this thesis. The inner stator could be applied to both the angled stator design and the concentrically stacked designs to further increase the power density and the modularity at the cost of creating a potentially very complex machine.

9.2.3 Dynamic Loss Experiments with Combined Magnetic Fields

An electromagnet design was introduced in chapter 8, which allows to apply combined magnetic fields to a superconducting tape or a stack of tapes. Applying combined magnetic fields to superconducting tapes allows to mimic the electromagnetic environment in machines without the need to build a prototype. It was shown through simulations that the DC background field plays a crucial role in regard to the superconductor loss characteristics. Further researching the loss characteristics through experiments could result in an even better understanding of the loss properties of superconductors.

9.2.4 Structural and Thermal Design

The electromagnetic design of electrical machines was the main focus of this research work. However, the design of electrical machines is inherently a multi-physics endeavour. The novel designs of the double claw pole machine introduced in this paper would greatly benefit form detailed structural and thermal analysis to identify further avenues to improve upon the designs.

9.2.5 Rotary Prototype

While modelling of electrical machines can offer good insights into their performance further insights can be gained from operating actual prototypes. In particular, in regard to superconducting machines where that are still a lot of uncertainties in regard to the superconducting field windings, cooling systems and structural design. These issues can be most effectively addressed through experimental work.

9.3 Conclusion

The aim of this thesis was to further increase the power density of the original double claw pole machine while maintaining a cost-effective and modular design. To achieve this purpose, the original design of the double claw pole generator was systematically investigated, and shortcomings were identified and addressed, which resulted in developing several machine concepts applicable to a multitude of rotating electrical machine topologies. Additionally, extensive superconductor modelling was done during this research work and several novelties were discovered, which further added to the understanding of the loss characteristics of superconductors in rotating electrical machines.

It is believed that the proposed designs in this thesis make the double claw pole generator even more competitive in the high-temperature superconducting generator market.

Appendix

Appendix A MATLAB Code for 10 MW DCPG design

The MATLAB code for the 10 MW design is shown below, it can relatively easily be adjusted to the different design highlighted in this thesis by changing the relevant parameters as described in the various chapters.

```
%Secant method for double claw pole machine
%26/01/2017

clear all

%%%%%%%%%%%%%%%%%%%%%%%%%%%%%%%%%%%%%%%%%%%%%%%%%%%%%%%%%%%%%%%%%%%
%%%%%%
%%Define constants

%Values in mm but divided by 1000 to change to m

i=1;  %Set iteration index for B loop to 1
ii=1; %Set iteration index for MMF loop to 1

R_in = 2288/1000; %Inner radius*
N_pole = 88; %Number of poles*
N_polemax = 192;
%while N_pole < N_polemax
l_claw1 = 120/1000; %Claw pole length from top to elbow
l_claw2b = 440/1000; %length of large claw pole bottom part
l_claw2t = 210/1000; %length of large claw pole top part
l_claw = 393/1000; %Total claw pole length
l_claws = 289/1000; %Length of small claw pole
h_claw = 351/1000; %Claw pole height
h_core = 393/1000; %Core pole height
h_gap = 121/1000; %Total air gap height*
l_backcore = 100/1000; %back core length
h_backcore = 351/1000; %Test for angled tooth stator back core
l_w = 172/1000; %Coil length (from side)
l_t = 5/1000; %Height of tooth (claw pole)
% core_to_pole_ratio = 0.85; %Core to pole ratio
core_to_pole_ratio = 0.85; %Core to pole ratio
core_to_pole_ratiomax = 0.95; %Core to pole ratio
% while core_to_pole_ratio < core_to_pole_ratiomax
R_mean = R_in + h_core + 0.5*h_gap; %Mean machine radius
 a_g = 2*R_in/1000; %Air gap*
Theta_pole = 2*pi/N_pole; %Pole angle
%T_core = 2*R_in * sin(0.5*Theta_pole*core_to_pole_ratio); %Pole
pitch*
T_core = R_in*Theta_pole*core_to_pole_ratio;
alpha = 30*pi/180; %30 degrees in radians, alpha is the angle of the
claw pole bend at the elbow
N_coil = round(3*N_pole/4); %Number of coils
% N_coil = 32;
R_2 = R_in+h_core+0.5*(h_gap+h_claw);
T_coil = 2*pi*R_mean/N_coil; %Coil pitch
```

```
tooth_mean_coil_ratio = 0.5; %Tooth width to coil ratio
t_tooth = T_coil*tooth_mean_coil_ratio; %Tooth width
tw_ratio = 0.25; %Width of coil to coil pitch ratio


k = 64; %Number of steps
d_alpha = 360/N_pole/k; %Rotational angle per step



%Permeability of air
u0 = 1.257e-6; %permeability of air
%Permeability (ur(B)) of Vacoflux 50 approximation using a
combination of 4 fourier series

       %constants for ur(B) approximation
       a0 = -4932;
       a1 = -2221;
       b1 = 1.688e+04;
       a2 = 6495;
       b2 = 3133;
       a3 = 2664;
       b3 = -2937;
       a4 = -895.7;
       b4 = -651.2;
       w =  1.377;

%Variables for reluctances (Equivalent length and areas)

%Inner stator
kfringis = 1.5;
l_is = (l_claw2t-2*a_g); %Inner stator equivalent length
A_is = h_core*T_core*kfringis; %Inner stator area
Ris_nour = (l_is/(A_is*u0)); %Inner stator reluctance without iron
permeability

%Inner air gap
kfring = 1.2;
l_iag = a_g; %Air gap length
A_iag = h_core*T_core*kfring; % Air gap area
Riag = l_iag/(A_iag*u0); %Inner air gap reluctance

%Claw poles
h_core_s = 290/1000; %shortest core height for claw poles
l_bup = (pi/2-alpha)*0.5*h_core; %Length of b part of small claw
pole
A_bup = h_core_s*T_core; %Area of b part of small claw pole

l_blow = l_bup; %Length of b part of big claw pole
A_blow = A_bup; %Area of b part of big caw pole

l_de = 0.5*h_claw*cos(alpha)+l_t; %Length of d and e parts of small
claw pole
A_de = h_claw * T_core; %Area of d and e parts of small claw pole
```

```
l_2a = 2*l_claw1; %Equivalent length for straight section of large
claw pole
A_2a = h_core*T_core; %Area for straight section of large claw pole

Rbup_nour = l_bup/(A_bup*u0); %Rbup reluctance without iron
permeability
Rblow_nour = Rbup_nour; %Rblow reluctance without iron permeability
Rde_nour = l_de/(A_de*u0); %Rde reluctance without iron permeability
R2a_nour = l_2a/(A_2a*u0); %R2a reluctance without iron permeability

%Outer air gap
kfringog = 1.15;
l_oag = a_g; %Air gap length
A_oag = h_claw*T_core*kfringog; %Air gap area
Roag = l_oag/(A_oag*u0); %Outer air gap reluctance

%Outer stator
l_os1 = 2*l_w+l_backcore; %Equivalent length through the back core
A_os1 = h_claw*t_tooth; % Tooth area
l_os2 = T_coil; %Back core equivalent
length%%%%%%%%%%%%%%%%%%%%%%%%%%%%%%%%%%%%%%TCOIL
A_os2 = l_backcore*h_backcore; %Back core area
Ros1_nour = l_os1/(A_os1*u0); %Outer stator reluctance from tooth
into middle of back core
Ros2_nour = l_os2/(A_os2*u0); %Outer stator reluctance from one
tooth to the next through the back core

%Cross leakage flux
l_crossin = sqrt((0.5*(h_core+h_gap))^2+(0.75*l_claw)^2);
% l_crossin = sqrt(h_gap^2+(0.75*l_claw)^2);
A_crossin = (h_claw/(2*cos(alpha))+l_t)*T_core;
l_crossout = l_crossin;
A_crossout = A_crossin;
Rlcrossin = l_crossin/(A_crossin*u0); %Cross leakage reluctance
Rlcrossout = Rlcrossin; %Crossleakage reluctance

%Claw leakage flux
kfringl = 1.6;
m_r = 1; %Misalignment ratio 1 = no misalignment
% l_lclaw = sqrt(T_coil^2+(h_claw^2*m_r));
T_leakage = (R_in*Theta_pole*(1-
core_to_pole_ratio)+((R_in+h_claw)*Theta_pole*(1-
core_to_pole_ratio)))/2;
l_lclaw = T_leakage;
%A_lclaw = h_claw*l_t+(h_claw/2)^2*tan(alpha);
A_lclaw = 1.4*(l_t*h_claw+(h_claw^2*tan(alpha))/4)*kfringl;

Rlclaw = l_lclaw/(A_lclaw*u0); %Claw leakage reluctance

%Zig zag flux
l_zigzag = 2*sqrt(a_g^2+(T_coil/2)^2);
A_zigzag = h_claw*T_core;
Rzigzag = l_zigzag/(A_zigzag*u0); %Zig zag reluctance
%MMF
MMF_begin = 34200;
MMF_max = 60000;
MMF_ideal = 32400; %Ideal MMF of the SC winding
```

```
MMF = MMF_begin;

%%
%START SECANT-METHOD ALGORITHM

%Initial guesses to start algorithm


%FIRST GUESS for Phi(n)
Phin = [0.06; 0.06; 0.06; 0.06; 0.06];

%SECOND GUESS for Phi(n2)
Phin2 = [0.05; 0.05; 0.05; 0.05; 0.05];

%Error
e = abs(Phin2 - Phin);

while e(1) > 1e-10|| e(2) > 1e-10 || e(3) > 1e-10 || e(4) > 1e-10 ||
e(5) > 1e-10

F = [MMF;0;0;0;0];

%Bn values in Tesla for Phin guess
Bn = [Phin(1)/A_is; %Bn(1) = Bisn
     (Phin(1)-Phin(5))/A_iag; %Bn(2) = Biagn
     (Phin(1)-Phin(5))/A_bup; %Bn(3) = Bbupn
     (Phin(2)-Phin(5))/A_blow; %Bn(4) = Bblown
     (Phin(1)-Phin(2))/A_crossin; %Bn(5) = Bcrossinn
      Phin(5)/A_crossout; %Bn(6) = Bcrossoutn
     (Phin(2)-Phin(3))/A_lclaw; %Bn(7) = Blclawn
     (Phin(3)-Phin(5))/A_de; %Bn(8) = Bden
     (Phin(3)-Phin(4))/A_zigzag; %Bn(9) = Bzigzagn
     (Phin(4)-Phin(5))/A_oag; %Bn(10) = Boagn
     (Phin(4)-Phin(5))/A_os1; %Bn(11) = Bos1n
     (Phin(4)-Phin(5))/A_os2/2; %Bn(12) = Bos2n
      Phin(1)/A_2a]; %Bn(13) = B2a

%Vacoflux50 permeability for Bn
%urn(1) permeability for inner stator
%urn(2) permeability for Bbup
%urn(3) permeability for Bblow
%urn(4) permeability for Bde
%urn(5) permeability for Bos1
%urn(6) permeability for Bos2
%urn(7) permeability for B2a

if Bn(1) <= 2.33
   urn(1) =
a0+a1*cos(Bn(1)*w)+b1*sin(Bn(1)*w)+a2*cos(2*Bn(1)*w)+b2*sin(2*Bn(1)*
w)+a3*cos(3*Bn(1)*w)+b3*sin(3*Bn(1)*w)+a4*cos(4*Bn(1)*w)+b4*sin(4*Bn
(1)*w);
else
   urn(1) = 52.4671;
end

if Bn(3) <= 2.33
```

```
   urn(2) =
a0+a1*cos(Bn(3)*w)+b1*sin(Bn(3)*w)+a2*cos(2*Bn(3)*w)+b2*sin(2*Bn(3)*
w)+a3*cos(3*Bn(3)*w)+b3*sin(3*Bn(3)*w)+a4*cos(4*Bn(3)*w)+b4*sin(4*Bn
(3)*w);
else
   urn(2) = 52.4671;
end

if Bn(4) <= 2.33
   urn(3) =
a0+a1*cos(Bn(4)*w)+b1*sin(Bn(4)*w)+a2*cos(2*Bn(4)*w)+b2*sin(2*Bn(4)*
w)+a3*cos(3*Bn(4)*w)+b3*sin(3*Bn(4)*w)+a4*cos(4*Bn(4)*w)+b4*sin(4*Bn
(4)*w);
else
   urn(3) = 52.4671;
end

if Bn(8) <= 2.33
   urn(4) =
a0+a1*cos(Bn(8)*w)+b1*sin(Bn(8)*w)+a2*cos(2*Bn(8)*w)+b2*sin(2*Bn(8)*
w)+a3*cos(3*Bn(8)*w)+b3*sin(3*Bn(8)*w)+a4*cos(4*Bn(8)*w)+b4*sin(4*Bn
(8)*w);
else
   urn(4) = 52.4671;
end

if Bn(11) <= 2.33
    urn(5) =
a0+a1*cos(Bn(11)*w)+b1*sin(Bn(11)*w)+a2*cos(2*Bn(11)*w)+b2*sin(2*Bn(
11)*w)+a3*cos(3*Bn(11)*w)+b3*sin(3*Bn(11)*w)+a4*cos(4*Bn(11)*w)+b4*s
in(4*Bn(11)*w);
else
    urn(5) = 52.4671;
end

if Bn(12) <= 2.33
    urn(6) =
a0+a1*cos(Bn(12)*w)+b1*sin(Bn(12)*w)+a2*cos(2*Bn(12)*w)+b2*sin(2*Bn(
12)*w)+a3*cos(3*Bn(12)*w)+b3*sin(3*Bn(12)*w)+a4*cos(4*Bn(12)*w)+b4*s
in(4*Bn(12)*w);
else
    urn(6) = 52.4671;
end

if Bn(13) <= 2.33
    urn(7) =
a0+a1*cos(Bn(13)*w)+b1*sin(Bn(13)*w)+a2*cos(2*Bn(13)*w)+b2*sin(2*Bn(
13)*w)+a3*cos(3*Bn(13)*w)+b3*sin(3*Bn(13)*w)+a4*cos(4*Bn(13)*w)+b4*s
in(4*Bn(13)*w);
else
    urn(7) = 52.4671;
end
%Reluctance calucation for Bn
Risn = Ris_nour/urn(1);
Rbupn = Rbup_nour/urn(2);
Rblown = Rblow_nour/urn(3);
Rden = Rde_nour/urn(4);
Ros1n = Ros1_nour/urn(5);
```

```
Ros2n = Ros2_nour/urn(6);
R2an = R2a_nour/urn(7);

%Reluctance matrix

Rn = [2*(Riag+Rbupn+Rlcrossin)+R2an+Risn -2*Rlcrossin 0 0 -
2*(Riag+Rbupn);
     -2*Rlcrossin 2*(0.5*Rlclaw+Rblown+Rlcrossin) -2*(0.5*Rlclaw) 0
-2*Rblown;
     0 -2*(0.5*Rlclaw) 2*(0.5*Rlclaw+2*Rden+Rzigzag) -2*Rzigzag -
2*(2*Rden);
     0 0 -2*Rzigzag 2*(Rzigzag+2*Roag+Ros1n+Ros2n) -
2*(2*Roag+Ros1n+Ros2n);
     -2*(Riag+Rbupn) -2*Rblown -2*(2*Rden) -2*(2*Roag+Ros1n+Ros2n)
2*(Rlcrossout+Rblown+2*Rden+2*Roag+Riag+Ros1n+Ros2n+Rbupn)];

% Calculate fn = Rn*Phin - F
fn = Rn*Phin - F;

%%%%%%%%%%%%%%%%%%%%%%%%%%%%%%%%%%%%%%%%%%%%%%%%%%%%%%%%%%%%%%%%%%%%
%%%%%%%

%Bn2 values in Tesla for Phin guess
Bn2 = [Phin2(1)/A_is; %Bn2(1) = Bisn2
      (Phin2(1)-Phin2(5))/A_iag; %Bn2(2) = Biagn2
      (Phin2(1)-Phin2(5))/A_bup; %Bn2(3) = Bbupn2
      (Phin2(2)-Phin2(5))/A_blow; %Bn2(4) = Bblown2
      (Phin2(1)-Phin2(2))/A_crossin; %Bn2(5) = Bcrossinn2
       Phin2(5)/A_crossout; %Bn2(6) = Bcrossoutn2
      (Phin2(2)-Phin2(3))/A_lclaw; %Bn2(7) = Blclawn2
      (Phin2(3)-Phin2(5))/A_de; %Bn2(8) = Bden2
      (Phin2(3)-Phin2(4))/A_zigzag; %Bn2(9) = Bzigzagn2
      (Phin2(4)-Phin2(5))/A_oag; %Bn2(10) = Boagn2
      (Phin2(4)-Phin2(5))/A_os1; %Bn2(11) = Bos1n2
      (Phin2(4)-Phin2(5))/A_os2/2; %Bn2(12) = Bos2n2
       Phin2(1)/A_2a]; %Bn2(13) = B2an2
save_Bn2(i,:) = Bn2;

%Vacoflux50 permeability for Bn2
%urn2(1) permeability for inner stator
%urn2(2) permeability for Bbup
%urn2(3) permeability for Bblow
%urn2(4) permeability for Bde
%urn2(5) permeability for Bos1
%urn2(6) permeability for Bos2
%urn2(7) permeability for B2a

if Bn2(1) <= 2.33
    urn2(1) =
a0+a1*cos(Bn2(1)*w)+b1*sin(Bn(1)*w)+a2*cos(2*Bn(1)*w)+b2*sin(2*Bn(1)
*w)+a3*cos(3*Bn(1)*w)+b3*sin(3*Bn(1)*w)+a4*cos(4*Bn(1)*w)+b4*sin(4*B
n(1)*w);
else
    urn2(1) = 52.4671;
end

if Bn2(3) <= 2.33
```

```
    urn2(2) =
a0+a1*cos(Bn2(3)*w)+b1*sin(Bn2(3)*w)+a2*cos(2*Bn2(3)*w)+b2*sin(2*Bn2
(3)*w)+a3*cos(3*Bn2(3)*w)+b3*sin(3*Bn2(3)*w)+a4*cos(4*Bn2(3)*w)+b4*s
in(4*Bn2(3)*w);
else
    urn2(2) = 52.4671;
end

if Bn2(4) <= 2.33
    urn2(3) =
a0+a1*cos(Bn2(4)*w)+b1*sin(Bn2(4)*w)+a2*cos(2*Bn2(4)*w)+b2*sin(2*Bn2
(4)*w)+a3*cos(3*Bn2(4)*w)+b3*sin(3*Bn2(4)*w)+a4*cos(4*Bn2(4)*w)+b4*s
in(4*Bn2(4)*w);
else
    urn2(3) = 52.4671;
end

if Bn2(8) <= 2.33
    urn2(4) =
a0+a1*cos(Bn2(8)*w)+b1*sin(Bn2(8)*w)+a2*cos(2*Bn2(8)*w)+b2*sin(2*Bn2
(8)*w)+a3*cos(3*Bn2(8)*w)+b3*sin(3*Bn2(8)*w)+a4*cos(4*Bn2(8)*w)+b4*s
in(4*Bn2(8)*w);
else
    urn2(4) = 52.4671;
end

if Bn2(11) <= 2.33
    urn2(5) =
a0+a1*cos(Bn2(11)*w)+b1*sin(Bn2(11)*w)+a2*cos(2*Bn2(11)*w)+b2*sin(2*
Bn2(11)*w)+a3*cos(3*Bn2(11)*w)+b3*sin(3*Bn2(11)*w)+a4*cos(4*Bn2(11)*
w)+b4*sin(4*Bn2(11)*w);
else
    urn2(5) = 52.4671;
end

if Bn2(12) <= 2.33
    urn2(6) =
a0+a1*cos(Bn2(12)*w)+b1*sin(Bn2(12)*w)+a2*cos(2*Bn2(12)*w)+b2*sin(2*
Bn2(12)*w)+a3*cos(3*Bn2(12)*w)+b3*sin(3*Bn2(12)*w)+a4*cos(4*Bn2(12)*
w)+b4*sin(4*Bn2(12)*w);
else
    urn2(6) = 52.4671;
end

if Bn2(13) <= 2.33
    urn2(7) =
a0+a1*cos(Bn2(13)*w)+b1*sin(Bn2(13)*w)+a2*cos(2*Bn2(13)*w)+b2*sin(2*
Bn2(13)*w)+a3*cos(3*Bn2(13)*w)+b3*sin(3*Bn2(13)*w)+a4*cos(4*Bn2(13)*
w)+b4*sin(4*Bn2(13)*w);
else
    urn2(7) = 52.4671;
end
save_urn2(i,:) = urn2(1);
save_urn25(i,:) = urn2(5);

%Reluctance calucation for Bn
Risn2 = Ris_nour/urn2(1);
Rbupn2 = Rbup_nour/urn2(2);
```

```
Rblown2 = Rblow_nour/urn2(3);
Rden2 = Rde_nour/urn2(4);
Ros1n2 = Ros1_nour/urn2(5);
Ros2n2 = Ros2_nour/urn2(6);
R2an2 = R2a_nour/urn2(7);
save_Risn2(i,:) = Risn2;
%Reluctance matrix

Rn2 = [2*(Riag+Rbupn2+Rlcrossin)+R2an2+Risn2 -2*Rlcrossin 0 0 -
2*(Riag+Rbupn2);
     -2*Rlcrossin 2*(0.5*Rlclaw+Rblown2+Rlcrossin) -2*(0.5*Rlclaw) 0
-2*Rblown2;
     0 -2*(0.5*Rlclaw) 2*(0.5*Rlclaw+2*Rden2+Rzigzag) -2*Rzigzag -
2*(2*Rden2);
     0 0 -2*Rzigzag 2*(Rzigzag+2*Roag+Ros1n2+Ros2n2) -
2*(2*Roag+Ros1n2+Ros2n2);
     -2*(Riag+Rbupn2) -2*Rblown2 -2*(2*Rden2) -
2*(2*Roag+Ros1n2+Ros2n2)
2*(Rlcrossout+Rblown2+2*Rden2+2*Roag+Riag+Ros1n2+Ros2n2+Rbupn2)];

% Calculate fn = Rn*Phin - F
fn2 = Rn2*Phin2 - F;
save_fn2(i,:) = fn2;
%Calculate new Phi vector (Phin3)
Phin3 = Phin2 - (fn2./((fn2-fn)./(Phin2-Phin)));
save_Phin3(i,:) = Phin3;
%Error
e = abs(Phin3 - Phin2);

%Iteration index
i=i+1;
%Replace previous values with newly calculated ones
Phin = Phin2;
Phin2 = Phin3;
end

%% Calculate Flux Linkage

    t_w = T_coil * tw_ratio;
    Bnew = Bn2(10);

    ro_coil = T_coil/2;
    ri_coil = T_coil/2 - t_w;


    B_peak = 4/pi*Bnew*sin(pi*(core_to_pole_ratio)/2);
    n_seg = 20; %Number of segments

    T_pole_coil = (R_mean*2*pi*(1-tw_ratio)/N_coil);

    h_coil = h_claw;

    dr = (ro_coil-ri_coil)/n_seg;

    ri = ones(1,n_seg);
    Phi_coil = ones(1,n_seg);
```

```
    for j = 1:n_seg
    %radius of each segment
    ri(j) = ri_coil + j*dr;
    %magnetic flux of each segment
    Phi_coil(j) =
2*B_peak*h_coil*T_pole_coil*sin(pi*ri(j)/T_pole_coil)/pi;
    end

    %flux linkage
    lambda_peak = mean(Phi_coil);
%%
%Power calculation

%Constants
rpm = 10; %Rotations per minute
N_t = 96; %Number of turns per stator coil
N_tmax = 150;
ii = 0;
% while N_t < N_tmax
fill_factor = 0.75;

freq = (N_pole/2)*rpm*2*pi/60; %Electrical frequency in radians
E_max = N_t*(Phin3(4)-Phin3(5))*freq; %Max induced voltage per coil
%E_max = N_t*lambda_peak*freq; %Max induced voltage per coil
E_rms = E_max/sqrt(2);

%Resistance of coil
coil_length = N_t*2*(R_mean*2*pi*(1-tw_ratio)/N_coil+h_claw); %in m
% coil_length = N_t*2*(h_core+T_core/2+T_core+T_core/2);
coil_area = l_w*(R_mean*2*pi*tw_ratio/N_coil)*fill_factor/N_t; %in
m^2
% coil_area = (T_core/2*l_w)*fill_factor/N_t;
coil_resistance = 1.68e-8*coil_length/coil_area;

%Current in coil
J_rms = 5e6; %Current density in A/m^2
I_rms = J_rms*coil_area;
% I_rms = 438;
J_rmsact = I_rms/coil_area;
%Total copper loss
Cu_loss = I_rms^2*coil_resistance*N_coil*2;

%Total electrical power per coil
P_coil = E_rms*I_rms;
P_coil_out = P_coil-I_rms^2*coil_resistance;
eff = P_coil_out*2*N_coil/(P_coil*2*N_coil+71000);
eff_cu = P_coil_out*2*N_coil/(P_coil*2*N_coil);
P_out_total = 2*P_coil_out*N_coil;

%MMF = MMF+1000;
% ii = ii + 1;
% save_Phin3_MMF(ii,:) = Phin3;
% save_MMF(ii,:) = MMF;
% save_Bn2_MMF(ii,:) = Bn2;
% N_pole = N_pole+4;
% save_Phin3_Npole(ii,:) = Phin3;
% save_Npole(ii,:) = N_pole;
```

```
% core_to_pole_ratio = core_to_pole_ratio + 0.01;
% save_Phin3_ratio(ii,:) = Phin3;
% save_ratio(ii,:) = core_to_pole_ratio;
% save_Bn2_ratio(ii,:) = Bn2;
%
% N_t = N_t+5;
% ii = ii+1;
%
% save_Pouttotal(ii,:) = P_out_total;
% save_freq(ii,:) = freq;
% save_R(ii,:) = coil_resistance;
% save_E_rms(ii,:) = E_rms;
% save_eff(ii,:) = eff;
% save_I(ii,:) = I_rms;
% save_J(ii,:) = J_rmsact;
% end

% %%
% %Calculate active mass
%
% d_steel = 7650;
% %Small claw poles
% small_claws_area = 2*((h_core+h_claw)/2)*l_claws;
%
% large_claw_area =
2*((h_core*(l_clawlb/2))+0.5*(h_claw+h_core)*(l_claw-
(l_t1/cos(alpha2))-l_t2-
(l_clawlb/2))+(l_t2*h_claw)+(l_t1*h_claw)+((h_claw^2*alpha2)/2));
% %Large claw poles
%
% %Total rotor mass
% small_claws_mass = small_claws_area*T_core*d_steel;
% large_claw_mass = large_claw_area*T_core*d_steel;
% total_rotor_mass = (N_pole/2)*(small_claws_mass +
large_claw_mass);
%
% %Field core
% field_core_mass = ((pi*((R_in+2*h_core+h_gap)^2-
(R_in+h_core+h_gap)^2)))*2*l_claw1*d_steel;
```

Appendix B Cryostat Operational Manual

1. Create the vacuum

Before the cryostat can be used a vacuum needs to be created within the cryostat to minimize the heat load. This is done via two pumps. Figure B1 shows the setup for creating the vacuum.

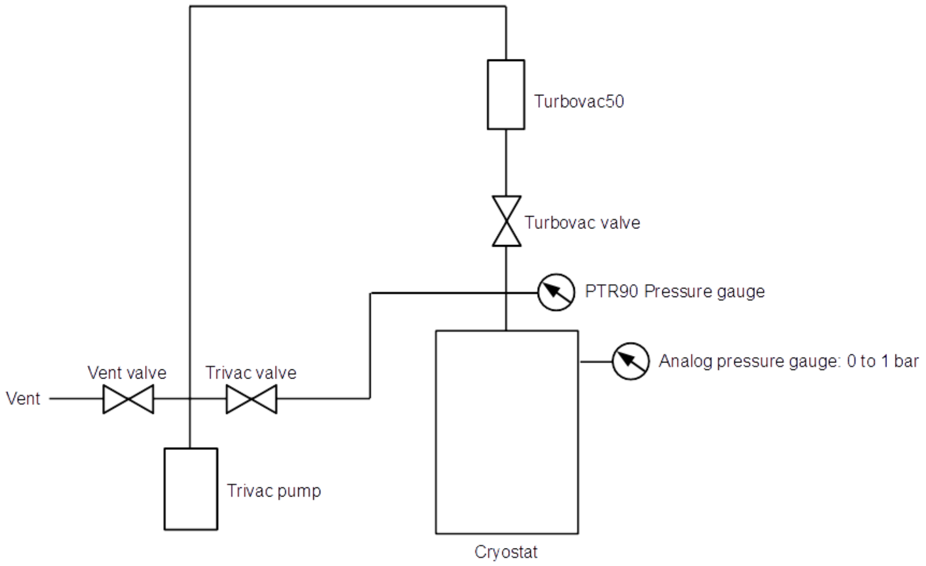

Figure B1. Setup for creating vacuum within the cryostat

The procedure to create the vacuum is as follows:

1) Make sure all valves are initially closed
2) Make sure the door of the cryostat is properly sealed
3) Turn on the Centre One display on the pump trolley, it will not show a value initially.
4) Remove the vent cover on the Trivac E2 pump (red cover)
5) Open the Trivac valve completely
6) Start the Trivac E2 pump, the pressure should start to drop immediately on the analogue pressure gauge, which is fixed to the cryostat itself.
7) Once the pressure goes towards 0 bar the Centre One display should start displaying the pressure in mbar in conjunction with the PTR90 pressure gauge.
8) Once the pressure reaches $1*10^{-1}$ mbar the Turbovac valve can be opened and the Turbovac50 pump can be turned on using the Turbotronik NT10 controller by simply pressing start.

9) The Trivac E2 and Turbovac50 combination can reach a vacuum as low as $5*10^{-8}$ mbar. The operational vacuum level should be between $1*10^{-5}$ to $1*10^{-7}$ mbar.

The pumps need to remain turned on during the duration of the experiment to maintain the operational vacuum.

Once the experiment is finished and the vacuum is not needed anymore the Turbovac50 pump should be turned off first followed by the Trivac E2 pump. The vent valve can then slowly be opened to let air gradually flow back into the cryostat until normal pressure has been restored.

2. Compressor and cooling head operation

Once the operational vacuum within the cryostat has been created the cryorefrigerator system may be used after having gone through the safety checks.

1) AL330 Cooling head capabilities

The cooling head operating range is shown in figure B2. The base temperature is 12 K (no load). The cooling power increases as the operating temperature increases, i.e. at 50 K the cooling head can provide a cooling power of 141 W and at 40 K a cooling power of 112 W. If the heat load at 40K is higher than 112 W, 50 K cannot be reached, and the experimental setup needs to be changed to reduce the heat load. The cooling head cools down to 80 K within 25 minutes (at no load).

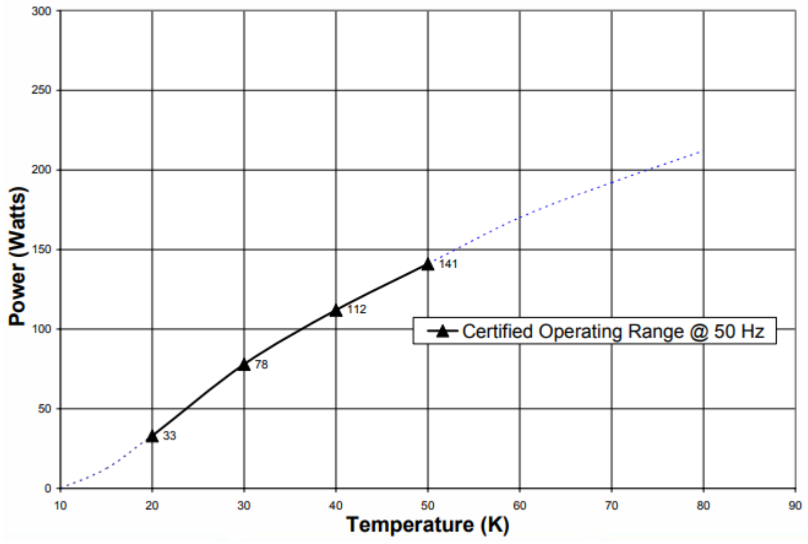

Figure B2. AL330 capacity curve (AL330 manual)

2) CP970 Compressor

The compressor is used to power the cooling head and provide it with helium. The compressor and cooling head system simply need to be turned on and the temperature controller is then used to control the temperature. However, before the system can be used certain factors need to be checked.

Before start-up

a) Check system pressure is 15.2 ± 0.34 bar
  - If pressure is too high, attach Aeroquip line and vent helium by slowly opening the service valve at a maximum rate of 0.34 bar per minute.
  - If pressure is too low, follow section A1 in the appendix.

b) Make sure the cold head motor cord is connected to the cold head and compressor.

c) Make sure all Aeroquip lines are securely fastened and connected correctly.

d) Make sure the flow rate and temperature range of the cooling water meet the requirements shown in figure B3.

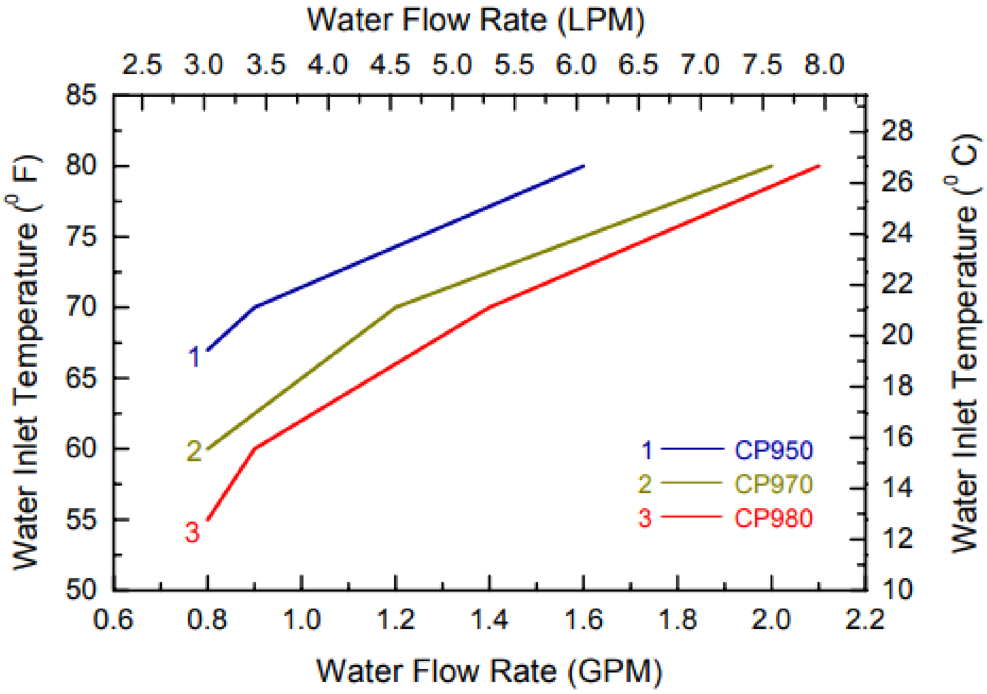

Figure B3. Required water flow rate depending on water inlet temperature (Relevant model: CP970)

e) Check that the circuit breaker is on

Start-up procedure

a) Turn the system on by pressing the power switch on the front panel
b) Check the pressure gauges for an immediate pressure differential of at least 13.76 bar between high and low pressure. Check for an increase in the high pressure and decrease in the low pressure.
   - If there is no immediate pressure differential, turn off immediately. Rewire 3-phase cord connections since the system is running in reverse.
c) Normal pressure ranges are between 6.2 to 7.9 bar on the low-pressure side and 20 to 21.4 bar on the high-pressure side. A typical pressure differential is 17.2 bar. The pressure differential reduces as the cold head cools down since it draws in more helium.

During operation, the pressure and temperature should be continuously monitored to ensure correct operation. If the pressure deviates from the typical values the system should be turned off immediately and the AL330 manual should be used to diagnose the fault.

3. Temperature control and measurements

To measure the temperatures in various locations in the cryostat or test subject, several temperature sensors are available.

The model of the temperature sensors is Cernox CX-1050AA. Their temperature range is from 4.2 K to 420 K. Each temperature sensor has an identification number, which begins with an ‘X’, for example, X71514. Each sensor has a calibration curve, which can be found on the provided CDs. The lab features three temperature monitors (Lake Shore Model 218) and one temperature controller (Lake Shore Model 336). The monitors can each display 8 temperatures.

Before the sensors can be used in conjunction with the monitors, the correct calibration curves need to be uploaded to the monitor. This is done via a laptop and two pieces of software. *Keysight Connection Expert 2018* is used to connect to the monitors or controller over a USB to GPIB adapter. The software automatically recognizes the device and connects automatically to it. To upload curves onto the monitor the software *Lake Shore Curve Handler* is used. The relevant calibration curve is opened from a CD via the software and can then be transferred onto the monitor to the desired address. Once all the calibration curves have been uploaded to the monitor it is ready to use.

To control the temperature of the cooling head, the temperature controller is used in conjunction with a heating plate, which is connected onto the cooling head itself. If the cooling head were to run without a load it would simply cool down to its base temperature, which is 12 K. The heating plate is used to provide a heat load to the cooling head, which then sets the operational temperature. Like the temperature monitors, temperatures sensors are connected to the controller for which calibration curves need to be uploaded following the same procedure as with the monitors. A sensor should be connected to the main point of interest (i.e. cooling head or test subject), the temperature at this location is then used as a reference point for controlling the temperature. A target temperature for this location is set via the temperature controller. The temperature controller then controls the heating plate to maintain the desired temperature at the target location by increasing and decreasing the heat load.

4. Helium refill for compressor

Before starting up the system pressure should be 15.2 ± 0.34 bar. If pressure is lower Helium needs to be refilled.

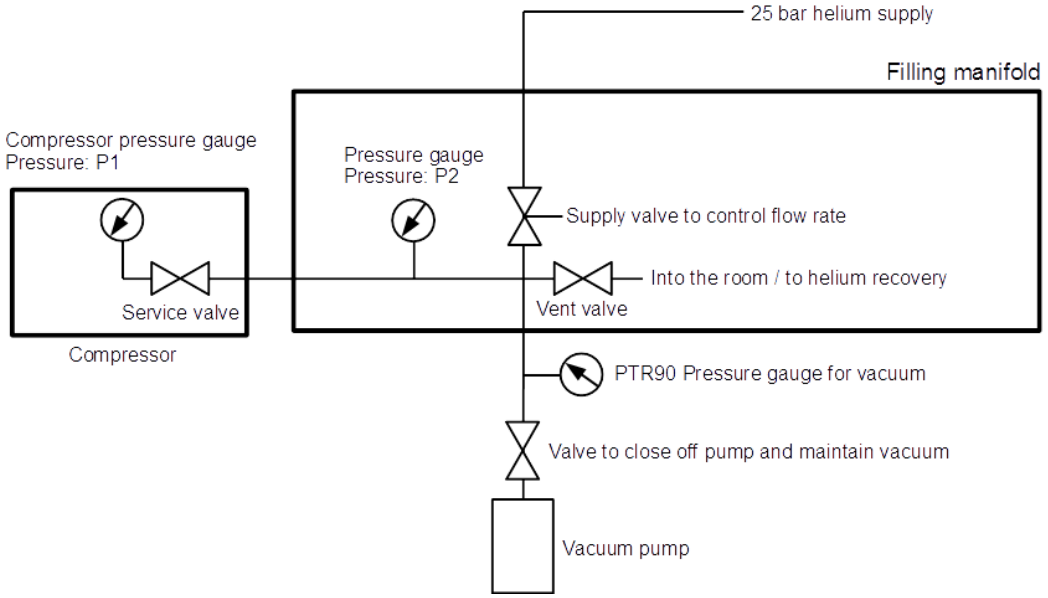

Figure B4. Refill system diagram

Procedure:

1) System is turned off
2) Entire system has cooled down to room temperature
3) Only high purity helium (minimum 99.999% purity) may be used.
4) Check that the helium source and regulator are capable of pressurizing to desired pressure. (Helium supply is 25 bar in the lab)
5) Confirm service valve is closed.
6) Make connections as shown in figure B4.
    - Compressor to manifold, Aeroquip line
    - Pump to manifold, Flexline with Aeroquip adapter
    - Vent into room, no connections / Vent to helium recovery
    - Helium supply to manifold, what hose?
7) Confirm all valves are closed.
8) Open vacuum valve.
9) Start pump and evacuate charging line to 50 microns ($6.5*10^{-3}$ kPa, $65*10^{-3}$ mbar).
10) Close vacuum valve and add 3.4 bar of helium.
11) Vent the system by opening the vent valve.
12) Close the vent valve, open vacuum valve again and evacuate charging line to 25 microns ($3.25*10^{-3}$ kPA, $32.5*10^{-3}$ mbar).
13) Close the vacuum valve and pressurize the line with the desired amount of helium pressure which depends on the pressure in the compressor.
    - P_1 = Compressor pressure, P_2 = line pressure, P_R = 15.2 bar (Recommended compressor pressure)
    - P_2 = 30.4 bar – P_1
14) Slowly open to service valve and fill the compressor with helium at a maximum filling rate of 0.34 bar per minute.
15) Once the desired pressure is reached (15.2 ± 0.34 bar), close the service valve.

5. Stored helium in the small cryostat during normal operation

P_1 = 1520 kPa

P_2= 101.325 kPa

V_1 = 21.5 l (worst case, all 3 cylinders are filled with helium)

Relevant equation: $P_1V_1 = P_2V_2$

$$V_2 = \frac{P_1}{P_2} \times V_1 = \frac{1520}{101.325} \times 21.5 = 322\ l$$

If the helium were to leak into the atmosphere the resulting oxygen concentration can be calculated to be:

Room volume approximately = 131m^3

Gaseous helium volume = 0.322m^3 (worst case)

The resulting volume of oxygen in the room, where 20.95% is the normal O2 level:

$$V_{O2} = 0.2095(V_R - V_G) = 0.2095(131 - 0.322) = 27.377m^3$$

Which then allows the resulting oxygen concentration to be calculated as:

$$\%O2 = 100 * \frac{27.377}{131} = 20.9\%$$

Hence, a very small amount of gaseous Helium is stored in the compressor + cooling head system, which does not affect the room oxygen concentration.

References

[1] World Economic Forum , "The Global Risks Report 2017, 12th Edition," World Economic Forum , Geneva, 2017.

[2] Lloberas J. *et al.*, "A review of high temperature superconductors for offshore windpower synchronous generatorsJ," *Renewable and Sustainable Energy Reviews,* vol. 38, pp. 404-414, 2014.

[3] Lee J. *et al.*, "GWEC Global Wind Report 2019," Global Wind Energy Council, Brussels, Belgium, 2020.

[4] Islam M. R. *et al.*, "A review of offshore wind turbine nacelle: Technical challenges,and research and developmental trends," *Renewable and Sustainable Energy Reviews,* vol. 33, pp. 161-176, 2014.

[5] Burchell J. W., "Advancement of Direct Drive Generator Systems for Offshore Renewable Energy Production," PhD Thesis, The University of Edinburgh, 2017.

[6] MAKE Consulting, "Global Wind Turbine Trends 2017," MAKE Consulting, 2017.

[7] General Electric, "Haliade-X 12 MW offshore wind turbine," General Electric, [Online]. Available: https://www.ge.com/renewableenergy/wind-energy/offshore-wind/haliade-x-offshore-turbine. [Accessed 07 07 2020].

[8] Lerch M. *et al.*, "Sensitivity analysis on the levelized cost of energy forfloating offshore windfarms," *Sustainable Energy Technologies and Assessments,* vol. 30, pp. 77-90, 2018.

[9] Song X. *et al.*, "Commissioning of the World's First Full-scale MW-class Superconducting Generator on a Direct Drive Wind Turbine," *IEEE Transactions on Energy Conversion,* no. 10.1109/TEC.2020.2982897, 2020.

[10] Hart K. *et al.*, "Improved cost of energy comparison of permanent magnet generators for large offshore wind turbines," in *European Wind Energy Association Conference and Exhibition,* 2014.

[11] Keysan O. *et al.*, "Designing the C-GEN lightweight direct drive generator for wave and tidal energy," *IET Renewable Power Generation,* vol. 6, no. 3, pp. 161 - 170, 2012.

[12] Faulstich S. *et al.* "Wind turbine downtime and its importance for offshore development," *Wind Energy,* vol. 14, no. 3, pp. 327-337, 2011.

[13] Polider H. *et al.*, "10 MW Wind Turbine Direct-Drive Generator Design with Pitch or Active Speed Stall Control," in *2007 IEEE International Electric Machines & Drives Conference,* Antalya, Turkey, 2007.

[14] Miura S. *et al.*, “Lightweight Design of Tens-MW Fully-Superconducting Wind Turbine Generators With High-Performance REBa2Cu3Oy Wires,” *Transactions on Applied Superconductivity,* vol. 30, no. 4, p. 5204106, 2020.

[15] Keysan O. and Mueller M., “A modular and cost-effective superconducting generator design for offshore wind turbines,” *Superconductor Science and Technology,* vol. 28, no. 3, p. 034004, 2015.

[16] Kails K. *et al.*, “Novel model of stator design to reduce the mass of superconducting generators,” *Superconductor Science and Technology,* vol. 31, no. 5, 2018.

[17] Maples B. *et al.*, “Comparative Assessment of Direct Drive High Temperature Superconducting Generators in Multi-Megawatt Class Wind Turbines,” National Renewable Energy Laboratory, Golden, Colorado, 2010.

[18] Snitchler G. *et al.*, “10 MW Class Superconductor Wind Turbine Generator,” *IEEE Transactions on Applied Superconductivity,* vol. 21, no. 3, pp. 1089-1092, 2011.

[19] Radebaugh R., “Refrigeration for Superconductors,” *Proceedings of the IEEE,* vol. 92, no. 10, pp. 1719-1734, 2004.

[20] Song X. *et al*, “Design Study of Fully Superconducting Wind Turbine Generators,” *IEEE Transactions on Applied Superconductivity,* vol. 25, no. 3, 2015.

[21] Heikkilä T.T., The Physics of Nanoelectronics, Oxford University Press, 2013.

[22] London F., “The electromagnetic equations of the supraconductor,” *Proc. Roy. Soc.,* vol. 149, no. 886, pp. 71-88, 1935.

[23] Yao M., Numerical Modelling of Superconducting Power Cables with Second Generation High Temperature Superconductors, PhD Thesis : The University of Edinburgh, 2019.

[24] Gorkov L. P. , “Microscopic derivation of the Ginzburg-Landau equations in the theory of superconductivity,” *Sov. Phys. JETP,* vol. 9, no. 6, pp. 1364-1367, 1959.

[25] Bardeen J. *et al*., “Microscopic theory of superconductivity,” *Phys. Rev.,* vol. 106, pp. 162-164, 1957.

[26] Van Delft D., “History and significance of the discovery of superconductivity by Kamerlingh Onnes in 1911,” *Physica C: Superconductivity,* vol. 479, pp. 30-35, 2012.

[27] Abrikosov A. A., “On the magnetic properties of superconductors of the second group,” *Sov. Phys. JETP-USSR,* vol. 5, no. 6, pp. 1174-1182, 1057.

[28] Bardeen J. *et al*., ““Theory of the motion of vortices in superconductors,” *Physical Review,* vol. 140, no. 4A, pp. A1197-A1207, 1965.

[29] Scanlan R. M. *et al*, “Superconducting materials for large scale applications,” *Proceedings of the IEEE,* vol. 92, no. 10, pp. 1639-1654, 2004.

[30] Zhang M., Study of second generation high temperature superconducting coils, PhD Thesis: University of Cambridge, 2013.

[31] Larbalestier D. *et al.*, “High-Tc superconducting materials for electric power applications,” *Materials For Sustainable Energy: A Collection of Peer-Reviewed Research and Review Articles from Nature Publishing Group,* vol. World Scientific, pp. 311-320, 2011.

[32] Shen B., Study of Second Generation High Temperature Superconductors: Electromagnetic Characteristics and AC Loss Analysis, PhD Thesis: Univesity of Cambridge, 2018.

[33] Grilli F., “Computation of Losses in HTS Under the Action of Varying Magnetic Fields and Currents,” *IEEE Transactions on Applied Superconductivity,* vol. 23, no. 1, p. 8200433, 2014.

[34] Oomen M.P., AC loss Supconducting Tapes and Cables, PhD Thesis: University of Twente, 2000.

[35] Sullivan C. R., “Computationally Efficient Winding Loss Calculation with Multiple Windings, Arbitrary Waveforms, and Two-Dimensional or Three-Dimensional Field Geometry,” *IEEE Transactions on Power Electronics,* vol. 16, no. 1, pp. 142-150, 2001.

[36] Liu G. *et al.*, “Numerical study on AC loss reduction of stacked HTS tapes by optimal design of flux diverter,” *Superconductor Science and Technology,* vol. 30, no. 12, pp. 1-12, 2017.

[37] Grilli F. *et al.*, “How filaments can reduce AC losses in HTS coated conductors: a review,” *Superconductor Science and Technology,* vol. 29, no. 8, pp. 1-16, 016.

[38] Norris W., “Calculation of hysteresis losses in hard superconductors carrying ac: isolated conductors and edges of thin sheets,” *Journal of Physics D: Applied Physics,* vol. 3, no. 4, pp. 489-507, 1970.

[39] Brandt E. H. *et al.*, “Type-II-superconductor strip with current in a perpendicular magnetic field,” *Physical review B,* vol. 48, no. 17, pp. 12893-12906, 1993.

[40] Nguyen D. N. *et al*, “Temperature Dependence of Total AC Loss in High-Temperature Superconducting Tapes,” *IEEE Transactions on Applied Superconductivity,* vol. 19, no. 4, pp. 3637-3644, 2009.

[41] Bean C. P., “Magnetization of hard superconductors,” *Physical Review Letters,* vol. 8, no. 6, pp. 250-253, 1962.

[42] Poole C. P., Superconductivity 2nd Edition, Elsevier Ltd., 2007.

[43] Kim Y., “Magnetization and Critical Supercurrents,” *Physical review letters,* vol. 129, pp. 528-535, 1963.

[44] Gömöry F., “Improvement of the self-field critical current of a high-Tc superconducting tape by the edge cover from soft ferromagnetic material,” *Applied Physics Letters,* vol. 89, p. 072506, 2006.

[45] Anderson P.W., “Theory of Flux Creep in Hard Supreconductors,” *Physical Review Letters,* vol. 9, no. 7, pp. 309-311, 1962.

[46] Rhyner J., “Magnetic properties and AC-losses of superconductors with power law current-voltage characteristics,” *Physica C,* vol. 212, no. 3-4, pp. 292-300, 1993.

[47] Naoyuki A. *et al*., “Numerical modelings of superconducting wires for AC loss calculations,” *Physica C: Superconductivity,* vol. 310, no. 1-4, pp. 16-29, 1998.

[48] Shanghai Superconductor, Shanghai Superconductor, [Online]. Available: http://www.shsctec.com/en/index. [Accessed 6 7 2020].

[49] Tixador P., “Development of superconducting power devices in Europe,” *Physica C: Superconductivity,* vol. 470, no. 20, pp. 971-978, 2010.

[50] Keysan O., Superconducting Generators for Large Offshore Wind Turbines, PhD Thesis: The University of Edinburgh, 2014.

[51] Iwata Y. *et al*., “Design of superconducting magnets for a compact carbon gantry,” *IEEE Transactions on Applied Superconductivity,* vol. 26, no. 4, 2016.

[52] Baird Y. *et al*., “Optimized Magnetic Design of Superconducting Magnets for Heavy Ion Rotating Gantries,” *Transactions on Applied Superconductivity,* vol. 30, no. 2, p. 4400108, 2020.

[53] Iwata Y. *et al*., “Design of a superconducting rotating gantry for heavy-ion therapy,” *Phys. Rev. Special Topics–Accelerators Beams,* vol. 15, no. 4, p. 044701, 2012.

[54] Geng J., “Mechanism of a high-Tc superconducting flux pump: Using alternating magnetic field to trigger flux flow,” *Applied Physics Letters,* vol. 107, p. 142601, 2015.

[55] Machura P. *et al*., “Loss characteristics of superconducting pancake, solenoid and spiral coils for wireless power transfer,” *Superconductor Science and Technology,* vol. 33, pp. 1-14, 2020.

[56] Machura P. *et al*., “Driving Range of Electric Vehicles Charged by Wireless Power Transfer,” *Transactions on Vehicular Technology,* vol. 69, no. 6, pp. 5968 - 5982, 2020.

[57] Corduan M. *et al*., “Topology Comparison of Superconducting AC Machines for Hybrid Electric Aircraft,” *IEEE Transactions on Applied Superconductivity,* vol. 30, no. 2, p. 5200810, 2020.

[58] D. Liu *et al*, “Comparison of 10 MW Superconducting Generator Topologies for Direct-Drive Wind Turbines,” in *IEEE International Electric Machines & Drives COnference*, Coeur D'Alene, Idaho, USA, 2015.

[59] Kim J. H. and Kim H. M., “Electromagnetic design of 10 MW class superconducting wind turbine using 2G HTS wire,” *Progress in Superconductivity and Cryogenics,* vol. 15, no. 3, pp. 29-34, 2013.

[60] Kalsi S. S., “Superconducting Wind Turbine Generator Employing MgB2 Windings Both on Rotor and Stator,” *IEEE Transaction on Applied Superconductivity,* vol. 24, no. 1, p. 5201907, 2014.

[61] Kostopoulos D. *et al.*, “Feasibility Study of a 10 MW MgB2 Fully Superconducting Generator for Offshore Wind Turbines,” in *EWEA Offshore Conference*, Frankfurt, Germany, 2013.

[62] Patel A. *et al.*, “Design considerations for fully superconducting synchronous motors aimed at future electric aircraft,” in *ESARS-ITEC 2018 Conference Proceedings*, Notthingham, UK, 2018.

[63] Klaus G. *et al*., “Design Challenges and Benefits of HTS Synchronous Machines,” in *2007 IEEE Power Engineering Society General Meeting*, Tampa, FL, USA, 2007.

[64] Kails K. *et al*., “Dynamic loss of HTS field windings in rotating electric machines,” *Superconductor Science and Technology,* vol. 33, no. 4, pp. 1-8, 2020.

[65] Abrahamsen A. B. *et al.*, “Superconducting wind turbine generators,” *IOPscience: Superconductor Science and Technology,* vol. 23, no. 3, pp. 1-8, 2010.

[66] Terao Y. and Sekino M., “Electromagnetic Design of 10 MW Class Fully Superconducting Wind Turbine Generators,” *IEEE Transactions on Applied Superconductivity,* vol. 22, no. 3, p. 5201904, 2012.

[67] Fair R. *et al*, “Next generation drive train-superconductivity for large-scale wind turbines,” in *Applied Superconductivty Conf.*, Portland, Oregon, 2012.

[68] Sung H.-J. *et al.,* “Practical Design of a 10 MW Superconducting Wind Power Generator Considering Weight Issue,” *IEEE Transactions on Applied Superconductivity* , vol. 23, no. 3, 2013.

[69] Marino I. *et al.,* “Lightweight MgB2 superconducting 10 MW wind generator,” *IOPScience: Superconductor Science and Technology,* vol. 29, no. 2, pp. 1-11, 2016.

[70] Abrahamsen A. G. *et al*., “Feasibility study of 5 MW superconducting wind turbine generator,” *Physica C,* vol. 471, no. 21-22, pp. 1464-1469, 2011.

[71] D. Liu *et al*., “Deliverable D3.42 First assessment of performance indicators of Superconducting direct drive and Pseudo magnetic direct drive generators,” Innwind, 2017.

[72] Gamble B. *et al*, “Full Power Test of a 36.5 MW HTS Propulsion Motor,” *IEEE Transactions on Applied Superconductivity,* vol. 21, no. 3, pp. 1083-1088, 2011.

[73] Parma V., “Cryostat Design CAS - CERN Accelerator School: Course on Superconductivity for Accelerators,” https://doi.org/10.5170/CERN-2014-005), Erice, Italy, 2014.

[74] Y. F. Bi, “Cooling and Coolers for HTS power applications,” *Applied Superconductivity and Electromagnetics* , vol. 4, no. 1, pp. 97-108, 2013.

[75] Frank M. *et al.,* “Thermosyphon Cooling System for the Siemens 400kW HTS Synchronous Machine,” *AIP Conference Proceedings,* vol. 710, pp. 859-866, 2004.

[76] Nick W. *et al.*, “Test Results from Siemens Low-Speed, High-Torque HTS Machine and Description of further Steps towards Commercialization of HTS Machines,” *Physica C: Superconductivity,* vol. 482, no. 20, pp. 105-110, 2012.

[77] Felder B. *et al.*, “A 100-W grade closed-cycle thermosyphon cooling system used in HTS rotating,” *AIP Conference Proceedings,* vol. 1434, no. 417, pp. 417-424, 2012.

[78] Kwon Y. W. *et al.,* “Performance test of a 1 MW class HTS synchronous motor for industrial application,” *Physica C,* vol. 468, pp. 2081-2086, 2008.

[79] Le T. D. *et al.*, “Thermal Design of a Cryogenics Cooling System for a 10 MW-Class High-Temperature Superconducting Rotating Machine,” *IEEE Transactions on Applied Superconductivity,* vol. 25, no. 3, pp. 1-5, 2015.

[80] Le T. D. *et al.*, “Conceptual design of current lead for large scale high temperature superconducting rotating machine,” *Progress in Superconductivity and Cryogenics,* vol. 16, no. 2, pp. 54-58, 2014.

[81] Iwasa Y., Case Studies in Superconducting Magnets: Design and Operational., New York: Springer-Verlag, 2009, pp. 248–252, 400–443, 457–458.

[82] Oerlikon Leybold, “Turbovac50 manual,” Oerlikon Leybold.

[83] Keysan O. and Mueller M., “A Homopolar HTSG Topology for Large Direct-Drive Wind Turbines,” *IEEE Transaction on Applied Superconductivity,* vol. 21, no. 5, pp. 3523-3531, 2011.

[84] Gieras J. F., Advancements in Electric Machines, Springer, 2008.

[85] Gieras J. F. and Wing M., Permanent Magnet Motor Technology, Marcel Dekker Inc, 2002.

[86] Maddison C. P., “Transverse Flux Machines For High Torque Applications,” PhD Thesis, University of Newcastle upon Tyne, 1999.

[87] Ibala A. & Masmoudi A., “A New Reluctance Model of a Claw Pole TFPM Using SMC for the Magnetic Circuit,” in *Ecologic Vehicles - Renewable Energies*, Monaco, 2009.

[88] Tovar-Barranco A. *et al*., "High torque density transverse flux permanent magnet machine design for wind power generation," in *2016 XXII International Conference on Electrical Machines (ICEM),* Lausanne, Switzerland, 2016.

[89] Zhang F. *et al*, "Study on a New Type of Permanent Magnet Claw Pole Motor with Outer Rotor," in *Joint International Conference on Power System Technology and IEEE Power India Conference*, New Delhi, India, 2008.

[90] Tidblad Lundmark S. K. *et al*, "Designs of Claw-Pole Motors for Industrial Applications," in *3rd IET International Conference on Power Electronics, Machines and Drives,* Dublin, Ireland, 2006.

[91] Keysan O. & Mueller M., "A Transverse Flux High-Temperature Superconducting Generator Topology for Large Direct Drive Wind Turbines," *Physics Procedia,* vol. 36, no. 2012, pp. 759-764, 2012.

[92] H. W. Derbas *et al*, "A Comparison of Nodal- and Mesh-Based Magnetic Equivalent Circuit Models," *IEEE Transactions on Energy Conversion,* vol. 24, no. 2, pp. 388 - 396, 2009.

[93] D. C. Horvath *et al,* "A Scaled Mesh/Nodal Formulation of Magnetic Equivalent Circuits With Motion," *IEEE Transactions on Energy Conversion,* vol. 34, no. 1, pp. 58 - 69, 2019.

[94] Vacuumschmelze, "Vacoflux 50 datasheet," http:\\www.vacuumschmelze.com, Received in 2017.

[95] Libert F. *et al*., "Manufacturing Methods of Stator Cores with Concentrated Windings," in *PEMD 2006*, Dublin, Ireland, 2006.

[96] Bernholz J. J. *et al*, "Analytical model for superconducting generators for wave energy systems," in *8th IET International Conference on Power Electronics, Machines and Drives*, Glasgow, UK, 2016.

[97] Kails K. *et al*, "Mass reduction of superconducting power generators for large wind turbines," *The Journal of Engineering,* vol. 2019, no. 17, pp. 3972-3975, 2019.

[98] Grauers A., Design of Direct-driven Permanent-magnet Generators for Wind, PhD thesis: Chalmers University of Technology, 1996.

[99] Qu R. *et al*, "Analysis and modelling of airgap & zigzag leakage fluxes in surface-mounted PM machine," *IEEE Transactions of Industry Applications* , vol. 40, no. 1, pp. 121-127, 2004.

[100] Keysan O. *et al*., "A modular and cost-effective superconducting generator design for offshore wind turbines," *Superconductor Science and Technology,* vol. 28, no. 3, p. 034004, 2015.

[101] Meier F., "Permanent-Magnet Synchronous Machines with Non-Overlapping Concentrated Windings for Low-Speed Direct-Drive Applications.," PhD dissertation, KTH Royal Institute of Technology, 2008.

[102] Zhu Z. Q. *et al*, “Influence of Design Parameters on Cogging Torque in Permanent Magnet Machines,” *IEEE Transactions on Energy Conversion*, vol. 15, no. 4, pp. 407-412, 2000.

[103] Zhu Z. Q. *et al*, “Influence of Pole and Slot Number Combinations on Cogging Torque in Permanent-Magnet Machines With Static and Rotating Eccentricities,” *IEEE Transactions on Industry Applications*, vol. 50, no. 5, pp. 3265 - 3277, 2014.

[104] Patterson D. J. *et al*, “A comparison of radial and axial flux structures in electrical machines,” in *Interational Electric Machines and Drives Conference*, Miami, Florida, 2009.

[105] Taran N. *et al*, “Coreless and Conventional Axial Flux Permanent Magnet Motors for Solar Cars,” *IEEE Transactions on Industry Applications*, vol. 54, no. 6, pp. 5907-5917, 2018.

[106] Torkaman H.*et al*, “Design of Rotor Excited Axial Flux-Switching Permanent Magnet Machine,” *IEEE Transactions on Energy Conversion*, vol. 33, no. 3, pp. 1175-1183, 2018.

[107] Wang Y. *et al*, “Development of a High-Performance Axial Flux PM Machine With SMC Cores for Electric Vehicle Application,” *IEEE Transactions on Magnetics*, vol. 55, no. 7, pp. 1-4, 2019.

[108] Bang D., “Design of transverse flux permanent magnet machines for large direct-drive wind turbines,” PhD Dissertation Delft University of Technology, 2010.

[109] Fujikura, “Model FYSC-SCH04 datasheet,” Fujikura, 2019.

[110] Kails K. *et al*, “T - formulation based numerical modelling of dynamic loss with a DC background field,” in *EUCAS 2019, Journal of Physics: Conference Series*, Glasgow, UK, 2019.

[111] Qiang Jiang Z. *et al*, “HTS Field Coil Optimization for Large Capacity Generators,” *IEEE Transactions on Applied Superconductivity*, vol. 26, no. 7, pp. 1-5, 2016.

[112] McDonald A.S. *et al*, “Structural mass in direct-drive permanent magnet electrical generators,” *IET Renewable Power Generation*, vol. 2, no. 1, pp. 3-15, 2008.

[113] A. Zavvos, “Structural Optimization of Permanent Magnet Direct Drive Generators for 5MW Wind Turbines,” PhD Thesis University of Edinburgh, 2013.

[114] Dorrell D. *et al*, “A Review of the Design Issues and Techniques for Radial-Flux Brushless Surface and Internal Rare-Earth Permanent-Magnet Motors,” *IEEE Transactions on Industrial Electronics*, vol. 58, no. 5, pp. 3741-3757, 2011.

[115] Ubani O. G. *et al*, “Analysis of an air-cored axial flux permanent magnet machine with Halbach array,” in *8th IET Int. Conf. on Power Electronics, Machines and Drives*, Glasgow, 2016.

[116] Keysan O. *et al.*, "C-GEN, a lightweight direct drive generator for marine energy converters," in *PEMD 2010*, Brighton, UK, 2010.

[117] Chan A. *et al.*, "Performance Comparisons Among Radial-Flux, Multistage Axial-Flux, and Three-Phase Transverse-Flux PM Machines for Downhole Applications," *IEEE Transactions on Industry Applications*, vol. 46, no. 2, pp. 779-789, 2010.

[118] Kails K. *et al.*, "Modular and Stackable Power Generators for Efficient Renewable Power Generation," *IET Renewable Power Generation*, vol. 13, no. 15, 2019.

[119] Kasap S. *et al.*, Springer Handbook of Electronic and Photonic Materials, Springer, 2017.

[120] Hoang T.-K. *et al.*, "Design of a 20-MW Fully Superconducting Wind Turbine Generator to Minimize the Levelized Cost of Energy," *IEEE Transactions on Applied Superconductivity*, vol. 28, no. 4, 2018.

[121] Nishimura T. *et al.*, "Potential for Torque Density Maximization of HTS Induction/Synchronous Motor by Use of Superconducting Reluctance Torque," *IEEE Transactions on Applied Superconductivity*, vol. 24, no. 3, 2014.

[122] Jia S. *et al.*, "A Novel Vernier Reluctance Fully Superconducting Direct Drive Synchronous Generator With Concentrated Windings for Wind Power Application," *IEEE Transactions on Applied Superconductivity*, vol. 26, no. 7, p. 5207205, 2016.

[123] Hassan G. G., "A Guide to UK Offshore Wind Operations and Maintenance," Scottish Enterprise and The Crown Estate, 2013.

[124] Cotrell J. *et al*, "Analysis of Transportation and Logistics Challenges Affecting the Deployment of Larger Wind Turbines: Summary of Results," NREL, 2014.

[125] Hong Z. *et al.*, "Numerical solution of critical state in superconductivity by finite element software," *Superconductor Science and Technology*, vol. 19, no. 12, pp. 1246-1252, 2006.

[126] Zermeño V. *et al.*, "Calculation of alternating current losses in stacks and coils made of second generation high temperature superconducting tapes for large scale applications," *Journal of Applied Physics*, vol. 114, 2013.

[127] Kails K. *et al.*, "Loss characteristics of HTS coated conductors in field windings of electric aircraft propulsion motors," *Superconductor Science and Technology*, vol. 33, no. 6, 2020.

[128] Adrianov V *et al.*, "Superconducting materials in oscillating and rotating magnetic fields," *Cryogenics*, vol. 25, no. 5, pp. 266-270, 1985.

[129] Oomen M. P. *et al.*, "Dynamic resistance in a slab-like superconductor with Jc (B) dependence," *Superconductor Science and Technology*, vol. 12, no. 6, 1999.

[130] Li Q *et al,* “Numerical modelling of dynamic loss in HTS-coated conductors under perpendicular magnetic fields,” *IEEE Transactions on Applied Superconductivity,* vol. 31, no. 3, pp. 1-6, 2018.

[131] Jiang Z. *et al*, “Dynamic resistance of a high-T c coated conductor wire in a perpendicular magnetic field at 77 K,” *Superconductor Science and Technology,* vol. 30, no. 3, p. 03LT01, 2017.

[132] Jiang Z. *et al,* “The dynamic resistance of YBCO coated conductor wire: effect of DC current magnitude and applied field orientation,” *Superconductor Science and Technology,* vol. 31, no. 3, 2018.

[133] Ainslie *et al.*, “Numerical modelling of dynamic resistance in high-temperature superconducting coated conductor wires,” *Superconductor Science and Technology,* vol. 31, no. 7, p. 074003, 2018.

[134] Jiang Z. *et al.*, “Dynamic resistance measurement of a four tape YBCO stack in a perpendicular magnetic field,” *IEEE Transactions on Superconductivity,* vol. 28, no. 4, pp. 1-5, 2017.

[135] Liu Y. *et al.*, “Dynamic resistance measurement in a YBCO wire under perpendicular magnetic field at various operating temperatures,” *Journal of Applied Physics,* vol. 126, p. 243904, 2019.

[136] Zermeño V. *et al.*, “A self-consistent model for estimating the critical current of superconducting devices Superconductor Science and Technology,” *Superconductor Science and Technology,* vol. 28, no. 8, 2015.

[137] Masson P.J. *et al.*, “High power density superconducting motor for all-electric aircraft propulsion,” *IEEE Transactions on Applied Superconductivity,* vol. 15, no. 2, pp. 2226-2229, 2005.

[138] Masson P.J. *et al.*, “Design of HTS Axial Flux Motor for Aircraft Propulsion,” *IEEE Transactions on Applied Superconductivity* , vol. 17, no. 2, pp. 1533-1536, 2007.

[139] Manolopoulos C. D. *et al*., “Stator Design and Performance of Superconducting Motors for Aerospace Electric Propulsion Systems,” *IEEE Transactions on Applied Superconductivity,* vol. 28, no. 4, 2018.

[140] Terao Y. *et al*., “Electromagnetic Design of Superconducting Synchronous Motors for Electric Aircraft Propulsion,” *IEEE Transactions on Applied Superconductivity* , vol. 28, no. 4, 2018.

[141] Fukuda S. *et al.*, “Design Study of 2-MW Fully Superconducting Synchronous Motors,” *IEEE Transactions on Applied Superconductivity,* vol. 28, no. 4, 2018.

[142] Dezhin D. S. *et al*., “Design and Testing of 200 kW Synchronous Motor with 2G HTS Field Coils,” *IOP Conf. Series: Earth and Environmental Science,* vol. 87, no. 3, pp. 1-7, 2017.

[143] Zhang H. *et al.*, “Dependence of Dynamic Loss on Critical Current and n-Value of HTS Coated Conductors,” *Superconductor Science and Technology,* vol. 29, no. 8, 2019.

[144] Zhang H. *et al.*, “Modelling of electromagnetic loss in HTS coated conductors over a wide frequency band,” *Superconductor Science and Technology,* vol. 33, no. 2, 2020.

[145] Wang M. *et al*., “An effective way to reduce AC loss of second-generation high temperature superconductors,” *Superconductor Science and Technology,* vol. 32, no. 1, pp. 1-7, 2018.

[146] Hekmati A. *et al.*, “Double-layer rotor magnetic shield performance analysis in hightemperature superconducting synchronous generators under shortcircuit fault conditions,” *Cryogenics,* vol. 80, pp. 147-153, 2016.

[147] Shen B. *et al.*, “Review of the AC loss computation for HTS using H formulation,” *Superconductor Science and Technology,* vol. 33, no. 3, pp. 1-13, 2020.

[148] Pei X. *et al.*, “AC Losses Measurement and Analysis for a 2G YBCO Coil in Metallic Containment Vessels,” *IEEE Transactions on Applied Superconductivity,* vol. 27, no. 4, 2017.

[149] Kim J.-H. *et al.*, “Transport AC Loss Measurements in Superconducting Coils,” *IEEE Transactions on Applied Superconductivity,* vol. 21, no. 3, 2011.

[150] Ainslie M., Transport AC loss in high temperature superconducting coils, PhD Thesis: University of Cambridge, 2014.